Design and Commissioning of Beamlines for the ALPHA Antihydrogen Experiment

Mark A. Johnson

A thesis submitted to the University of Manchester for the degree of
Doctor of Philosophy in the Faculty of Science and Engineering

School of Physics and Astronomy,

The University of Manchester and The Cockcroft Institute,

Manchester, United Kingdom,

2019

Contents

Number of words: 53,960

List of Figures

Abstract

One of the greatest problems facing modern physics is the apparent asymmetry between matter and antimatter. While the standard model of particle physics predicts that equal amounts of matter and antimatter were produced following the Big Bang, astronomical observations have revealed that our universe contains little or no primordial antimatter. Precision measurements of cold, trapped antiparticles can be used to probe fundamental symmetries, and may shed light on why antimatter is so scarce in our universe. The ALPHA experiment at the CERN Antiproton Decelerator studies magnetically trapped antihydrogen atoms, produced by slowly merging cold plasmas of positrons (e^+) and antiprotons ($\bar{p}$). The precision spectroscopy of antihydrogen has already provided unique, high-resolution tests of CPT invariance and theories of new physics beyond the standard model. During 2018, the ALPHA experiment was expanded with the addition of ALPHA-g, a vertical atom trap that is intended to make the first direct measurements of antimatter gravitation.

The efficient transport of $\bar{p}$ and e^+ plasmas into the ALPHA-g experiment will be essential to trapping large numbers of antihydrogen atoms. However, the transfer of low energy ($\lesssim$ 100 eV) charged particles between separate traps with strong magnetic fields is challenging for a variety of reasons. This thesis describes the design and commissioning of charged particle beamlines for the upgraded ALPHA experiment, and the methods that were used to overcome these challenges.

In this thesis, we first describe the development of a novel magnetic beamline for the ALPHA experiment. Semi-analytical and numerical models are used to characterise the dynamics of $\bar{p}$ and e^+ bunches within this beamline. Next, we describe the implementation of the ALPHA-g beamlines at CERN during 2018. We review the specifications of the beamline magnets, and describe the control system used to manage their operation. Finally, a range of diagnostic tools are developed to experimentally measure the properties of actual $\bar{p}$ and e^+ bunches. We combine data from a range of sources to evaluate the performance of the beamline, and show that large numbers of positrons and antiprotons can already be delivered to the ALPHA-g experiment. In summary, the work presented in this thesis is critical to a future ±1% measurement of antimatter gravitation, as well as continued precision measurements of antihydrogen atoms.

Declaration

The work contained within this thesis was undertaken between October 2015 and November 2018 while the author was a PhD student under the supervision of Dr William Bertsche at the University of Manchester. No portion of the work referred to in this thesis has been submitted in support of an application for another degree or qualification of The University of Manchester, or any other university or other institute of learning.

Copyright

iii. The ownership of certain Copyright, patents, designs, trademarks and other intellectual property (the "Intellectual Property") and any reproductions of copyright works in the thesis, for example graphs and tables ("Reproductions"), which may be described in this thesis, may not be owned by the author and may be owned by third parties. Such Intellectual Property and Reproductions cannot and must not be made available for use without the prior written permission of the owner(s) of the relevant Intellectual Property and/or Reproductions.

iv. Further information on the conditions under which disclosure, publication and commercialisation of this thesis, the Copyright and any Intellectual Property and / or Reproductions described in it may take place is available in the University IP Policy, in any relevant Thesis restriction declarations deposited in the University Library, The University Library's regulations and in The University's policy on Presentation of Theses.

Dedicated to Grandma and Grandad

Acknowledgements

First of all, thank you to my amazing family - Mum, Dad and Helen - for always believing in me, and supporting me even while I was studying away from home in Geneva. For as long as I can remember, you have always encouraged me to follow my dreams and make the most of every opportunity, and I couldn't have done this without you. I would like to thank my teachers from over the years, particularly Keith Caulkin, David Mercer and Nick Cowan, who inspired me to learn more about the universe and gave me the tools to do so.

During my PhD, I have been incredibly fortunate to work with a fantastic team of people within the ALPHA collaboration. I would like to thank my supervisor, Dr William Bertsche, for sharing his enthusiasm, guidance, and seemingly endless knowledge of physics throughout my PhD. I am grateful to the senior members of the ALPHA collaboration, particularly Prof. Jeff Hangst and Prof. Niels Madsen, for the opportunity to contribute to such an amazing experiment. I have learned an enormous amount from working with each and every member of the ALPHA collaboration, and I cannot thank them enough. ALPHA is a collaboration where students and young researchers can genuinely contribute to a cutting-edge scientific endeavour, and I cannot think of anywhere better to have completed my PhD studies.

I have been fortunate to share my time at ALPHA with many close friends and colleagues, who shared all of the excitement and frustration, and somehow made it bearable (and maybe even enjoyable) to work long hours and endless night shifts.

I would particularly like to thank Andrea Capra, Celeste Carruth, Andrew Evans, Tim Friesen, Pierre Grandemange, Jack Jones, Steven Jones, Alex Khramov, Pete Knapp, Dan Maxwell, Joseph McKenna, Patrick Mullan, Asia Peszka, Chris Rasmussen, Muhammed Sameed, Graham Stutter and Bruno Ximenez. The last few years would have been much harder without all of the coffee breaks, cycling adventures around Geneva, and regular trips to O'Brasseur. Special thanks go to my former flatmates, Alex Titterton and Tom Hadavizadeh, for putting up with strange working hours and endless night shifts during my PhD.

I would like to acknowledge the financial support of the Science and Technology Facilities Council (STFC) and the Cockcroft Institute towards this work. The highlight of my PhD was a two-year Long Term Attachment (LTA) placement to CERN, and I am grateful to all of the staff at the CERN UK Liason Office (UKLO) for their help during my stay in Geneva.

Author Contributions

The operation of the ALPHA experiment is made possible by the collaborative efforts of a large number of people. As a result, most work on the ALPHA experiment cannot be claimed by any single author, and the work presented in this thesis is no exception. I am proud to have worked with so many able and dedicated colleagues throughout the production of my PhD thesis.

- The development of the conceptual beamline design described in Chapter 3 of this thesis was primarily my own work. I personally developed all of the semi-analytical models and numerical simulation tools described in Chapters 3 and 4, and applied them to characterize and develop this beamline design.
- The electromechanical design of the beamline was a collaborative effort between myself, Dr William Bertsche, and a large number of engineering staff at STFC Rutherford Appleton Laboratory (RAL). The manufacture of the ALPHA-g beamline was primarily completed at RAL, with contributions from the CERN Normal Conducting Magnets (MNC) group. The physical assembly of the ALPHA-g apparatus was the result of intensive efforts by many members of the ALPHA collaboration, including the author.
- I was personally responsible for the design, assembly and commissioning of the control hardware and electronics described in Chapter 5. I wrote the majority of the control software for the beamline, with some initial help from Dr William Bertsche and Dr Daniel Maxwell.

- While the experimental commissioning of the ALPHA-g beamlines and particle traps was also a collaborative effort, I was heavily involved throughout this process. I personally led the commissioning of the beamline, and worked closely with Dr Chris Ørum Rasmussen and Dr Celeste Carruth on the commissioning of the ALPHA-g particle traps. Dr Andrea Capra and Dr Joseph McKenna led the commissioning of the TPC detector that is referred to in this thesis. Throughout this project I worked closely with Dr Muhammed Sameed, who led the recommissioning of the positron accumulator during 2018.

Publications

During the preparation of this thesis, the author contributed towards the operation of the ALPHA experiment and data taking for the following publications:

- **Observation of the 1S-2S transition in trapped antihydrogen** [3]

  M. Ahmadi et al., Nature, vol. 541, pp. 506–510, 2016

- **Observation of the hyperfine spectrum of antihydrogen** [4]

  M. Ahmadi et al., Nature, vol. 548, no. 7665, pp. 66–69, 2017

- **Antihydrogen accumulation for fundamental symmetry tests** [5]

  M. Ahmadi et al., Nature Communications, vol. 8, no. 1, p. 681, 2017

- **Characterization of the 1S–2S transition in antihydrogen** [2]

  M. Ahmadi et al., Nature, vol. 557, no. 7703, pp. 71–75, 2018

- **Observation of the 1S–2P Lyman-α transition in antihydrogen** [1]

  M. Ahmadi et al., Nature, vol. 561, no. 7722, pp. 211–215, 2018

- **Enhanced control and reproducibility of non-neutral plasmas** [6]

  M. Ahmadi et al., Phys. Rev. Lett., vol. 120, p. 025001, Jan 2018

Definitions and Symbols

Fundamental Constants

Symbol	**Name**	**Value**	**SI Units**
g	Gravitational acceleration	9.81	$\mathrm{m} \cdot \mathrm{s}^{-2}$
k_B	Boltzmann constant	1.38×10^{-23}	$\mathrm{J} \cdot \mathrm{K}^{-1}$
q	Elementary charge	1.60×10^{-19}	C
m_{e}	Rest mass of the electron	9.11×10^{-31}	kg
$m_{\bar{\mathrm{p}}}$	Rest mass of the proton	1.67×10^{-27}	kg
ε_0	Vacuum permittivity	8.85×10^{-12}	$\mathrm{F} \cdot \mathrm{m}^{-1}$
μ_0	Vacuum permeability	1.26×10^{-6}	$\mathrm{H} \cdot \mathrm{m}^{-1}$
μ_B	Bohr Magneton	9.27×10^{-24}	$\mathrm{J} \cdot \mathrm{T}^{-1}$

Particles and Bound States

Symbol	**Name**
e^+	Positron
e^-	Electron
$\bar{\mathrm{H}}$	Antihydrogen
p	Proton
$\bar{\mathrm{p}}$	Antiproton
$\bar{\mathrm{p}}\mathrm{He}^+$	Antiprotonic Helium
$h\nu$	Photon
$\pi^\pm$	Charged pion
π^0	Neutral pion

Vector Notation

Throughout this thesis, two coordinate systems are used extensively. In Cartesian coordinates, positions are decomposed into components along three fixed, orthogonal axes labelled x, y and z. In cyclindrical coordinates, the direction of the z axis remains fixed, while the position perpendicular to this axis is described by a distance $r = \sqrt{x^2 + y^2}$ and an angle $\theta = \tan^{-1}(y/x)$.

Vector Notation (Continued)

In this thesis, vector quantities are denoted by symbols in **bold face**. The three vector components are denoted using subscripts, such that
$\mathbf{a} = \left(a_x\,\hat{\imath} + a_y\,\hat{\jmath} + a_z\,\hat{k}\right) = \left(a_r\,\hat{r} + a_\theta\,\hat{\theta} + a_z\,\hat{k}\right)$.

Mathematical Symbols

Symbol	Definition	SI Units
$\mathbf{A}$	Magnetic vector potential	$\mathrm{T} \cdot \mathrm{m}$
$b_\perp$	Plasma radius	m
$\mathbf{B}$	Magnetic field	T
C	Capacitance	F
$\mathbf{E}$	Electric field	$\mathrm{V} \cdot \mathrm{m}^{-1}$
$E_\perp$	Transverse energy	J
$E_\parallel$	Longitudinal energy	J
f	General function	
$\mathbf{F}$	Force	N
i, j, k	Integer indices	
$\hat{\imath}$, $\hat{\jmath}$, $\hat{k}$	Cartesian unit vectors	
I_n	$n \times n$ Identity matrix	
J	Current density	$\mathrm{A} \cdot \mathrm{m}^{-2}$
k_l	Larmor wavenumber	m^{-1}
K	Perveance	
L	General length scale	m
$\mathcal{L}$	Lagrangian	J
m	Particle mass	kg
n	Number density	m^{-3}
N	Number of particles	
$\mathbf{p}$	Momentum	$\mathrm{kg} \cdot \mathrm{m} \cdot \mathrm{s}^{-1}$
P	Power	$\mathrm{J} \cdot \mathrm{s}^{-1}$
P_θ	Conserved angular momentum	$\mathrm{J} \cdot \mathrm{s}$
Q	Charge	C
r	Radius	m
r_L	Larmor radius	m
$\mathbf{R}$	Radius of curvature	m
s	Longitudinal distance	m

Mathematical Symbols (Continued)

Symbol	Definition	SI Units
t	Time	s
T	Temperature	K
$\mathbf{v}$	Velocity	$\mathrm{m} \cdot \mathrm{s}^{-1}$
V	Voltage	V
$\mathbf{x}$	Position	m
α	Skewness	
γ	Adiabaticity parameter	
Γ	Beam magnetization	m
ε	General small parameter	
$\varepsilon_\perp$	Transverse emittance	$\mathrm{m} \cdot \mathrm{rad}$
η	Baryon asymmetry of the universe	
θ	Azimuthal coordinate	rad
κ	Integration wavenumber	m^{-1}
μ	Magnetic moment	$\mathrm{J} \cdot \mathrm{T}$
ρ	Charge density	$\mathrm{C} \cdot \mathrm{m}^{-3}$
σ_E	Longitudinal energy spread	J
σ_τ	Longitudinal bunch length	m
$\sigma_\perp$	Transverse beam radius	m
τ_c	Cyclotron period	s
ϕ	Electric scalar potential	V
φ	Polar angle	rad
ω_c	Cyclotron frequency	s^{-1}
ω_r	Plasma rotation frequency	s^{-1}
Ω	Magnetic field matrix	

1 | Introduction

One of the greatest challenges facing modern physics is the apparent asymmetry between matter and antimatter. While the Standard Model (SM) of particle physics predicts that equal amounts of matter and antimatter should have been created following the Big Bang, astronomical observations have revealed that our universe contains little or no primordial antimatter. The ALPHA experiment at the CERN Antiproton Decelerator (AD) aims to provide unique tests of fundamental symmetries by studying the properties of magnetically trapped antihydrogen atoms. During 2018, the ALPHA experiment was expanded to include ALPHA-g, a tall, vertical atom trap designed to make the first precision measurements of antimatter gravitation. As part of this expansion, new charged particle beamlines were required to facilitate the transfer of cold positron and antiproton plasmas into the new atom trap prior to antihydrogen production. This thesis describes work towards the design, simulation and experimental commissioning of the ALPHA-g beamlines.

The structure of this thesis is as follows: Chapter 1 outlines our motivations for studying antimatter, and reviews the goals and recent achievements of experiments at the CERN AD facility. Chapter 2 explores simple analytical models and numerical simulation methods for describing the motions of charged particles in an electromagnetic field. Chapter 3 gives an overview of the final beamline design for the ALPHA experiment, while Chapter 4 details the results of numerical particle tracing simulations that were used to characterise and develop this design.

In Chapter 5, the physical hardware and control systems used to implement the design are described, while Chapter 6 summarises the performance of the beamlines during their commissioning, and presents an analysis of experimental data taken during this period. Finally, in Chapter 7 the results of this thesis are summarised, and future improvements to the ALPHA charged particle beamlines are explored.

1.1 A Short History of Antimatter

1.1.1 Prediction and Discovery

In 1928, Paul Dirac proposed an extension [7] to the famous Schrödinger equation that combined ideas from both quantum mechanics and the theory of special relativity. While this new equation offered two solutions that successfully described both spin states of the electron, it also allowed for two additional solutions with negative energies that initially proved difficult to interpret or even dismiss [8].

Over the following three years, further correspondence with Oppenheimer, Weyl [9] and other prominent physicists convinced Dirac that these solutions in fact described an entirely new particle, originally referred to as an "anti-electron" [10]. While such a particle was yet to be observed in nature, these solutions to the Dirac equation described a mirror image counterpart to the negatively charged electron, with exactly the same mass but an equal and opposite electric charge.

In one of the greatest successes of theoretical physics, these predictions were proven correct in 1932 with the discovery of the positron (denoted e^+) in cloud chamber experiments by Carl Anderson [11,12]. Today, it is known that for every particle in nature there exists a corresponding antiparticle, and the observation of the positron was soon followed by the discoveries of the antiproton (denoted $\bar{\mathrm{p}}$) and anti-neutron at the Bevatron accelerator facility between 1955 and 1956 [13,14].

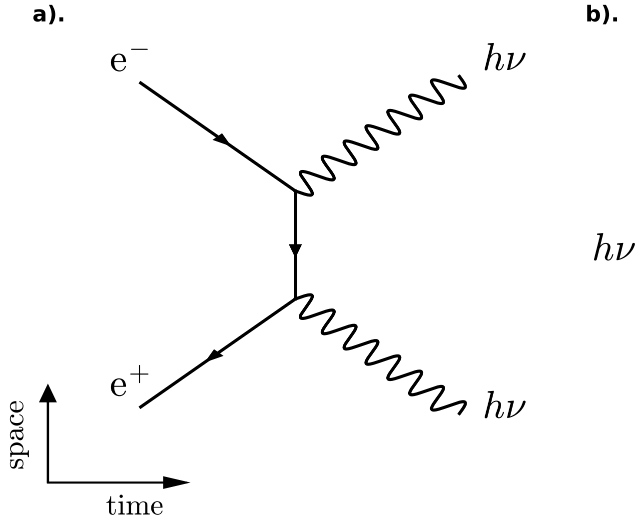

Figure 1.1: Leading order Feynman diagrams for the a). annihilation and b). pair production of an electron-positron pair

In addition to their opposing electric charges, particle-antiparticle pairs are also characterised by their distinctive interactions with one another. When placed into close proximity, antiparticles such as $\bar{\mathrm{p}}$ and e^+ can *annihilate* with their matter counterparts, entirely converting the mass and energy of both particles into a pair of energetic photons ($h\nu$) or massive decay products such as pions ($\pi^{\pm}$, π^0).

Conversely, an individual photon of sufficiently high energy can also undergo *pair production*, resulting in the spontaneous creation of a particle-antiparticle pair at the expense of the original photon. Figure 1.1 shows the simplest Feynman diagrams for each of these interactions between an electron and positron.

1.1.2 The Baryon Asymmetry Problem

The Standard Model of particle physics incorporates three fundamental symmetries: Charge conjugation (C), Parity inversion (P) and Time reversal (T). Charge conjugation refers to the inversion of all fundamental charges in nature, such as the electromagnetic charge and the colour charge involved in the strong interaction.

Likewise, the parity inversion and time reversal transformations reverse the coordinates used to describe an event in space and time, respectively.

Around the time when antimatter was first discovered, it was thought that all physical phenomena should be invariant under the action of any one of these transformations. In this case, antimatter should be an exact mirror image of normal matter, and the original amounts of matter and antimatter in any system should be conserved over time [15]. Since the local universe is overwhelmingly dominated by normal matter, and antimatter had only briefly been observed in cosmic rays and other high-energy phenomena, this raised the troubling prospect that our universe had simply been born with an enormous excess of normal matter.

Meanwhile, the early twentieth century also saw rapid advances in our understanding of the early universe. Theoretical work by Alexander Friedmann and Georges Lemaître [16–18] between 1922 and 1927 suggested that the universe itself was expanding over cosmological timescales, and this idea was soon backed up by Edwin Hubble's discovery of a distance-redshift relation for extragalatic objects in 1929 [19]. The concept of an expanding universe naturally led to the development of a new cosmological model based around an extremely hot and dense early universe, created in what is now known as the Big Bang. Throughout its development this model has proven highly successful, providing extremely accurate predictions for the power spectrum of temperature variations in the Cosmic Microwave Background (CMB) [20] and the abundances of light elements in the contemporary universe [21, 22].

In this model of cosmology, equal amounts of matter, antimatter and radiation would have existed while the universe was hot enough for pair production and annihilation to occur simultaneously in thermal equilibrium. However, once the expanding universe became too cold for pair production to continue, the vast majority of matter and antimatter would have been eliminated through annihilation interactions.

If our universe is truly dominated by normal matter, and contains little or no primordial antimatter, some process must have created a small excess of normal matter in the very early universe for the cosmos to evolve into its current state. The development of this excess is referred to as *baryogenesis*.

Clearly, the process of baryogenesis is incompatible with any model of fundamental physics in which matter and antimatter are exact mirror images of one another. In 1967, Andrei Sakharov set out three conditions [23] necessary for generating a baryon asymmetry in the universe. These "Sakharov criteria" are:

1. At least one baryon-number violating process,
2. Violation of the C and CP symmetries,
3. Interactions outside of thermal equilibrium.

While it was already well established that the C and P symmetries are maximally violated by processes involving the weak interaction [24], it was believed for many years that physical phenomena should still be invariant under the combined CP transformation. However, the 1964 discovery of CP violation in neutral kaon decays by James Cronin and Val Fitch [25] showed that this symmetry could also be broken.

In the modern framework of the standard model, the existence of CP violation is accounted for by a single complex phase in the Cabibbo-Kobayashi-Maskawa (CKM) matrix, which describes the mixing of quark flavours by the weak interaction [26]. Today, it is thought that only the combined CPT symmetry is still valid, and it can be shown that violation of this symmetry would have implications for other basic principles such as Lorentz invariance [27].

1.1.3 Contemporary Studies of Antimatter

The development of modern astronomical instruments has allowed us to set limits on the amount of antimatter remaining in the contemporary universe. For example, the baryon asymmetry of the universe can be defined as [15]

$$\eta = \left.\frac{N_B - N_{\bar{B}}}{N_B + N_{\bar{B}}}\right|_{T=3\mathrm{K}} = \left.\frac{N_B - N_{\bar{B}}}{N_\gamma}\right|_{T=3\mathrm{K}} \simeq \left.\frac{N_B}{N_\gamma}\right|_{T=3\mathrm{K}}, \tag{1.1}$$

where N_B is the number of baryons, $N_{\bar{B}}$ is the (negligible) number of antibaryons, and N_γ is the number of photons. This parameter can be evaluated by comparing a variety of astronomical data [20–22] to cosmological models, and is consistently found to be in the region of 10^{-10}. As such, the initial asymmetry between matter and antimatter in our universe is believed to have been exceptionally small.

Likewise, if significant regions of antimatter were to exist in isolation from the rest of the universe, annihilations at the boundaries between these regions and the normal interstellar medium should leave a distinctive signal in gamma ray spectra, with a broad peak centrered around the rest mass of the positron at 511 keV [26]. No such signal has yet been observed, implying that our universe is indeed dominated by matter across distance scales comparable to the size of the observable universe.

Given the extremely small value of η established by cosmological observations, it can be expected that the levels of CP violation required to produce a matter-dominated universe would be similarly small. However, the levels of CP violation indicated by recent measurements of standard model parameters appear insufficent for explaining the dominance of matter over antimatter that is seen today. As such, a wide range of experiments have been established to search for new sources of CP violation beyond the limits of the standard model.

Many contemporary experiments search for new sources of CP violation by making precision measurements of high energy phenomena. For example, the LHCb experiment at CERN's Large Hadron Collider (LHC) studies the decays of exotic hadrons produced in proton-proton collisions at an energy of 13 TeV [28–30]. Similarly, the T2K collaboration recently found hints of CP violation in the neutrino sector [31] by measuring the composition of an intense beam of neutrinos produced at J-PARC and detected by the Super-Kamiokande detector some 295 km away.

In addition to these efforts, it is also possible to search for symmetry violations at much lower energies by studying the properties of cold, trapped antiparticles. A range of experiments at the CERN Antiproton Decelerator facility [32] aim to make extremely precise measurements of trapped antiprotons and antihydrogen atoms, in order to compare these to similar measurements in normal matter. The ALPHA collaboration, which has operated an experiment at the AD since 2005, recently succeeded in making the first spectroscopic measurements of trapped antihydrogen atoms [1–4].

1.1.4 Antimatter Gravitation

In recent years, a number of authors have proposed alternative cosmological models [33, 34] where the gravitational acceleration of antimatter is different to that of normal matter. These models attempt to explain the dominance of matter over antimatter in our universe, while also offering a new perspective on cosmological problems posed by the apparent existence of dark matter [35] and dark energy [36, 37]. However, these models are not consistent with the Weak Equivalence Principle (WEP), a cornerstone of the theory of general relativity. The weak equivalence principle states that any test mass at a given point in space-time should experience exactly the same acceleration due to gravity, regardless of its composition or rest mass.

Many compelling arguments already exist to suggest that the gravitational acceleration of antimatter ($\bar{g}$) cannot be different to that of normal matter (g). However, no direct experimental evidence currently exists to confirm this. While a number of authors have attempted to use experiments involving normal matter to set limits on the gravitational acceleration of antimatter [38], these arguments are indirect and cannot be considered to be model independent. Directly measuring the gravitational acceleration of antimatter would therefore provide a unique test of one of the most successful theories in modern fundamental physics.

In recent years, measurements using trapped antihydrogen atoms have been used to constrain differences between the gravitational acceleration of matter and antimatter [39,40]. However, these measurements are insensitive to the most interesting regime where $\bar{g} \simeq g$ due to the geometry of the apparatus that was used. Over the coming years, the ALPHA-g experiment will measure the free fall acceleration of antihydrogen to within $\pm$ 1%.

1.2 Experiments with Cold Antimatter

1.2.1 The Antiproton Decelerator

The Antiproton Decelerator began operations at CERN in 1999, three years after its predecessor, the Low Energy Antiproton Ring (LEAR), had been shut down. While LEAR was originally designed as a storage ring for high-intensity antiproton beams, the AD was specifically optimised to provide low energy antiproton bunches to a range of experiments testing CPT invariance through the production and spectroscopy of $\bar{\mathrm{p}}$ bound states. The AD is a 188 m circumference synchrotron that provides a pulsed beam of around 3×10^7 $\bar{\mathrm{p}}$ to any one of five experimental areas, at a rate of one pulse every $\sim$ 100 seconds [32]. Figure 1.2 shows the locations of the AD and ALPHA within the CERN accelerator complex.

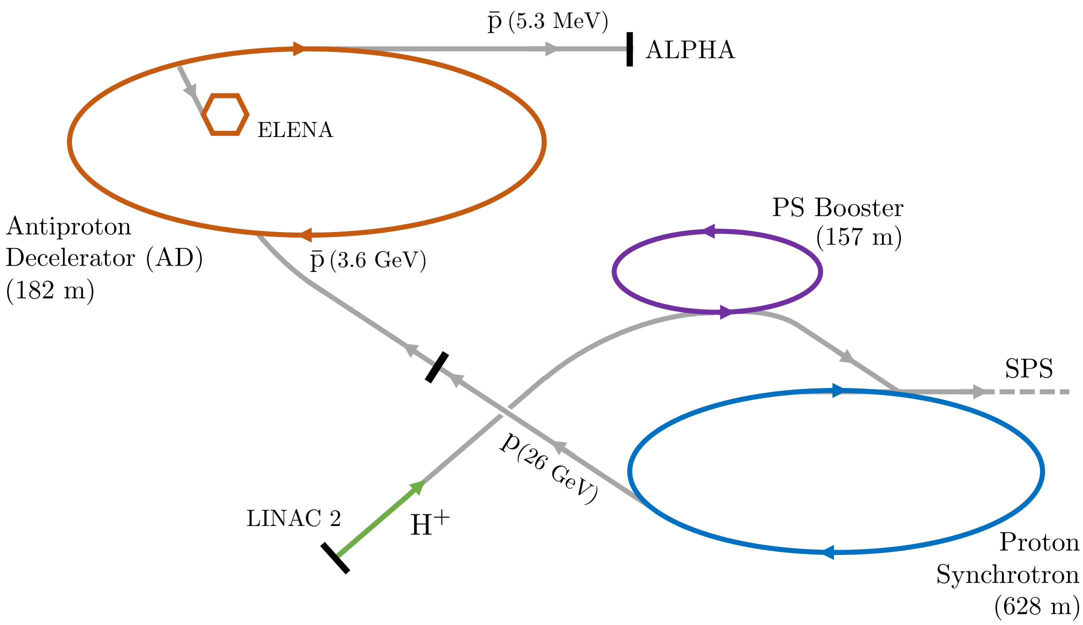

Figure 1.2: Simplified schematic showing the locations of the AD and ALPHA experiment within the CERN accelerator complex.

Antiprotons are produced for the AD by colliding the 26 GeV proton beam of the CERN Proton Synchrotron (PS) into a fixed iridium target. These collisions are sufficiently energetic that in a small fraction of cases, proton-antiproton pairs are produced as secondary particles. Due to their inverted, negative charges, the resulting antiprotons can be filtered out and injected into the AD ring with energies in the region of ~ 3.6 GeV.

Once captured by the AD, these energetic antiprotons must be decelerated by several orders of magnitude before they can be considered useful for trapping experiments. While the AD can gradually decelerate $\bar{p}$ bunches using a series of radiofrequency (RF) cavities, it must also combat the increase in beam divergence that is normally associated with this deceleration. As such, techniques such as stochastic cooling and electron cooling are employed during each AD cycle to control the size and momentum spread of the circulating $\bar{p}$ beam. At the end of a normal decelerator cycle, a ~ 100 ns long pulse of antiprotons is ejected to an experiment at an energy of 5.3 MeV, with a momentum spread of just ~ 0.01 % [32].

Many experiments at the AD use Penning traps (See Section 2.2 of this thesis) to confine and manipulate antiprotons and other charged particles [41,42]. However, $\bar{\mathrm{p}}$ bunches ejected by the AD are still far too energetic to be captured directly into a Penning trap. As a result, the majority of AD experiments employ degrader foils to scatter a fraction of the incoming $\bar{\mathrm{p}}$ to lower energies before attempting to capture them. This process is extremely inefficient, and typically results in the loss of $\sim 99\%$ of incoming antiprotons as they pass through the degrader foils.

The ASACUSA collaboration have developed a Radio Frequency Quadrupole (RFQD) system that focuses $\bar{\mathrm{p}}$ bunches in the transverse plane while further decelerating them to energies as low as 10 keV [32,43]. This device produces a significantly higher yield of useful antiprotons, with an efficiency of up to $\sim 25\%$.

In the near future, the performance of the AD will be significantly upgraded with the addition of ELENA, a secondary decelerator with a circumference of only 30 m [44]. Once operational, ELENA will accept $\bar{\mathrm{p}}$ bunches delivered by the AD and further decelerate them to an energy of 100 keV before extraction to the experiments. This reduction in beam energy should allow experiments to use much thinner degrader foils, and therefore drastically increase the number of antiprotons caught per cycle.

1.2.2 The Antihydrogen Atom

Antihydrogen ($\bar{\mathrm{H}}$) is the stable bound state of a positron and antiproton. According to the CPT theorem, atomic antihydrogen should have exactly the same energy levels, mass and electric charge as the simple hydrogen atom around which much of modern physics was developed. Our advanced understanding of the hydrogen atom's structure, both in terms of theory and experiment, makes antihydrogen an ideal candidate for highly sensitive tests of CPT invariance.

By precisely measuring the properties of antihydrogen atoms and comparing these to existing measurements in normal hydrogen, it should be possible to test concepts such as CPT symmetry and Lorentz invariance to unprecedented levels of precision. These comparisons allow us to constrain models of new physics such as the Standard Model Extension [45] that can explicitly violate Lorentz invariance, and will accommodate processes that break the CPT symmetry as a result.

For example, the 1S-2S transition of the hydrogen atom has an extremely narrow natural linewidth of only 1.3 Hz. This transition can be excited through a two-photon transition by irradiating hydrogen atoms with an ultraviolet (UV) laser at a wavelength of 243 nm. Recent state-of-the-art measurements of the hydrogen 1S-2S transition frequency by Theodor Hänsch and colleagues have achieved a relative precision better than one part in 10^{14} [46, 47]. Developing the tools for a similar measurement in antihydrogen would allow us to test CPT invariance at the highest precision, and has been a primary goal of the AD physics program since its inception.

In addition to precision spectroscopy experiments, cold antihydrogen can also be used to probe the effect of gravity on antimatter. Historically, attempts to directly measure the effect of gravity on a pure antimatter system have proven impossible, primarily due to the short lifetimes of most antimatter species and the relative weakness of the gravitational interaction. While some species such as e^+ are readily available in nature and can be held for long timescales in storage rings or charged particle traps, they are subject to electromagnetic forces that can easily overwhelm the small influence of gravity. In contrast, antihydrogen should be electrically neutral and have a long lifetime when held in isolation from normal matter, making it ideal for tests of the weak equivalence principle. In recent years, measuring the gravitational acceleration of antihydrogen has become a major goal for several AD experiments [48, 49], which are described in detail in the following section.

1.2.3 Antihydrogen Experiments

The first antihydrogen produced in a laboratory was observed by the PS210 collaboration during experiments at the LEAR facility in 1995. In these experiments, a xenon (Xe) gas target was placed into the path of an intense, relativistic (~ 2 GeV) $\bar{\text{p}}$ beam circulating within the LEAR storage ring. Occasionally, $\bar{\text{p}}$ passing through this target would be scattered by a Xe nucleus, resulting in the production of an electron-positron pair [32]. In a small fraction of cases, the resulting e^+ would emerge from the target with a velocity matching that of the scattered $\bar{\text{p}}$, leading to the production of a fast-moving antihydrogen atom.

Over 15 hours of beam time, around a dozen antihydrogen atoms were detected using this method [50]. In 1998, the E862 experiment at Fermilab also succeeded in detecting 57 $\bar{\text{H}}$ atoms using a similar apparatus [51]. However, the small numbers of fast-moving $\bar{\text{H}}$ that could be produced using this technique made it unsuitable for precision experiments.

With the commissioning of the AD in 1999, attention began to turn towards the production of cold antihydrogen atoms. The first antihydrogen atoms to be produced from trapped plasmas of $\bar{\text{p}}$ and e^+ were independently reported by the ATHENA [52, 53] and ATRAP [54] collaborations in 2002. In these experiments, antiprotons were captured from the AD and stored inside a Penning-Malmberg trap (see Section 2.2), where they could be combined with an overlapping cloud of positrons accumulated using a buffer gas trap [55]. Although far colder than the anti-atoms previously produced by experiments at LEAR, the $\bar{\text{H}}$ formed by ATHENA and ATRAP would either annihilate or be ionized too quickly for useful studies of its properties.

In 2010, the ALPHA collaboration [56] reported the first trapping of antihydrogen atoms using a shallow magnetic minimum trap [57].

Shortly afterwards, this milestone was also achieved by the ATRAP collaboration [58] and by the following year, further experiments with the ALPHA apparatus had succeeded in confining $\bar{\mathrm{H}}$ for timescales of 1000 seconds or more [59]. Semi-classical calculations [58, 60] indicate that $\gtrsim 99\%$ of $\bar{\mathrm{H}}$ atoms should relax into the ground state within half a second of confinement. Therefore, the antihydrogen atoms produced by ALPHA and ATRAP were finally suitable for precision spectroscopy.

Today, the AD hosts six experiments (AEgIS, ALPHA, ASACUSA, ATRAP, BASE and GBAR) pursuing a variety of different physics goals. The ALPHA experiment [56], described in Section 1.3 of this thesis, aims to precisely measure the properties of antihydrogen atoms held within a shallow (~ 0.54 K) magnetic minimum trap. While the ALPHA apparatus was primarily designed to make detailed measurements of the $\bar{\mathrm{H}}$ spectrum, it has also been used to test the charge neutrality [61,62] and gravitational mass [39] of trapped antihydrogen atoms. The ATRAP collaboration, who also intend to characterise the spectra of antihydrogen atoms held inside a magnetic minimum trap, employ a slightly different trap geometry and $\bar{\mathrm{H}}$ detection scheme [58, 63].

Meanwhile, the ASACUSA collaboration intend to study $\bar{\mathrm{H}}$ produced in the form of a spin-polarized beam [64]. By probing such a beam with microwave radiation as it traverses a magnetically field-free region, the hyperfine splitting of antihydrogen's ground state can be measured to a high precision [65]. In experiments such as ALPHA and ATRAP, these hyperfine transitions are dramatically shifted by the strong magnetic fields of the neutral atom trap. In 2010, ASACUSA demonstrated the production of cold $\bar{\mathrm{H}}$ inside a cusp trap geometry [66], and later detected anti-atoms that had been ejected from this trap in the form of an atomic beam [67].

More recently, the AEgIS and GBAR experiments were established to pursue the first measurements of antimatter's gravitational acceleration.

Like ASACUSA, the AEgIS apparatus [49] was also designed to produce cold antihydrogen beams, which will be passed through a Moiré deflectometer [68] to form an interference pattern on an emulsion detector with a high spatial resolution [69]. By determining the shift of the Moiré pattern imaged on this detector, the in-flight deflection of the $\bar{\mathrm{H}}$ beam under gravity should be measurable to a precision of $\sim 1\%$.

The GBAR collaboration recently completed the initial installation of their apparatus at CERN, and will pursue a novel scheme to produce neutral antihydrogen from the photoionisation of ultracold ($\sim$10 μK) $\bar{\mathrm{H}}^+$ ions held inside a linear Paul trap [48,70,71]. Upon escaping from the trap volume, the neutral $\bar{\mathrm{H}}$ will fall a known distance towards an annihilation detector at the base of the apparatus, allowing the time of flight between their ionisation and annihilation to be reconstructed. Using this method, the GBAR collaboration hope to measure the free fall acceleration of antihydrogen to within ±1% by the year 2021.

Since first trapping antihydrogen in 2010, the ALPHA collaboration have made significant progress towards probing a number of antihydrogen's optical [1–3] and hyperfine [4, 72] transitions. Figure 1.3 shows a Breit-Rabi diagram for the 1S, 2S and 2P energy levels of the hydrogen atom. A selection of recent results published by the ALPHA collaboration are highlighted below:

Hyperfine Spectroscopy of Antihydrogen

When placed into an external magnetic field, the ground state of the hydrogen atom is split into four separate hyperfine states due to coupling between the magnetic moment of the proton and the motion of the orbiting electron. While two of these states gain energy in an increasing magnetic field, and can therefore be confined by a three-dimensional magnetic minimum trap, the remaining hyperfine states will seek out higher magnetic fields and are untrappable as a result.

In a uniform 1 T magnetic field, transitions between these hyperfine states can be induced by exposing hydrogen atoms to microwave radiation at a resonant frequency of around $\sim$ 29 GHz.

In 2012, the ALPHA collaboration observed the first ever quantum transitions in antihydrogen by exposing small numbers of trapped anti-atoms to resonant microwave radiation, leading to their ejection from the magnetic minimum trap [72]. During 2016, a similar technique was used to measure the ground state hyperfine splitting of antihydrogen. In these experiments, the frequency of the injected microwaves was gradually stepped across the two resonant frequencies where trapped $\bar{\mathrm{H}}$ should be spin flipped and ejected from the neutral atom trap. By searching for the onset of annihilation events as the microwave frequency hit each of these resonances, and measuring the difference in frequency between them, the hyperfine splitting was found to be 1420.4 ± 0.5 MHz. This result is consistent with CPT invariance to a precision of around 4×10^{-4} [4].

1S-2S Spectroscopy

One of the primary goals of the ALPHA experiment is to precisely characterise the 1S-2S transition of trapped antihydrogen atoms. As such, the ALPHA-II apparatus was designed so that UV laser light could be introduced to a Fabry-Pérot build-up cavity inside the cryogenic, Ultra High Vacuum (UHV) space of the atom trap itself. When this cavity is locked to the resonant frequency of the 1S-2S transition, trapped $\bar{\mathrm{H}}$ passing through the centre of the atom trap can be excited into the 2S state by the absorption of two counter-propagating 243 nm photons.

Excited anti-atoms are readily ejected from the magnetic minimum trap, either due to ionisation (caused by the absorption of an additional 243 nm photon) or through a single-photon decay into an untrapped (high-field-seeking) hyperfine state.

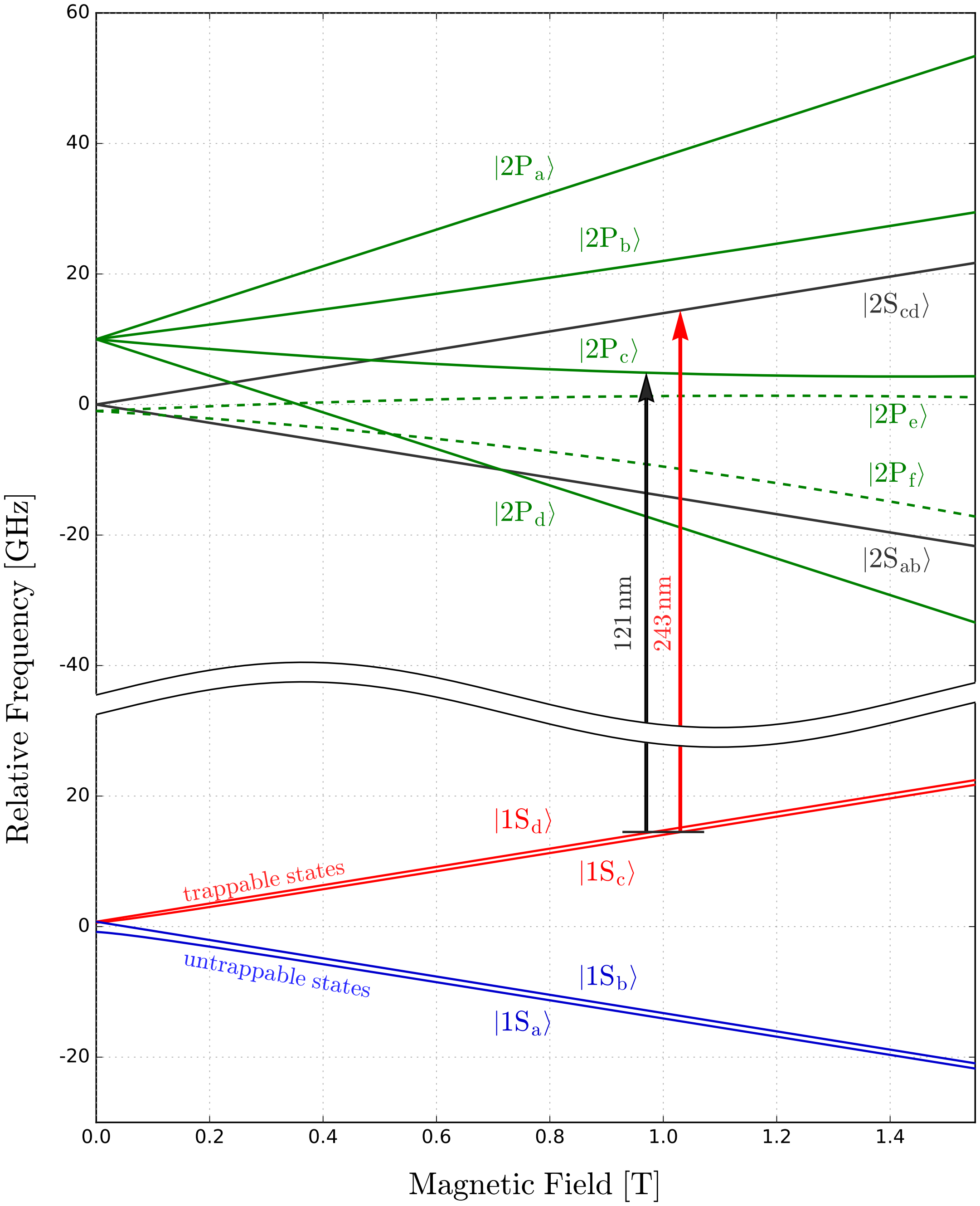

Figure 1.3: Breit-Rabi diagram showing the calculated energies of hydrogen atoms in the 1S, 2S and 2P states as a function of the local magnetic field strength [1]. The mean frequency difference between the 1S and 2S states $f_{\mathrm{1S-2S}} = 2.4661 \times 10^{15}$ Hz has been supressed along the vertical axis. The red arrow shows the 1S-2S transition, which can be excited via a two-photon interaction by exposing hydrogen atoms to UV radiation at a wavelength of 243 nm. The black arrow shows the 1S-2P Lyman-α transition, which can be excited using laser radiation at a wavelength of 121 nm.

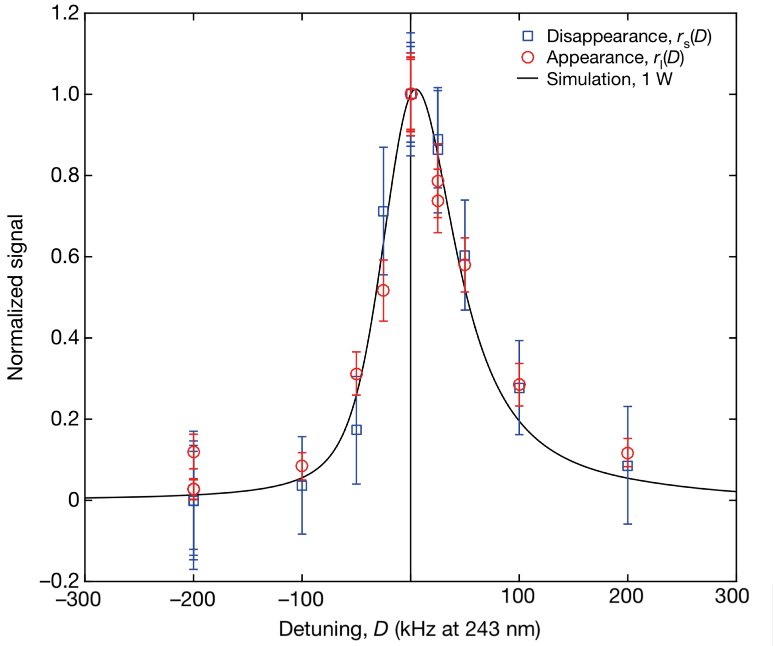

Figure 1.4: Lineshape for the 1S-2S transition in antihydrogen as measured by the ALPHA collaboration [2]. The smooth line was generated by simulating the response of hydrogen atoms in the ALPHA-II atom trap, and is not a fit to the data.

As such, the excitation of trapped antihydrogen into the 2S state can be inferred either from the 'disappearance' of anti-atoms left over at the end of an experiment, or from the 'appearance' of annihilation events during a laser exposure period. The ALPHA-II atom trap is enclosed by a sensitive three-layer silicon vertex detector that is able to reconstruct and count annihilation events resulting from either of these loss mechanisms.

In 2016, the ALPHA collaboration used the above methods to demonstrate the first ever laser spectroscopy of antihydrogen [3]. By resonantly driving the 1S-2S transition at the frequency expected for the same excitation in normal hydrogen, the antihydrogen 1S-2S transition frequency was found to be consistent with CPT invariance to a relative precision of 2×10^{-10}.

Over the following year, this measurement was improved upon by exposing trapped $\bar{\mathrm{H}}$ to laser light detuned from the resonant frequency by up to ± 200 kHz [2].

The resulting lineshape (Figure 1.4) characterises the frequency response of the narrow 1S-2S transition in the ALPHA-II atom trap. Using this data, the central 1S-2S frequency was determined to a relative precision of 2×10^{-12}, an improvement by two orders of magnitude over the previous 2016 result. While even this result falls short of the standards attained by hydrogen spectroscopy experiments [46,47], future improvements to the experimental procedure and the ALPHA apparatus promise even more competitive measurements.

Lyman-α Spectroscopy

The 1S-2P transition of the hydrogen atom (or Lyman-α spectral line, at a wavelength of 121.5 nm) is best known for its use as a tracer of hydrogen gas in astronomical surveys. However, Lyman-α radiation has also been used in the laboratory for the Doppler cooling of hydrogen atoms to temperatures as low as 8 mK [73].

If populations of trapped antihydrogen atoms could be laser cooled to such low temperatures, this would yield significant improvements in precision measurements of a number of their physical properties [74]. Recently, a pulsed Lyman-α laser system has been developed for the ALPHA experiment, allowing the introduction of 121 nm photons into the atom trap volume for 1S-2P spectroscopy and laser cooling experiments [75].

Antihydrogen atoms excited into the $2\mathrm{P}_c$ state by the absorption of a single 121 nm photon have a small probability of decaying back into an untrappable branch of the 1S ground state. As such, the existence of resonant interactions with an incoming laser can, in principle, be inferred from the appearance of annihilation events during laser exposures. However, due to the reduced integrated power of the pulsed Lyman-α laser used by the ALPHA collaboration, much longer exposure times would be required to clearly observe the 1S-2P transition in this way.

By searching for annihilation events in a short time window following each pulse of the 121 nm laser, the ALPHA collaboration were able to distinguish ejected $\bar{\mathrm{H}}$ atoms from a background of cosmic ray events during these long laser exposures, and reported the first observation of antihydrogen's 1S-2P transition in 2018 [1].

In addition to antihydrogen experiments, the AD also hosts a vibrant physics programme based around trapped antiprotons and antiprotonic helium. The BASE experiment [76], which aims to draw precise comparisons between the properties of the proton and antiproton, have recently succeeded in measuring the $\bar{\mathrm{p}}$ charge-to-mass ratio with a sensitivity of around one part in 10^{12} [77]. In 2013, the ATRAP collaboration measured the magnetic moment of a single antiproton to within $\sim$ 4.4 parts per million (ppm) [78], and more recent measurements using the BASE apparatus have determined this quantity at the level of a few parts per billion [79,80].

Meanwhile, the ASACUSA collaboration have found success in probing the spectrum of antiprotonic helium ($\bar{\mathrm{p}}\mathrm{He}^+$), the bound state of a positive helium ion and antiproton. These experiments have led to measurements of the antiproton-to-electron mass ratio at a precision of $\sim 8 \times 10^{-10}$ [81,82]. The ASACUSA collaboration have also measured the annihilation cross-sections for $\bar{\mathrm{p}}$ on atomic nuclei at a range of energies [83–85].

1.3 The ALPHA Experiment

The remainder of this chapter focuses solely on the ALPHA experiment, and gives an overview of the apparatus and methods used to produce and trap cold antihydrogen atoms. Particular attention is given to parts of the apparatus that have influenced the design of the ALPHA-g charged particle beamlines. Figure 1.5 shows the overall structure of the ALPHA apparatus.

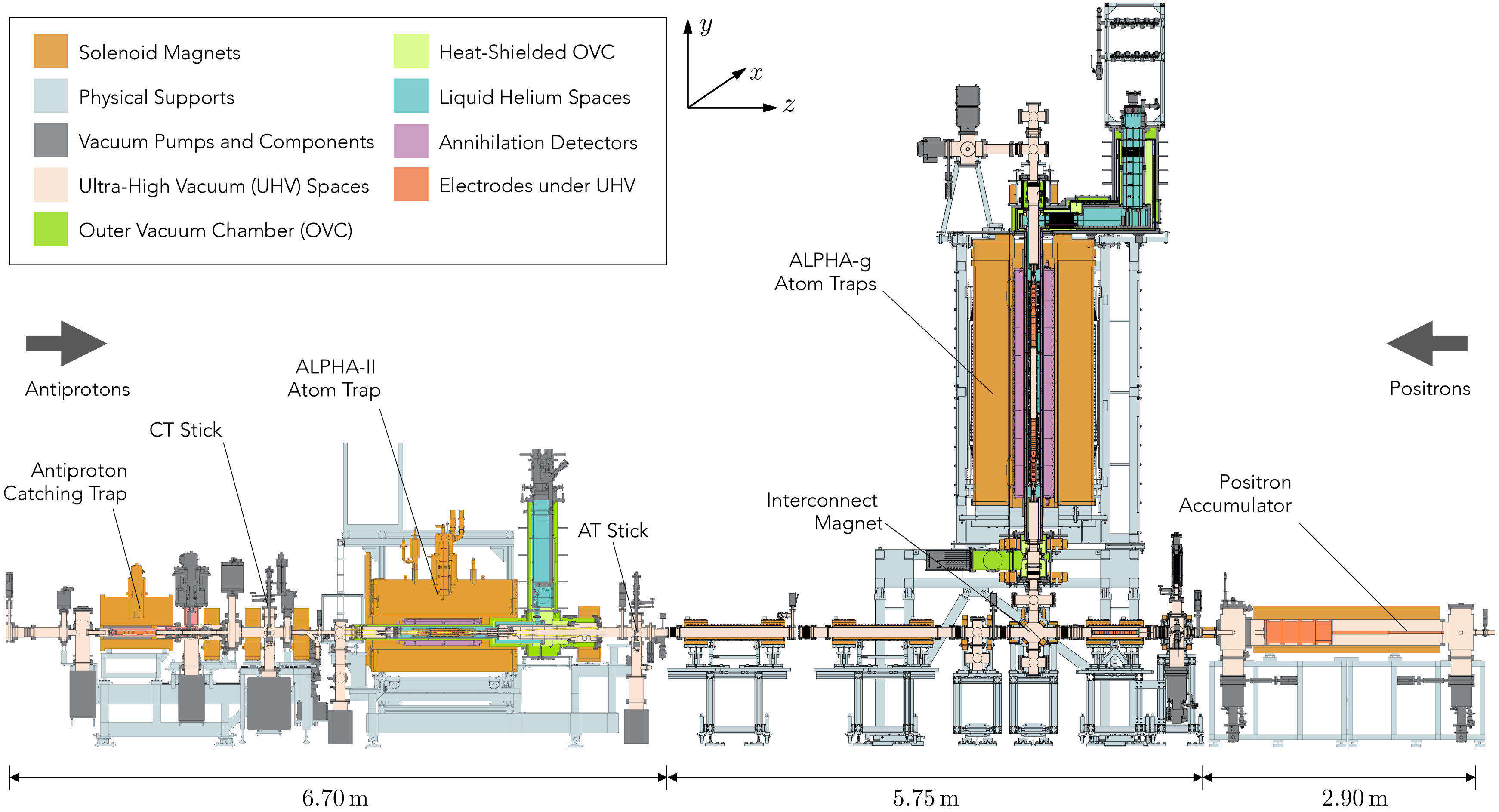

Figure 1.5: Cross-sectional schematic of the ALPHA apparatus following installation of the ALPHA-g experiment during the second half of 2018.

The Penning-Malmberg trap is a device for the confinement and manipulation of charged particles [86–88]. Throughout the ALPHA apparatus, these traps are used to prepare cold plasmas of $\bar{\mathrm{p}}$ and e^+ prior to antihydrogen synthesis [56]. Each Penning-Malmberg trap consists of a series of hollow cylindrical electrodes, immersed inside a uniform magnetic field that is oriented along the axis of the electrode stack. Voltages are applied to the electrodes to create electrostatic potentials, which confine particles along the trap axis. Charged particles are confined perpendicular to the trap axis as a result of their cyclotron motions in the external magnetic field. A more complete discussion of the dynamics of trapped charged particles is given in Section 2.2 of this thesis.

Penning-Malmberg traps are well-suited for experiments with cold antimatter for a variety of reasons. For example, the open-ended nature of this geometry allows particles to be introduced to the trap volume along the axis of the electrode stack. Likewise, these openings at either end of the device allow good optical access for introducing various types of radiation to trapped antiparticles, and are ideal for evacuating residual gases from the trap volume in order to produce and maintain UHV conditions. Under a high quality vacuum, and in the absence of external heat sources, trapped antiparticles can be held within a Penning-Malmberg trap for timescales of months or more [89].

Currently, the ALPHA apparatus can be divided into five distinct sections, including four separate particle traps and the charged particle beamlines that connect them. The following sections of this thesis review the design and operation of each of area of the ALPHA apparatus highlighted in Figure 1.5.

1.3.1 The Antiproton Catching Trap

The Catching Trap (CT) is a purpose-built device that captures and cools energetic antiprotons delivered to ALPHA from the AD.

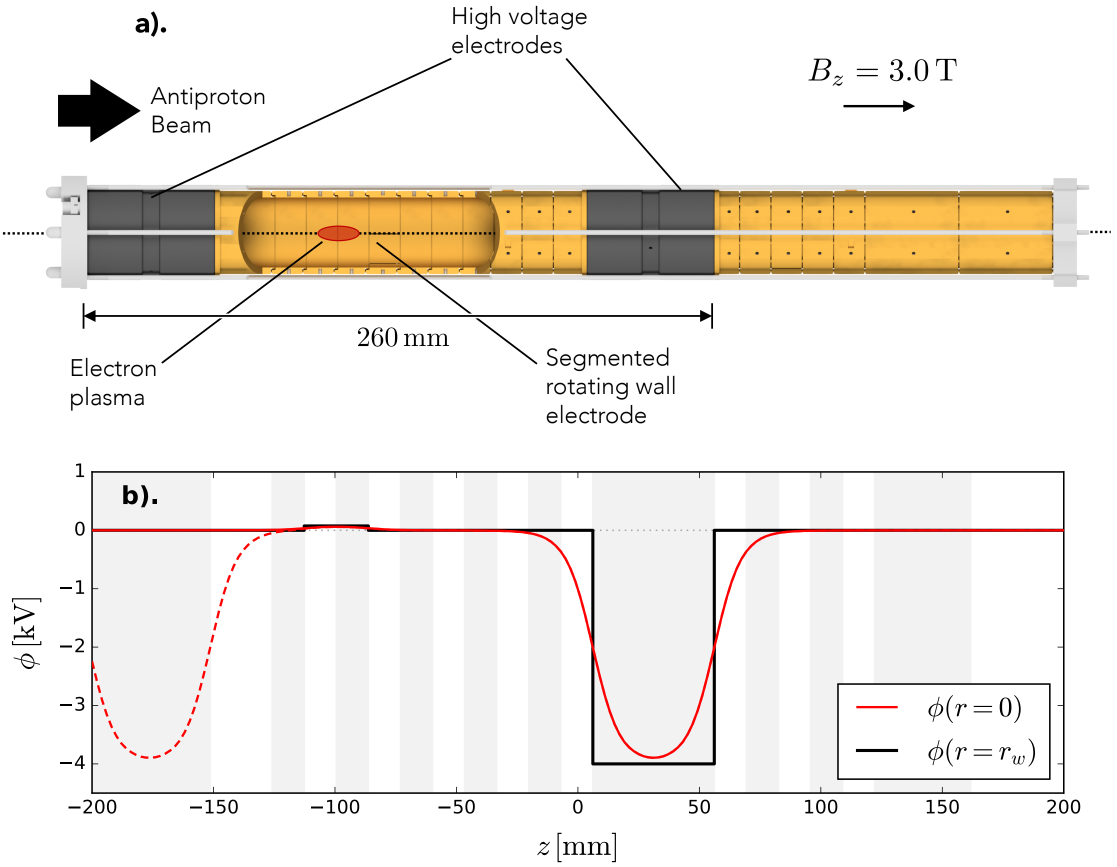

Figure 1.6: a). Schematic showing the layout of the catching trap electrode stack and b). potential ϕ used to capture antiprotons from the CERN AD. The solid (dashed) red line shows the on-axis potential immediately before (after) $\bar{\mathrm{p}}$ capture.

This area of the apparatus comprises a cryogenic Penning-Malmberg trap with two special high voltage (5 kV) electrodes, spaced between a total of eighteen smaller electrodes as shown in Figure 1.6. The central volume of the catching trap is immersed inside a uniform 3 T axial magnetic field that is produced by an external superconducting solenoid.

Antiproton bunches are delivered to ALPHA from the AD every $\sim$ 100 seconds at an initial energy of 5.3 MeV, and must be cooled agressively if any particles are to be retained within the catching trap. As such, the incoming beam is initially passed through a series of degrader foils, where it develops a large longitudinal energy spread due to collisions with stationary aluminium and beryllium nuclei.

After traversing these degrader foils, antiprotons propagate into the volume of the catching trap, where a small fraction of particles with sufficiently low kinetic energies can be caught between the two high-voltage electrodes as shown in Figure 1.6.

Antiprotons caught between the high voltage electrodes of the catching trap can still possess energies of up to $\sim$ 5 keV, and must be cooled into a shallow potential well before being compressed radially and transferred on to other particle traps. As such, $\bar{\mathrm{p}}$ bunches are injected directly into a pre-loaded electron plasma, where they are cooled sympathetically by Coulomb collisions between the two species. Unlike antiprotons, light particles such as e^- are efficiently cooled by their emission of cyclotron radiation in the strong 3 T magnetic field of the catching trap, and can quickly radiate the excess energy of the antiprotons until both species are in thermal equilibrium.

After several seconds, the potentials applied to the high voltage electrodes can be dropped, leaving around 10^5 $\bar{\mathrm{p}}$ mixed into the electron plasma, and resulting in the loss of any remaining hot antiprotons [56]. At this stage, the remaining $\bar{\mathrm{p}}$ are confined to a short potential well, and are fully equilibrated with a plasma of around 2.4×10^7 electrons. Due to the high density of electrons and small number of antiprotons in this region, the dynamics of the $\bar{\mathrm{p}}$ cloud are primarily dictated by the self fields of the electron plasma. This allows for the radial compression of both species through the application of a ‘rotating wall’ electric field at one end of the plasma [90].

Immediately after this compression, a series of pulsed electric fields are applied to the plasma to remove any electrons, while leaving behind the $\bar{\mathrm{p}}$ cloud with minimal heating. Typically, the remaining antiprotons are left with a radial size of $\sim$ 0.4 mm and a transverse temperature in the region of 350 K, and can be moved to one of the two $\bar{\mathrm{H}}$ atom traps.

Particle	**Antiproton** ($\bar{\mathrm{p}}$)	**Positron** (e^+)
Source	Catching trap	Positron accumulator
Particles N	$\sim 10^5$	10^8
Axial magnetic field B_z [T]	3.0	0.15
Plasma radius $\sigma_\perp$ [mm]	0.4	1.0
Temperature T [K]	350	10^3

Table 1.1: Table summarising the typical properties of $\bar{\mathrm{p}}$ and e^+ plasmas immediately before ejection from their respective particle traps.

1.3.2 The Positron Accumulator

Unlike antiprotons, positrons are readily available in nature from the β^+ decays of many common isotopes. In the ALPHA apparatus, positrons are derived from a sodium-22 ($^{22}\mathrm{Na}$) source and formed into a slow beam by directing them through a solid film of condensed neon (Ne). While $^{22}\mathrm{Na}$ naturally emits positrons with a wide range of energies up to 545 keV, the layer of neon thermalizes and moderates the energies of passing e^+ to around 1 eV, with an efficiency of 0.5% [56, 91].

Upon leaving the source chamber, positrons are guided into a Surko-type buffer gas trap [92] where they are cooled and accumulated into a dense plasma. This device, which is also based around the Penning-Malmberg trap geometry, is designed to allow the introduction of nitrogen (N_2) molecules into the vacuum space to act as a cooling gas for the incoming e^+ beam. While passing through a gas of nitrogen molecules, positrons rapidly lose energy through the excitation process

$$\mathrm{e}^+ + \mathrm{N}_2 \rightarrow \mathrm{e}^+ + {\mathrm{N}_2}^* \,,$$

losing around 9 eV of kinetic energy during each collision [93]. By introducing a pressure gradient into the nitrogen gas along the length of the accumulator, e^+ can be encouraged to accumulate within a potential well at one end of the trap.

Typically, around 30% of positrons passing through the accumulator will be captured, forming into a dense plasma of up to 10^8 particles after several minutes of accumulation time [56]. Once again, this cloud of particles will exhibit the collective behaviours of a non-neutral plasma, and can be compressed radially by the application of rotating wall potential [94]. Upon request, the remaining N_2 gas can be evacuated from the trap volume, allowing the accumulated e^+ to be extracted as a pulsed beam and guided into one of the $\bar{H}$ mixing traps.

1.3.3 Charged Particle Diagnostics

In the ALPHA apparatus, a wide variety of diagnostic tools are used to measure and optimise the properties of charged plasmas prior to antihydrogen synthesis. These tools include devices such as Micro-Channel Plates (MCPs) that are placed directly into the path of a plasma, as well as external scintillating detectors [95] that are sensitive to the annihilations of $\bar{p}$ and e^+ on background gases or structures within the UHV space of the apparatus. Many of these tools are assembled together onto instruments informally known as ‘sticks’, which can be inserted into the ALPHA beamline in a number of positions to expose different devices to an incoming plasma.

Typically, each stick is equipped with the following:

- **A Faraday Cup** (FC) to determine the number of particles in a plasma. The Faraday cup is essentially a small capacitive plate which accumulates charge when it is bombarded with ions or other charged particles. After being exposed to a short ($\sim 1\ \mu$s) pulse of $\bar{p}$ or e^+ ejected from a particle trap, the Faraday cup will discharge over a time period set by its own capacitance C_F and the resistance to ground. When measured using an amplifier with a high input impedance, the voltage on the Faraday cup will decay exponentially over a few milliseconds, producing a signal that can be amplified and used to infer the amount of charge that was initially deposited.

Approximating the Faraday cup as a simple capacitor, the total charge is given by $Q = C_{\mathrm{F}}V$, where V is the peak voltage on the surface of the device.

- **An MCP** and phosphor screen assembly, that can be used to image the transverse distribution of charged particles in a plasma [96], or to precisely count small numbers of particles. The MCP acts as a gain medium for incoming particles by producing an avalanche of secondary electrons, which impact upon the surface of the phospor screen and cause it to flouresce. The resulting flourenscence can be imaged by triggering a camera directed through a window into the UHV system.

  The gain of the MCP is set by applying voltages on either side to accelerate charged particles across it and then onwards towards the phosphor screen. The front-to-back voltage difference can be tuned to achieve gains of up to 3×10^4 for leptons, and higher gains for antiprotons [96]. When no voltages are applied, the front plate of an MCP typically has a capacitance of ~ 1 nF, and can be used to as a rudimentary Faraday cup to measure the amount of charge in a trapped plasma.

- **An electron gun** that can be used to load e^- plasmas into particle traps prior to the arrival of antiprotons. Although the electron gun is not a diagnostic tool in itself, it can be used with a source of microwave radiation for in-situ measurements of the magnetic field within a particle trap [97].

- **A pass-through electrode** that allows the free passage of plasmas between particle traps. These electrodes are usually grounded, but can be biased up to 5 kV to act as Einzel lenses or to provide blocking potentials for beam energy measurements.

In addition, the MCP can be used to determine the axial temperature of a trapped non-neutral plasma [98]. In the simplest case, consider a single-component plasma trapped inside an infinitely deep electrostatic well, with a thermal distribution of particle energies. When the depth of this well is gradually reduced to a finite value ϕ, the rate at which charge can escape is given by the expression

$$\frac{\mathrm{d}\ln(Q)}{\mathrm{d}\phi} = -\frac{|q|}{k_B T}\,, \tag{1.2}$$

where T is the plasma temperature, k_B is the Boltzmann constant, and q is the fundamental unit charge. The temperature of a trapped plasma can therefore be measured by slowly lowering the potential at one end of an electrostatic well, so that charged particles gradually escape in one direction towards an MCP. By relating the charge deposited on the MCP to the instantaneous well depth throughout this process, we can derive the plasma temperature using a fit to the resulting curve. This technique has proved invaluable to optimising the characteristics of trapped $\bar{\mathrm{p}}$ and e^+ plasmas prior to antihydrogen production in the ALPHA experiment.

In addition, the ALPHA apparatus is equipped with an array of caesium iodide (CsI) detectors and scintillator panels that can be moved around the surrounding experimental zone. Caesium iodide crystals emit light when exposed to ionising radiation such as the products of a $\bar{\mathrm{p}}$ or e^+ annihilation [95, 99]. Small packages containing a CsI crystal, along with appropriate electronics to detect the emission of scintillation light, can therefore be used as compact beam loss monitors. In the ALPHA experiment, each CsI crystal is packaged with a Silicon Photomultiplier (SiPM) chip that detects and amplifies flashes of scintillation light. These detectors are easily saturated by short, intense bursts of radiation and have a long fall-off time of $\sim 700\ \mu$s, making them poorly suited for applications beyond simply indicating the loss of particles around a given area of the experiment.

Where improved time resolution or single-particle counting capability is required, larger plastic scintillating panels can be deployed to key areas of the experiment. Flashes of scintillation light produced by these panels are detected and amplified using either a fast SiPM chip, or a magnetically-shielded Photomultiplier Tube (PMT) that converts incoming photons into a small electrical current using the photoelectric effect. When the output of a PMT detector is read directly into an amplifier with a high input impedance, it produces a voltage waveform that is proportional to the intensity of the incident radiation, with a typical time resolution of $\lesssim 2$ ns. These detectors can therefore resolve the time structures of short bursts of radiation, such as the annihilation of $\bar{\mathrm{p}}$ or e^+ plasmas ejected from a particle trap in the form of a pulsed beam.

1.3.4 The ALPHA-II Atom Trap

The horizontal ALPHA-II atom trap is a 1.5-meter long device designed for the production and precision spectroscopy of trapped antihydrogen atoms. In this section of the apparatus, the UHV space of a cryogenic Penning-Malmberg trap is enclosed by a series of superconducting magnets that can be energized to impose a shallow magnetic minimum around the centre of the trap. These magnets are immersed in a reservoir of liquid helium (LHe) in order to maintain superconductivity at a temperature of approximately ~ 4 K. This section of the experiment closely resembles the central portion of the original ALPHA apparatus [56], but incorporates additional features for the precision spectroscopy of trapped $\bar{\mathrm{H}}$.

Prior to antihydrogen formation, e^+ and $\bar{\mathrm{p}}$ plasmas are transferred from their respective particle traps and moved into a series of thin-walled electrodes at the centre of the ALPHA-II apparatus. Initially, both species are held next to one another using a nested potential well.

After further cooling [100], and techniques to ensure the size and reproducibility of each plasma [6], the $\bar{\mathrm{p}}$ and e^+ clouds are slowly merged across one another by manipulating the Penning trap potentials around the centre of the atom trap. Before mixing, the positron temperature is usually in the region of ~ 20 K, depending on the density of the plasma and exact sequence of manipulations that were used to prepare it [5]. In this regime, antihydrogen formation can occur through three-body recombination [101],

$$\bar{\mathrm{p}} + \mathrm{e}^+ + \mathrm{e}^+ \rightarrow \bar{\mathrm{H}} + \mathrm{e}^+ \, ,$$

where the binding energy of the $\bar{\mathrm{H}}$ is carried away by an additional positron. While the cross-section for this reaction is strongly dependent on the initial temperature of the positron plasma, the momentum of the resulting $\bar{\mathrm{H}}$ is dominated by that of its $\bar{\mathrm{p}}$ nucleus. Although this process can result in the production of up to 3×10^4 antihydrogen atoms from a cloud of $\sim 10^5$ $\bar{\mathrm{p}}$ during a typical mixing cycle [5], only a small fraction are cold enough to be confined within the magnetic minimum trap.

After recombination, neutral antihydrogen atoms can no longer be confined using the electromagnetic fields of a Penning-Malmberg trap. However, antihydrogen atoms can still be trapped by exploiting the coupling of their magnetic moment to a strongly inhomogeneous external magnetic field. The force **F** on a neutral atom is given by

$$\mathbf{F} = -\nabla \left(\mu \cdot \mathbf{B} \right) \, , \tag{1.3}$$

where μ is the magnetic moment of the atom and **B** is the applied magnetic field. As such, atoms with a magnetic moment anti-aligned to the applied magnetic field are considered trappable, and can be confined by the application of a magnetic minimum around the trap centre.

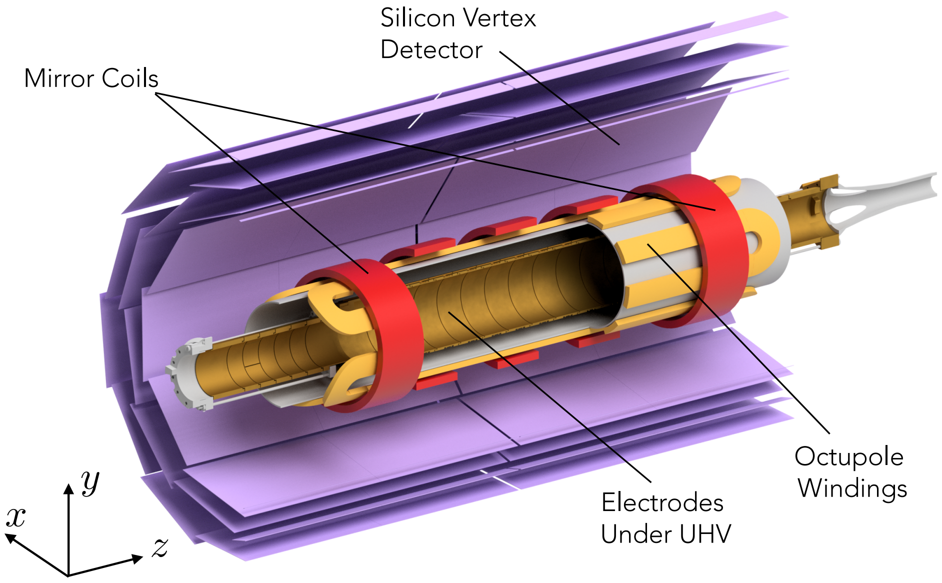

Figure 1.7: Simplified schematic showing the basic layout of the ALPHA-II atom trap. An external solenoid enclosing the entire device and cryogenic systems associated with the superconducting trap magnets are not shown.

Figure 1.7 shows a simplified schematic of the ALPHA-II atom trap. The central portion of the atom trap is enclosed by a series of superconducting magnets, which are wound directly onto the surface of the beam pipe in a configuration known as an Ioffe-Pritchard trap. When energized, these magnets produce a three-dimensional magnetic minimum around the centre of the atom trap. Field gradients along the trap axis are generated by a series of short solenoids (mirror coils), while radial gradients towards the walls of the trap are produced by a long octupole magnet.

The depth of this trap can be estimated by comparing the minimum magnetic field at its centre to the strongest magnetic field at the electrode walls. In temperature units, the trap depth is given by the expression

$$T_{\max} = \frac{\mu}{k_B}\left(\sqrt{B_r^2 + B_z^2} - B_z\right), \tag{1.4}$$

where B_r is the radial component of the magnetic field close to the electrode walls and B_z is the background magnetic field oriented along the axis of the trap.

The magnetic moment of a hydrogen atom in the ground state is approximately given by the Bohr magneton, $\mu_B \simeq 9.27 \times 10^{-24}$ J/T. In the ALPHA-II experiment, with a background magnetic field of $B_z = 1.0$ T, the neutral atom trap has a depth of approximately ~ 0.54 K.

When the neutral atom trap is energized during the mixing of $\bar{\mathrm{p}}$ and e^+ plasmas in the centre of the atom trap, a small fraction of the coldest antihydrogen atoms can be trapped and held over long timescales [59]. Until 2016, the average trapping rate of the ALPHA apparatus was typically limited to ~ 0.5 atoms/attempt. However, recent improvements in the procedures used to prepare and slowly merge charged plasmas [6] have resulted in a forty-fold increase in the average trapping rate. In addition, techniques have now been developed to accumulate trapped antihydrogen from subsequent mixing cycles, allowing up to 10^3 atoms to be confined simultaneously and held for several hours [5]. These advances were critical to the recent spectroscopy measurements detailed in Section 1.2 of this thesis.

Trapped antihydrogen is typically lost through one of three mechanisms: either an annihilation on background gases within the trap volume, a transition into an untrappable quantum state following exposure to resonant laser or microwave radiation, or the fast ramp down (FRD) of the neutral atom trap at the end of an experiment.

In each of these cases, the annihilation of the $\bar{\mathrm{p}}$ nucleus will result in the production of energetic pions ($\pi^{\pm}$, π^0), which pass through the three concentric layers of a Silicon Vertex Detector (SVD) enclosing the central volume of the atom trap [102]. By reconstructing the three-dimensional trajectories of charged pions through the detector volume, the locations of annihilation events (vertices) can be identified by searching for instances where multiple charged particle tracks simultaneously intersect at a single point in space.

A range of cuts are then applied to distinguish real annihilations from a background of primarily cosmic ray events. Vertices are selected based on their position within the atom trap, and other variables such as the number of tracks originating from each vertex [102]. For example, the annihilation of an antiproton escaping from the atom trap will result in three or more tracks that intersect close to the electrode walls, whereas cosmic rays will typically leave a shower of parallel tracks that pass vertically through the detector.

A range of multivariate analysis (MVA) machine learning tools [103] have also been developed to discriminate between real annihilations and background events. In this method, a random forest [104] approach is used to classify events based upon an expanded set of variables [72] that describe the topology of each event recorded by the detector. These algorithms are trained using two distinct sets of data, containing either a large number of annihilation events from the mixing of e^+ and $\bar{p}$ plasmas, or only cosmic rays recorded while the experiment was otherwise inactive. This method is able to identify real annihilation events more efficiently, while also offering an improved suppression of the cosmic ray background rate.

To facilitate the precision spectroscopy of trapped $\bar{H}$, the ALPHA-II experiment is designed so that laser radiation can be introduced at small angles to the trap axis. Furthermore, the neutral atom trap incorporates three additional mirror coils towards its centre that can be used to flatten the magnetic field along the trap axis. Since many spectral lines are shifted by the application of an external magnetic field, this flattening increases the volume in which trapped anti-atoms can interact with a resonant laser.

1.3.5 The ALPHA-g Atom Trap

In many respects, the design of the ALPHA-g atom trap closely resembles that of the ALPHA-II experiment.

However, this area of the apparatus must meet a number of additional design constraints in order to precisely measure the gravitational acceleration of antihydrogen. By comparing Equation 1.3 to the force of gravity on a single antihydrogen atom, we can derive an upper limit for the size of uncontrolled magnetic field gradients across the ALPHA-g atom trap

$$\left|\frac{\partial B}{\partial z}\right|_{\max} = \frac{mg}{|\mu|}\left(\frac{\delta g}{g}\right) , \tag{1.5}$$

where m is the mass of the hydrogen atom, g is the local acceleration due to gravity, and $\delta g/g$ is the required precision of the measurement. To evaluate Equation 1.5, we assume that the WEP is valid so that antihydrogen experiences exactly the same gravitational acceleration as normal hydrogen ($\bar{g} = g = 9.81\,\mathrm{m/s^2}$) on Earth. In this case, magnetic field gradients across the ALPHA-g atom trap must be controlled to within $\sim 2 \times 10^{-5}$ T/m to achieve a precision ±1% gravity measurement.

To meet this requirement, the ALPHA-g trap magnets and external solenoid were designed to produce a well defined magnetic field around the centre of the apparatus. Whereas the ALPHA-II experiment includes only one region for the production and trapping of $\bar{\mathrm{H}}$, the ALPHA-g apparatus incorporates two such regions, separated equally from the magnetic centre of the experiment. This allows for the cancellation of systematic errors across the apparatus, and helps to limit the effects of persistent currents [105] in the superconducting trap magnets. Both mixing traps also incorporate additional mirror coils and octupole windings, which will be used to further control the magnetic fields sampled by trapped $\bar{\mathrm{H}}$.

The ALPHA-g atom trap is enclosed by a radial Time Projection Chamber (TPC) [106] for the reconstruction of $\bar{\mathrm{H}}$ annihilation events [107]. This type of detector is regularly used in high-energy physics experiments to reconstruct the trajectories of energetic particles in three dimensions [108, 109].

In this detection scheme, pions moving radially outwards from the centre of the trap pass through a cylindrical chamber filled with argon (Ar) and carbon dioxide (CO_2) gases at room temperature and atmospheric pressure. The ionisation of this gas mixture results in the production of electrons that drift outwards towards anode wires spaced around the walls of the chamber. These electrons produce a small electrical current on the anode wires, and also on readout pads spaced along the length of the gas chamber. By comparing the timing of these signals across different channels, the three-dimensional track of a charged pion can be reconstructed and traced back to the annihilation vertex.

The ALPHA-g apparatus was designed with the goal of determining the direction of antihydrogen's gravitational acceleration within a few months of operation. The precision of this measurement would then be improved to the level of ±1% over the following years. In a typical measurement scheme, the mirror coils that provide axial confinement for the neutral atom trap are ramped down over several seconds, allowing any trapped $\bar{\mathrm{H}}$ to escape along the length of the trap. Due to the gravitational potential along the length of the experiment, an excess of $\bar{\mathrm{H}}$ are expected to annihilate at one end of the trap compared to the other [40].

1.3.6 Charged Particle Beamlines

Until 2018, each section of the ALPHA apparatus was constrained to one horizontal axis. In this configuration, the catching trap and positron accumulator were located immediately to either side of the ALPHA-II atom trap. However, to facilitate the installation of the ALPHA-g experiment during 2018, the positron accumulator was moved approximately ~ 5.8 m from its original position. As shown in Figure 1.5, the ALPHA-g experiment was installed ~ 9.2 m from the centre of the catching trap, perpendicular to the original axis of the apparatus.

This expansion of the ALPHA experiment required that new beamlines were installed to facilitate the transfer of $\bar{\mathrm{p}}$ and e^+ plasmas into both atom traps. These beamlines must be able to operate in any one of three primary configurations:

1. **Antiprotons to ALPHA-g**: In this configuration, $\bar{\mathrm{p}}$ plasmas extracted from the catching trap must pass through the existing ALPHA-II apparatus, before encountering a sharp right-angled turn beneath the ALPHA-g atom trap. After being steered through this region, $\bar{\mathrm{p}}$ bunches must be captured inside the volume of the new atom trap.
2. **Positrons to ALPHA-g**: In a mirror image of the previous configuration, the beamline must guide e^+ bunches from the positron accumulator into the bore of the ALPHA-g atom trap, passing through a sharp right-angled turn in the process.
3. **Positrons to ALPHA-II**: In this mode of operation, the beamline must guide e^+ bunches along a straight, horizontal path to be captured inside the ALPHA-II experiment.

In each of these cases, the region directly beneath the ALPHA-g experiment is responsible for determining the overall trajectory of $\bar{\mathrm{p}}$ and e^+ bunches as they move along the beamline. This region is known as the interconnect, must be able to steer charged particles in either direction around a sharp bend, or otherwise allow them to pass through uninhibited.

Conventionally, charged particle beamlines will operate in one of two general regimes. The first of these, known as a magnetic lattice beamline, is typically used to guide high energy charged particle beams through storage rings [110] or linear accelerators. In this scheme, a repeating set of multipolar magnetic fields is used at regular intervals along the beamline to influence the dynamics of a passing beam.

In general, dipole magnetic fields are used for beam steering, while alternating quadrupole magnets are used to achieve strong focusing of the beam in the transverse plane [111, 112]. Additional magnets such as sextupoles can also be used to correct higher-order effects such as beam chromaticity. This scheme is particularly effective at relativistic energies, since the magnetic force exerted on a charged particle is proportional to its momentum at right angles to the local magnetic field.

At lower energies, electrostatic beamlines are often used to control the dynamics of charged particle beams. In this regime, voltages are applied to a series of conductive elements spaced along the beam path. These elements generate strong electrostatic fields that accelerate passing charged particles along a given direction. Components such as electrostatic deflectors, quadrupoles and lenses can be used to modify the size and direction of a beam in a well-prescribed manner. Typically, the electrostatic regime is favoured in cases where the fields required for a magnetic beamline would be particularly weak, and therefore easily distorted by external magnetic fields or permeable magnetic materials.

The design of the ALPHA apparatus has a number of characteristics that would cause significant problems for either of the two beamline schemes discussed above. While a more quantitative discussion of this topic will be given in Section 3.1 of this thesis, a short overview is given here for completeness. Primarily, the maximum energy at which charged particles can be transferred around the ALPHA apparatus is dictated by the particle traps used to store $\bar{\mathrm{p}}$ and e^+ plasmas prior to $\bar{\mathrm{H}}$ synthesis.

For example, since the maximum voltage that can be applied to a standard electrode in the catching trap is ~ 140 V, the highest energy at which $\bar{\mathrm{p}}$ bunches can be extracted is of a similar magnitude. In a magnetic lattice beamline, extremely weak magnetic fields would be required to guide a beam of such low energy.

These would easily be distorted by the patchwork of stray fields between the various ALPHA particle traps, making a magnetic lattice beamline highly impractical.

Equally, the extraction of pulsed $\bar{\text{p}}$ and e^+ beams from Penning-Malmberg traps into an electrostatic beamline is highly non-trivial. Non-neutral plasmas held inside a strong axial magnetic field have a conserved angular momentum, which couples their transverse size to the strength of the local magnetic field. The extraction of $\bar{\text{p}}$ and e^+ plasmas into a region with no residual magnetic field will therefore result in an enormous expansion of the beam envelope.

While a number of recent works have demonstrated the extraction of electrostatically-guided e^+ beams from Penning-Malmberg traps with strong magnetic fields, these extraction schemes typically require a complex geometry of permeable magnetic components and electrostatic lenses [113–115]. Furthermore, the trajectories of electrostatically guided $\bar{\text{p}}$ and e^+ beams are likely to be influenced by the stray magnetic fields of nearby particle traps. Although permeable magnetic shielding can be employed to protect sensitive areas of the beamline from external magnetic fields, the amount of shielding required to achieve this for the ALPHA experiment would be prohibitively expensive.

For the ALPHA-g beamlines, an alternative scheme was developed to guide low energy $\bar{\text{p}}$ and e^+ beams between particle traps with strong axial magnetic fields. Rather than using a periodic lattice of multipole magnets, charged particles are channeled through a series of short solenoids that provide continual focusing in the transverse plane. In this approach, the magnetic field along the beamline can be made arbitrarily strong, mitigating the effects of stray magnetic fields and avoiding the need to extract particles into a field-free region at any point. Equally, charged particles can be steered through a change of direction by constructing a region of curved magnetic field lines.

Due to their conserved angular momenta, $\bar{\text{p}}$ and e^+ bunches will typically follow the direction of the local magnetic field when propagating at sufficiently low energies. The interconnect region must therefore be able to produce curved magnetic field lines that connect either the catching trap or positron accumulator to the ALPHA-g experiment In addition, this magnet must be able to guide e^+ bunches through a horizontal magnetic field, allowing them to propagate towards the ALPHA-II experiment.

2 | Charged Particle Dynamics

The following chapter reviews a range of tools that can be used to model the motions of charged particles in an electromagnetic field. In particular, we explore the different analytical models and numerical methods that were used to model the motion of $\bar{\mathrm{p}}$ and e^+ bunches through the ALPHA apparatus. Section 2.1 describes the analytical guiding centre approximations, which can be used to estimate the paths of charged particles in simple electromagnetic fields. Section 2.2 reviews the dynamics of non-neutral plasmas in Penning-Malmberg traps, while Section 2.3 explores the propeties of charged particle beams extracted from these devices. Finally, Section 2.4 describes numerical methods that can be used to solve the full equation of motion for charged particles in an arbitrary electromagnetic field.

2.1 Motions of Single Charged Particles

The equation of motion for a single charged particle in an electromagnetic field is given by the Lorentz force law [116],

$$\mathbf{F} = m\frac{\mathrm{d}\mathbf{v}}{\mathrm{d}t} = q\left(\mathbf{E} + \mathbf{v} \times \mathbf{B}\right) \ , \tag{2.1}$$

where $\mathbf{E}$ and $\mathbf{B}$ are vectors representing the electric and magnetic fields, and q and m indicate the charge and mass of the particle, respectively. As usual, $\mathbf{v}$ is the velocity of the particle and t denotes the passage of time.

Real electromagnetic fields may have complicated dependencies on both space and time, resulting in trajectories that are difficult or impossible to solve analytically. However, in simple cases, the motions of charged particles can be decomposed into a series of oscillations and drifts known as the guiding centre approximations [116]. A number of these approximations can often be combined to describe how charged particles will behave in more complex, realistic electromagnetic fields.

2.1.1 Guiding Centre Approximations

Uniform Static Electromagnetic Fields

First, consider a charged particle moving through only a magnetic field. Figure 2.1 shows the universal coordinate system that will be used to consider the motions of single particles. In a homogenous magnetic field, we can choose a co-ordinate system so that the direction of the field is oriented along one axis, with $\mathbf{B} = B_z\,\hat{k}$. In this case, the three components of Equation 2.1 can be decoupled, so that [116]

$$\ddot{v}_x = -\left(\frac{qB_z}{m}\right)^2 v_x\,, \qquad \ddot{v}_y = -\left(\frac{qB_z}{m}\right)^2 v_y\,, \qquad \dot{v}_z = 0\,, \tag{2.2}$$

where dots denote derivates with respect to time. The transverse (x and y) components of Equation 2.2 are the equations of motion for a simple harmonic oscillator, with a characteristic frequency known as the cyclotron frequency [116, 117],

$$\omega_{\mathrm{c}} = \left(\frac{qB_z}{m}\right)\,. \tag{2.3}$$

When projected onto the transverse plane, this motion will trace out a circle around a point known as the guiding centre. The radius of this orbit is given by the Larmor radius, defined as

$$r_L = \left(\frac{mv_\perp}{qB_z}\right)\,, \tag{2.4}$$

where $v_\perp = \left(v_x^2 + v_y^2\right)^{1/2}$ is the velocity perpendicular to the magnetic field.

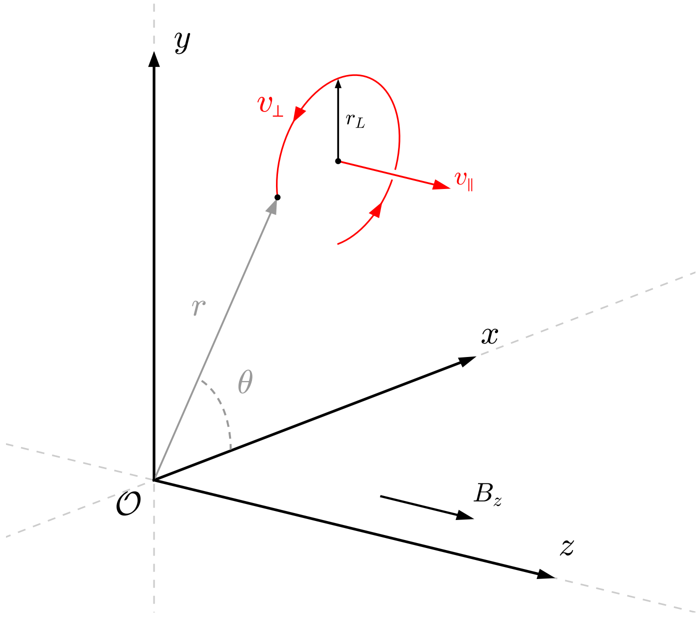

Figure 2.1: Diagram showing the universal co-ordinate system used to consider the motions of single particles. Arrows shown in red indicate the transverse and longitudinal components of the particle velocity.

Since the magnetic field produces no acceleration along the z axis, any initial velocity along this direction is simply retained. The general trajectory of any charged particle in a uniform magnetic field is therefore a helix, extending along the direction of the magnetic field.

Consider now the addition of a uniform electrostatic field to the case described above. Since our original system was azimuthally symmetric about the z axis, we can choose an electric field that points within the xz plane without any loss of generality. This results in three coupled equations for the motion of the particle

$$\dot{v}_x = \frac{q}{m}E_x + \omega_c v_y \,, \qquad \dot{v}_y = -\omega_c v_x \,, \qquad \dot{v}_z = \frac{q}{m}E_z \,. \tag{2.5}$$

Along the z axis, the electric field simply accelerates particles parallel to the magnetic field lines. Once again, the equations of motion for the transverse degrees of freedom can be doupled by taking the derivative with respect to time [116].

After doing so, we find that

$$\ddot{v}_x = -\omega_c^2 v_x \,, \qquad \frac{\mathrm{d}^2}{\mathrm{d}t^2}\left(v_y + \frac{E_x}{B_z}\right) = -\omega_c^2\left(v_y + \frac{E_x}{B_z}\right) \,, \tag{2.6}$$

which is simply Equation 2.2 with an additional drift velocity E_x/B_z perpendicular to the directions of the electric and magnetic fields. In general, the drift velocity is given by the equation

$$\mathbf{v}_{\mathrm{E\times B}} = \frac{\mathbf{E}\times\mathbf{B}}{|B|^2} \,, \tag{2.7}$$

and is known as an $\mathbf{E}\times\mathbf{B}$ drift. This result is important to understanding the behaviour of non-neutral plasmas in Penning-Malmberg traps. By replacing the electric field $\mathbf{E}$ in this expression with an arbitrary force, it is possible to derive guiding centre drifts for a range of different forces. The drift velocity for a general force $\mathbf{F}$ is given by

$$\mathbf{v}_{\mathrm{drift}} = \frac{1}{q}\left(\frac{\mathbf{F}\times\mathbf{B}}{|B|^2}\right) \,, \tag{2.8}$$

similar to the form of Equation 2.7.

Non-uniform Magnetic Fields

In many cases, the magnetic field is not homogeneous, and can vary in strength or direction along the path of a charged particle. Maxwell's equations dictate that the strength of a magnetic field cannot change without the magnetic field lines either converging or diverging as a result. However, by considering a magnetic field that only changes in either strength or direction, we can derive two drift velocities that represent a realistic non-uniform magnetic field when combined together.

Consider first a magnetic field that increases in strength along the y axis, without any change in direction along z. During each cyclotron period, charged particles will sample a magnetic field that is stronger on one side of their orbit than the other.

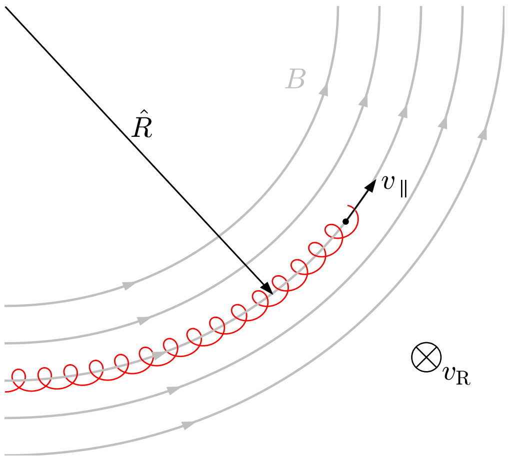

Figure 2.2: Schematic showing the magnetic field and charged particle trajectory that are considered to derive the curvature drift, Equation 2.14.

If the typical length scale L of the magnetic field gradient is large enough that $r_L \ll L$, we can expand the force on the particle parallel to the gradient

$$m\dot{v}_y = -qv_x B_z(y) = -qv_\perp \cos(\omega_c t)\left[B_0 + r_L \cos(\omega_c t)\frac{\partial B_z}{\partial y}\right] . \tag{2.9}$$

When integrated over many cyclotron oscillations, the first term of this expansion averages out to zero. However, the second term encapsulates the effect of the magnetic field gradient, and produces an overall force on the guiding centre

$$\tilde{F}_y = \pm\frac{1}{2}qv_\perp r_L\left(\frac{\partial B_z}{\partial y}\right) . \tag{2.10}$$

Using a similar expansion, it can be shown that the force parallel to the x axis averages out to zero over each cyclotron period. Equation 2.10 can be combined with Equation 2.8 to find the associated drift velocity [116]

$$\mathbf{v} = \pm\frac{1}{2}\frac{v_\perp r_L}{|B|}\left(\frac{\partial B_z}{\partial y}\right)\hat{\imath} . \tag{2.11}$$

Gradients in the magnetic field strength will therefore cause the guiding centre to drift in a direction perpendicular to both the magnetic field and its gradient.

In full generality and three dimensions, this drift velocity is given by the expression

$$\mathbf{v}_{\nabla \mathrm{B}} = \pm \frac{1}{2} v_{\perp} r_L \left(\frac{\mathbf{B} \times \nabla |B|}{|B|^2} \right) , \tag{2.12}$$

and is known as a grad B drift. It is important to remember that this derivation is only valid where the typical length scale of gradients in the magnetic field is much larger than a single cyclotron orbit. In the regime where particles can sample significant inhomogeneities during a single orbit, they can adopt complex trajectories that are poorly described by the guiding centre approximations.

Finally, consider a region of magnetic field lines that are uniformly dense, but change direction around a constant radius of curvature R as shown in Figure 2.2. Charged particles following any one of these field lines due to their cyclotron motion will experience a centripetal force

$$\mathbf{F}_R = \frac{m v_{\parallel} \mathbf{R}}{|R|^2} , \tag{2.13}$$

where $v_{\parallel}$ is the component of the particle velocity tangential to the local magnetic field. According to Equation 2.8, this force will result in a drift perpendicular to both the magnetic field and the direction of its curvature.

The associated drift velocity can be written as [116]

$$\mathbf{v}_R = \frac{m v_{\parallel}^2}{q B^2} \left(\frac{\mathbf{R} \times \mathbf{B}}{|R|^2} \right) . \tag{2.14}$$

The addition of this curvature drift is important when considering devices such as the ALPHA-g interconnect, which guide charged particles through an area of curved magnetic field lines. Where the steering radius R is particularly small, or the magnetic field that is used to guide particles is relatively weak, large curvature drifts can force particles into the plane of Figure 2.2 and significantly displace them from their intended trajectory.

2.1.2 Adiabatic Invariants

For charged particles undergoing cyclotron motion in a slowly varying magnetic field (as defined in the derivation of Equation 2.11) it can be shown that the magnetic moment ascribed to each particle's orbit is conserved adiabatically [116]. This quantity is defined as

$$\mu = \frac{1}{2}\frac{mv_\perp^2}{B_z} = \frac{E_\perp}{B_z}\,, \tag{2.15}$$

where $E_\perp$ is the transverse kinetic energy of the particle. The magnetic moment μ is an example of an adiabatic invariant, a quantity associated with some periodic motion that is conserved even when that motion is slowly perturbed.

By assuming the conservation of μ between any two points in a magnetic field, we can derive path-invariant scaling laws for a number of dynamical variables. For example, by comparing Equation 2.15 at two points z and z_0 we find that [116,118]

$$v_\perp(z) = v_\perp(z_0)\sqrt{\frac{B(z)}{B(z_0)}}\,. \tag{2.16}$$

Charged particles will therefore transfer energy into their cyclotron motions as they move into a stronger magnetic field.

Since the Larmor radius depends on both the transverse velocity and the magnetic field strength, it will also scale such that

$$r_L(z) = r_L(z_0)\sqrt{\frac{B(z_0)}{B(z)}}\,, \tag{2.17}$$

resulting in smaller cyclotron oscillations in a stronger magnetic field. Since magnetic fields cannot do work, conservation of the total energy demands that changes in the transverse velocity of a particle are accompanied by a similar change in its longitudinal velocity.

The corresponding change in the longitudinal energy is given by the expression

$$\delta E_{\parallel} = E_{\perp}\left(z_0\right)\left[1 - \frac{B\left(z\right)}{B\left(z_0\right)}\right], \tag{2.18}$$

where $\delta E_{\parallel}$ is the change in kinetic energy between the two points. The longitudinal velocity of any particle undergoing cyclotron motion can therefore be reduced to zero if it encounters a sufficiently strong magnetic field. This causes it to be deflected (or mirrored) backwards along its original path.

Equation 2.18 is only valid if the magnetic moment of a particle is conserved adiabatically. Particles that move through weak or rapidly-varying magnetic fields can begin to move non-adiabatically, breaking the conservation of μ. In this regime, magnetic mirroring can start to occur in much weaker magnetic fields than would otherwise be expected. In the following section, we review the conditions required for these non-adiabatic dynamics to develop.

2.1.3 Breakdown of Adiabatic Invariants

Many of the guiding centre approximations are only valid where the magnetic field varies slowly along the path of a charged particle. In general, this condition can be expressed as $r_L \ll L$, where L is the typical size of variations in the magnetic field. However, this condition is relatively abstract, and it will be more useful to understand the exact conditions where the guiding centre approximations begin to break down.

Consider the motion of any charged particle through a static, inhomogenous magnetic field in the laboratory frame. In the rest frame of the guiding centre, this particle experiences a magnetic field that varies only as a function of time due to its own velocity through the external field.

The transverse components of Equation 2.2 can therefore be rewritten as

$$\ddot{v}_i = \left[\frac{qB(t)}{m}\right]^2 v_i \,, \tag{2.19}$$

where $i \in \{x, y\}$. This equation takes the general form

$$\varepsilon^2 \frac{\mathrm{d}^2 y}{\mathrm{d}x^2} = f\left(x\right) y\left(x\right) \,, \tag{2.20}$$

where ε is a small prefactor such as the inverse of the charge-to-mass ratio, and $f\left(x\right)$ is an arbitrary function of the independent variable x. This is the general equation for a nonlinear harmonic oscillator. As a result, Equation 2.19 has solutions that can be approximated using the Wentzel-Kramers-Brillouin (WKB) method [118]. To first order, these solutions can be written as [119]

$$x_i\left(t\right) \simeq \frac{c_{\pm}}{\sqrt{B\left(t\right)}} \exp\left[\pm i \frac{q}{m} \int_0^t B\left(t'\right) \mathrm{d}t'\right] \tag{2.21}$$

where $c_{\pm}$ are integration constants and x_i denotes either of the transverse degrees of freedom. This solution meets many of our expectations for a particle undergoing cyclotron motion in a gently varying magnetic field. For example, the particle oscillates within the transverse plane at the instantaneous cyclotron frequency, with an amplitude that scales as the inverse square root of the local magnetic field.

This class of solution is well established, and can be shown to be valid if

$$\omega^2 \gg \left| \frac{3}{4} \left(\frac{\dot{\omega}}{\omega}\right)^2 - \frac{1}{2} \frac{\ddot{\omega}}{\omega} \right| \,, \tag{2.22}$$

where $\omega\left(t\right) = qB\left(t\right)/m$ is the angular frequency of the nonlinear oscillator. In general, it is more useful to write this condition in terms of the magnetic field itself, rather than the oscillation frequency of a particular particle.

Transforming back into the laboratory frame to write this condition in terms of a static, inhomogeneous magnetic field, we find that

$$\frac{mE_{\parallel}}{q^2B_z^2}\left|\frac{3}{2}\left(\frac{1}{B_z}\frac{\partial B_z}{\partial z}\right)^2-\frac{1}{B_z}\frac{\partial^2 B_z}{\partial z^2}\right| \ll 1 \tag{2.23}$$

must be satisfed in order to guarantee that particles propagate adiabatically. For convenience, many authors use a simpler definition of the adiabaticity parameter,

$$\gamma=\frac{\tau_c v_z}{B_z}\frac{\partial B_z}{\partial z}\,, \tag{2.24}$$

where $\tau_c = 2\pi/\omega_c$ is the cyclotron period [115].

Knowledge of these conditions allows us to construct smoothly-varying magnetic fields that promote the adiabatic transfer of charged particle beams. Where these conditions are not met, charged particles can adopt complex orbits that are difficult or even impossible to describe analytically. In this regime, the approximations derived in Section 2.1.1 of this thesis are no longer valid, and alternative methods must be used to solve the equation of motion for each particle.

2.2 Penning-Malmberg Traps

As discussed in Chapter 1 of this thesis, Penning-Malmberg traps are used throughout the ALPHA experiment to confine and manipulate clouds of charged particles. As a result, $\bar{\text{p}}$ and e^+ bunches moving through the ALPHA-g beamlines will originally have been extracted from one of these traps. The initial distribution of positions and velocities in the beam will therefore depend primarily on the equilibrium state of the original trapped plasma. For this reason, it is essential to understand the dynamics of $\bar{\text{p}}$ and e^+ plasmas confined within Penning-Malmberg traps.

As described in Section 1.3, the basic geometry of a Penning-Malmberg trap is azimuthally symmetric about axis of the electrode stack. The Lagrangian for a collection of N charged particles in a poloidal magnetic field ($\partial/\partial\theta = B_\theta = 0$) is given by the expression [118]

$$\mathcal{L} = \sum_{i=1}^{N} \frac{1}{2} m \left(\dot{r}^2 + r^2 \dot{\theta}^2 + \dot{z}^2 \right) + q r \dot{\theta} A_\theta - q\phi\left(r,\, z,\, t\right) \,, \tag{2.25}$$

where $A_\theta\left(r,\, z\right)$ is the only non-zero component of the magnetic vector potential, and $\phi\left(r,\, z,\, t\right)$ is the electric scalar potential. The index i runs over all of the particles in the ensemble.

Since θ is an ignorable co-ordinate in Equation 2.25, the Euler-Lagrange equation dictates that there is a strictly conserved angular momentum for the entire system. In a uniform magnetic field, this canonical angular momentum can be written as

$$P_\theta = \frac{\partial \mathcal{L}}{\partial \dot{\theta}} = \sum_{i=1}^{N} m r^2 \dot{\theta} + \frac{1}{2} q r^2 B_0 \,, \tag{2.26}$$

where B_0 indicates the strength of the applied magnetic field. By dividing the total angular momentum by the number of particles in the ensemble, we can obtain the average value for a single particle $\langle P_\theta \rangle \simeq q B_0 \sigma_\perp^2 / 2$, where $\sigma_\perp$ is the root-mean-squared deviation of particles from the trap axis. This quantity is conserved even for particles that are extracted from the trap, and will therefore influence the dynamics of trap-based $\bar{\mathrm{p}}$ and e^+ beams. In the limit of a strong magnetic field, the first term of Equation 2.26 can be neglected, and so the conserved angular momentum directly couples the radial size of a plasma $\sigma_\perp$ to the local magnetic field strength.

As well as the potentials generated by the trap electrodes, trapped particles are influenced by a space charge potential that arises due to the distribution of charge in the surrounding plasma.

The scalar potential in Equation 2.25 can therefore be written as $\phi = \phi_{\text{ext}} + \phi_{\text{self}}$, where ϕ_{ext} is the external potential from the trap electrodes and ϕ_{self} is the space charge potential of the particles themselves. Both potentials are governed by the Poisson equation, such that [120]

$$\nabla^2 \phi_{\text{ext}} = 0\,, \tag{2.27}$$

$$\nabla^2 \phi_{\text{self}} = -\rho\left(r,\, z\right)/\varepsilon_0 \tag{2.28}$$

where $\rho\left(r,\, z\right)$ is the charge density at a given point within the trap volume, and ε_0 is the permittivity of free space.

At equilibrium, the distribution of charge within a non-neutral plasma is dictated by the Boltzmann equation [94],

$$\rho\left(r,\, z\right) = f\left(r\right) \exp\left[-\frac{q\left(\phi_{\text{ext}} + \phi_{\text{self}}\right)}{k_B T}\right]\,, \tag{2.29}$$

where $f\left(r\right)$ is an arbitrary function describing the radial density of the plasma. Together, Equations 2.28 and 2.29 are known as the Poisson-Boltzmann equation, relating the distribution of particles in a non-neutral plasma to their own space charge potential ϕ_{self}. The self-consistent interaction between these two functions can lead to waves and other instabilities in trapped plasmas, and forms the basis for collective behaviour in clouds of trapped charged particles. The Poisson-Boltzmann equation is indirectly used to measure the axial temperature of trapped plasmas, using the method outlined in Section 1.3.3 of this thesis [98].

According to the cold fluid theory of plasma confinement [94], a trapped non-neutral plasma at equilibrium will generate a space charge potential so that the total potential along the trap axis is invariant. Therefore, there is no net transport of particles along the length of the plasma.

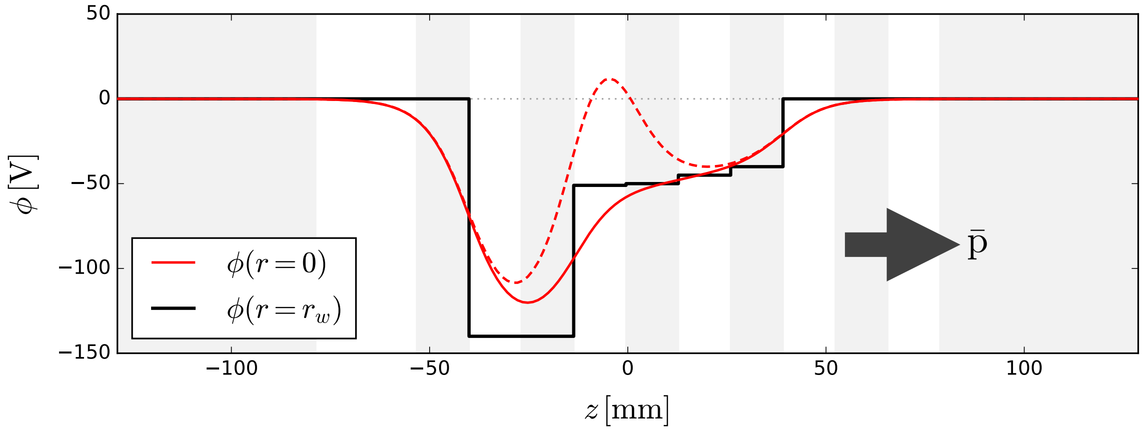

Figure 2.3: Plot showing the potentials used to eject antiprotons from the catching trap at an energy of ∼ 50 eV. The dashed line shows the on-axis potential immediately prior to beam ejection.

Perpendicular to the trap axis, however, the charged particles in a non-neutral plasma will repel one another, generating a radial electric field that is approximately constant along the length of the plasma. In combination with the magnetic field, this causes particles to undergo a two-frequency rotation about the trap axis, with angular frequencies given by the expression [94, 120]

$$\omega_r^{(\pm)} = \frac{\omega_c}{2} \pm \sqrt{\frac{\omega_c^2}{4} - \frac{qE_r}{mr}}\,, \tag{2.30}$$

where E_r is the radial component of the electric field. For small radial electric fields ($|qE_r/mr| \ll \omega_c^2$), the fast rotation frequency $\omega_r^{(+)}$ is the cyclotron frequency, while the slow rotation has a frequency $\omega_r^{(-)} \simeq E_r/rB$. This slow rotation corresponds to a bulk $\mathbf{E} \times \mathbf{B}$ rotation of the entire plasma about the trap axis.

In addition to their periodic motions about the trap axis, charged particles will also oscillate along the length of the electrostatic potential produced by the trap electrodes. In a harmonic potential well $\phi_{\text{ext}}(z)$ with no space charge, this motion takes place at a characteristic bounce frequency that is independent of the particle energy. As such, trapped charged particles will sample the length of an external potential over a characteristic time scale set by their bounce frequency ω_z.

As well as dictating the spatial distribution of particles in a trapped plasma, the electric potential also plays a role in defining the distribution of particle velocities. At thermal equilibrium, the combined position-velocity distribution function is given by the product of Equation 2.29 and a Maxwellian velocity distribution, which is shifted by the plasma rotation frequency $\omega_r r\,\hat{\theta}$ [94, 120]

$$f\left(\mathbf{r},\,\mathbf{v}\right) = f\left(r\right)\exp\left[\frac{m}{k_B T}\left(\mathbf{v}+\omega_r r\,\hat{\theta}\right)^2 + \frac{q\phi\left(r,\,z\right)}{k_B T}\right]. \tag{2.31}$$

In the rotating reference frame of the plasma, the charged particles have a Maxwell-Boltzmann distribution of velocities at thermal equilibrium, similar to that of an ideal gas. This distribution determines the initial spread of transverse velocities in p̄ and e^+ bunches extracted into the ALPHA-g beamlines.

2.3 Dynamics of Trap-Based Beams

Charged particles can be extracted from a Penning-Malmberg trap in the form a pulsed beam by quickly reducing the depth of an asymmetric potential well, as shown in Figure 2.3. Many of the properties of the resulting beam are determined by the state of the plasma immediately before its extraction. For example, while the mean energy of the beam is set by the potential from which it was released, the pulse length is typically set by the rate at which the trap can be opened at one end.

In order to produce short ($\lesssim 1$ μs) bunches of p̄ and e^+ using this method, the trap depth must be reduced to zero over a time scale that is much faster than the single particle bounce frequency. In general, the minimum spread of energies within the beam is set by the axial temperature of the plasma immediately prior to its extraction. While trapped non-neutral plasmas can routintely be cooled to cryogenic temperatures, fast switching of the electrode voltages can introduce phase-space filamentation, resulting in an energy spread upwards of ~ 1 eV.

Charged particle beams are considered to be magnetized if the typical Larmor radius is much smaller than the transverse distribution of particles in the beam, so that $r_L \ll \sigma_\perp$. In this regime, charged particles will typically move in helices along the direction of the local magnetic field. Magnetized beams are commonly encountered in electron coolers [121], where a magnetized beam of electrons is used to dampen the thermal motion of particles in a co-propagating beam of ions or other heavy particles. Pulsed beams of charged particles that are extracted from Penning-Malmberg traps can also be considered to be magnetized.

In general, magnetized beams have a large conserved angular momentum that dominates the dynamics of their motion through an external electromagnetic field. For example, by comparing the mean value of Equation 2.26 at any two points in a strong magnetic field, we find that the beam envelope scales in a similar manner to many other dynamical variables

$$\sigma_\perp\left(z\right) = \sigma_\perp\left(z_0\right)\sqrt{\frac{B\left(z_0\right)}{B\left(z\right)}}\,, \tag{2.32}$$

so that the transverse size of the beam decreases in a stronger magnetic field. This scaling relationship assumes that the first term of Equation 2.26 can be neglected at all times, and is therefore invalid in magnetic fields that are weak or have large field gradients.

However, by considering the motion of a single charged particle travelling at small angles to the total beam velocity, it is possible to derive a beam envelope equation that is valid for all magnetic fields. For this purpose, it is useful to introduce the beam magnetisation $\Gamma = \langle P_\theta \rangle / m v_z$, where v_z is the beam velocity along the magnetic field lines. In addition, we assume that the beam propagates at a constant energy, and remains in the non-relativistic ($v_z \ll c$) regime at all times.

In this case, the beam envelope equation is given by [117, 121]

$$\frac{\mathrm{d}^2\sigma_\perp}{\mathrm{d}z^2} + k_l^2\sigma_\perp - \frac{K}{4\sigma_\perp} - \frac{\varepsilon_\perp^2 + \Gamma^2}{\sigma_\perp^3} = 0, \tag{2.33}$$

where K is the generalised perveance, representing the space charge of the beam, $\varepsilon_\perp$ is the transverse emittance, and $k_l = \omega_c/2v_z$ is the larmor wavenumber, representing the focusing effect of the external magnetic field. The transverse emittance of a charged particle beam is a measure of its combined position and velocity spread within the transverse plane. In the absence of external heating or coupling between the degrees of a freedom, the transverse emittance is conserved during the motion of a charged particle beam [117].

Statistically, the transverse emittance is defined as

$$\varepsilon_\perp = \sqrt{\langle x_i^2\rangle\langle (x_i')^2\rangle - \langle x_i\, x_i'\rangle^2}\,, \tag{2.34}$$

where x_i is the position of a particle projected into one of the transverse degrees of freedom, with $i \in \{x,\, y\}$. The parameter $x_i' = v_i/v_z$ is the divergence angle of that particle with respect to the overall beam velocity. Angled brackets $\langle ... \rangle$ are used to indicate an averaging over all particles in the beam. A beam with a large emittance cannot be focused down to a small point without a corresponding increase in its divergence. For a beam with an uncorrelated transverse phase space and a thermal distribution of transverse velocities, the transverse emittance can be approximated as $\varepsilon_\perp \simeq \sigma_\perp\sqrt{3k_BT/2E_\parallel}$.

For many applications, the transverse emittance is a key figure of merit in evaluating the performance of a beamline or storage ring. However, for the ALPHA-g beamlines, the emittance of $\bar{\mathrm{p}}$ and e^+ bunches delivered to a particle trap is a poor figure of merit, since trapped plasmas can be cooled to cryogenic temperatures soon after being captured.

Parameter	**Antiprotons** ($\bar{\text{p}}$)	**Positrons** (e^+)	**Units**
Plasma Radius $\sigma_\perp$	0.4	1.0	mm
Plasma Length σ_z	4.0	150	mm
Magnetic Field B_z	3.0	0.15	T
Beam Energy $E_\parallel$	50	50	eV
Temperature T	350	1000	K
Larmor Radius r_L	8.37	6.61	μm
Magnetization Γ	235	3140	mm · mrad
Emittance $\varepsilon_\perp$	12.0	50.8	mm · mrad

Table 2.1: Summary of typical source parameters for $\bar{\text{p}}$ and e^+ beams ejected from particle traps within the ALPHA apparatus.

Table 2.1 lists the typical characteristics of $\bar{\text{p}}$ and e^+ beams extracted from the catching trap and positron accumulator, respectively. The magnetic fields used to confine particles within these traps will often result in the production of strongly magnetized beams, such that $\Gamma \gg \varepsilon_\perp$.

Equation 2.33 is a nonlinear ordinary differential equation that has no trivial solution for an arbitrary magnetic field. In the case of a uniform magnetic field, the general solution to this equation is a beam envelope that oscillates about an initial value σ_0, produced as the focusing effect of the external magnetic field competes against the defocusing effects of the space charge and emittance. Since the characteristics of these oscillations depend on the initial conditions of the beam, it is possible to produce a matched beam that propagates with a constant envelope σ_0. A condition for this behaviour can be derived by setting the first term of Equation 2.33 to zero, so that

$$k_l^2 \sigma_0 - \frac{K}{\sigma_0} - \frac{\varepsilon_\perp + \Gamma^2}{\sigma_0^3} = 0\,. \tag{2.35}$$

In diffuse, strongly magnetized beams with negligible space charge and $\Gamma \gg \varepsilon_\perp$, this condition is always satisfied in a uniform magnetic field. As such, beams extracted from Penning-Malmberg traps initially propagate with a fixed envelope, which can begin to oscillate as the magnetic field varies along the beam path.

In general, pulsed beams extracted from Penning-Malmberg traps will have some distribution of energies along their direction of travel. This spread of energies will typically cause the length of each bunch to increase as it moves along its direction of travel. As discussed later in Section 3.1.3 the maximum bunch length that can be delivered by the ALPHA-g beamlines is limited by the electrostatic potentials that are used to capture $\bar{\mathrm{p}}$ and e^+ bunches. It is therefore important to minimise the bunch length by reducing both the initial length of an extracted plasma, and its spread of energies along the beamline.

Throughout this thesis, we define the bunch length σ_τ as the envelope that encloses 95% of beam particles within the time domain. In a trapped non-neutral plasma, the particle velocities are distributed evenly between both directions along the trap axis. As a result, the initial length of an extracted $\bar{\mathrm{p}}$ or e^+ bunch is approximately $\sigma_\tau = 2\sigma_z/v_z$ where σ_z is the physical length of the trapped plasma. Assuming a normal distribution of particle energies, we define the energy spread such that 68% of particles are within σ_E of the centroid beam energy. In the context of the ALPHA experiment, $\bar{\mathrm{p}}$ and e^+ bunches are typically extracted with an energy spread of a few percent. The longitudinal phase space of a beam is defined by the distribution of particles in time (δt) and energy (δE) around the mean value of each quantity.

Particles that propagate over long timescales will typically separate according to their longitudinal velocity, so that more energetic particles move towards the head of each bunch. However, if the longitudinal (δt, δE) phase space is manipulated so that these particles are moved towards the tail of each bunch, the bunch length σ_τ will initially decrease. As a result, bunching can be achieved by using a time-dependent electrostatic potential to modify the distribution of particle energies [122]. The longitudinal compression of $\bar{\mathrm{p}}$ and e^+ bunches is mentioned in Section 7.1.3 of this thesis.

2.4 Numerical Simulation Methods

In many cases, the trajectories of charged particles through an arbitrarily complex electromagnetic field cannot be described analytically. As a result, it is often necessary to find numerical solutions to the Lorentz equation, by incrementally advancing the position and velocity of a charged particle over a large number of discrete time steps. At each step of the integration, the electromagnetic fields are evaluated at the current position of a given particle, and used to modify its velocity according to Equation 2.1. Where the time step of the integration is much shorter than the period of the fastest dynamics that are to be resolved, this approach can accurately reproduce the paths of charged particles through a complex electromagnetic field.

For many decades, the Boris (or 'leapfrog') algorithm has been widely used to numerically calculate the trajectories of charged particles [123, 124]. This algorithm is a symplectic stepper that is described by the equations

$$\mathbf{x}_{(k+1)} = \mathbf{x}_k + \mathbf{v}_{(k+1)}\delta t\,, \tag{2.36}$$

$$\mathbf{v}_{(k+1)} = \mathbf{v}_k + \frac{q\delta t}{m}\left[\mathbf{E}_k + \left(\frac{\mathbf{v}_k + \mathbf{v}_{(k+1)}}{2}\right) \times \mathbf{B}_k\right]\,, \tag{2.37}$$

where $\mathbf{x}_k$ is the particle position at a time t_k after k discrete time steps of length δt. At each step, the particle velocity $\mathbf{v}_k$ is evaluated at $t_{(k-1/2)}$. This offset of half a time step between the evaluation of the particle position and velocity is characteristic of the leapfrog integration scheme. Throughout the integration, the electric and magnetic fields $\mathbf{E}_k$ and $\mathbf{B}_k$ are evaluated at the current position of the particle.

At first glance, Equation 2.37 appears to be implicit due to the appearance of both $\mathbf{v}_k$ and $\mathbf{v}_{(k+1)}$ in the cross product on the right hand side.

However, an explicit expression for the velocity can be obtained by writing the magnetic field in terms of a dimensionless matrix

$$\Omega_k = \frac{q\delta t}{2m} \begin{bmatrix} 0 & -B_z & B_y \\ B_z & 0 & -B_x \\ -B_y & B_x & 0 \end{bmatrix}_k . \tag{2.38}$$

By rewriting the cross product in Equation 2.37 as a matrix product, the velocity component of the leapfrog algorithm can be written in an explicit form. Substituting Equation 2.38 into Equation 2.37, it is found that

$$\mathbf{v}_{(k+1)} = \left(I_3 + \Omega_k\right)^{-1} \left(I_3 - \Omega_k\right) \mathbf{v}_k + \frac{q\delta t}{m} \left(I_3 + \Omega_k\right)^{-1} \mathbf{E}_k \, , \tag{2.39}$$

where I_3 is the 3×3 identity matrix.

Over the years, the leapfrog algorithm has been shown to have a number of advantages over other common numerical integration schemes. For example, while algorithms such as the fourth-order Runge-Kutta method have a finite integration error at each step that may add coherently, the leapfrog algorithm can accurately follow the path of a charged particle over an arbitrary number of time steps [123]. In the absence of an electric field, the leapfrog method will conserve the energy of a particle exactly over many time steps. This characteristic of the algorithm is particularly important when following charged particles through a system where different dynamics can emerge over very different timescales.

For example, antiprotons propagating through the ALPHA-g charged particle beamlines have a cyclotron motion that is initially very fast, with a period of $\sim 10^{-8}$ seconds. However, the time taken for a 50 eV $\bar{\mathrm{p}}$ bunch to travel between the catching trap and ALPHA-g atom trap is on the order of 120 μs.

Since the cyclotron motions of single particles play an important role in determining the overall beam dynamics, it is important that these motions are accurately resolved throughout the duration of a simulated particle transfer. Likewise, while some integration schemes would require multiple evaluations of the electromagnetic fields at each time step, the leapfrog method only requires one evaluation of each field per iteration. This is particularly useful in plasma physics simulations, where the dynamics are dominated by space-charge forces that are computationally intensive to evaluate [124].

When using the leapfrog algorithm in the context of a magnetic beamline, it is important that the magnetic field in Equation 2.37 is accurately evaluated at each time step. In the absence of ferromagnetic materials and hysteresis effects, magnetic fields can only be produced by the flow of an electrical current through space. In this case, the total magnetic field at any position can be evaluated directly using the Biot-Savart law.

The magnetic field at a position $\mathbf{x}$ due to the flow of current through a three-dimensional conductor can be written as

$$\mathbf{B}\left(\mathbf{x}\right) = \frac{\mu_0}{4\pi}\int_V \frac{\mathbf{J}\times\mathbf{r}}{|r|^3}\,\mathrm{d}^3 r\,, \tag{2.40}$$

where μ_0 is the permeability of free space, $\mathbf{J}$ is the current density and $\mathbf{r}$ is the displacement vector from an infinitesimal volume element $\mathrm{d}^3 r$. In this form of the Biot-Savart law, the integral runs over the entire volume of the conductor V.

Where current is allowed to flow through a number of separate conductors with overlapping magnetic fields, their magnetic fields can simply be added together using the principle of superposition. Conveniently, the solutions to Equation 2.40 are proportional to the absolute value of the current density $|J|$.

Once the magnetic field of a conductor has been calculated for a specific current density, this scaling behaviour can be exploited to find further solutions for arbitrary current densities by multiplying the magnetic field accordingly.

Throughout this thesis, the postprocessor component of the Opera3d software package [125] is used to numerically evaluate magnetic fields within the ALPHA apparatus. This software includes a fast Biot-Savart solver that can be used to calculate the magnetic fields of simple conductors at any point in three-dimensional space. In this solver, solenoid magnets are treated as hollow cylindrical conductors that carry a uniform azimuthal current density through their entire conducting cross section. However, a real solenoid magnet will typically be built up by winding a single length of wire into many thousands of azimuthal turns and radial layers around a common axis. The Opera3d postprocessor neglects the internal structure of solenoid magnets, replacing the array of individual windings with an averaged uniform current density.

3 | Beamline Design for ALPHA

The following chapter describes the development of a beamline design suitable for the ALPHA experiment. In Section 3.1, we discuss a range of factors that inform the design of the ALPHA-g beamlines, and show that a number of common beamline designs are unsuitable for the ALPHA experiment as a result. We describe the novel beamline design that was developed to transport $\bar{\mathrm{p}}$ and e^+ bunches around the ALPHA experiment at energies of $\lesssim 100$ eV. Section 3.2 describes the different elements that make up the ALPHA-g beamlines, while Section 3.3 reviews the design of the interconnect magnet, which is primarily responsible for the steering of $\bar{\mathrm{p}}$ and e^+ bunches throughout the ALPHA apparatus. Throughout this chapter, the simple analytical approximations that were derived in Chapter 2 of this thesis are used to model the dynamics of charged particles within the ALPHA-g beamlines. In many cases, analytical models are used to optimise the beamline design without resorting to the use of numerical simulations, which are fully explored in Chapter 4.

3.1 Design Considerations

The following section describes considerations that must be accounted for in the design of the ALPHA-g beamlines. Section 3.1.1 reviews a range of factors that influence the overall beamline design, while Section 3.1.2 evaluates different schemes that could be used to transport $\bar{\mathrm{p}}$ and e^+ bunches throughout the ALPHA apparatus. Finally, Section 3.1.3 describes the requirements that must be met by a successful beamline design, while Section 3.1.4 outlines practical considerations that constrain the design of the beamline elements.

3.1.1 Limiting Factors

During charged particle transfers in the ALPHA experiment, $\bar{\mathrm{p}}$ or e^+ bunches are extracted along the axis of one Penning trap, and must be guided into another using a suitable electromagnetic field. These particle traps have a number of characteristics that will constrain the design of any beamlines used to transfer charged particles between them. These properties can be summarised as follows:

Limited Beam Energies

In a typical Penning-Malmberg trap, the maximum voltage that can applied to any given electrode is generally limited to a few hundred volts. This limit is primarily dictated by to the electromechanical properties of the trap components, as well as the heating effect of high voltages on trapped plasmas. In practical terms, the electrode voltages are limited by the maximum potential difference that can be applied to neighbouring electrodes without the risk of electrical discharge. Discharge between the electrodes or their internal signal transmission lines will cause damage to the apparatus, and can often liberate gases from the surfaces of the electrodes into the vaccum space of the trap itself.

While some electrodes can be made to withstand voltages of up to several kilovolts, these designs are often much larger than the electrodes in a typical Penning trap. As a result, high voltage electrodes generally offer more restricted access to the trap volume, and are only employed in specialised devices such as the antiproton catching trap. Throughout most of the ALPHA apparatus, the trap electrodes must be small enough to facilitate a range of delicate plasma manipulations, while also allowing good optical access to the enclosed UHV space of each particle trap.

As described in Section 2.2 of this thesis, the energies of $\bar{\mathrm{p}}$ and e^+ bunches extracted from Penning-Malmberg traps are determined by the potentials that were used to confine them immediately before their release.

Since most of the electrodes within the ALPHA apparatus can only be biased to a maximum of ± 140 V, this limits the nominal energy of any beamline design that does not include significant modifications to the existing particle traps.

Stray Magnetic Fields

Each section of the ALPHA apparatus is enclosed by a large solenoid, which provides the magnetic field used to confine plasmas within a Penning-Malmberg trap. With the exception of the positron accumulator, these magnets are superconducting devices that can produce a maximum magnetic field of several Tesla. Each solenoid generates a significant stray magnetic field that spills out across the rest of the apparatus, resulting in a background magnetic field as high as $\sim 10^2$ Gauss between particle traps. For example, there is a residual magnetic field of ~ 50 Gauss at a distance of two metres from the magnetic centre of the ALPHA-II experiment. The magnetic environment of the ALPHA experiment must therefore be characterised as a complex patchwork of overlapping magnetic fields. This environment is incompatible with beamline elements that would use weak electric or magnetic fields to guide passing $\bar{\mathrm{p}}$ or e^+ bunches. Throughout this thesis, the magnetic field of the Earth is assumed to be small compared to the stray fields of nearby particle traps, and is therefore neglected.

Beam Extraction

As shown in Section 2.2, charged particles extracted from a strong magnetic field will have a large conserved angular momentum. The conservation of this angular momentum (Equation 2.26) couples the transverse size of the beam to the local magnetic field strength. In regions where the magnetic field strength is reduced towards zero, beams can expand radially and particles may be lost through collisions with structures in the surrounding UHV space. As a result, $\bar{\mathrm{p}}$ and e^+ bunches extracted from Penning-Malmberg traps cannot trivially be extracted into a beamline with no axial magnetic field.

In recent years, a number of authors have developed methods to extract e^+ plasmas into electrostatic beamlines from Penning traps with strong magnetic fields [113–115]. However, as discussed in Section 1.3.6, these schemes typically require a complex geometry of permeable magnetic components and electrostatic lenses. As a result, it would be impractical to use these techiniques for the extraction of $\bar{\mathrm{p}}$ and e^+ bunches in the context of the ALPHA experiment.

3.1.2 Choice of Beamline

Having identified the above constraints, we can begin to consider and rule out different beam transport schemes for the ALPHA-g beamlines. Charged particle beamlines will often operate in one of two basic regimes, using either electrostatic fields or multipolar magnetic fields.

Magnetic Lattice Beamlines

In a magnetic lattice beamline, charged particles are guided using a regular lattice of multipolar magnetic fields. The direction of the beam can be controlled using dipole magnets, which produce a magnetic field that is perpendicular to the beam velocity. Focusing in the transverse plane is generally achieved using quadrupole magnets. The magnetic field required to steer charged particles about a certain radius of curvature is given by the expression [112]

$$B_{\mathrm{dipole}} = \frac{p_z}{qR}\,, \tag{3.1}$$

where p_z is the relativistic beam momentum and R is the radius of curvature.

Since the magnetic component of Lorentz force (Equation 2.1) is proportional to the particle velocity, large steering forces can be achieved using relatively modest magnetic fields. For relativistic charged particle beams, a magnetic field of 1 T will achieve the same steering effect as an electrostatic field of 3×10^8 V/m [112].

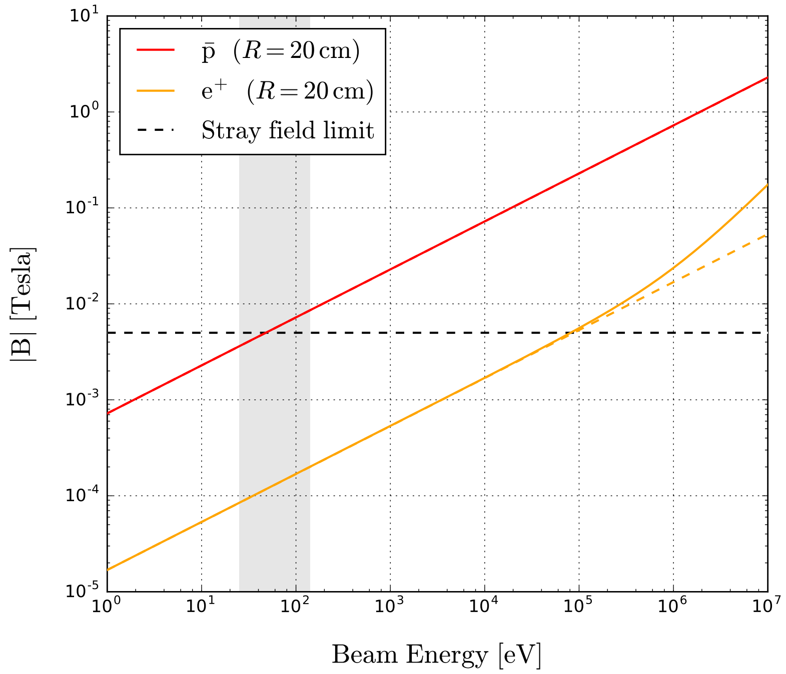

Figure 3.1: Magnetic fields required to steer beams of $\bar{p}$ and e^+ about a 20 cm radius of curvature for different beam energies up to 10 MeV. The shaded region shows the range of energies accessible to the ALPHA experiment, while the horizontal dashed line indicates the typical stray magnetic field between particle traps.

However, the magnetic fields required to implement this type of beamline for low energies are extremely small. In this regime, magnetic field errors can easily be introduced by the stray fields of neighbouring magnets or ferromagnetic materials.

Figure 3.1 shows the magnetic field required to steer $\bar{p}$ and e^+ beams of different energies around a 20 cm radius of curvature. Within the range of energies accessible to the ALPHA experiment, the magnetic fields required to steer $\bar{p}$ and e^+ bunches are comparable to the residual magnetic field between particle traps. For positrons, the stray field level is only exceeded at energies above $\sim$ 100 keV, which cannot be achieved using the ALPHA apparatus. Magnetic lattice beamlines are therefore unsuitable for the ALPHA experiment.

Electrostatic Beamines

Electrostatic beamlines are often used to guide charged particles with energies less than $\sim$ 100 keV.

In this regime, the beam dynamics are controlled by applying voltages to conductive surfaces spaced along the beam path. Charged particles are accelerated along the direction of the local electric field. This type of beamline has a number of advantages, given that electrostatic elements are generally more compact and produce fewer stray fields outside their own volume. The direction of a beam can be controlled using devices such as deflectors and electrostatic quadrupoles, which produce an electric field perpendicular to the beam velocity. Similarly, elements such as Einzel lenses can be used to reduce the size of the beam within the transverse plane. From 2021, electrostatic beamlines will be used to guide $\bar{\mathrm{p}}$ bunches to the AD experiments at an energy of 100 keV [44].

At first glance, electrostatic beamlines appear well-suited to the ALPHA experiment, requiring very modest voltages to steer $\bar{\mathrm{p}}$ and e^+ beams with energies $\lesssim$ 100 eV. However, electrostatic beamlines would be difficult to implement due to the residual magnetic fields that exist throughout the ALPHA apparatus. In a magnetic field of $\sim$ 50 Gauss, the Larmor radius for a positron is approximately 5 mm. This distance is considerably shorter than the $\sim$ 20 cm radius of curvature that is required for the interconnect magnet. The trajectories of electrostatically guided e^+ bunches are therefore likely to be distorted by the stray fields of nearby particle traps.

Furthermore, the extraction of $\bar{\mathrm{p}}$ and e^+ plasmas from Penning-Malmberg traps into an electrostatic beamline with essentially no magnetic field is highly non-trivial. As stated earlier, the use of electrostatic beamlines would require that charged particles are extracted from their Penning traps using a complex geometry of electrostatic lenses and highly permeable magnetic elements [113–115]. Without a suitable extraction scheme, the beam envelopes for $\bar{\mathrm{p}}$ and e^+ would rapidly expand as the strength of the magnetic field decreases along the beamline. Electrostatic beamlines are therefore unsuitable for use within the ALPHA experiment.

Solenoid Focusing Channel

An alternative to the schemes that have already been discussed is to transport $\bar{\mathrm{p}}$ and e^+ bunches through a series of solenoids that connect the different particle traps. In this regime, the charged particles form a magnetized beam and should move along the magnetic field lines when transported at a suitably low energy. As a result, their motions can be described used the simple approximations derived in Chapter 2 of this thesis. In a strong magnetic field, the beam envelope is dictated by the strength of the local magnetic field according to Equation 2.32.

This type of beamline design avoids many of the problems faced by magnetic and electrostatic beamlines. For example, the stray magnetic fields between particle traps should help to focus $\bar{\mathrm{p}}$ and e^+ bunches, instead of distorting their trajectories. Since charged particles are never extracted into a region with no magnetic field, there is no need to develop extraction schemes involving magnetic shielding and electrostatic lenses. In the regime where charged particles robustly follow the direction of the magnetic field due to their cyclotron motions, steering can be achieved by producing a region of curved magnetic field lines.

3.1.3 Design Requirements

Modes of Operation

Unlike many accelerators and storage rings, the ALPHA-g beamlines must be able to transport several species of particles along a number of different beam paths. Table 3.1 details the different modes of operation that must be fulfilled by the ALPHA-g beamlines. In addition to transporting $\bar{\mathrm{p}}$ and e^+ bunches into the two $\bar{\mathrm{H}}$ atom traps, the beamlines must also be used to extract particles from each trap to a nearby diagnostics station in a controlled manner. Electron plasmas must also be loaded into the ALPHA-II and ALPHA-g experiments for the sympathetic cooling of $\bar{\mathrm{p}}$ bunches captured from the beamlines.

Name	**Species**	**Source**	**Target**
Antiproton transfer	$\bar{\text{p}}$	Catching trap	ALPHA-g
Positron transfer	e^+	Positron accumulator	ALPHA-g
Positron transfer	e^+	Positron accumulator	ALPHA-II
Electron Loading	e^-	Diagnostics stations	ALPHA-g
Plasma Extraction	$\bar{\text{p}}$ / e^+ / e^-	ALPHA-g	Diagnostics stations

Table 3.1: Table detailing the various modes of operation that must be fulfilled by the ALPHA-g beamlines. The locations of the particle traps and diagnostics stations are indicated in Figures 1.5 and 3.3.

Since electron plasmas are accumulated from the emission of electron guns mounted at the diagnostics stations, it must be possible to guide particles into the two atom traps from these locations.

In order to operate the ALPHA-g experiment, $\bar{\text{p}}$ bunches must be extracted from the catching trap and guided along the length of the ALPHA-II apparatus before entering the new beamlines. The ALPHA-II apparatus must therefore be treated as part of the antiproton beamline, even though it cannot be modified to improve the dynamics of passing $\bar{\text{p}}$ bunches. As a result, it is important to understand the dynamics of $\bar{\text{p}}$ bunches throughout ALPHA-II apparatus before attempting to model their behaviour within the ALPHA-g beamlines.

Several of the beam paths described in Table 3.1 involve a change of direction, where particles must be steered into the ALPHA-g experiment from either the catching trap or positron accumulator. However, it must also be possible to transport e^+ bunches into the ALPHA-II experiment along a horizontal beam path that runs directly underneath the ALPHA-g atom trap. The area below the ALPHA-g experiment must therefore incorporate a compact beamline element that can steer charged particles in any one of several directions. This critical area of the beamline is referred to as the interconnect.

Assuming that $\bar{\mathrm{p}}$ and e^+ bunches closely follow the direction of the local magnetic field, the interconnect must steer particles through a region of curved magnetic field lines, which connect the ALPHA-g experiment to either the catching trap or positron accumulator. In a separate configuration, the interconnect must produce a magnetic field along the horizontal direction of the beamline, in order to guide e^+ bunches into the ALPHA-II experiment. The design of the interconnect magnet proved to be particularly challenging, and is discussed in detail in Section 3.3 of this thesis.

During the operation of the ALPHA experiment, it is important that the properties of trapped $\bar{\mathrm{p}}$ and e^+ plasmas can be measured, in order to optimise the rate of $\bar{\mathrm{H}}$ production. The properties of trapped plasmas can only be measured by extracting them to a nearby diagnostics station, where the magnetic field is often weaker by several orders of magnitude. Throughout this extraction process, plasmas must be extracted in a way that preserves information about their original state within the trap volume. When extracted through a slowly-varying magnetic field, the transverse size of a plasma will scale as a function of the local magnetic field according to Equation 2.32. Since this scaling behaviour is path-independent, the original size of a plasma can be calculated from its measured size and the magnetic field around the diagnostics station. However, when particles are extracted through a magnetic field that varies rapidly along the beam path (with $\gamma \gtrsim 1$), Equation 2.32 is no longer valid. In this regime, information about the original state of the extracted plasma is not retained.

Bunch Parameters

Upon arriving in one of the ALPHA particle traps, charged particles delivered by the ALPHA-g beamlines must be captured using an electrostatic potential well. In order to capture a large fraction of the incoming particles, $\bar{\mathrm{p}}$ and e^+ bunches must fit within an envelope that is dictated by the geometry of the receiving particle trap.

By considering the design of the ALPHA-g experiment, we can set limits on this envelope for both the transverse and longitundinal degrees of freedom.

First, we consider factors that limit the transverse size and displacement of p̄ and e^+ bunches delivered to the ALPHA-g experiment. Upon entering the ALPHA-g atom trap, charged particles must pass through an aperture of approximately ∼ 12 mm before continuing into the volume of the trap electrodes. This aperture is dictated by the mechanical design of the cryostat that maintains the experiment at a temperature of ∼ 4 K, and is not influenced by the beamline in any way. As a result, there is an upper limit for the transverse size of p̄ and e^+ bunches as they are guided into the strong magnetic field of the atom trap.

Table 1.1 lists the initial properties of plasmas extracted from the catching trap and positron accumulator. Using Equation 2.32, we can estimate the transverse size of p̄ and e^+ bunches in the 1.0 T magnetic field of the ALPHA-g experiment. For example, p̄ bunches that have propagated adiabatically from the catching trap should expand to a radius of $\sigma_\perp \sim 0.7$ mm within the ALPHA-g experiment. Likewise, e^+ plasmas extracted from the 0.15 T magnetic field of the positron accumulator should contract to a radius of ∼ 0.4 mm. However, as discussed in Section 2.3 of this thesis, Equation 2.32 is not valid for charged particle beams that propagate through weak or inhomogeneous magnetic fields.

Non-neutral plasmas that are displaced from the axis of a Penning-Malmberg trap are vulnerable to diocotron instabilites [94, 120]. In this type of instability, the displacement of the plasma relative to the trap axis results in an image charge on the surface of the nearby electrodes. The electric field of this image charge can cause the centre of the plasma to undergo a bulk $\mathbf{E} \times \mathbf{B}$ rotation around the trap axis, which can become unstable and force particles towards the electrode walls.

Plasmas loaded into a Penning trap at even small displacements from the trap axis can therefore become unstable, leading to the radial expansion and loss of $\bar{\mathrm{p}}$ and e^+ plasmas over a timescale of seconds or less.

Antiprotons delivered to the ALPHA-II and ALPHA-g experiments must be caught inside an electron plasma, which is pre-loaded into the trap before the arrival of each $\bar{\mathrm{p}}$ bunch. Electrons are used to sympathetically cool the captured $\bar{\mathrm{p}}$ cloud between its arrival in the experiment and the eventual formation of antihydrogen. While the size of an electron plasma can be controlled and optimised using the rotating wall technique [90], it must be centered close to the trap axis in order to avoid the emergence of diocotron instabilities. As a result, antiprotons must be delivered within ~ 0.5 mm of the ALPHA-g trap axis in order to maximise their overlap with the pre-loaded electron plasma.

Charged particles with very large transverse velocities may be lost due to magnetic mirroring within the strong magnetic field of the ALPHA-g experiment. The magnetic moment $\mu = E_{\perp}/B_z$ of a charged particle beam couples its mean transverse energy to the strength of the local magnetic field. In the regime where particles move adiabatically through the ALPHA-g beamlines, this quantity is conserved at all times. However, in areas of the beamline with weak magnetic fields or large field gradients, charged particles can transfer energy between their transverse and longitudinal degrees of freedom.

In this regime, the magnetic moment of the beam can increase dramatically, causing its longitudinal velocity to decrease as it enters a stronger magnetic field. If the magnetic moment of a $\bar{\mathrm{p}}$ or e^+ bunch exceeds a certain threshold, particles will no longer be able to enter the ALPHA-g atom trap, and will instead be deflected due to magnetic mirroring.

In the ALPHA experiment, non-neutral plasmas are typically cooled to temperatures of $\lesssim$ 350 K within their respective particle traps. These initial conditions result in p̄ and e^+ bunches that are initially extracted with very small magnetic moments of $\mu \lesssim 10^{-2}$ eV/T. In general, positron bunches will propagate adiabatically even in weak magnetic fields. However, antiprotons are much more likely to adopt non-adiabatic motions due to their larger rest mass (see Section 2.1.3 of this thesis).

Antiprotons delivered to the ALPHA-g experiment at an energy of 50 eV must have a magnetic moment of less than 50 eV/T to avoid being lost due to magnetic mirroring. Below this threshold, the emittance of the beam is not relevant, since p̄ clouds can be cooled to low temperatures after being captured inside the ALPHA-g Penning trap. It is therefore important that antiprotons do not encounter large magnetic field gradients or weak magnetic fields along their path to the ALPHA-g experiment.

During a charged particle transfer, p̄ and e^+ bunches are extracted from one particle trap, and must be captured by another after propagating through the beamlines. We can set limits on the longitudinal size of bunches delivered by the beamlines by considering the process used to capture them inside the ALPHA-g experiment.

Before particles are extracted from either the catching trap or positron accumulator, voltages are applied to the electrodes of the receiving particle trap to create an electrostatic potential well along the trap axis. Initially, one end of the potential well is left open, so that incoming charged particles are able to pass into the trap volume. Once a p̄ or e^+ bunch has been delivered to the particle trap, a blocking potential is raised behind the charged particles to trap them within the potential well. Figure 3.2 shows the potentials used to capture antiprotons inside the ALPHA-g Penning trap.

The delay between particles being extracted from one trap and captured in another is known as the gate time. This timing is set deterministically, and must be optimised in order to capture the maximum number of particles from an incoming pulse. For example, if the gate time is too short, then both ends of the potential well will already be closed by the time a $\bar{\mathrm{p}}$ or e^+ bunch is delivered to the trap. The incoming particles will therefore encounter a blocking potential upon their arrival, and will not be captured. Conversely, if the gate time is too long, then the incoming particles will sample the entire length of the trap and escape before a blocking potential is raised to capture them.

By considering the time taken for particles to sample the length of a potential well, we can constrain the maximum length of bunches delivered by the beamlines. If particles from the head of the bunch have already escaped from the potential well before those within the tail have arrived, it will be impossible to optimise the gate time so that 100% of particles are captured. For a Gaussian pulse of $\bar{\mathrm{p}}$ or e^+, we require that

$$\sigma_\tau \lesssim 2L\sqrt{\frac{m}{2E_\parallel}}\,, \tag{3.2}$$

where σ_τ is the time interval enclosing 95% of particles, and L is the length of the catching potential shown in Figure 3.2.

This simple model assumes that the incoming particles propagate along the potential well at a fixed kinetic energy. In practice, the potentials used to capture $\bar{\mathrm{p}}$ and e^+ bunches can be optimised to accept much longer bunch lengths. Further optimisation of the catching process is briefly discussed in Chapter 7 of this thesis.

The electrostatic potentials used to capture $\bar{\mathrm{p}}$ and e^+ bunches cannot be made arbitrarily long for a number of reasons. For example, the finite length of the ALPHA-g Penning trap may be shared between multiple plasmas at any given time.

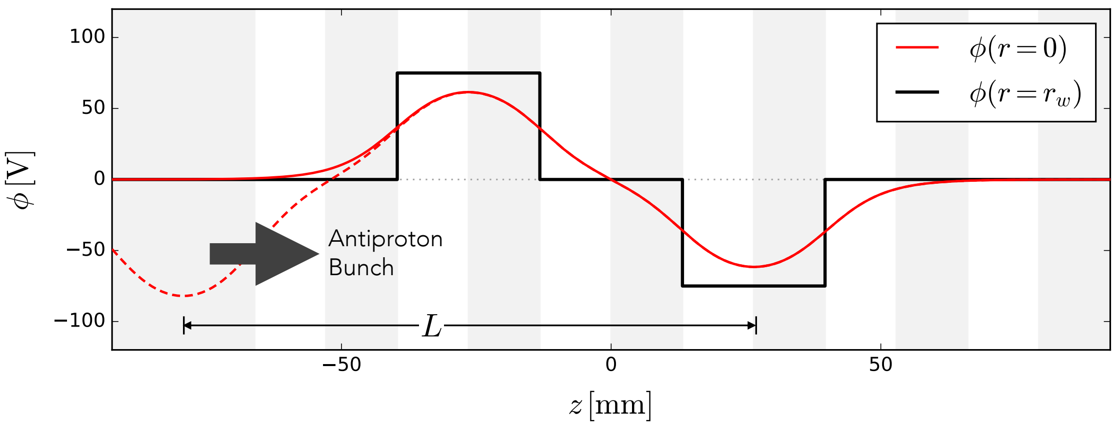

Figure 3.2: Potentials used to capture antiproton bunches inside the ALPHA-g atom trap during a charged particle transfer. The solid red line shows the potential as a $\bar{\mathrm{p}}$ bunch is launched from the catching trap, while the dashed line shows the potential after the bunch has been captured.

To accumulate antihydrogen over several successive mixing cycles, $\bar{\mathrm{p}}$ bunches must be captured using a $\sim$ 100 mm potential well, while the remainder of the trap is used for a range of positron plasma manipulations. As a result, the length of the potential L in Equation 3.2 cannot easily be varied to maximise the number of captured antiprotons. Instead, the bunch length σ_τ must be minimised so that significant numbers of $\bar{\mathrm{p}}$ are not lost as a result of their finite bunch length.

3.1.4 Practical Considerations

In addition to the physics requirements that have already been discussed within this chapter, the beamline design will be constrained by a wide range of practical considerations. For example, the UHV system of the beamline must produce a high enough quality of vacuum that $\bar{\mathrm{p}}$ and e^+ bunches are not degraded by collisions with background gases during a particle transfer. Similarly, the electromechanical properties of the beamline magnets must be chosen so that the magnets do not regularly overheat during the operation of the experiment. At worst, overheating of the beamline magnets will result in short term disruption to the experimental program, while permanent damage to any of the magnets would result in significant downtime while the beamline is repaired.

Vacuum System

From the earliest stages of their design, the ALPHA-g beamlines were intended to be modular, consisting of independent sections that can easily be separated from one another. This type of design facilitates easier maintenance of the beamline, and allows sections of the apparatus to be removed and upgraded in future. In addition, magnet designs can be shared between sections of the beamline that have similar functions. The vacuum system of the beamline must therefore be built from independent sections that can easily be separated from one another.

The ALPHA-g beamlines are directly connected to both of the $\bar{\mathrm{H}}$ mixing traps, where $\bar{\mathrm{p}}$ and e^+ plasmas must be held over long timescales. Vacuum conditions within the beamline must therefore be comparable to those in both of the atom traps, at pressures of $\lesssim 10^{-9}$ mbar. Since vacuum pumps cannot be installed at arbitrary locations along the beamline, the conductivity of the beam pipe must be taken into account. A vacuum system with a high conductivity can be evacuated using fewer pumping stations, since the flow of background gases is not impeded by small apertures or other restrictions.

Magnet Designs

During operation of the ALPHA-g beamlines, there are many situations where the beamline will be operated either continually, or in a pulsed mode with a high duty cycle. For example, while loading electrons into the ALPHA-g atom trap, some beamline magnets may be energized for up to 20 seconds while particles are collected from the emission of a nearby electron gun. In this regime, it is important that the magnets do not reach high temperatures due to the resistive heating of their windings. Each of the beamline magnets will be cooled by continually flowing water around the outer surface of their windings. However, limiting the temperatures of the magnets will still impose constraints on the maximum currents that they can safely carry.

As discussed in Section 2.4, each beamline magnet was originally treated as cylindrical conductor carrying a uniform azimuthal current density. Each magnet was therefore specified in terms of its outer dimensions and nominal current density, neglecting the individual windings that make up a real electromagnet. For a copper cylinder carrying a uniform current density J_θ, the amount of power dissipated through the resistive heating of each magnet can be estimated as

$$P = \pi \rho_{\mathrm{cu}} J_\theta^2 L \left(R_o^2 - R_i^2\right) , \tag{3.3}$$

where L is the axial length of the solenoid, ρ_{cu} is the resistivity of copper and R_i and R_o are the inner and outer radius of the cylinder, respectively.

Since the heating power of a solenoid scales quadratically as a function of its current density, magnets that operate with high currents will be vulnerable to overheating. Detailed electromechanical information about each of the beamline magnets will only be available after the development of a full winding design. However, the current density of each magnet was originally limited so that it would dissipate less than $\lesssim 1$ kW of power during normal operation of the beamline.

3.2 Beamline Elements

Figure 3.3 shows the overall layout of the ALPHA-g beamlines, separated into six sections labelled from A - F. The modular design of the beamline means that several of these sections share a common basic geometry. With the exception of the interconnect magnet, each section of the beamline can be regarded as either a beamline module or diagnostics station. The following sections describe how the analytical approximations derived in Chapter 2 were used to model and optimise the behaviour of $\bar{\mathrm{p}}$ and e^+ bunches within each beamline element. Section 3.2.1 describes the dynamics of $\bar{\mathrm{p}}$ bunches passing through the ALPHA-II experiment, while Section 3.2.2 reviews the design of the three beamline modules.

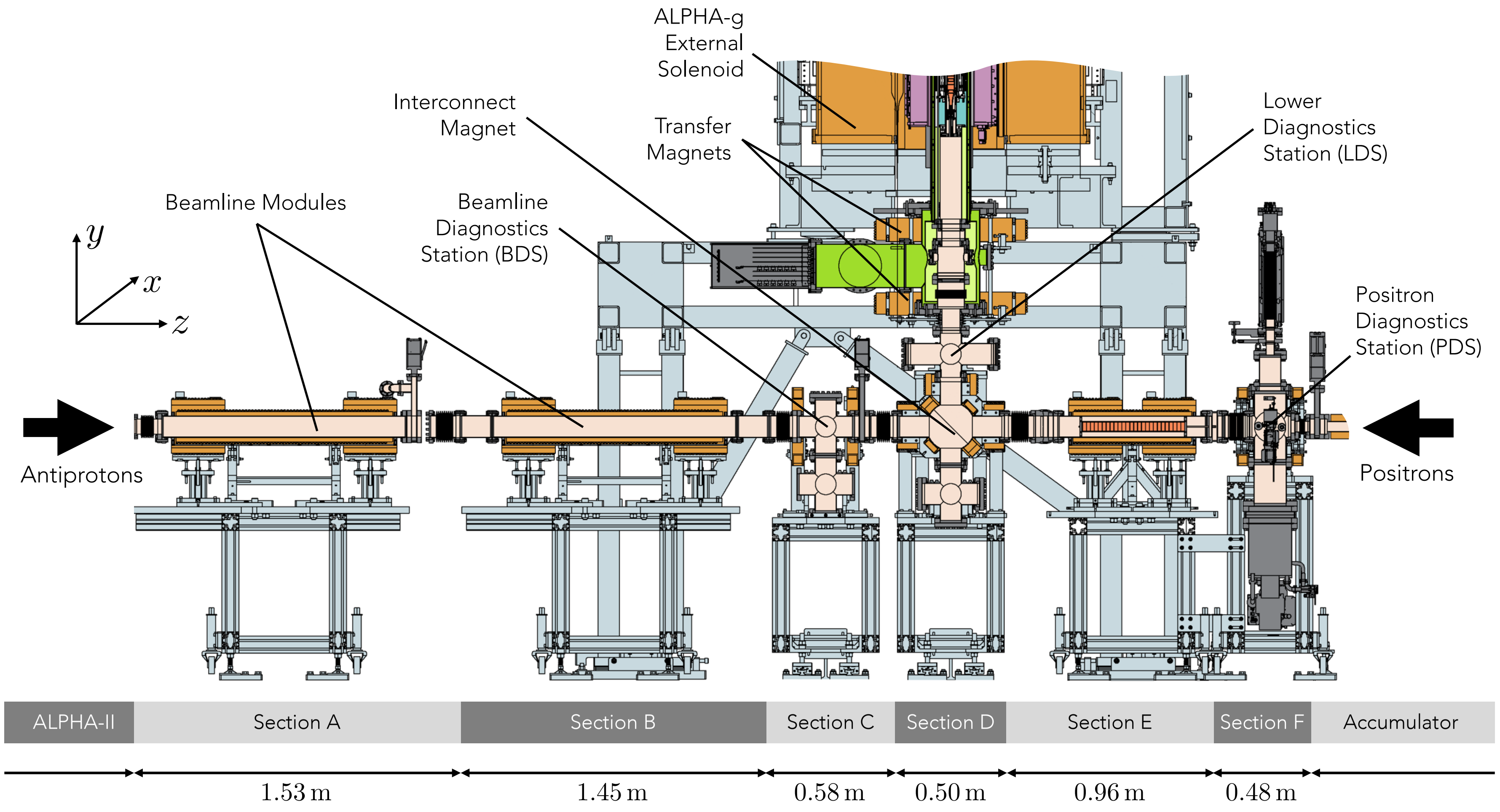

Figure 3.3: Cross-sectional schematic showing the layout of the ALPHA-g charged particle beamlines, separated into a number of individual sections. Components are shaded according to the legend in Figure 1.5.

Section 3.2.3 describes diagnostics stations that are spaced along the beamline. Finally, Section 3.2.4 discusses the effect of the ALPHA-g external solenoid on the beamlines, and Section 3.2.5 describes large solenoids that are used to extract plasmas from the atom trap.

3.2.1 The ALPHA-II Beamline

As described in Section 3.1.3, the ALPHA-II experiment must be regarded as part of the antiproton beamline, even though it cannot be modified to improve the dynamics of passing $\bar{\mathrm{p}}$ bunches. After their extraction from the catching trap, $\bar{\mathrm{p}}$ bunches propagate through a series of short solenoids before entering the ALPHA-II atom trap, with a magnetic field of 1.0 T. After passing through this area of the apparatus, antiprotons are channeled through a final short solenoid before finally entering the ALPHA-g beamlines. Figure 3.4(a) shows the magnetic field strength experienced by $\bar{\mathrm{p}}$ bunches as a function of their displacement from the centre of the catching trap.

The magnetic field strength varies significantly throughout the ALPHA-II experiment, from a maximum of 3.0 T within the catching trap to a minimum of ~ 100 Gauss around the beginning of the new beamlines. According to Equation 2.32, these fluctuations will cause the beam envelope to vary considerably within the space of several metres. It is therefore important to understand the dynamics of $\bar{\mathrm{p}}$ bunches as they are extracted through the ALPHA-II experiment. The analytical models derived in Chapter 2 of this thesis can be used to model the dynamics of $\bar{\mathrm{p}}$ bunches without the use of computationally intensive particle tracing simulations.

For example, the beam envelope equation (Equation 2.33) can be used to calculate the transverse size of $\bar{\mathrm{p}}$ bunches extracted with the initial conditions listed in Table 2.1. Figure 3.4(c) shows a numerical solution to the beam envelope equation, which was obtained using a Runge-Kutta integrator with a fixed step size.

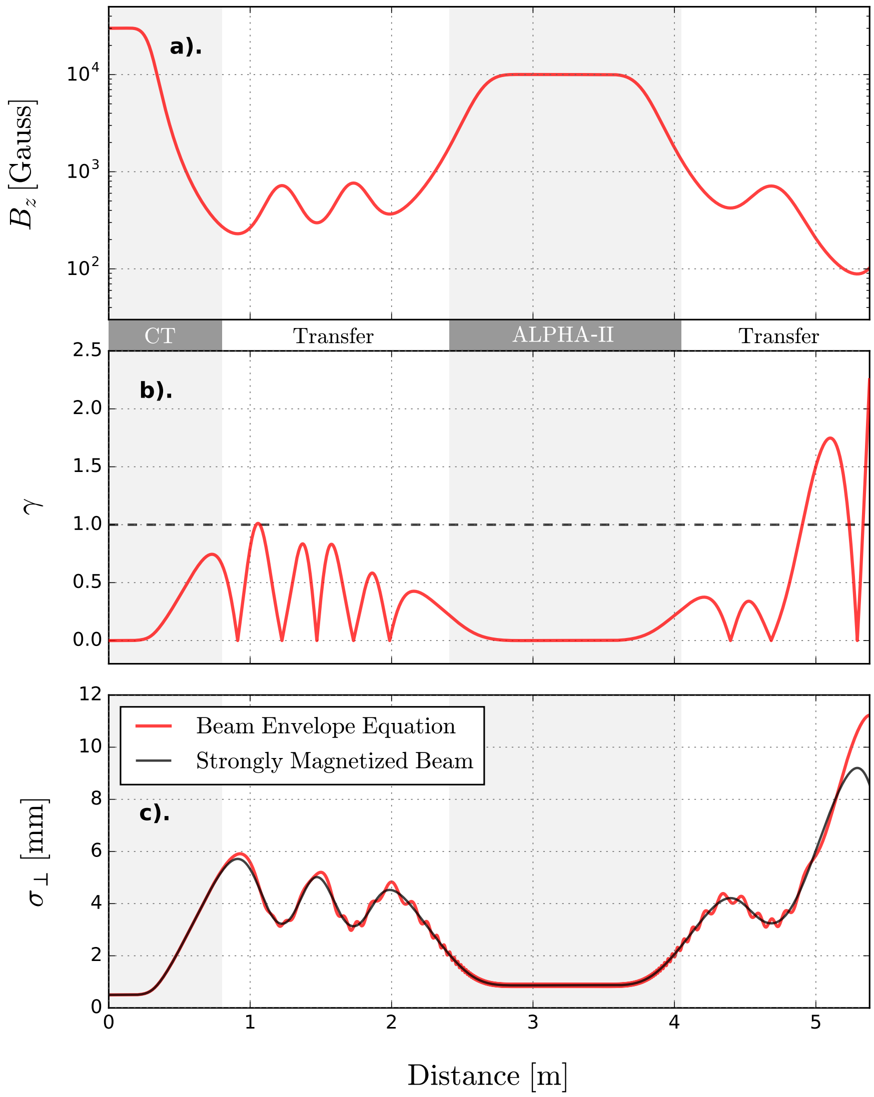

Figure 3.4: Analytical calculations indicating the properties of p̄ bunches as they move through the ALPHA-II apparatus. Panel a). shows the local magnetic field strength, while panel b). shows the adiabaticity parameter γ and panel c). shows different models of the transverse beam envelope $\sigma_\perp$.

Figure 3.4(c) also includes a second calculation for comparison, where the p̄ beam is assumed to have a path-independent envelope that is given by Equation 2.32

Calculations of the magnetic field can also be used to evaluate whether p̄ bunches will propagate adiabatically through the ALPHA-II apparatus. By evaluating the adiabaticity parameter γ at each point along the beamline, we can identify areas where antiprotons may adopt non-adiabatic motions.

However, the value of γ does not indicate how these effects will modify the dynamics of $\bar{\text{p}}$ and e^+ bunches. In regions where $\gamma \gtrsim 1$, numerical particle tracing simulations are required to accurately model the motions of single antiprotons. Figure 3.4(b) shows γ for a 50 eV $\bar{\text{p}}$ bunch moving along the length of the ALPHA-II apparatus.

Figure 3.4 shows that antiprotons will propagate adiabatically ($\gamma \lesssim 1$) throughout the majority of the ALPHA-II apparatus. As a result, their motions can accurately be modelled using the simple guiding centre approximations derived in Chapter 2 of this thesis. In this regime, the transverse size of each $\bar{\text{p}}$ bunch is primarily dictated by the conservation of its angular momentum. The solutions to the beam envelope equation can therefore be approximated using Equation 2.32, so that the transverse size of the beam depends only on the local magnetic field strength.

3.2.2 Beamline Modules

Antiproton bunches delivered to the ALPHA-g experiment must travel along a $\sim$ 3.5 m straight section of the beamline (Sections A and B in Figure 3.3), which connects the ALPHA-II experiment to the interconnect magnet. Positron bunches must also be guided along a short horizontal section of the beamline (Section F in Figure 3.3) before reaching the interconnect, where they can be steered into either of the $\bar{\text{H}}$ mixing traps. As discussed in Section 2.3, magnetized beams will expand in the transverse plane as the strength of the magnetic field decreases. Straight section of the ALPHA-g beamlines must therefore focus $\bar{\text{p}}$ and e^+ bunches using an axial magnetic field.

Straight sections of the ALPHA-g beamlines are divided into a number of beamline modules that share the same basic geometry. Each of these modules acts as a long solenoid through which $\bar{\text{p}}$ and e^+ bunches can be transported along the beamline. Figure 3.5 shows the cross section of a single beamline module, while Table 3.2 lists the properties of each magnet in this schematic.

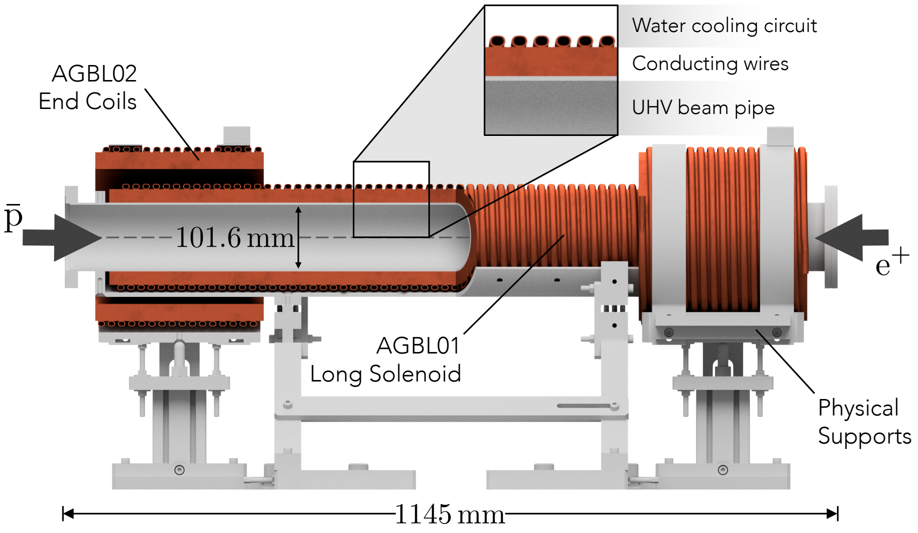

Figure 3.5: Schematic showing one of three beamline modules installed as part of the ALPHA-g charged particle beamlines.

Identifier	**Description**	**Count**	**Diameter [mm]**		**Length [mm]**
			Inner	Outer	
AGBL01-1	Long solenoid	2	101.6	141.6	1012.6
AGBL01-2	Short solenoid	1	101.6	141.6	557.0
AGBL02	End coil	6	200.0	250.0	250.0

Table 3.2: Table detailing the outer dimensions of magnets comprising the three beamline modules. The given dimensions indicate only the envelope of the magnet windings, and do not include external structures or water cooling infrastructure.

Each beamline module includes a single long solenoid (AGBL01) that is wound closely around the circumference of the UHV beam pipe, while each end of the beam pipe is enclosed by a pair of short solenoids (AGBL02). These magnets can be translated by up to 230 mm along the length of each module, to control the magnetic field in between sections of the beamline.

The modular design of the ALPHA-g beamlines means that sections of the vacuum system must be separated using components such as gate valves and flexible bellows. These components create drift spaces between sections of the beamline, where magnets cannot easily be installed to control the dynamics of $\bar{p}$ and e^+ bunches.

For this reason, the ALPHA-g beamline modules were designed to produce a large amount of stray magnetic field around their ends. These stray fields help to guide charged particles between different sections of the beamline.

The stray field around each beamline module was maximised by increasing the inner diameter of each magnet in Table 3.2. While a long, narrow solenoid will produce a negligible magnetic field outside of its own volume, magnets with a large diameter compared to their own length will produce a stronger stray magnetic field. The diameter of the beam pipe running through each module was therefore increased to $\sim$ 101.6 mm, even though $\bar{\mathrm{p}}$ and e^+ bunches should be confined to within a few millimetres of the beamline axis. This improves the uniformity of the magnetic field along the beamline, and also increases its vacuum conductance so that fewer pumping stations are require to achieve a low pressure throughout the apparatus.

In addition, the short solenoids that enclose either end of each beamline module were designed to move outwards into the spaces between sections of the apparatus. When positioned in this way, the end coils substantially increase the magnetic field within the drift spaces, and can greatly improve the beam dynamics of $\bar{\mathrm{p}}$ bunches.

We can demonstrate the effect of these magnets using a number of simple analytical calculations. Figure 3.6(a) shows the magnetic field between the ALPHA-II atom trap and the interconnect, where the beamline module end coils have been positioned to create an inhomogeneous magnetic field along the beamline. In comparison, Figure 3.7(a) shows the same calculation once the end coils have been moved to their maximum displacement from the centre of each beamline module. Clearly, this configuration produces a much more uniform magnetic field along the length of the beamline. In both cases, the current in each magnet has been kept constant, while the positions of the end coils have been adjusted by up to $\sim$ 235 mm.

Identifier	**Current Density [A/cm^2]**	**Power [W]**	**Field [Gauss]**
AGBL01-1	200	520	500
AGBL01-2	200	285	495
AGBL02	200	300	435

Table 3.3: Nominal operating point for each magnet within the ALPHA-g beamline modules. Power calculations assume that the resistivity of copper is a constant $\rho_{\text{cu}} = 1.68 \times 10^{-8}\,\Omega$ m at an operating temperature of 40 °C.

Table 3.3 lists the nominal operating point for each beamline magnet in Figure 3.6 and 3.7. In Figure 3.6, the magnetic field varies by almost two orders of magnitude along the length of the beamline.

We can evaulate how these changes in the magnetic field affect the dynamics of $\bar{\text{p}}$ bunches by using the analytical models derived in Chapter 2 of this thesis. Figures 3.6(b) and 3.7(b) show the adiabaticity parameter γ for a 50 eV $\bar{\text{p}}$ bunch moving through the magnetic field shown in the first panel of each figure. In Figure 3.6, $\bar{\text{p}}$ bunches are likely to adopt non-adiabatic motions in several areas of the beamline where $\gamma \gtrsim 1$. These regions line up with drift spaces between sections of the beamline, where the magnetic field decays rapidly outside of the beamline modules.

In contrast, γ remains small in Figure 3.7, where the end coils have been positioned to produce a more uniform magnetic field along the $\bar{\text{p}}$ beam path. In this configuration, $\bar{\text{p}}$ bunches are more likely to move adiabatically, with trajectories that are accurately described by the approximations derived in Chapter 2 of this thesis. However, some risk of non-adiabatic behaviour remains around the interface between the ALPHA-II experiment and the ALPHA-g beamlines, where $\gamma \simeq 2$. This suggests that numerical simulations are required to model the dynamics of $\bar{\text{p}}$ bunches as they travel through this region of the apparatus. Conveniently, the adiabaticity parameter is consistently much smaller for e^+ bunches compared to antiprotons due to their much lighter rest mass.

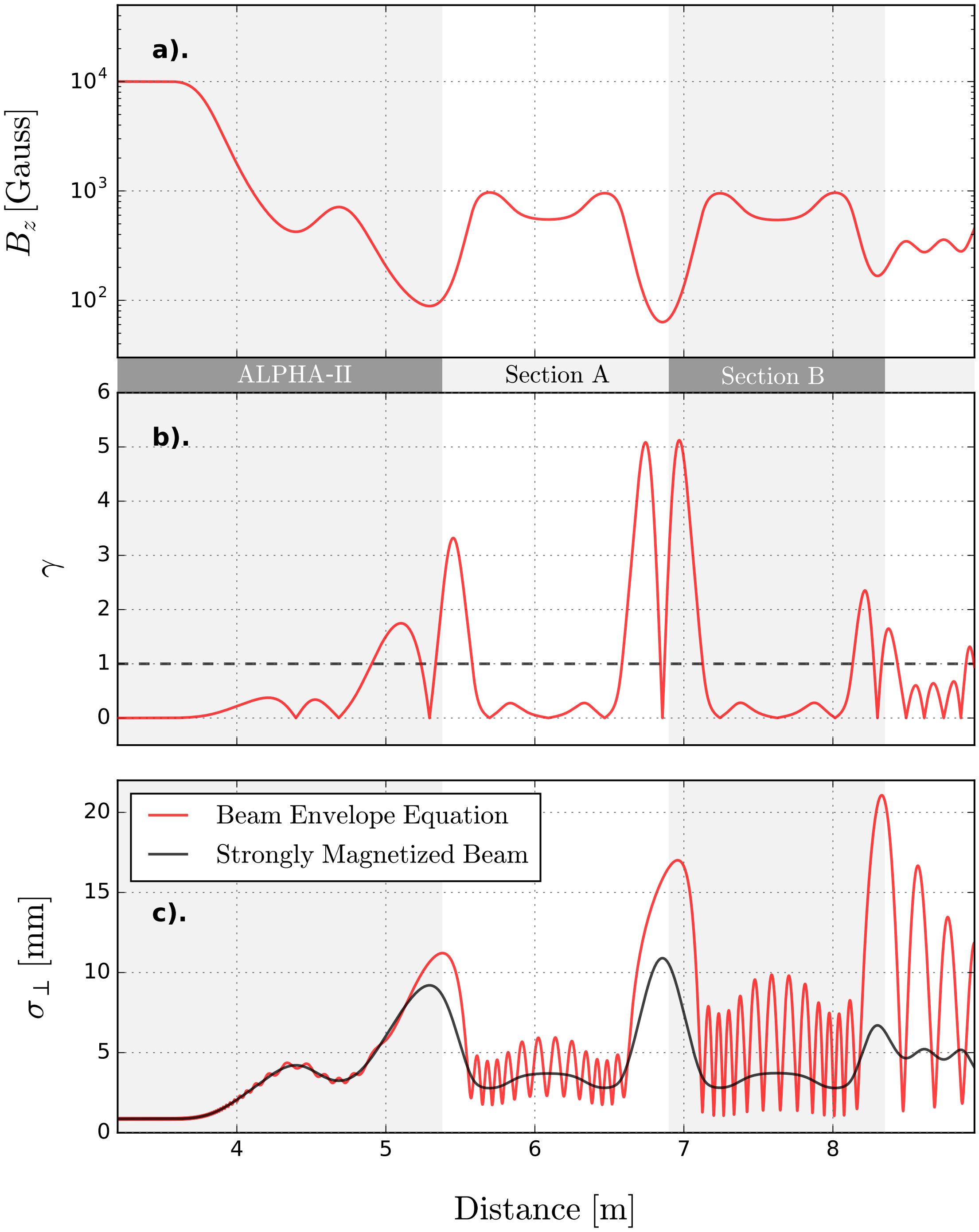

Figure 3.6: Analytical calculations indicating the properties of $\bar{\mathrm{p}}$ bunches moving between the ALPHA-II atom trap and ALPHA-g interconnect magnet. In this configuration, the beamline module end coils have been retracted to create an inhomogeneous magnetic field along the length of the beamline. Panel a). shows the magnetic field experienced by $\bar{\mathrm{p}}$ bunches, while panel b). shows the adiabaticity parameter γ and panel c). shows different models for the beam envelope $\sigma_\perp$. The horizontal axis has been shaded to indicate the extent of each beamline section, as shown in Figure 3.3.

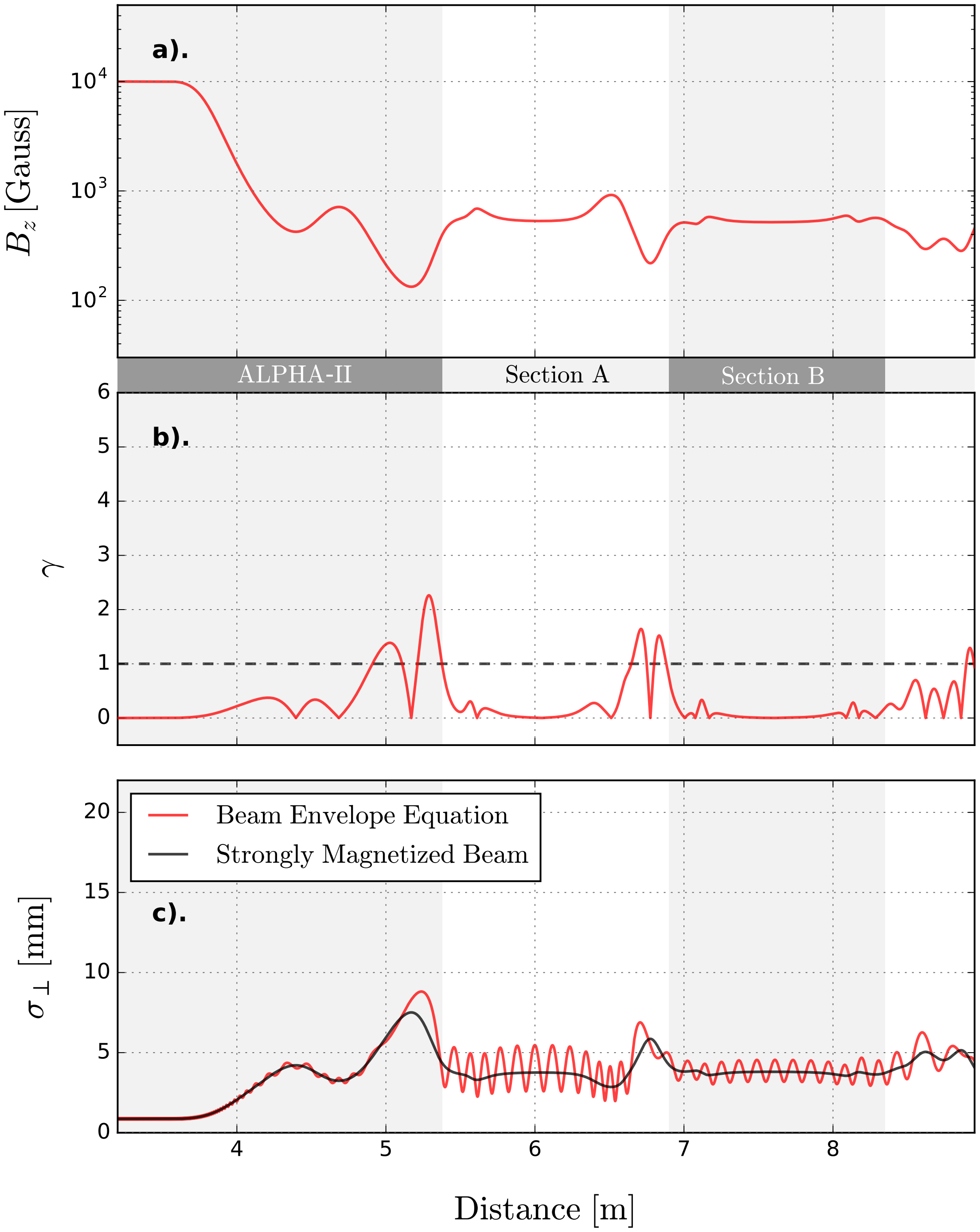

Figure 3.7: Analytical calculations indicating the properties of $\bar{p}$ bunches moving between the ALPHA-II atom trap and ALPHA-g interconnect magnet. In this configuration, the positions of the beamline module end coils have been optimised to create a uniform magnetic field along the length of the beamline. Panel a). shows the magnetic field experienced by $\bar{p}$ bunches, while panel b). shows the adiabaticity parameter γ and panel c). shows different models for the beam envelope $\sigma_\perp$. The horizontal axis has been shaded to indicate the extent of each beamline section, as shown in Figure 3.3.

Positrons should robustly follow the direction of the magnetic field throughout the ALPHA experiment, and can therefore be modelled using the guiding centre approximations.

The magnetic field of each beamline configuration can also be used to estimate the $\bar{\mathrm{p}}$ beam envelope, using the equations derived in Section 2.3 of this thesis. Figures 3.6(c) and 3.7(c) compare the transverse size of a 50 eV $\bar{\mathrm{p}}$ bunch moving through the magnetic field shown in the upper panel of each figure. The most accurate model of the beam envelope is given by Equation 2.33, which accounts for the emmitance, space charge and magnetization of each $\bar{\mathrm{p}}$ bunch. The beam envelope equation was solved for each magnetic field map using a Runge Kutta integrator with a fixed step size, starting from the initial conditions in Table 2.1. In a strong and slowly-varying magnetic field, the beam envelope depends only on the local magnetic field, and can be approximated using Equation 2.32. Figures 3.6 and 3.7 show solutions for both models of the beam envelope.

In the inhomogeneous magnetic field of Figure 3.6, $\bar{\mathrm{p}}$ bunches start to adopt an oscillating beam envelope shortly after entering the ALPHA-g beamlines. The transverse size of the beam $\sigma_\perp$ gradually increases along the beamline, reaching a maximum size of $\sim$ 20 mm just after the second beamline module. This envelope is much larger than might otherwise be indicated by Equation 2.32, suggesting that $\bar{\mathrm{p}}$ bunches are adversely affected by the weak magnetic fields between sections of the beamline. In contrast, the beam envelope in Figure 3.7 bears a much closer resemblance to the path-independent approximation given by Equation 2.32. In this configuration, $\bar{\mathrm{p}}$ bunches reach a maximum size of $\sigma_\perp \sim 8$ mm as the beam passes through a magnetic field of $\sim$ 100 Gauss around the entrance to the beamlines.

In summary, the simple approximations derived in Chapter 2 were initially used to optimise the performance of different beamline elements.

The use of analytical models in this manner avoids the need for computationally intensive numerical simulations. Similar analytical models can be used to investigate the dynamics of $\bar{\mathrm{p}}$ and e^+ bunches within different areas of the ALPHA-g beamlines. The dynamics of $\bar{\mathrm{p}}$ bunches are strongly influenced by the weak magnetic fields between different sections of the ALPHA apparatus. In a number of these regions (where $\gamma \gtrsim 1$) antiprotons can adopt non-adiabatic motions that are difficult to model analytically. This suggests that numerical particle tracing simulations are required to fully understand the dynamics of antiproton bunches moving through the ALPHA-g beamlines.

3.2.3 Diagnostics Stations

The ALPHA-g beamlines incorporate a number of diagnostics stations, which are used to measure the properties of $\bar{\mathrm{p}}$ and e^+ bunches as they move between the various particle traps. The Beamline Diagnostics Station (BDS) is primarily intended to measure $\bar{\mathrm{p}}$ bunches immediately before the entrance to the interconnect. However, the BDS can also be used to measure the properties of e^+ bunches extracted towards the ALPHA-II experiment. The Positron Diagnostics Station (PDS) is located immediately next to the positron accumulator, and is intended to optimise the properties of e^+ plasmas before their extraction into the beamline. The two diagnostics stations are labelled as sections C and F in Figure 3.3.

Both diagnostics stations share the same overall geometry to fulfil similar roles within the beamline design. The BDS and PDS are both built around a stick device (see Section 1.3.3), which can be inserted into the beamline to expose a range of diagnostic tools to oncoming charged particles. For the ALPHA-g experiment, the stick design that had previously been deployed for the ALPHA-II apparatus was modified to become bidirectional. With this new design, $\bar{\mathrm{p}}$ and e^+ bunches can be measured irrespective of their direction along the beamline.

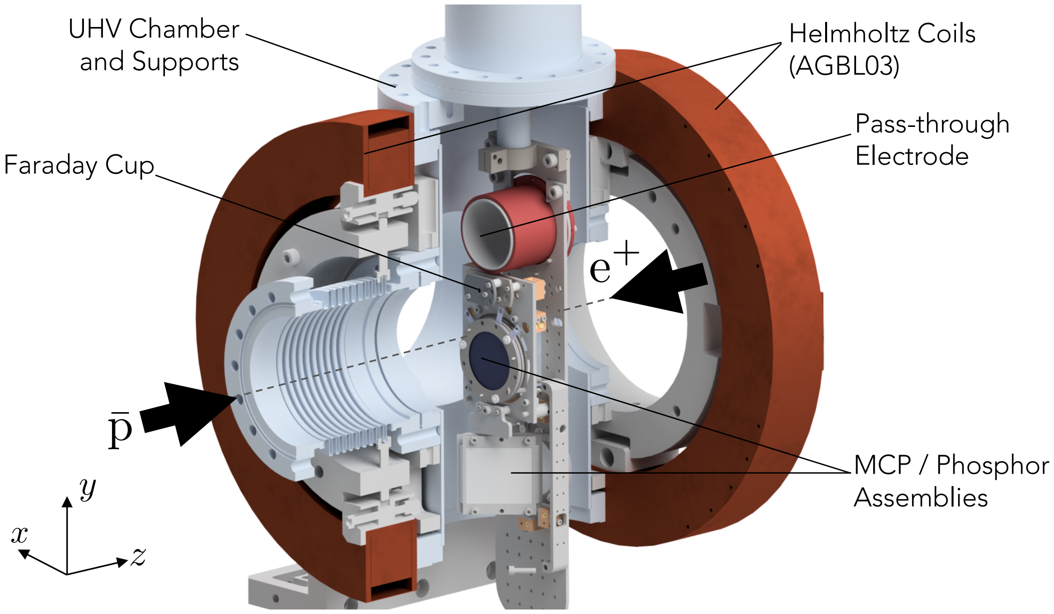

Figure 3.8: Schematic showing a cutaway view of the Positron Diagnostics Station (PDS). The various diagnostic devices are described in Section 1.3.3 of this thesis.

The two diagnostics stations are equipped with a pair of Helmholtz coils (AGBL03), which produce a magnetic field of $\sim$ 400 Gauss along the direction of the beamline. These magnets are spaced around the midplane of each diagnostics station, producing a uniform field in both r and z around the central point where particles interact with a measurement device.

The Helmholtz coils must operate in multiple roles during operation of the ALPHA-g beamlines. Primarily, they maintain the magnetic field that guides $\bar{p}$ and e^+ bunches along the beamline, allowing particles pass through each diagnostics stations when there are no measurement devices in the beamline. In addition, the Helmholtz coils provide a well-defined magnetic field around the centre of each diagnostics station. In the regime where $\gamma \lesssim 1$, Equation 2.32 can be used to relate the measured size of a plasma to its original size in a different magnetic field. Table 3.4 lists the original design parameters for the Helmholtz coils.

As well as hosting a range of measurement tools, the diagnostic stations provide much of the vacuum pumping that keeps the beamline under UHV conditions.

Parameter	**Value**	**Units**
Identifier	AGBL03	
Inner Diameter	265	mm
Outer Diameter	345	mm
Length	41	mm
Current Density	410	A/cm^2
Power	440	W
Peak Magnetic Field	275	Gauss

Table 3.4: Design parameters for the Helmholtz coils installed on the ALPHA-g beamline diagnostics stations. Power calculations assume that the resistivity of copper is $\rho_{\mathrm{cu}} = 1.68 \times 10^{-8}\,\Omega$ m at an operating temperature of 40 °C.

As stated earlier, the diameter of the beam pipe is relatively large ($\sim$ 101.6 mm) throughout much of the ALPHA-g beamlines. This results in a high vacuum conductivity, allowing the beamline to be evacuated using fewer vacuum pumps. While both diagnostic stations are equipped with a turbomolecular pump to initially achieve high vacuum conditions, the BDS is also equipped with an ion pump and can achieve pressures below 10^{-9} mbar after baking to approximately 100 °C for several days. Similarly, the PDS is equipped with a cryopump, and can produce similarly low pressures after baking of the vacuum system.

3.2.4 The ALPHA-g External Solenoid

The ALPHA-g experiment is enclosed by a 2.8 m superconducting external solenoid that produces a uniform magnetic field of 1.0 T. This magnetic field is primarily required to hold $\bar{\mathrm{p}}$ and e^+ plasmas within the ALPHA-g Penning trap prior to antihydrogen production. However, the external solenoid also adds a uniform background to the neutral atom trap that is used to confine antihydrogen atoms. It is therefore important that the magnetic field of the external solenoid is uniform to within $\sim 10^{-5}$ T/m throughout the volume of the atom trap. Failure to achieve this field quality around the centre of the atom trap would result in the introduction of magnetic field gradients, and reduce the precision of a future gravity measurement.

The design of the external solenoid is further constrained by the effect of its magnetic field on the $\bar{\mathrm{p}}$ and e^+ beamlines that run directly beneath it. Since the centre of the solenoid is only 2.6 metres above the horizontal axis of the ALPHA-g beamlines, charged particles passing underneath it will experience an additional magnetic field that will misalign them from their intended trajectories. This effect will be particularly pronounced within the interconnect magnet, where the magnetic field must be carefully shaped to steer $\bar{\mathrm{p}}$ and e^+ bunches through a change of direction in the beamline. The external solenoid must therefore incorporate some form of shielding to reduce the effect of its stray magnetic field on other parts of the apparatus.

The design of the ALPHA-g external solenoid incorporates a number of features in order to meet these requirements. For example, the windings of the solenoid are split into two separate layers, with the central inner windings enclosed by a second layers of ‘shield’ windings at a larger diameter. The direction of current in the outer winding is reversed, so that magnetic field lines escaping from the ends of the inner windings are pulled into the volume of the outer shielding layer. This geometry therefore reduces the stray magnetic field of the solenoid, and improves the uniformity of its field around the centre of the ALPHA-g experiment.

The design of the external solenoid was developed iteratively with other members of the ALPHA collaboration. After each update to the magnet design, a series of field maps were generated to accurately represent the external solenoid in numerical models of the ALPHA-g experiment. For example, some members of the collaboration evaluated how the magnet design would affect the dynamics of trapped antihydrogen atoms. In particular, numerical simulations were used to check that each iteration of the magnet would allow gravitational effects to be measured at the $\pm 1\%$ level. Detailed models of the external solenoid were also used in simulations of the ALPHA-g beamlines, to study the effects of its stray field on passing charged particles.

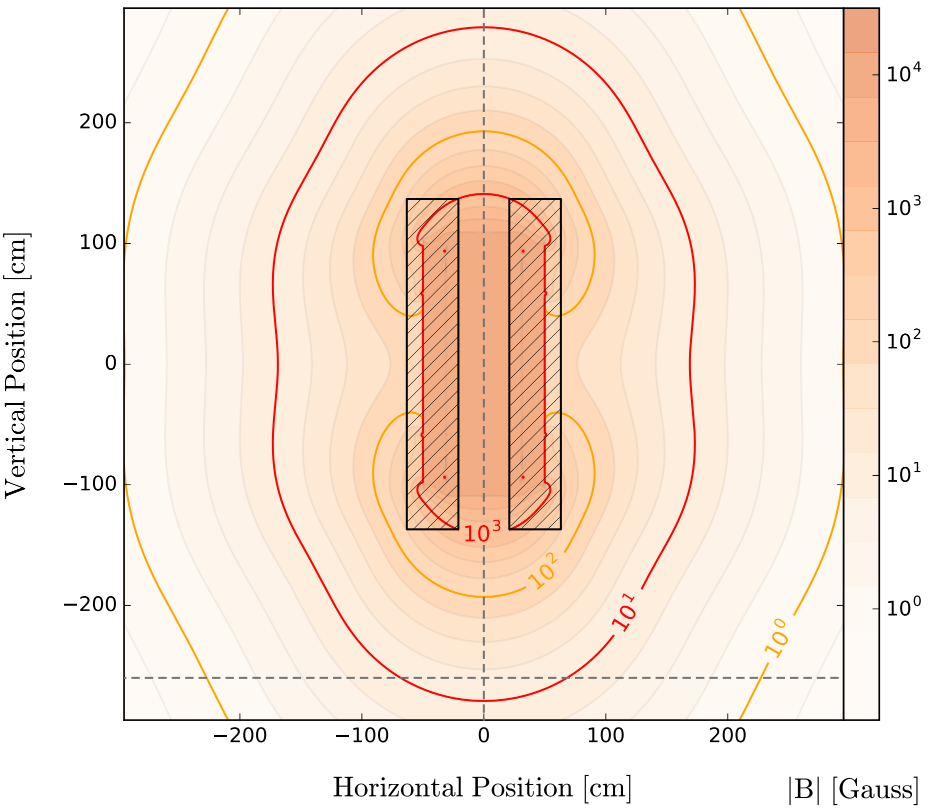

Figure 3.9: Contour plot showing the magnetic field of the ALPHA-g external solenoid magnet, with logarithmically spaced contours. The dashed lines show the axes of the charged particle beamlines, while the hatched areas show the envelope of the magnet itself.

Throughout the development of the ALPHA-g external solenoid, magnetic field maps were used to represent the effects of the solenoid in numerical models of the beamlines. Figure 3.9 shows the magnetic field of the final solenoid design at its nominal operating point of ~ 1.0 T. As shown in Figure 3.9, the external solenoid generates a significant stray field across the ALPHA-g beamlines, even after considerable optimisation of its design. This stray field contributes around ~ 50 Gauss to the total magnetic field of the interconnect, and will distort the the magnetic field in this sensitive area of the beamline. It is therefore important to account for the effects of the external solenoid in detail when modelling the trajectories of $\bar{\text{p}}$ and e^+ bunches through the interconnect, irrespective of whether numerical or analytical models are used.

Parameter	Value	Units
Identifier	AGBL08	
Inner Diameter	605	mm
Outer Diameter	700	mm
Length	100	mm
Current Density	250	A/cm^2
Power	1.02	kW
Peak Magnetic Field	226	Gauss

Table 3.5: Design parameters for the large transfer coils installed between the interconnect magnet and ALPHA-g external solenoid

3.2.5 ALPHA-g Transfer Magnets

As well as the two diagnostics stations spaced along horizontal length of the beamlines, a third diagnostics station will be installed below the ALPHA-g atom trap. The Lower Diagnostics Station (LDS) is located above the interconnect in Figure 3.3. This area of the beamline will be used to measure the properties of $\bar{p}$ and e^+ bunches steered through the interconnect magnet, as well as non-neutral plasmas extracted from the ALPHA-g experiment.

As discussed in Section 3.1.3, it is important that trapped $\bar{p}$ and e^+ plasmas can be extracted from the ALPHA-g experiment in a controlled manner for diagnostic measurements. In the limit where $\gamma \lesssim 1$ along the path of an extracted plasma, Equation 2.32 can be used to find its original transverse size from measurements taken in a much weaker magnetic field. It is therefore important that the magnetic field between the LDS and the ALPHA-g experiment can be tailored to ensure that particles are extracted adiabatically through this region.

Even after accounting for the stray field of the ALPHA-g external solenoid, charged particles extracted to the LDS will move through a magnetic field that decays to $\sim$ 100 Gauss within less than two metres.

In this regime, $\bar{\mathrm{p}}$ and e^+ are unlikely to behave adiabatically during their extraction, and may adopt a beam envelope that is poorly described by Equation 2.32. Two large solenoid magnets (AGBL08) will therefore be installed between the LDS and the bottom of the ALPHA-g experiment. Table 3.5 lists the original design parameters for these magnets. As well as shaping the magnetic fields used the extract particles from the ALPHA-g experiment, these magnets help to guide $\bar{\mathrm{p}}$ and e^+ bunches between the interconnect and the new atom trap.

While the positions of the transfer coils are constrained by the mechanical design of the ALPHA-g cryostat (see Figure 3.3), the current in each magnet can be optimised to produce a smoothly-varying magnetic field along the vertical axis of the experiment. Our figure of merit for this optimisation is the maximum value of γ along the path of an extracted plasma. In the regime where $\max(\gamma) \lesssim 1$, particles will move adiabatically, with a path-independent beam envelope that is given by Equation 2.32.

Figure 3.10(a) shows the magnetic field between the centre of the ALPHA-g atom trap and the LDS for two different configurations. If both transfer coils are turned off entirely, the magnetic field decays rapidly as particles are extracted towards the diagnostics station. This results in a large adiabaticity parameter for $\bar{\mathrm{p}}$ bunches around the location of the LDS. However, if the current in each magnet is optimised to produce a smooth and monotonically decreasing magnetic field, the adiabaticity parameter is much smaller. This suggests an improvement in the dynamics of the extracted particles. In Figure 3.10 the current in each transfer coil has been optimised using a Monte Carlo method. In this approach, many combinations of currents were generated at random, and evaluated to identify the configuration with the lowest adiabaticity parameter.

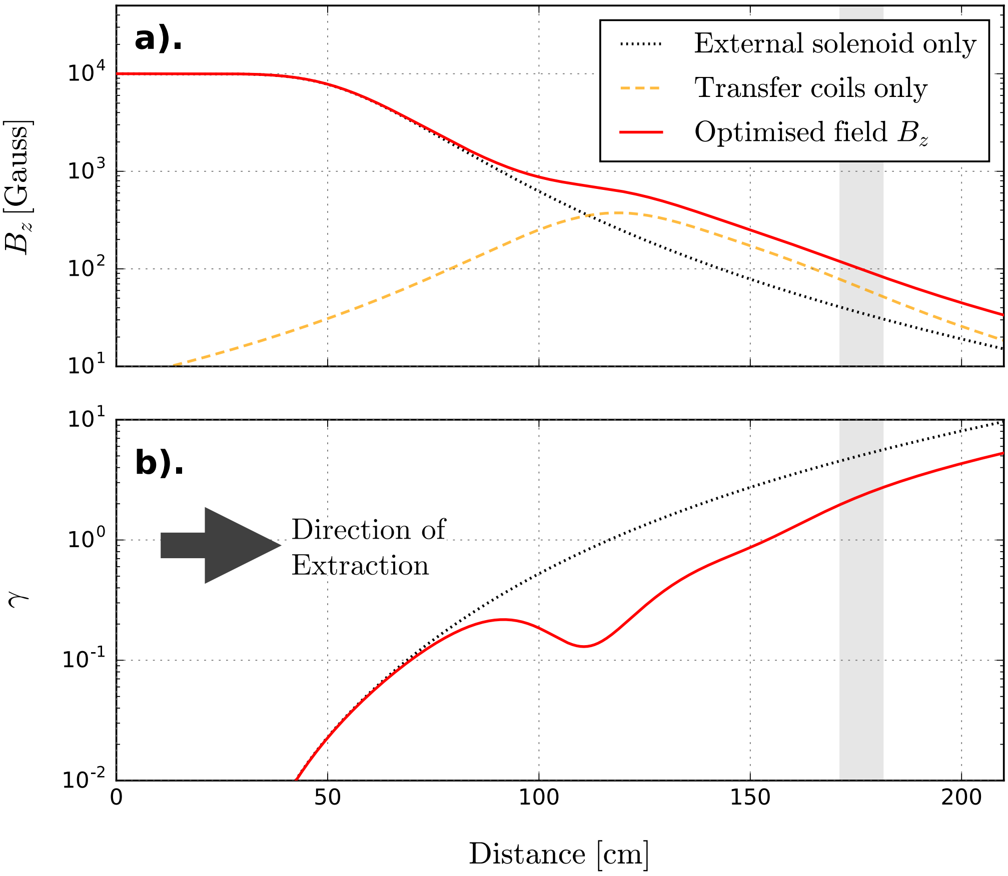

Figure 3.10: a). Magnetic field used to extract particles from the ALPHA-g experiment to the LDS (shown as a shaded region), and b). adiabaticity parameter γ for antiprotons extracted through this magnetic field. The magnetic field of only the external solenoid is shown as a dashed line, while the red line shows an optimised magnetic field obtained by powering the two large transfer coils (AGBL08).

The solutions proposed by this optimisation method were further constrained by considering the transverse size of plasmas extracted to the LDS. In order to image extracted plasmas using an MCP, their transverse size must remain smaller than the MCP diameter, but also become large enough to be imaged clearly without excessive optical magnification. For each configuration, we used Equation 2.32 to estimate the transverse size of an extracted plasma at the LDS, and discarded configurations where the plasma would expand by a factor of less than 10 or more than 20. Typically, this optimisation favours smaller expansion parameters in order to maximise the total magnetic field.

As shown in Figure 3.10, this optimisation of the magnetic field results in smaller values of γ compared to the case where only the external solenoid is used to extract particles from the ALPHA-g experiment. However, even with the optimised magnetic field, it is not possible to ensure that $\gamma \lesssim 1$ within the vicinity of the LDS. Numerical particle tracing simulations must therefore be used to check that Equation 2.32 is valid for $\bar{\mathrm{p}}$ plasmas extracted using this magnetic field.

3.3 The Interconnect

The interconnect magnet (labelled as section D in Figure 3.3) is located directly below the ALPHA-g experiment, and is responsible for steering $\bar{\mathrm{p}}$ and e^+ bunches throughout the ALPHA apparatus. As discussed in Section 2.3, charged particles should follow the direction of the magnetic field after being extracted along the axis of a Penning trap with energies of $\lesssim$ 100 eV. As a result, $\bar{\mathrm{p}}$ and e^+ bunches can be steered through the interconnect using a region of tightly curved magnetic field lines.

Equally, the interconnect must be able to produce a horizontal magnetic field that allows e^+ bunches to be transported into the ALPHA-II experiment. The design of a magnet that can produce each of these configurations is not straightforward, and requires many independent windings arranged around a compact steering region.

3.3.1 Basic Dynamics

In order to evaluate how closely charged particles will follow the direction of a curved magnetic field, we can compare the distance covered during each cyclotron period to the path length around a given radius of curvature. By taking the ratio of these two length scales, we obtain a parameter that is analogous to Equation 2.24 for particles moving through a curved magnetic field.

This expression of the adiabaticity parameter can be written as

$$\gamma_r = \frac{4mv_z}{qB_zR}, \tag{3.4}$$

where R is the curvature of the magnetic field. Consider a simple version of the interconnect, where the magnetic field lines curve around a constant 25 cm radius of curvature, with a field strength of $\sim$ 500 Gauss at this radius. For a 50 eV e^+ bunch, the adiabaticity parameter for this geometry is around 7×10^{-3}. Each positron will therefore undergo thousands of cyclotron oscillations as it passes through the interconnect. Since the change in the magnetic field during each cyclotron orbit is very small, e^+ bunches will closely follow the magnetic field lines.

However, the adiabaticity parameter is much larger for $\bar{p}$ bunches at the same energy, with $\gamma_r \sim 0.33$. This suggests that while $\bar{p}$ may follow the magnetic field lines, their trajectories are not necessarily along the magnetic field lines. As a result, more complicated dynamics may emerge as antiprotons pass through the interconnect. Analytical calculations must therefore be applied with caution, and numerical simulations may be required to fully predict the motions of single antiprotons.

Assuming for the moment that both $\bar{p}$ and e^+ bunches will follow the direction of the magnetic field lines, we can consider the various guiding centre drifts that they may exhibit while moving through the interconnect. The most obvious motion that is relevant to this geometry is the curvature drift derived in Section 2.1.1 of this thesis. To find the direction of the curvature drift, we refer to the axes shown in Figure 3.3. At the entrance to the interconnect, $\bar{p}$ bunches initially follow a magnetic field oriented along the $+z$ axis, with a curvature vector that points along $-y$. Due to their negative charge, $\bar{p}$ bunches will therefore experience a curvature drift along the $+x$ axis according to Equation 2.14.

The total displacement of the beam due to this curvature drift can be approximated

$$\delta x = \frac{\pi}{qB}\sqrt{\frac{E_{\parallel} m}{2}}\,. \tag{3.5}$$

Light particles such as e^- and e^+ will experience relatively small curvature drifts as they pass through the interconnect, being displaced by ~ 0.8 mm from their intended trajectories. However, this displacement is much larger for antiprotons. For the simple geometry that was described earlier, 50 eV $\bar{p}$ bunches will be displaced by ~ 32 mm from the axis of the ALPHA-g experiment if their curvature drifts are not corrected. The interconnect must therefore incorporate steering perpendicular to both axes of the beamline, in order to correct the curvature drifts of $\bar{p}$ bunches.

3.3.2 Magnetic Field Design

Different designs for the interconnect magnet can be evaluated by studying their magnetic field within the plane of the beamline. Numerical models of the magnetic field were therefore used extensively during the initial design of the interconnect. These models allowed a range of different geometries to be evaluated, leading to a basic design that could then be tested more rigourously using numerical particle tracing simulations.

Within the interconnect, charged particles should always move along the direction of the local magnetic field. The simplest interconnect geometry therefore consists of three solenoids, which are aligned to each of the paths taken by $\bar{p}$ and e^+ through the device. The magnetic field produced by this geometry is shown in Figure 3.11.

In Figure 3.11, the two solenoids along the horizontal axis of the beamline carry opposing electrical currents. As a result, the horizontal component of the magnetic field is zero around the $(z = 0)$ midplane.

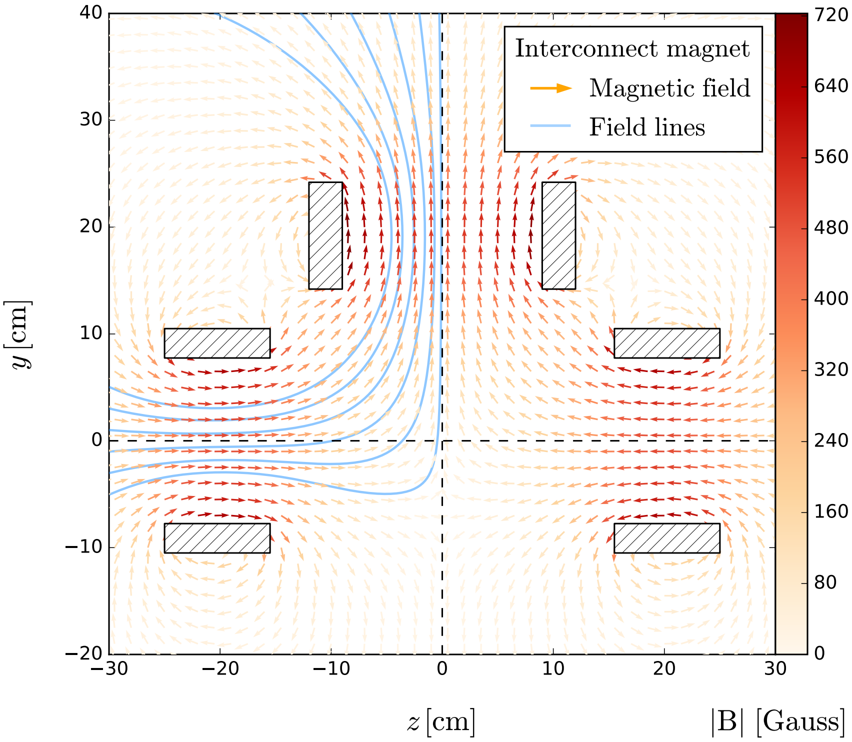

Figure 3.11: Quiver plot showing the magnetic field produced by three solenoids arranged along two orthogonal axes. The hatched areas show the cross sections of the magnet windings in the yz plane.

This results in a divergent magnetic field around the centre of the interconnect, where particles should begin to change direction in a controlled manner. However, this simple geometry has already started to produce some useful features. For example, some magnetic field lines that enter the interconnect through either side of Figure 3.11 eventually leave close to the vertical axis.

The geometry shown in Figure 3.11, can be improved by enhancing the B_z component of the magnetic field around the centre of the interconnect. Figure 3.12 shows the magnetic field produced by two identical solenoids arranged at right angles to one another, and rotated by 45 ° around the nominal beamline axes. In this configuration, the direction of current in both magnets can be chosen so that their magnetic fields cancel along one axis, but add together along the other. This geometry is clearly unphysical, given that the windings of the two magnets intersect in space.

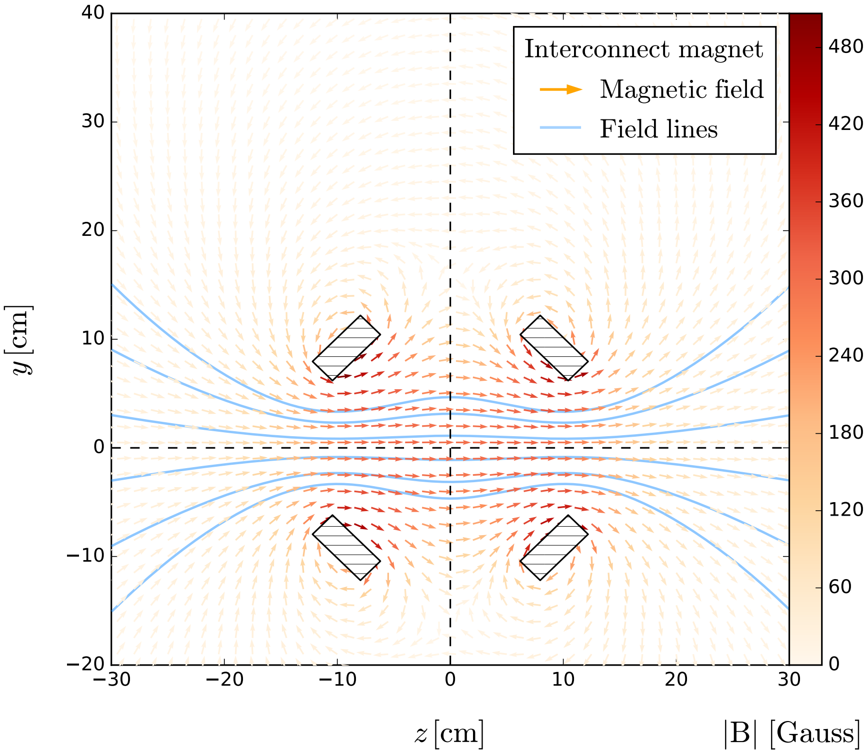

Figure 3.12: Quiver plot showing the magnetic field produced by two identical solenoids arranged at right angles to one another. The hatched areas show the cross sections of the magnet windings in the yz plane.

However, it produces a horizontal magnetic field without obstructing any of the beam paths that must be accessible to $\bar{\mathrm{p}}$ and e^+ bunches.

The final design for the interconnect magnet incorporates both of these configurations to produce a region of curved magnetic field lines beneath the ALPHA-g experiment. Figure 3.13 shows the final mechanical design for the interconnect. This design features three solenoids aligned to the horizontal and vertical axes of the beamline, and a pair of overlapping solenoids arranged to replicate Figure 3.12. Table 3.6 lists the original design parameters for each of these magnets.

The central volume of the interconnect is enclosed by a spherical vacuum chamber with an inner diameter of 225 mm. Three beam pipes with a diameter of ∼ 100 mm emerge from this chamber between the windings of the two overlapping solenoids.

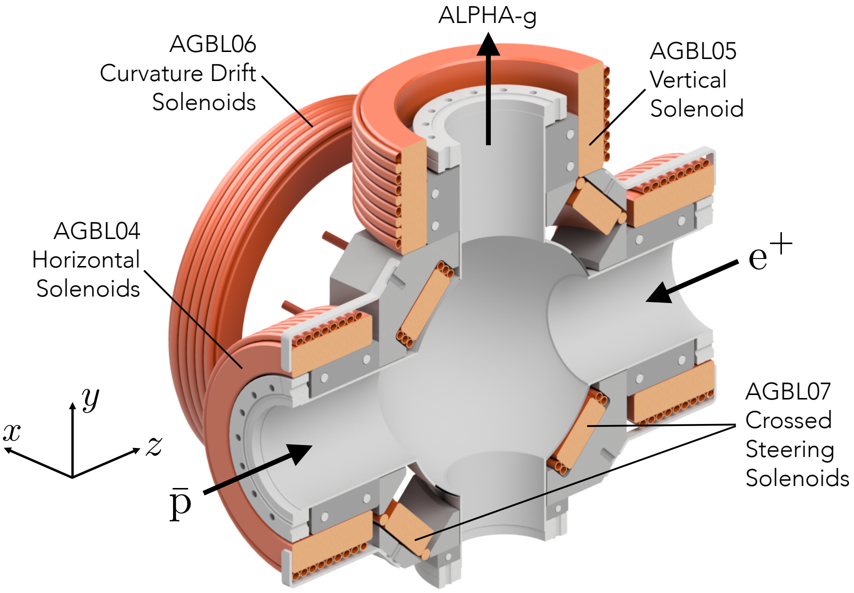

Figure 3.13: Schematic showing a cross section of the final interconnect magnet design. Support structures and UHV components are shaded in light grey, while magnet windings are highlighted in orange.

Identifier	**Description**	**Count**	**Diameter [mm]**		**Length [mm]**
			Inner	Outer	
AGBL04	Horizontal solenoid	2	155	210	95
AGBL05	Vertical solenoid	1	180	240	100
AGBL06	Drift correction coil	2	260	320	60
AGBL07-1	Inner crossed solenoid	1	235	285	60
AGBL07-2	Outer crossed solenoid	1	290	340	60

Table 3.6: Table detailing the overall dimensions of the interconnect magnets. These dimensions specify only the envelope of the magnet windings and do not include external infrastructure such as water cooling layers.

Each magnet is wound closely around the central vacuum chamber to maximise the magnetic field strength along the paths of $\bar{p}$ and e^+ bunches. The UHV flange at the base of the interconnect is used for additional vacuum pumping, and provides laser access to the central volume of the ALPHA-g experiment.

Figure 3.14 shows the magnetic field within the midplane of the interconnect during a $\bar{p}$ transfer to the ALPHA-g experiment.

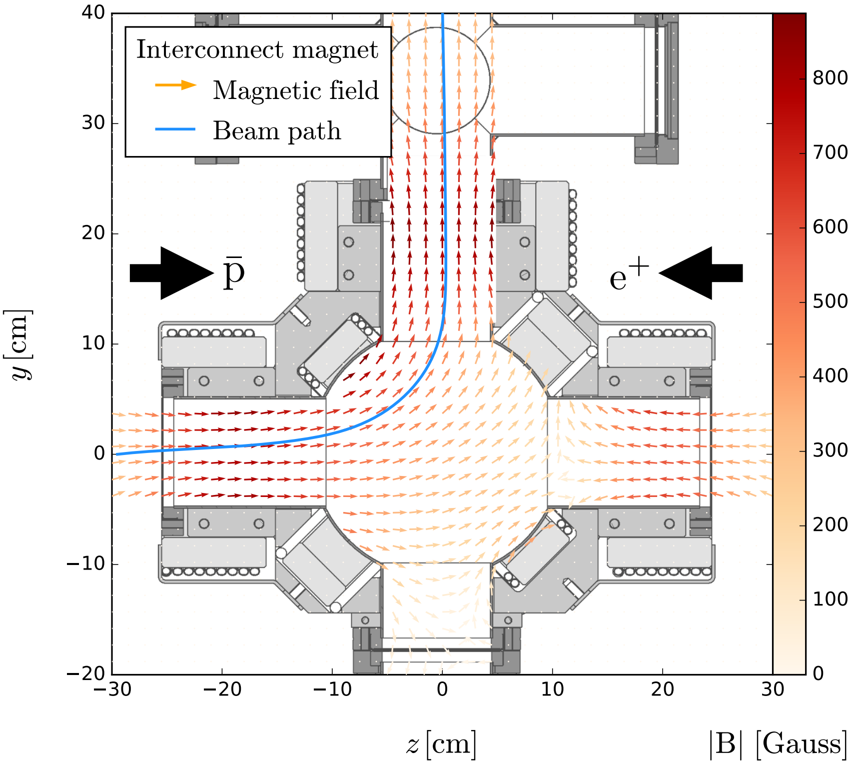

Figure 3.14: Quiver plot showing the magnetic field within the midplane of the interconnect during a p̄ transfer to the ALPHA-g experiment. The solid blue line shows the path of a massless charged particle beam that follows the direction of a magnetic field through the interconnect.

The magnetic field in this diagram includes stray field contibutions from the ALPHA-g external solenoid, and the two large transfer magnets (AGBL08) that are installed beneath it. The direction of the magnetic field in the interconnect can be reversed by switching the direction of current in the two overlapping solenoids. This allows the interconnect to be switched between the different configurations used to transport p̄ and e^+ bunches into the ALPHA-g experiment.

As shown in Figure 3.13, two additional magnets (AGBL06) are arranged on either side of the interconnect to produce a magnetic field along the $-x$ axis. These magnets are used to correct against the curvature drifts experienced by p̄ bunches within the interconnect. When energised, both magnets displace the magnetic field lines in the opposite direction to the antiproton drift velocity.

Assuming that $\bar{\mathrm{p}}$ bunches closely follow the magnetic field lines, the currents in these magnets can be tuned so that the displacement of the field lines will counteract the curvature drift of the beam.

Throughout the design of the interconnect magnet, numerical simulations were used to calculate the trajectories of $\bar{\mathrm{p}}$ and e^{+} bunches through this complex region of the apparatus. These simulations are discussed in detail in Chapter 4 of this thesis. Using these simulation tools, the design of the interconnect was gradually optimised to facilitate greater control over the dynamics of charged particle beams. The use of numerical simulations allowed many iterations of the interconnect design to be tested within a relatively short period of time. As a result, even small changes in the beamline design could be evaluated quickly. Throughout this process, the physical size of the interconnect magnet was gradually reduced, creating a stronger magnetic field within the central vacuum chamber and reducing the chance of particles being lost through ballistic collisions.

4 | Numerical Particle Tracing Simulations

The following chapter describes numerical particle tracing simulations that were used to model the dynamics of $\bar{\mathrm{p}}$ and e^+ bunches moving through the ALPHA-g beamlines. These simulations were used to evaluate and further develop the beamline design that was discussed in Chapter 3 of this thesis. Section 4.1 describes numerical tools that were developed to model the motions of charged particles through an arbitrary electromagnetic field. Section 4.2 outlines results that were obtained by applying these tools to investigate the transverse dynamics of $\bar{\mathrm{p}}$ and e^+ bunches. Finally, Section 4.3 describes simulations that show how antiprotons can be captured within the ALPHA-g experiment using a Penning trap.

4.1 Numerical Simulation Tools

In order to simulate the trajectories of charged particles through the ALPHA-g beamlines, a range of numerical simulation tools were developed. The following sections describe the structure of these tools, and the computational methods that were used to accurately model the ALPHA-g beamlines. Section 4.1.1 outlines the motivations for developing new simulation tools, while Section 4.1.2 describes the structure of each program that was written to simulate the ALPHA-g beamlines. Finally, Section 4.1.3 describes how the electromagnetic field of each beamline element was evaluated, and Section 4.1.4 outlines the computational methods that were employed during simulations of the beamline.

The majority of the simulations described in this chapter were used to study the dynamics of $\bar{\text{p}}$ bunches moving through the ALPHA-g beamlines. While light particles such as e^+ and e^- should robustly follow the magnetic field lines between particle traps, antiprotons are expected to have more complex motions due to non-adiabatic effects within several areas of the beamline.

4.1.1 Motivation

As shown in Chapter 3 of this thesis, a great deal can be learned about the dynamics of $\bar{\text{p}}$ and e^+ bunches by considering simple analytical models. However, some areas of the beamline will produce complex dynamics that cannot be understood using analytical models alone. As shown in Section 3.2, antiprotons are expected to move non-adiabatically through several areas of the ALPHA-g beamlines. For instance, $\bar{\text{p}}$ bunches moving through the interconnect will sample a magnetic field that varies over distances much shorter than a typical cyclotron orbit. As a result, numerical particle tracing simulations are required to solve the equation of motion for particles moving through these areas of the beamline.

In the regime where the guiding centre approximations are no longer valid, it is difficult to accurately model the bulk properties of an entire $\bar{\text{p}}$ or e^+ bunch. Simulations of the ALPHA-g beamlines must therefore calculate the trajectories of single particles, accounting for the external magnetic fields of the beamline as well as the space charge forces within each bunch. In order to accurately model the motions of single particles, their cyclotron motions must be resolved over timescales as short as 3.6×10^{-11} seconds. Similarly, simulations of the beamline must accurately represent a superposition of all the magnetic fields that exist throughout the ALPHA apparatus.

Many well-established particle tracing codes can provide all of the features required to simulate the ALPHA-g beamlines.

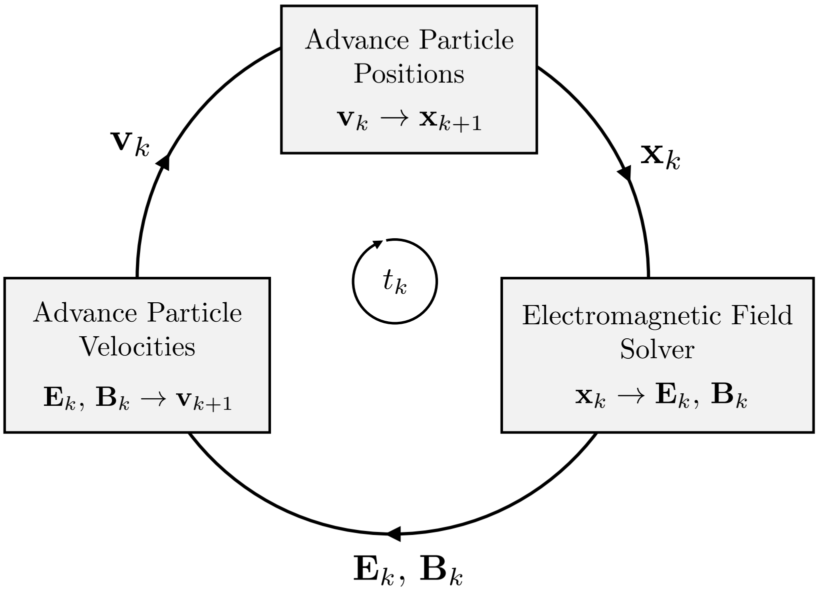

Figure 4.1: Diagram showing the structure of a basic particle pushing code. The electromagnetic field solver can incorporate separate solvers for space charge fields as well as those imposed by the beamline elements.

For example, commerical tools such as GPT [126] can accurately follow charged particles through an arbitrary electromagnetic field, accounting for space charge effects [127,128] as well as external fields imposed by the beamline elements. However, configuring these codes to provide the exact features that are required to model the full ALPHA-g beamline was expected to be time consuming in itself. Instead, a number of simple particle tracing codes were developed for the explicit purpose of modelling the ALPHA-g beamlines. The use of specialized simulation tools provides full control over the algorithms that are used to solve the Lorentz equation, as well as the methods used to calculate the electromagnetic fields.

4.1.2 General Considerations

Figure 4.1 shows the basic structure of a numerical particle tracing code. In general, this type of code will incorporate an algorithm for solving the Lorentz equation, and a separate solver that computes the electromagnetic fields experienced by each particle.

The electromagnetic field solver may include separate components for calculating the self fields of the charged particles, as well as the external fields imposed by the beamline elements. The leapfrog algorithm outlined in Section 2.4 of this thesis was used to solve the Lorentz equation for single p̄ and e^+ moving through an arbitrary magnetic field. This algorithm can be used to accurately follow the trajectories of charged particles over long timescales when used with an appropriately small time step [123]. As a result, the leapfrog algorithm is ideal for studying systems where charged particles with a fast periodic motion must be followed over long timescales.

Charged particle beams are typically influenced by space charge forces, which develop due to the long-range interaction of the particles within each bunch. These forces are difficult to model by their very nature. For example, in a diffuse p̄ bunch containing $\sim 10^4$ particles, direct calculation of the interactions between particles would require 10^8 evaluations of the Coulomb force at each time step. Clearly, this approach is too computationally intensive for simulations where the electromagnetic fields must be calculated at each time step.

In the context of the ALPHA-g beamlines, space charge forces can often be neglected when considering diffuse p̄ bunches. The effect of space charge interactions can be evaluated by considering the electric field within an infintely long plasma column with a uniform charge density ρ. By applying Gauss' law to this distribution, it can be shown that the radial component of the electric field within the plasma volume is $E_r = \rho r/2\varepsilon_0$. In this regime, the bulk $\mathbf{E} \times \mathbf{B}$ rotation frequency of the plasma (Equation 2.30) in a uniform magnetic field can be expressed as

$$\omega_r^{(-)} \simeq \frac{1}{2}\frac{nq}{\varepsilon_0 B_z} \tag{4.1}$$

where $n = \rho/q$ is the uniform number density of particles within the plasma column.

Based on Equation 4.1, the typical $\mathbf{E}\times\mathbf{B}$ rotation frequency of a $\bar{\mathrm{p}}$ plasma in the catching trap is $\omega_r^{(-)} \simeq 1.5\times10^5\ \mathrm{s}^{-1}$. By comparison, antiprotons extracted from the catching trap at an energy of 50 eV should take $\sim 117.5\ \mu$s to propgate along the ALPHA-g beamlines. The period of a single $\mathbf{E}\times\mathbf{B}$ rotation is therefore comparable to the time of flight of a typical $\bar{\mathrm{p}}$ bunch. Clearly, the transverse dynamics of $\bar{\mathrm{p}}$ bunches moving through the ALPHA-g beamlines are dominated by single-particle motions rather than collective space charge effects.

Simple analytical models can also be used to estimate the space charge potential ϕ_{self} within a trapped non-neutral plasma. By integrating the radial electric field between the electrode walls and a point $r \leq \sigma_\perp$, the self potential is found to be [94]

$$\phi\left(r\right) = \frac{qn\sigma_\perp^2}{4\varepsilon_0}\left[1 + 2\ln\left(\frac{r_w}{\sigma_\perp}\right)\right] - \frac{qnr^2}{4\varepsilon_0}\,, \tag{4.2}$$

where r_w is the radius of the trap electrodes. For $\bar{\mathrm{p}}$ plasmas held within the catching trap with the parameters listed in Table 2.1, the maximum self potential is of the order ~ 0.3 V. Since this potential is much smaller than the longitudinal beam energy ($q\phi_{\mathrm{self}} \ll E_\parallel$), space charge forces will also have a negligible effect on the longitudinal dynamics. However, dense e^+ plasmas extracted from the positron accumulator have dynamics that are often dominated by space charge effects.

Space charge forces were neglected in the simulations of $\bar{\mathrm{p}}$ bunches that are described in this chapter. In this regime, the simulation requirements are reduced significantly, and simulations can be used to quickly evaluate many iterations of the beamline design.

4.1.3 Electromagnetic Fields

As shown in Figure 4.1, the electromagnetic fields must be calculated at the location of every particle at each step of a particle tracing simulation.

The following section outlines methods that were used to evaluate the electromagnetic fields of the ALPHA-g beamlines. A variety of numerical and analytical methods were used to represent the fields produced by different beamline elements.

Magnetic Fields

The magnetic fields of the ALPHA-g beamline magnets were calculated numerically using the Biot-Savart solver of the OPERA3D software package [125]. Since each beamline magnet is cylindrically symmetric, its magnetic field can be represented using only the B_r and B_z field components within the $(r,\ z)$ plane. The field around each magnet was calculated individually, and exported on a regular grid of $(r,\ z)$ positions in its own reference frame. After calculating the field of each magnet individually, the magnetic field can be found at any position in space by summing the contributions from nearby magnets with an appropriate co-ordinate transformation.

Typically, the field of each magnet was exported at a fixed current density, on a regular grid with a resolution of $\delta r = \delta z = 2.5$ mm. The use of smaller grid spacings was found to have no effect on the simulation results. At this resolution, the magnetic field between grid vertices can be calculated using two-dimensional cubic interpolation. The gradient of the magnetic field was calculated by applying a four-point central finite difference operator [129] to the values in each field map.

As discussed in Chapter 3 of this thesis, the dynamics of $\bar{\mathrm{p}}$ or e^+ bunches are strongly influenced by stray magnetic fields in between sections of the beamline. It is therefore important to accurately represent these stray fields, in order to model the trajectories of charged particles between different areas of the apparatus. As a result, the field map for each beamline magnet was extended to include a large volume outside of the magnet windings themselves. The boundaries of each field map were truncated around the 0.01 Gauss contour of that magnet, so that the stray fields were fully accounted for in each particle tracing simulation.

As described in Section 2.4, the field produced by each beamline magnet is a linear function of the current density that is passed through its windings. Field maps that have been calculated for a fixed current density can therefore be scaled linearly to represent any other current density. Since each magnet is represented by a field map calculated for a fixed current density J_0, the total magnetic field at any position $\mathbf{x}$ can be written as

$$\mathbf{B}_{\text{tot}}\left(\mathbf{x}\right) = \sum_{k=1}^{N} \left(\frac{J_k}{J_0}\right) \mathbf{B}_k\left(J_0,\, \mathbf{x}_k\right) \,, \tag{4.3}$$

where J_k is the current density in the k^{th} magnet, with a magnetic field of $\mathbf{B}_k$ at position $\mathbf{x}_k$ in its own reference frame. Since the field map for each magnet is defined within its own reference frame, the positions x_k must be found by transforming between the global co-ordinate system of the beamline and that of each magnet. Since these transformations are applied at the beginning of each simulation, the positions and orientations of the magnets can be adjusted without needing to generate new field maps. As a result, changes in the beamline geometry or magnet currents can easily be simulated provided that the dimensions of the magnets remain fixed.

Electric Fields

In order to simulate how p̄ and e^+ bunches are captured from the beamlines, it is necessary to evaluate the electrostatic potentials that are produced within the ALPHA-g Penning trap. Throughout the ALPHA apparatus, electrostatic potentials are generated by applying voltages to hollow, cylindrical electrodes.

In numerical simulations of the ALPHA-g beamlines, the electrostatic potentials that are used to capture p̄ and e^+ bunches were calculated semi-analytically. Figure 4.2 shows the simple geometry that was considered to derive the potential around a single electrode. In this geometry, a voltage V has been applied to the surface of one electrode with an axial length L. This electrode is held between two grounded electrodes with an identical radius r_w.

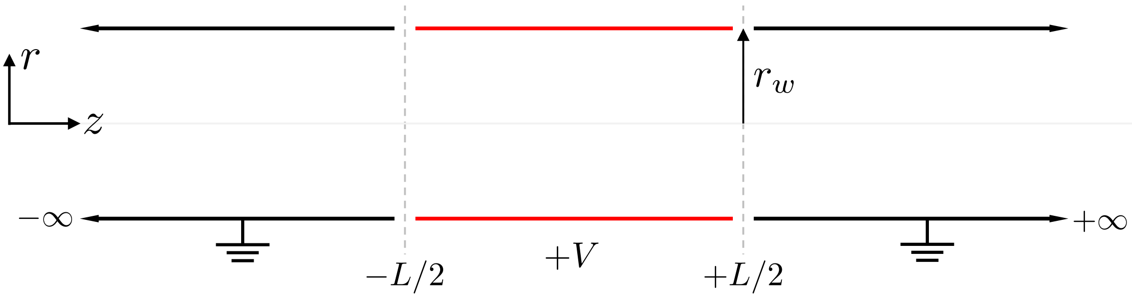

Figure 4.2: Line diagram showing the simplified geometry that was considered to derive the electrostatic potential inside a hollow, cyclindrical electrode.

In the absence of any enclosed charge, the electric potential in Figure 4.2 is given by the Laplace equation,

$$\nabla^2 \phi\left(r,\, z\right) = 0\,. \tag{4.4}$$

Any valid solution to this equation must satisfy the boundary conditions shown in Figure 4.2, such that

$$\phi\left(z,\, r = r_w\right) = \begin{cases} V & \text{if } |z| \leq L/2\,, \\ 0 & \text{otherwise}\,, \end{cases} \tag{4.5}$$

along the inner surface of the electrode, and $\phi\left(r,\, z\right) = 0$ in the limit where $z \to \pm\infty$. After accounting for these boundary conditions, the solutions to Equation 4.4 can be written in terms of an integral,

$$\phi\left(r,\, z\right) = \frac{2V}{\pi} \int_0^\infty \frac{\mathrm{d}\kappa}{\kappa} \frac{I_0\left(\kappa r\right)}{I_0\left(\kappa r_w\right)} \sin\left(\frac{\kappa L}{2}\right) \cos\left(\kappa z\right)\,, \tag{4.6}$$

where the $I_0\left(x\right)$ are modified Bessel functions of the first kind. The integration variable κ has the dimensions of a wavenumber, and should not appear in any exact solution to Equation 4.6.

In most numerical particle tracing simulations, the particle trajectories depend on the electric field rather than having an explicit dependence on the electric potential.

The electric field is defined by the equation

$$\mathbf{E}\left(r,\, z\right) = -\nabla\phi\left(r,\, z\right)\ . \tag{4.7}$$

By combining Equations 4.6 and 4.7, analytical expressions can be found for the two non-zero components of the electric field. For example, the axial component of the electric field in Figure 4.2 can be written as

$$E_z = \frac{2V}{\pi}\int_0^\infty \frac{I_0\left(\kappa r\right)}{I_0\left(\kappa r_w\right)}\sin\left(\frac{\kappa L}{2}\right)\sin\left(\kappa z\right)\mathrm{d}\kappa\,. \tag{4.8}$$

In Penning-Malmberg traps, many electrodes are stacked together to produce arbitrary electric potentials along the trap axis. In this geometry, the principle of superposition can be used to find the total electric field generated by the electrode stack at a given point in space. For a trap with N electrodes at a fixed radius r_w, the electric field any position with $r \leq r_w$ can be written as

$$\mathbf{E}_{\mathrm{tot}}\left(r,\, z\right) = \sum_{k=1}^{N}\mathbf{E}_k\left(r,\, z - z_k\right)\ , \tag{4.9}$$

where the summation variable k runs over all N electrodes at axial positions z_k. Since Equation 4.8 cannot be solved analytically, numerical methods were developed to evaluate the electric fields produced by the ALPHA-g Penning trap.

The integrand of Equation 4.8 oscillates as a function of κ, with an amplitude that is given by the ratio of two Bessel functions. The amplitude of the two Bessel functions decays exponentially for large values of the integration variable k. The step size of any numerical integrator must be much smaller than the period of the fastest oscillation term in Equation 4.8, such that $\delta k \ll 2\pi\cdot\min\left[\left(2/L\right),\, \left(1/z\right)\right]$. At each step of the integration, the integrand of Equation 4.8 was evaluated numerically and summed.

The integral was truncated once each component of the electric field had converged to at least one part in 10^4.

4.1.4 Computational Methods

The dynamics of $\bar{\mathrm{p}}$ and e^+ bunches moving through the ALPHA-g beamlines were simulated using a Monte Carlo approach. In this type of simulation, a physical problem is solved for a large number of different initial conditions, which represent a much larger number of states within the original system under study.

The initial position and velocity of each particle in simulated $\bar{\mathrm{p}}$ or e^+ bunch was drawn in a pseudorandom manner from a set of pre-defined distributions. In a pseudorandom process, the initial states of the particles are generated deterministically, but will pass statistical tests for randomness [130]. Initial distributions were chosen based on the particular dynamics that were to be investigated in each simulation. For example, Section 4.2.1 describes how particles were initialised to simulate the transverse dynamics of $\bar{\mathrm{p}}$ and e^+ bunches moving through the ALPHA-g beamlines. Similarly, Section 4.3.1 outlines the initial distributions that were used to simulate how $\bar{\mathrm{p}}$ bunches can be captured inside the ALPHA-g atom trap. Once the initial position and velocity of each particle had been defined, its trajectory was calculated by solving the equations of motion (Equation 2.37).

In the absence of space charge forces, the trajectory of each particle within a $\bar{\mathrm{p}}$ or e^+ bunch is independent of the positions and velocities of the other particles. As a result, the equation of motion for each particle can be solved independently, accounting only for the electromagnetic fields of the beamline elements. In this regime, many particle tracks can be calculated in parallel on separate processors. The parallelization of particle tracing simulations allows large numbers of tracks to be calculated within a relatively short period of time, making efficient use of the available computing resources.

Numerical simulations of the ALPHA-g beamlines were implemented in the PYTHON programming language, and run through CERN batch computing system [131]. The PYTHON programming language incorporates accessible tools that can be used to parallelise simple calculations. Similarly, the CERN batch computing system allows computationally intensive tasks to be divided between a large number of processors on separate computers. Each computer independently deals with a small fraction of the overall problem, so that the resources of each machine can be shared to efficiently handle a single computing task. Typically, each beamline simulation would involve up to 10^4 independent particles, distributed across ten or more CPU cores.

4.2 Transverse Beam Dynamics

As described in Chapter 3 of this thesis, the ALPHA-g beamlines are primarily designed to control the transverse size and position of $\bar{\mathrm{p}}$ and e^+ bunches. Many of the beamline elements have complex magnetic fields, which may have a non-linear effect on the paths of charged particles. Numerical simulations were therefore designed to model the transverse dynamics of charged particles moving through a three-dimensional representation of the ALPHA-g beamlines.

4.2.1 Initialisation

The initial states of positrons and antiprotons were chosen to represent the equilibrium distribution of charged particles held inside a Penning-Malmberg trap. Since simulations of the ALPHA-g beamlines were primarily intended to model the transverse dynamics of $\bar{\mathrm{p}}$ and e^+ bunches, the longitudinal structure of each bunch was initially neglected. As a result, particles were drawn from a point-like longitudinal phase space, starting from a fixed position along the beamline with a uniform kinetic energy of 50 eV.

As discussed in Chapter 2, trapped charged particles will oscillate in the transverse plane about a point known as their guiding centre.

At the beginning of each simulation, the guiding centre of each particle was displaced from the beamline axis to a new location within the transverse envelope $\sigma_\perp$ of the $\bar{\mathrm{p}}$ or e^+ beam. The radius of the guiding centre was drawn from a flattened Gaussian distribution, defined by the equation

$$f\,(r)\,\mathrm{d}r \;\sim\; \exp\left[-\left(\frac{r}{b_\perp}\right)^n\right]\,\mathrm{d}r\,, \tag{4.10}$$

where $b_\perp$ is the typical transverse size of the plasma and n is a dimensionless exponent. For $n = 2$, particles are normally distributed about the beamline axis with an r.m.s beam radius of $\sigma_\perp = \sqrt{2}\,b_\perp$. For larger values of n, the distribution is increasingly flattened around its centre, with a sharp edge at $r \simeq b_\perp$. Figure 4.3(a) shows examples of this distribution for $n = 2$ and $n = 10$.

Historically, Equation 4.10 has been found to fit well to MCP images of $\bar{\mathrm{p}}$ and e^+ plasmas taken throughout the ALPHA apparatus. This distribution therefore represents the charge density function integrated along the length of a trapped non-neutral plasma. The guiding centres of $\bar{\mathrm{p}}$ and e^+ were distributed around the trap axis by selecting an azimuthal coordinate for each particle, drawn from a uniform distribution with $0 \leq \theta_r \leq 2\pi$.

Each particle was assigned an initial speed from a Maxwellian distribution defined by the equation

$$f\,(v)\,\mathrm{d}v \;\sim\; v^2 \exp\left[-\frac{mv^2}{2k_BT}\right]\,\mathrm{d}v\,, \tag{4.11}$$

where T is the temperature of the original plasma. A typical Maxwellian distribution is shown in Figure 4.3(b). This distribution was chosen to reflect the spread of particle speeds in a trapped non-neutral plasma at thermal equilibrium (Equation 2.31). In reality, the velocity of each particle is given by the sum of its own thermal motion and the $\mathbf{E} \times \mathbf{B}$ rotation of the entire plasma.

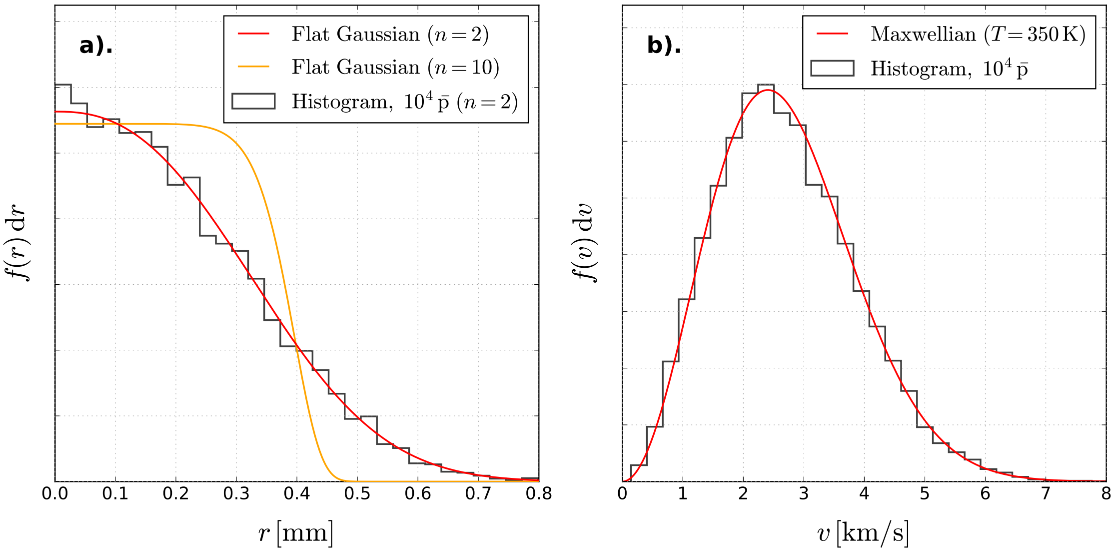

Figure 4.3: Distributions used to initialize p̄ bunches in numerical simulations of the ALPHA-g beamlines. Panel a). shows the radial distribution of guiding centres (Equation 4.10) and panel b). shows a Maxwellian distribution of particle speeds (Equation 4.11). For each distribution, a histogram is shown to indicate the properties of 10^4 simulated antiprotons.

In simulations of the ALPHA-g beamlines, the bulk rotations of p̄ and e^+ plasmas were neglected when assigning velocities to individual particles. Using the analytical models discussed in Section 4.1.2, we estimate that this changes the initial velocities of positron and antiprotons by less than ~ 2.5 %.

The transverse component of the velocity $v_\perp$ was selected by choosing a polar coordinate at random within the range $0 \leq \varphi \leq \pi$, so that $v_\perp = v\cos(\varphi)$. Once again, the direction of the transverse velocity was chosen at random by selecting a phase angle from a uniform distribution between $0 \leq \theta_v \leq 2\pi$. The transverse velocity of each particle can therefore be decomposed such that

$$v_x = v_\perp \cos(\theta_v)\ , \qquad v_y = v_\perp \sin(\theta_v)\ . \tag{4.12}$$

Finally, each particle was displaced from its guiding centre by the Larmor radius (Equation 2.4) corresponding to its transverse velocity.

The direction of this displacement is correlated to direction of the transverse velocity, so that each particle will oscillate about its own guiding centre. As a result, the initial position of each particle is given in full by the expression

$$x = r\cos(\theta_r) + \frac{mv_\perp}{qB_z}\sin(\theta_v) \ , \tag{4.13}$$

$$y = r\sin(\theta_r) - \frac{mv_\perp}{qB_z}\cos(\theta_v) \ . \tag{4.14}$$

As described in Section 4.1.2, the timescale of the fastest dynamics in a $\bar{\mathrm{p}}$ or e^+ bunch is set by the cyclotron frequency ω_c. These dynamics must be fully resolved in order to accurately model the motions of single charged particles over long timescales. As a result, the equation of motion for each particle was integrated with a time step at least 20 times shorter than the period of a single cyclotron oscillation. For example, antiprotons held within the 3.0 T magnetic field of the catching trap have a cyclotron period of ~ 21.8 ns. When simulating the dynamics of $\bar{\mathrm{p}}$ bunches, a fixed time step of 10^{-9} s was used to fully resolve the cyclotron motion of each particle. For longer time steps, charged particles simulated in a uniform magnetic field would begin to move away from their guiding centres after many cyclotron periods.

4.2.2 Beam Steering

In order to simulate the trajectories of charged particles through the ALPHA-g beamlines, suitable currents were first identified for the interconnect magnets. As shown in Section 3.3, light particles such as positrons will robustly follow the direction of the magnetic field while moving through the interconnect. However, the paths of antiprotons through the interconnect can only be modelled numerically.

Initially, suitable currents for the interconnect magnets were estimated by assuming that both $\bar{\mathrm{p}}$ and e^+ would follow the magnetic field lines, as shown in Figure 3.14.

Magnet Identifier	**Current Density [A/cm^2]**	
	Antiproton Setpoint	Positron Setpoint
AGBL04	400	280
AGBL05	420	260
AGBL06	260	0
AGBL07-1	495	265
AGBL07-2	495	265
AGBL08	250	250

Table 4.1: Currents used to steer p̄ and e$^+$ bunches through the interconnect magnet in simulations of the ALPHA-g charged particle beamlines.

Corrections to these currents were calculated iteratively, by repeatedly simulating the trajectories of p̄ bunches launched from the catching trap. In each simulation, the p̄ beam position was measured directly above the interconnect for a fixed set of magnet currents. Between simulations, the current in each magnet was adjusted in small increments until the p̄ beam was aligned to within ~ 0.1 mm of the ALPHA-g trap axis above the interconnect.

Table 4.1 lists the current densities that were found to steer simulated p̄ and e$^+$ bunches into the ALPHA-g atom trap. In general, the interconnect magnets were simulated with higher currents during p̄ transfers, so that particles were more likely to move adiabatically. The currents used to steer positrons through the interconnect are very close to those that were predicted based on the magnetic field lines alone.

After steering both p̄ and e$^+$ through the interconnect, the current in each magnet was varied to characterise its effect on the beam position. Figure 4.4 shows how the antiproton beam position varies as a function of the current in a number of interconnect magnets. The transverse beam position has been decomposed into two components along orthogonal axes labelled as x and z. The direction of each axis is indicated by an arrow in Figure 3.13.

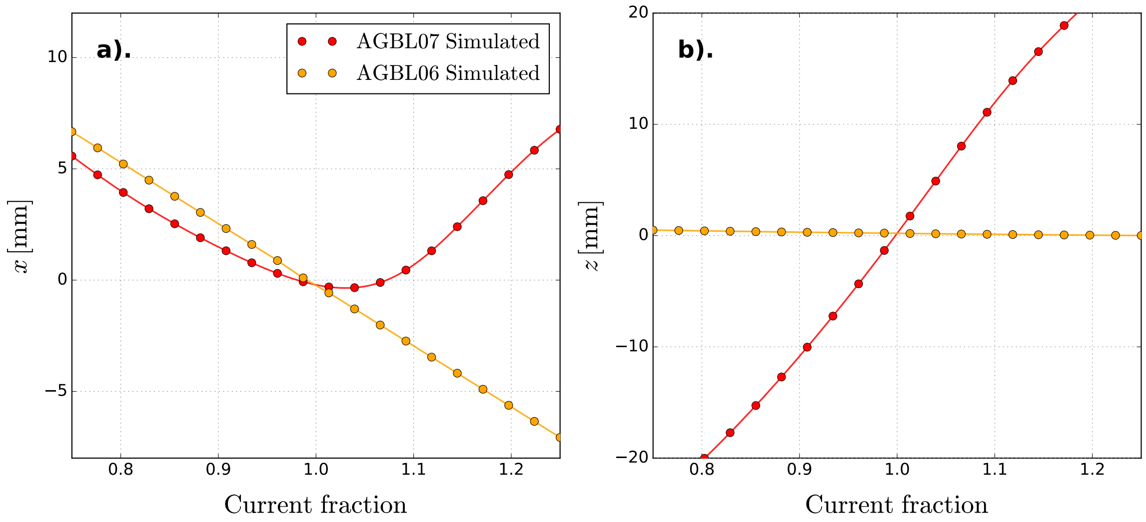

Figure 4.4: Simulated current scans showing the antiproton beam position at the lower diagnostics station (LDS) as a function of the current in some of the interconnect magnets. The two panels show the components of the beam position along orthogonal axes, which are marked as arrows in Figure 3.13.

As shown in Figure 4.4, a number of the interconnect magnets translate the beam position linearly along only one axis. For example, changing the current in the two curvature drift correction coils (AGBL06) will move the beam primarily along the x axis. Similarly, the currents in the two crossed solenoids (AGBL07) can be adjusted together to move the beam along the horizontal z axis of the beamline.

The crossed solenoids have a non-linear effect on the $\bar{\text{p}}$ beam position along the x axis. Based on analytical models alone, these magnets were not expected to translate the beam position along this direction. This effect may be due to the dependence of the $\bar{\text{p}}$ curvature drift (Equation 3.5) on the strength of the magnetic field within the interconnect. Equation 3.5 assumes that the magnetic field of the interconnect has a uniform strength, but changes direction along the path of a $\bar{\text{p}}$ or e^+ bunch. However, the true magnetic field of the interconnect is highly inhomogenous even over short distances. This may result in curvature drifts that have a more complex dependence on the strength of the magnetic field within the interconnect.

By representing the beam position as a function of the current density in each magnet, we can write that

$$\delta x_j = \sum_{k=1}^{N} \delta J_k \left(\frac{\partial x_j}{\partial J_k} \right) \bigg|_{\mathbf{x}=\mathbf{x}_0} , \tag{4.15}$$

where x_j is the j^{th} component of the transverse beam position, and J_k is the current in the k^{th} interconnect magnet. The coefficients of this expansion must be calculated around a given beam position $\mathbf{x}_0$ using simulated steering scans such as those shown in Figure 4.4. These coefficients can be interpreted as the elements of a transfer matrix, which encodes how the beam position responds to changes in the currents of the interconnect magnets.

By inverting Equation 4.15, it is possible to find combinations of magnets that translate the beam along only one axis. Around the two setpoints listed in Table 4.1, the AGBL06 and AGBL07 interconnect magnets translate the beam along axes that are almost paralle to the x and z axes in Figure 3.13. However, at large displacements from this setpoint, the AGBL07 magnets begin to have a non-linear effect on the beam position along the x axis. Small changes to the beam position can therefore be made using only two sets of interconnect magnets.

4.2.3 Beam Envelopes

As well as characterising the steering of $\bar{\text{p}}$ and e^+ bunches, numerical simulations can be used to calculate their beam envelopes throughout the ALPHA-g beamlines. Before evaluating the transverse size of a charged particle beam, a suitable coordinate system must be established to define the radial position of each particle. Within the interconnect, the velocities of $\bar{\text{p}}$ or e^+ bunches will change direction with a short radius of curvature. As a result, the transverse and longitudinal position of each particle must be defined in a way that can be applied at any point along the ALPHA-g beamlines.

In simulations of the ALPHA-g beamlines, the longitudinal direction of the beam was defined by the orientation of the local magnetic field. For consistency, the direction of the magnetic field was evaluated at the geometric centre of each $\bar{\mathrm{p}}$ or e^+ bunch. The transverse position of each particle is therefore defined as its displacement within a plane normal to the local magnetic field. The longitudinal distance s travelled by a beam particle at the k^{th} time step is defined as

$$s_k = \left| \sum_{i=1}^{k} \frac{\mathbf{v}_i \cdot \mathbf{B}_i}{B_i} \delta t \right| , \tag{4.16}$$

where $\mathbf{B}_i$ is the magnetic field at the i^{th} time step. Using these definitions, the transverse size of a $\bar{\mathrm{p}}$ or e^+ bunch can be calculated at any point along the beamline.

Figure 4.5(a) shows how the transverse size of a 50 eV $\bar{\mathrm{p}}$ beam varies as it moves between the ALPHA-II atom trap and ALPHA-g experiment. Similarly, Figure 4.5(b) shows the magnetic field strength at the centre of the $\bar{\mathrm{p}}$ bunch as a function of its longitudinal position. By solving the beam envelope equation (Equation 2.33) for this magnetic field, the results of the numerical simulation can be compared against the analytical models that were used in Section 3.2.2 of this thesis. In Figure 4.5(a), a numerical solution to the beam envelope equation is shown alongside the result obtained from particle tracing simulations.

Clearly, the beam envelope that is obtained from particle tracing simulations is closely approximated by the analytical model that was used in Section 3.2.2 of this thesis. As shown in Figure 4.5, the two solutions only begin to diverge as the $\bar{\mathrm{p}}$ bunch enters the interconnect (beamline section D). The magnetic field within this area of the beamline is not cylindrically symmetric, and so Equation 2.33 is no longer valid. However, after passing through the interconnect, the final transverse size of the $\bar{\mathrm{p}}$ beam is essentially consistent between both models.

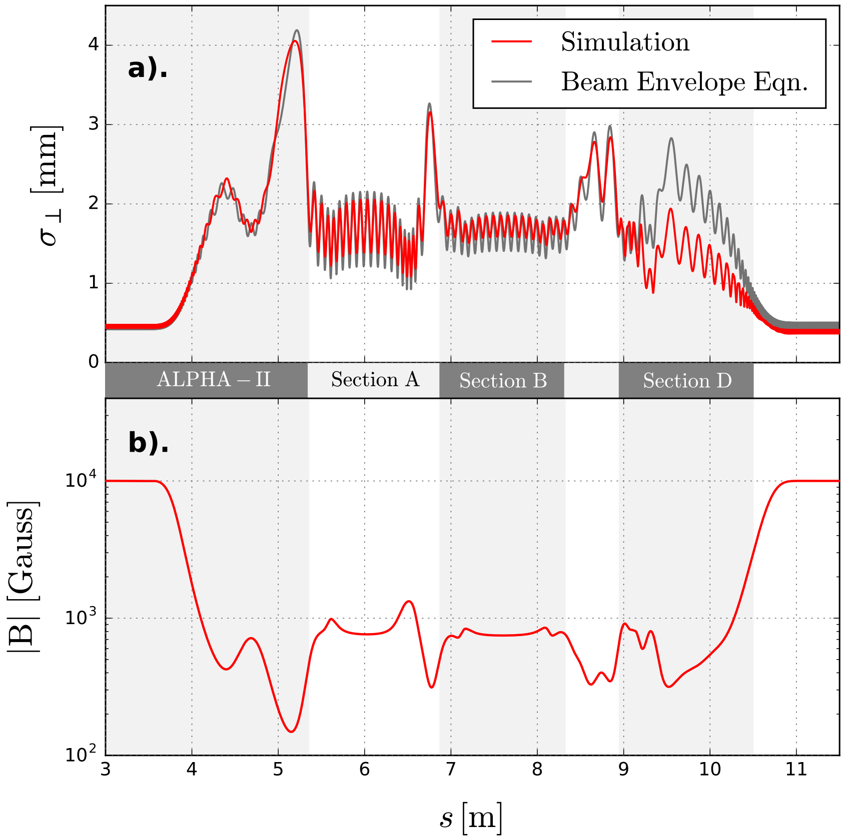

Figure 4.5: Transverse $\bar{\text{p}}$ beam envelope $\sigma_\perp$ as a function of longitudinal distance travelled along the beamline. Panel a). compares the simulated beam envelope to a numerical solution to the beam envelope equation (Equation 2.33). Panel b). shows the size of the magnetic field experienced by $\bar{\text{p}}$ moving along the beamline.

Within the 1.0 T magnetic field of the ALPHA-g atom trap, the beam has a typical transverse size of $\sigma_\perp = 0.45$ mm. This is easily small enough to avoid mechanical apertures within the Penning trap when the beam has accurately been steered through the interconnect.

Figure 4.6 shows the simulated transverse beam profile of a 50 eV $\bar{\text{p}}$ bunch passing through the locations of the beamline diagnostics station (BDS) and lower diagnostics station (LDS). These locations were chosen to provide a direct comparison with experimental data, such as MCP images obtained during the commissioning of the beamlines. Each beam profile was constructed by plotting the distribution of $\sim 10^4$ antiprotons that were initially launched from the catching trap.

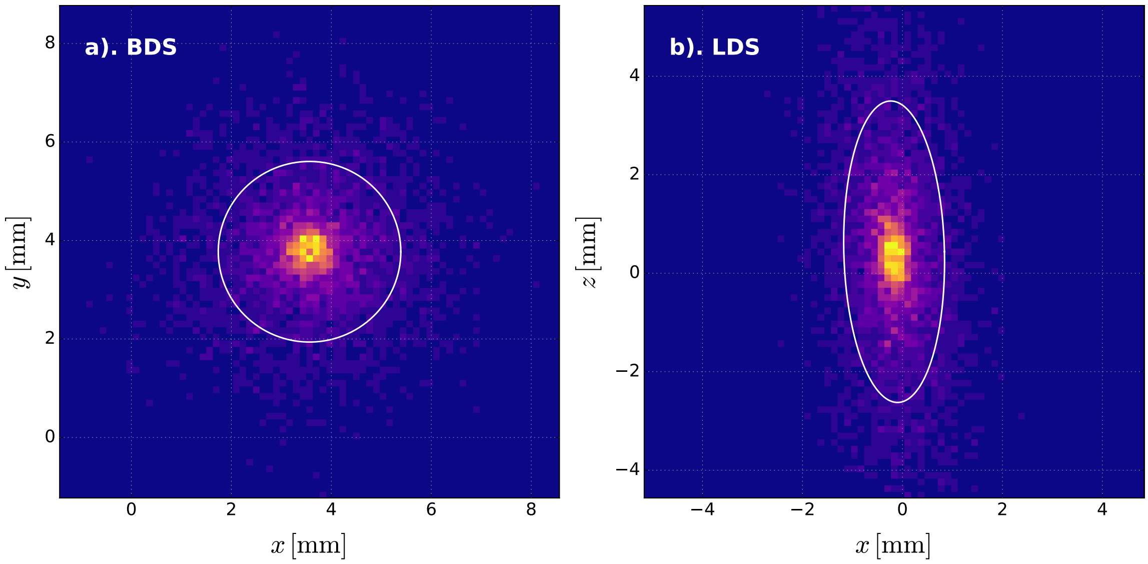

Figure 4.6: Simulated $\bar{\mathrm{p}}$ beam profiles reconstructed at a). the beamline diagnostics station (BDS) and b). the lower diagnostics station (LDS) from a simulation of 10^4 antiprotons. The r.m.s size of the beam is shown as a solid white line.

As expected, the beam profile at the BDS is rotationally symmetric around its centre, with a typical transverse size of $\sigma_\perp = 1.83$ mm. However, the beam appears to become elongated along the z axis after propagating through the interconnect. When imaged at the LDS, the $\bar{\mathrm{p}}$ bunch has a radius of $\sigma_x = 1.01$ mm along the x axis, and a size of $\sigma_z = 3.06$ mm along the z axis of the beamline. This elongation appears to be caused by the magnetic field of the interconnect mixing the transverse and longitudinal degrees of freedom of the beam. A similar change was observed in the beam profiles of e^+ bunches.

4.2.4 Non-adiabatic Effects

As shown in Figure 3.7, the ALPHA-g beamlines include several regions where $\gamma \gtrsim 1$ for $\bar{\mathrm{p}}$ bunches. During non-adiabatic motion, the transverse and longtudinal degrees of freedom are allowed to mix, violating the conservation of the magnetic moment μ. In general, the charged particles in a magnetized beam will initially have very little transverse energy in comparison to their energetic longitundinal motions.

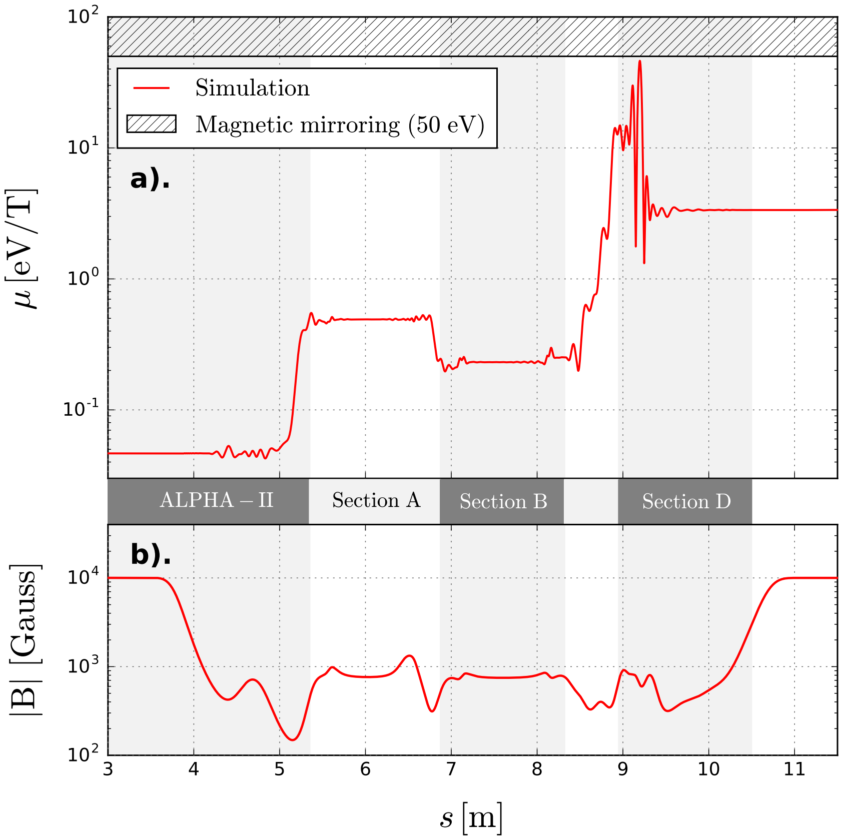

Figure 4.7: Average magnetic moment μ of particles in a 50 eV $\bar{p}$ beam moving through the ALPHA-g beamlines. The shaded region in panel a). indicates regions where the beam will undergo magnetic mirroring in a field of 1.0 T. Panel b). shows the magnetic field experienced by $\bar{p}$ as a function of distance along the beamline.

As a result, non-adiabatic motion will tend to result in large amounts of energy being transferred into the cyclotron motions of single particles, causing the magnetic moment to increase dramatically.

Figure 4.7 shows how the magnetic moment of a 50 eV $\bar{p}$ beam varies as it moves between the ALPHA-II atom trap and ALPHA-g experiment. Initially, the simulated $\bar{p}$ bunch was launched from the 3.0 T magnetic field of the catching trap with the initial conditions listed in Table 2.1. While the magnetic moment is generally conserved in regions where the magnetic field is strong and slowly varying, it increases dramatically between some sections of the beamline. In particular, there is a large increase in the vicinity of the interconnect, where the beam encounters a magnetic field that varies over distances comparable to a single Larmor radius.

Upon arriving within the 1.0 T magnetic field of the ALPHA-g atom trap, each antiproton stores around $\sim 6\%$ (3 eV) of its total energy within its cyclotron motion.

In early simulations of the ALPHA-g beamlines, $\bar{\mathrm{p}}$ bunches were found to undergo magnetic mirroring upon encountering the 1.0 T magnetic field of the atom trap. During magnetic mirroring, antiprotons transfer all of their kinetic energy into their cyclotron motion, and are therefore deflected backwards along the beamline. As a consequence, magnetic mirroring presents an unusual beam loss mechanism, which can result in particles being lost without ever encountering a physical barrier. The shaded region in Figure 4.7 indicates values of the magnetic moment μ that would result in magnetic mirroring for particles with a total energy of 50 eV.

Throughout the development of the beamline design, improvements were made to minimise the impact of non-adiabatic effects on the dynamics of $\bar{\mathrm{p}}$ bunches. For example, the overall size of the interconnect was reduced significantly to boost the magnetic field at its centre. Increasing the magnetic field in this way supresses the adiabaticity parameter γ and therefore limits the severity of non-adiabatic effects within the interconnect. In each simulation, magnetic mirroring was identified by tracking the longitudinal position of each particle after every time step. Any particle that began to move backwards along the beamline ($s_{k+1} \leq s_k$) was considered to have been lost, and was removed from the simulation. In the final beamline design, no particles were lost due to magnetic mirroring, despite passing through several regions where $\gamma \geq 1$.

4.2.5 Plasma Extraction

As discussed in Section 3.2.5, is it important that charged plasmas can be extracted from the ALPHA-g atom trap in a way that preserves information about their original state.

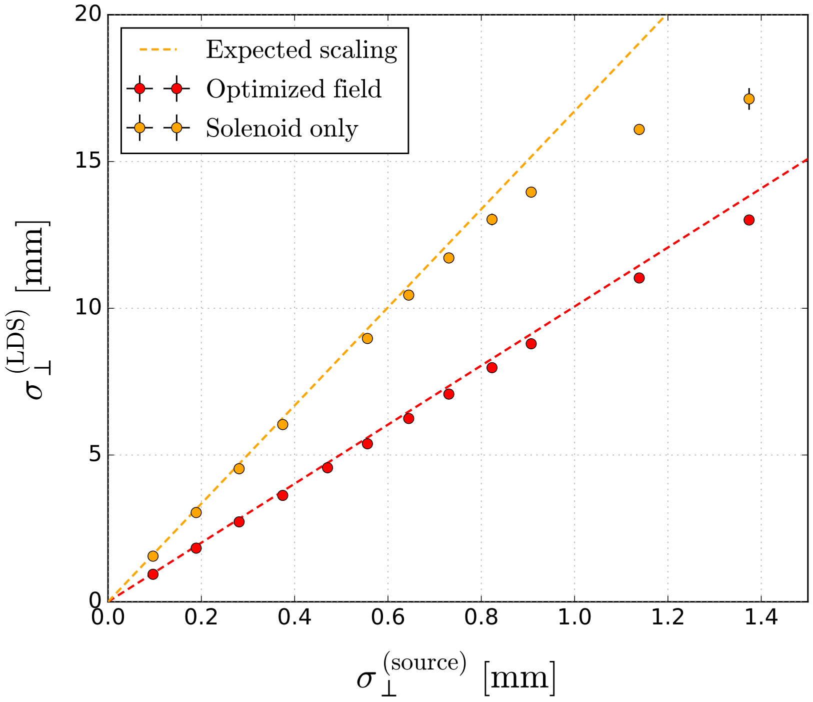

Figure 4.8: Transverse size $\sigma_\perp$ of simulated $\bar{\mathrm{p}}$ clouds extracted to the LDS as a function of their original size within the ALPHA-g atom trap. Data points in red show the size of antiproton plasmas extracted through the optimised magnetic field shown in Figure 3.10. Data points in orange correpond to simulations using ony the stray magnetic field of the ALPHA-g external solenoid.

Ideally, the measured size of a $\bar{\mathrm{p}}$ or e^+ plasma will scale linearly as a function of its initial size within the atom trap, as dictated by Equation 2.32. Numerical particle tracing simulations were used to model the extraction of antiproton clouds from the ALPHA-g atom trap through a range of different magnetic fields.

Figure 4.8 shows the transverse size of antiproton plasmas extracted to the LDS as a function of their original size inside the ALPHA-g atom trap. Antiprotons were extracted from the 1.0 T magnetic field of the atom trap at an energy of 24 eV. Two sets of simulation data are shown for comparison. In one set of simulations, antiprotons were extracted to the LDS using only the stray magnetic field of the ALPHA-g external solenoid. In the other set of simulations, the large transfer coils (AGBL08) were energised to produce the magnetic field shown in Figure 3.10.

This magnetic field has been numerically optimised to minimise the adiabaticity parameter γ, as described in Section 3.2.5. The expected scaling behaviour from Equation 2.32 is shown as a dashed line for each data set.

Clearly, $\bar{\mathrm{p}}$ clouds extracted through the optimised magnetic field shown in Figure 3.10 will expand linearly as a function of their original size. For antiproton plasmas with an initial size of up to 3.0 mm, there is a maximum deviation of $\sim$ 6.2 % from the scaling behaviour suggested by Equation 2.32. However, $\bar{\mathrm{p}}$ clouds that are extracted using only the stray field of the ALPHA-g external solenoid can deviate significantly from Equation 2.32. In this regime, the final transverse size of antiproton plasmas extracted to the LDS can be much larger than any of the diagnostic devices used to measure their properties.

4.3 Longitudinal Dynamics

As well as modelling the transverse dynamics of $\bar{\mathrm{p}}$ and e^+ bunches, numerical simulations were used to study how antiprotons are captured inside the ALPHA-g Penning trap. Section 4.3.1 outlines the structure of these calculations, and describes how antiprotons were initialised at the start of each simulation. Section 4.3.2 details a number of simulation results, and discusses how the number of $\bar{\mathrm{p}}$ captured in the atom trap can be maximised.

4.3.1 Initialisation

As described in Section 3.1.3 of this thesis, $\bar{\mathrm{p}}$ and e^+ bunches are captured by constructing an electrostatic potential well along the axis of the ALPHA-g experiment. Figure 3.2 shows the potentials used to capture antiprotons in the uniform 1.0 T magnetic field of the atom trap. The particle capture process is clearly dominated by the longitudinal dynamics of incoming $\bar{\mathrm{p}}$ and e^+ bunches.

In a uniform magnetic field, the axial component of Equation 2.37 reduces to

$$v_{z,\,k+1} = v_{z,\,k} + \frac{q\delta t}{m} E_{z,\,k}\,, \tag{4.17}$$

where $v_{z,\,k}$ is the longitudinal velocity measured at the k^{th} time step of the simulation. The discarded transverse components of Equation 2.37 simply describe cyclotron motion at a fixed radius about the guiding centres. As a result, the capture of antiprotons from the ALPHA-g beamlines can be treated as a one-dimensional problem to first order.

The capture of p̄ bunches from the ALPHA-g beamlines was modelled by tracing the axial positions of antiprotons as they move towards the potential shown in Figure 3.2. In these simulations, particles were launched from within the uniform magnetic field of the ALPHA-g atom trap, with a realistic longitudinal phase space. In each p̄ bunch, particles were initialised along the trap axis with a distribution

$$f\left(z\right)\,\mathrm{d}z = \frac{1}{\sqrt{2\pi\sigma_z^2}}\,\exp\left[-\frac{\left(z - z_0\right)^2}{2\sigma_z^2}\right]\,\mathrm{d}z\,, \tag{4.18}$$

where $\sigma_z = v_{\parallel}\sigma_\tau/4$ is the physical envelope enclosing 68% of particles and z_0 is the mean position of the beam. The initial position of the beam was chosen such that $|q\phi\left(z\right)| \ll E_{\text{beam}}$ for all particles in the distribution.

Similarly, the longitudinal velocity of each particle was drawn from a normal distribution. The velocity was assumed to be correlated to the position of each particle within the p̄ bunch, such that

$$v_z = \left[\frac{2E_{\text{beam}}}{m} + \frac{2\sigma_E}{\sigma_z m}\left(z - z_0\right)\right]^{1/2}\,, \tag{4.19}$$

where E_{beam} is the mean energy, and σ_E is the typical spread of particle energies.

This distribution assumes that each bunch has propagated far enough for the antiprotons to separate according to their longitudinal velocities. Consider a 50 eV $\bar{p}$ bunch extracted with an initial length of ~ 4.5 mm and an energy spread of approximately 2 eV. Under these initial conditions, it takes $\lesssim 1.8$ μs for the most energetic antiprotons at the tail of each bunch to overtake the reference particle. Since this timescale is much shorter than the 117.5 μs taken for $\bar{p}$ bunches to propagate into the ALPHA-g atom trap, Equation 4.19 is a good approximation.

In each simulation, the electric potential well in Figure 3.2 was closed after a predetermined number of timesteps. Changes in the on-axis potential were assumed to have a rise time of 10^{-7} seconds, consistent with the properties of the real ALPHA-g Penning trap electronics. Since there is no natural timescale for the longitudinal motion of a single antiproton, the time step in Equation 4.17 was chosen to be much smaller than the time constant of the electrodes. Typically, a time step of 10^{-9} s was used to integrate the equation of motion for each antiproton.

4.3.2 Antiproton Capture

As discussed in Section 3.1.3 of this thesis, the $\bar{p}$ gate time is defined as the delay between antiprotons being extracted from the catching trap, and subsequently being captured in the ALPHA-g Penning trap. Experimentally, the $\bar{p}$ gate time must be set to within $\lesssim 1$ μs in order to capture a large fraction of the incoming antiprotons. Numerical simulations were used to model the capture of $\bar{p}$ bunches for a range of gate times and bunch lengths.

At the beginning of each simulation, antiprotons were displaced by ~ 500 mm from the centre of the potential shown in Figure 3.2. Each $\bar{p}$ bunch was initialised with a 95% bunch length of 0.5 $\mu\text{s} < \sigma_\tau < 7$ μs. The incoming beam was assumed to have a mean energy of 50 eV, and a Gaussian energy spread of $\sigma_E = 1.5$ eV.

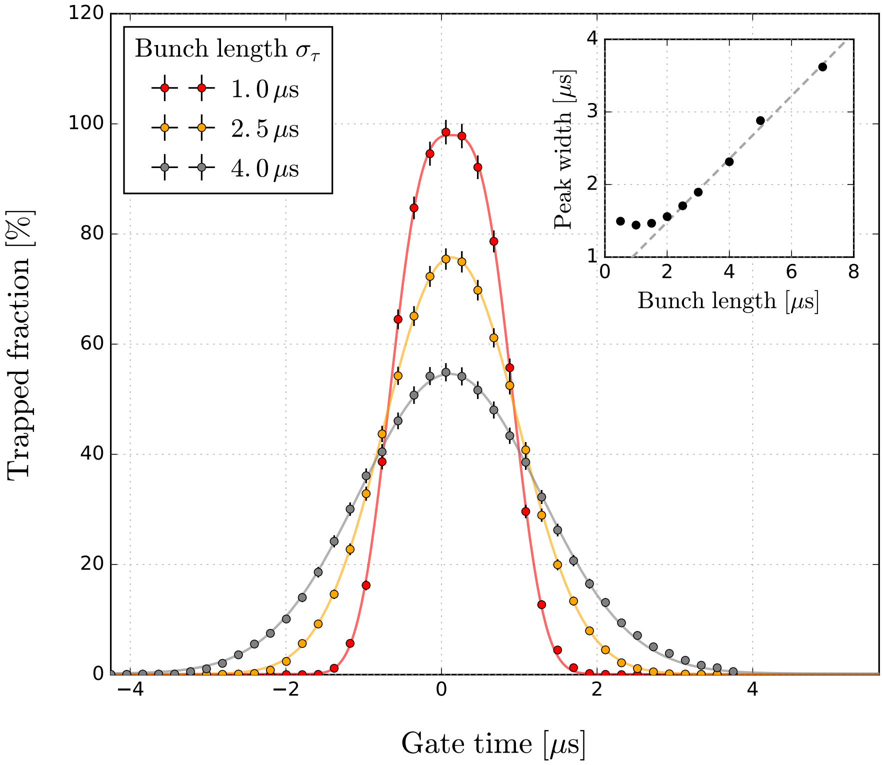

Figure 4.9: Fraction of particles caught from a $\sim$ 50 eV $\bar{\mathrm{p}}$ bunch arriving in the ALPHA-g atom trap as a function of the gate time. Simulated curves are shown for a number of bunch lengths between 1 μs $\leq \sigma_\tau \leq$ 4 μs. A flatenned Gaussian function has been fitted to each data set, and is shown as a solid line for comparison.

For each bunch length, simulations were used to evaluate the fraction of antiprotons that are captured for a range of gate times between 1 μs and 9 μs. Particles were considered to have been captured if they remained within -100 mm $\leq z \leq$ 50 mm of Figure 3.2 after a period of 2 ms had elapsed in each simulation.

Figure 4.9 shows how the number of captured antiprotons varies as a function of the gate time and bunch length σ_τ. The horizontal axis has been shifted relative to the optimal gate time of approximately 5.3 μs. In practice, the gate time for a real $\bar{\mathrm{p}}$ transfer is given by adding this delay to the time of flight for antiprotons travelling into the ALPHA-g experiment from the catching trap. Based on the simulations described in Section 4.2 of this thesis, we expect a gate time of $\sim$ 123.3 μs for antiprotons extracted with an energy of 50 eV.

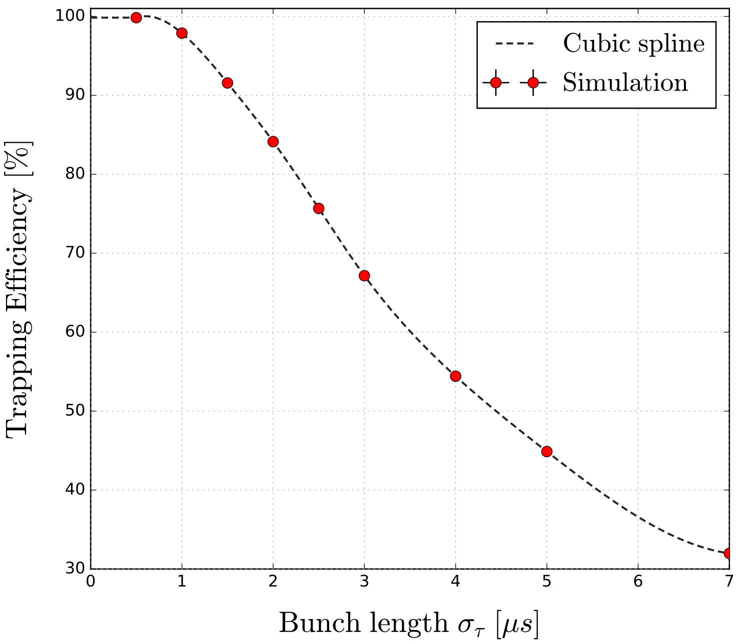

Figure 4.10: Maximum percentage of particles captured from a 50 eV $\bar{\mathrm{p}}$ bunch for a range of bunch lengths between 0.5 μs $\leq \sigma_\tau \leq$ 7 μs. A cubic spline has been fitted to the simulation results, and is shown as a dashed line. The error bars indicate counting uncertainties in the simulation data, but are too small to be visible.

Clearly, the number of particles captured from each $\bar{\mathrm{p}}$ bunch depends strongly on the gate time. The inset plot shows the typical width of the fitted curve for each bunch length. For an infinitely short $\bar{\mathrm{p}}$ bunch, the gate time must be tuned to within ± 1 μs to capture all of the incoming antiprotons. As the bunch length increases, a small fraction of antiprotons can be captured even when the gate time is shifted significantly from its optimal value.

Even after optimising the gate time, the number of captured particles depends strongly on the bunch length of the incoming antiprotons. Figure 4.10 shows how the maximum number of captured antiprotons depends on the bunch length σ_τ. A cubic spline has been fitted to the simulation data in order to compare the trapping efficiencies for different bunch lengths. Clearly, a bunch length of $\lesssim 1$ μs is required to capture more than 95 % of particles from an incoming $\bar{\mathrm{p}}$ bunch. This limit is consistent with the analytical calculations presented in Section 3.1.3 of this thesis.

For a bunch length of $\sigma_\tau = 2$ μs, approximately 16.5% of antiprotons are lost during each transfer as a result of their finite bunch length. This figure excludes any scattering losses along the beamline, or magnetic mirroring as particles enter the strong magnetic field of the ALPHA-g atom trap.

As discussed in Section 4.2.4, antiprotons will transfer $\sim$ 3 eV of kinetic energy into their transverse degrees of freedom while moving along the beamline. This mixing between the degrees of freedom will create a spread of particle energies along the beamline, and increase the longitudinal emittance of each $\bar{\text{p}}$ bunch. In simulations of the ALPHA-g beamlines, $\bar{\text{p}}$ bunches were launched from the catching trap with a point-like longitudinal phase space. Upon reaching the 1.0 T magnetic field of the atom trap, each $\bar{\text{p}}$ bunch had developed an energy spread of approximately 1.2 eV. As a result, simulated $\bar{\text{p}}$ bunches would expand to a length of $\sigma_\tau \sim 0.41$ μs after passing through the beamlines. This value represents the minimum bunch length for antiprotons that are originally extracted with a point-like longitudinal phase space.

5 | Beamline Implementation

The ALPHA-g experiment and its associated beamlines were installed at CERN during 2018, with the aim of commissioning the new apparatus using trapped antihydrogen before the end of the year. From 2019 - 2021, the CERN accelerator complex will be shut down for a period of planned upgrades and maintenance, meaning that antiprotons will be unavailable for over two years after the initial commissioning of the new experiment. While the ALPHA-g atom trap was only assembled during the latter half of the year, the charged particle beamlines were installed several months earlier to facilitate a short period of antihydrogen physics with the ALPHA-II atom trap. The commissioning of the ALPHA-g experiment was therefore subject to strict time constraints, making it important that the new beamlines could be assembled quickly and operated reliably after their installation.

The following chapter describes the physical hardware that was manufactured and installed to achieve the beamline design outlined in Chapter 3 of this thesis. Section 5.1 presents the measured properties of the beamline magnets, and reviews the sensors and interfaces that are used to connect each magnet to an external control system. Likewise, Section 5.2 describes the design of this control system, and gives an outline of the different hardware and software components that are used to manage the ALPHA-g beamlines. Section 5.3 summarises how the final implementation of the beamlines impacts their performance and stability.

The ALPHA-g beamlines were installed in two phases, beginning with a simple horizontal beamline that would transfer positrons into the ALPHA-II atom trap.

While this chapter will primarily refer to the final version of the beamline that was used towards the end of the year, it is also important to describe this earlier configuration so that the experimental data in Chapter 6 of this thesis can be properly contextualised.

5.1 Beamline Magnets

The ALPHA-g beamline magnets were manufactured at STFC Rutherford Appleton Laboratory (RAL) between November 2017 and August 2018, along with their mechanical support structures and some unique parts of the beamline vacuum system. Additional manufacturing was carried out in parallel by the CERN magnet technology group, who were responsible for the Helmholtz coils (AGBL03) that were installed on both beamline diagnostics stations. Before any manufacturing began, detailed designs were shared and discussed with both groups to ensure that the final beamline installation would achieve the parameters of the conceptual design outlined in Chapters 3 and 4 of this thesis.

The following sections of this thesis describe the final specifications of the ALPHA-g beamline magnets, ranging from their electromechanical properties to the various sensors and protective devices that are integrated into each magnet. In many cases, these specifications have evolved from those presented in Chapter 3 after accounting for additional mechanical constraints within the beamline geometry. Section 5.1.3 briefly describes the commissioning of the magnets, including measurements of their magnetic fields and operating temperatures that were made in a controlled environment before their installation.

5.1.1 Electromechanical Design

Throughout the design of the ALPHA-g beamlines, each magnet was treated as a hollow cylinder carrying a uniform current density through its entire cross section.

Property	**Conducting Area**	**Insulated Wire**	**Units**
Width	2.50	2.70	mm
Height	1.25	1.40	mm
Area	3.13	3.78	mm^2
Fill Factor	0.83		
Winding Density	0.26		mm^{-2}
Resistivity	1.75×10^{-8}		$\Omega \cdot \text{m}$

Table 5.1: Properties of the copper wire that was used for manufacturing of the ALPHA-g beamline magnets. The resistivity of the wiret is an estimate that assumes an operating temperature of 40 °C.

However, real solenoids are generally built up from many turns of wire arranged in layers around the circumference of a cylindrical former. For this reason, the specifications in Chapter 3 of this thesis were used only to define the envelope and nominal operating point of each magnet. Many of the electrical properties of the beamline magnets can be estimated by combining these specifications with information about the wire that was used for their construction.

Table 5.1 outlines the properties of the copper wire that was used to manufacture the ALPHA-g beamline magnets. Since this wire has a rectangular cross section, the magnet windings can be arranged into a closely packed lattice with minimal space between neighbouring turns. This particular wire has a large fill factor, defined as the ratio of its conducting cross section to the total insulated area of the wire. These properties mean that each magnet can be modelled as if it carries a uniform current density through its entire cross section, neglecting the internal structure formed by individual turns of wire. As a result, no detailed studies were undertaken to compare the true magnetic fields of the beamline magnets to the Biot-Savart approximations that had been calculated previously.

Table 5.2 details the final specifications for the ALPHA-g beamline magnets. In many cases, the dimensions of the magnets have been adjusted to accommodate features such as water cooling circuits or mechanical mounting points.

This table includes a number of electrical properties for each magnet, such as the expected resistance of the windings and their nominal operating current and voltage. These calculations assume that the windings are formed from pure copper at an operating temperature of 40 °C. The ALPHA-g beamline magnets were designed with a large number of turns, and will therefore produce the required magnetic fields at modest currents of 15 A or less. However, the magnet windings have large resistances as a result, and will continually dissipate up to $\sim$ 1.3 kW of power while energized.

Primarily, the maximum operating current of each magnet is dictated by the resistive heating of its windings when an electrical current is passed through them. Without external cooling, many of the magnets will reach temperatures in excess of 100 °C after operating at their nominal currents for several minutes. Overheating of the ALPHA-g beamline magnets beyond a temperature of 130 °C may result in thermal damage and should be strictly avoided.

Each magnet is cooled continually by flowing water through a layer of copper tubing around the outer circumference of its windings. For the majority of magnets, this circuit has a circular cross section with a diameter of 10 mm. However, the four Helmholtz coils (AGBL03) that were manufactured at CERN feature a cooling circuit with a rectangular cross section, which increases the amount of contact between the flow of water and the windings themselves. The outer surface of each magnet was coated in a layer of thermally conductive resin to maximise the rate of heat transfer between the windings and their water cooling circuit.

Typically, charged particle transfers through the ALPHA-g beamlines are separated by at least two minutes while $\bar{\mathrm{p}}$ and e^+ plamas are accumulated within their respective particle traps. The beamline magnets can therefore be operated in a pulsed mode, so that sections of the beamline are shut down during periods of inactivity.

In this mode of operation, the average heating rates of the magnets are significantly reduced, allowing them to briefly operate at much higher currents during charged particle transfers. Between transfers, the currents supplied to the magnets can be ramped slowly between different setpoints over a period of several seconds. While many of the beamline magnets have large inductances (Table 5.2), the size of any induced voltages can be reduced by limiting the ramp rates of the magnets to a few amperes per second.

Due to the sensitivity of the ALPHA-g experiment to magnetic field errors, permeable magnetic materials were eliminated from the construction of the apparatus as much as possible. Components within the vacuum system of the beamlines are therefore manufactured from non-magnetic type 316LN stainless steel, while the support structures around the beamline are built from type 6061 aluminium. As a result, the magnetic fields around the beamline are produced only by the currents flowing through the magnets themselves, and not by the magnetization of nearby ferromagnetic materials.

5.1.2 Sensors and Interfaces

Each magnet is fitted with a number of sensors and protective devices that are used to safeguard them against accidental damage while in use. The following section outlines the role of each type of sensor, and describes how they were integrated into the beamline control system that is described later in this chapter.

The main mechanism that can cause damage to the beamline magnets is overheating. To minimize the risk of thermal damage, a number of interlocks are enforced to prevent the magnets from operating beyond a certain temperature. Primarily, each magnet is fitted with a series of thermocouples, which are used to monitor the temperature of the windings through an external control system.

Identifier	Radius [mm]		Length [mm]	Turns	Resistance [Ω]	Inductance [mH]	Nominal Operating Point		
	Inner	Outer					Current [A]	Voltage [V]	Power [W]
Beamline Modules									
AGBL01-1	50.8	70.8	1012.6	5358	11.8	353.6	7.6	88.8	671
AGBL01-2	50.8	70.8	710.5	3759	6.46	185.7	7.6	48.8	369
AGBL02	100.0	125	250	1653	6.63	363.2	7.6	50.1	379
Diagnostic Stations									
AGBL03	132.5	171.9	41.1	428	2.32	80.2	15.5	35.9	556
Interconnect Magnet									
AGBL04	77.5	105.0	95.0	691	2.25	78.0	10.6	23.9	253
AGBL05	90.0	120.0	100.0	794	2.97	120.4	9.8	29.2	287
AGBL06	130.0	160.0	60.0	476	2.45	85.7	10.8	26.4	285
AGBL07-1	117.5	142.5	60.0	397	1.84	53.4	15.1	27.8	420
AGBL07-2	145.0	170.0	60.0	397	2.22	70.44	14.0	31.1	434
Transfer Coils									
AGBL08	302.5	350.0	100.0	1257	14.5	1588.7	9.5	136.9	1294

Table 5.2: Table detailing the final specifications for each of the magnets that are used throughout the ALPHA-g beamlines. A detailed description of how each magnet is used within the overall design of the beamlines can be found in Chapter 3 of this thesis.

Where possible, these sensors are embedded inside the windings of the magnets, and positioned to measure the highest temperature within the copper mass at any given time. Readings from the thermocouples are used to enforce software interlocks, so that the beamline control system will automatically shut down magnets that have exceeded a certain threshold temperature.

As well as thermocouples, each magnet was fitted with a single bimetallic switch on its outer surface. These switches will open after reaching a temperature of approximately 70 °C, and are connected directly to hardware interlocks on the magnet power supplies. Once the thermal switch on an overheating magnet has opened, the supply of current to that magnet is shut down immediately without any intervention from the beamline control software. These switches should protect the magnets in the event of a software failure, which could otherwise leave them powered without enforcing software interlocks to protect them against thermal damage.

Each section of the beamline is supplied with electrical current and cooling water through an interface panel that is mounted to the support structure directly below it. In keeping with the concept of a modular design, these panels gather the interfaces for each magnet into one location, so that sections of the apparatus can easily be disconnected and moved off the beamline for maintenance.

Cooling water is distributed throughout each section of the beamline through a pair of stainless steel manifolds, which are fitted with pressure sensors so that the change in water pressure across each group of magnets can be monitored continually. These sensors are used to implement further safety interlocks, so that sections of the beamline are shut down if the flow of water to that area has been interrupted. We measured the largest pressure differential across the beamline modules, with a typical difference of approximately 2 bar between the supply and return manifolds.

5.1.3 Measurement and Commissioning

Before being dispatched to CERN, the beamline magnets were tested to ensure basic functionality as well as consistency with their original specifications. Primarily, these tests were used to calibrate the magnetic field at the centre of each magnet as a function of current, and to determine their nominal operating temperatures under controlled conditions. Table 5.3 shows the results of these measurements, comparing the strength of each magnet to the value suggested by analytical calculations. Since many of the magnets initially reached high temperatures after a period of continual operation, additional water cooling circuits were installed to bring their temperatures into a more acceptable range.

Since the ALPHA-g experiment was assembled under strict time constraints, there was no opportunity for detailed characterisation of the field produced by each beamline magnet. However, studies using the simulation tools described in Chapter 4 of this thesis had already indicated that the beamline would be tolerant of magnetic field errors. As a result, these measurements were not considered essential for the initial commissioning of the apparatus. Nonetheless, measurements of the magnetic fields at the centres of the magnets (Table 5.2) were found to be in good agreement with Biot-Savart calculations to within a few percent.

After installation onto the beamline, the magnets were tested to ensure that their various temperature sensors were functioning correctly. Each magnet was powered at a current of at least 10 A without any water cooling, while the temperature of the windings was monitored continually using a handheld thermocouple reader. The state of the thermal switch was checked periodically to calibrate it against the core temperature of the windings. Many of these switches were found to be ineffective due to being installed on the outer surfaces of the magnets.

Identifier	**Current [A]**	**Field [Gauss]**		**Temperature [°C]**
		Measured	Expected	
Beamline Modules				
AGBL01-1	7.65	500.0	505.3	30.0
AGBL01-2	7.65	500.0	499.9	27.6
AGBL02	7.75	500.0	478.2	38.2
Diagnostics Stations				
AGBL03	12.0	275.0	264.0	80.1
Interconnect				
AGBL04	10.6	467.0	449.7	55.7
AGBL05	10.0	455.0	430.4	74.9
AGBL06	12.0	252.0	242.8	91.0
AGBL07-1	15.0	285.8	280.8	64.4
AGBL07-2	15.0	246.0	233.8	77.2
Transfer Magnets				
AGBL08	10.0	270.0	239.2	58.0

Table 5.3: Measured properties of the ALPHA-g beamline magnets under controlled conditions on a test bench. Temperatures were measured at the inner surface of the windings after a period of continual operation with a regulated flow of cooling water $\gtrsim 1.8$ L/min

In many cases, the core temperatures of the magnets would rise above 110 °C without triggering a hardware interlock, and further testing was aborted to protect the magnets from overheating.

Once fully assembled, the vacuum system of the beamline was baked at a constant temperature of 110 °C for several days, producing a base vacuum pressure of $\sim 2 \times 10^{-9}$ mbar throughout the apparatus. In order to bake sections of the beamline where the vacuum system is enclosed by the windings of the magnets, the magnets themselves were used as heaters. A feedback system was implemented to regulate the current in each magnet as a function of its measured temperature, so that the vacuum system was maintained at a constant temperature during baking.

While the majority of the beamline was installed ahead of the ALPHA-II physics run during June 2018, the interconect was not completed for an additional month due to the complexity of its design. As a result, a solenoid that was originally built for the ELENA project was loaned to ALPHA, and installed in place of the interconnect in the original configuration of the beamline. This magnet was used to generate a magnetic field of ~ 225 Gauss within the space vacated by the interconnect, allowing most of the beamline to be commmissioned with electrons, positrons and antiprotons. Critically, the installation of this magnet allowed positrons to be transferred into the ALPHA-II atom trap for the production of trapped antihydrogen.

5.2 Control System

The operation of the beamline is managed by an external control system, which handles the states of the magnets while responding to information about their temperatures and environment. This section describes the hardware and software components that are involved in the implementation of this control system (Figure 5.1).

The beamline control system must operate in two complementary roles at the same time. Primarily, this system is responsible for managing the states of the beamline magnets, and co-ordinating the overall operation of the beamline with other parts of the experiment such as particle traps and diagnostic devices. Additionally, the control system must also protect the beamline by refusing to power magnets that are overheating, and limiting the rates at which magnets can be ramped between different operating points.

5.2.1 Power Supplies

Each of the beamline magnets is powered individually using a programmable DC power supply. Details of the exact power supply that was used for each magnet can be found in Appendix B.

These units are operated in a current-limited mode at all times, so that the magnetic fields along the beamline are determined only by the output currents of the magnet power supplies. Power supplies were chosen based on the expected resistances of the magnets, so that each magnet can be provided with at least 150% of its nominal operating current, while the interconnect magnets can operate at up to 200% of their nominal magnetic fields. The beamline magnets are powered using Delta Elektronika [132] regulated DC power supplies, which are controlled remotely using isolated analog programming interfaces that allow their outputs to be set by an external control system.

When controlled through these interfaces, the states of the power supplies are programmed by applying voltages to a series of high impedance connections at the back of each unit. The output current and voltage of each power supply are programmed in proportion to two independent analog voltages within a range of 0 - 5 V_{DC}, so that applying 5 V to the appropriate programming connection will request either the maximum current or voltage of the power supply. Likewise, the outputs of the power supplies can be monitored in real time by measuring a pair of voltages that are read out through separate channels of the same interface. Finally, each power supply can be shut down remotely by setting a single digital line that is connected through an additional channel of the programming interface.

When transferring charged particles into the the ALPHA-g experiment, the interconnect must be switched between two different field configurations by reversing the direction of current in the two diagonal windings (AGBL07) around its centre. Since suitable bipolar power supplies were not available for these magnets, a relay system was implemented to control the direction of the current provided by their power supplies. As a result, a pair of heavy-duty mechanical relays are connected in series between these magnets and their respective power supplies.

When closed, these relays reverse the direction of current through the magnet windings, and therefore reverse the direction of the magnetic field within the interconnect.

Each relay is switched independently by setting a digital line that is controlled by the beamline control system. Software interlocks were implemented so that the interconnect relays cannot be opened or closed while current is being supplied to either of the magnets. Switching the state of a relay in this situation can result in electrical discharge betwen the relay contacts, and may also induce large voltages within the magnet windings themselves. Both possibilities would result in damage to the interconnect magnets or their associated relay system.

Finally, the current supplied to each beamline magnet is measured using a shunt connected in series with the output of its respective power supply. These devices are well calibrated resistors that can withstand large currents with very little variation in their temperature or electrical resistance. By measuring the potential difference across the length of each shunt, the currents flowing to the beamline magnets can be measured to a precision of better than ±1 mA. While the states of the power supplies are already reported through the monitoring outputs of their programming interfaces, measurements from the shunts are typically more precise and can be used to verify the values reported by the power supplies.

5.2.2 Control Hardware

The ALPHA-g beamline control system is assembled around a National Instruments Compact RIO (cRIO) device [133], which incorporates a number of interface modules that allow it to communicate with external devices. These interface modules handle the input and output of analog [134, 135] and digital [136] signals, as well as serial communication with external measurement devices [137]. The cRIO is equipped with a microprocessor that can be configured to run software written in the National Instruments LabVIEW programming environment.

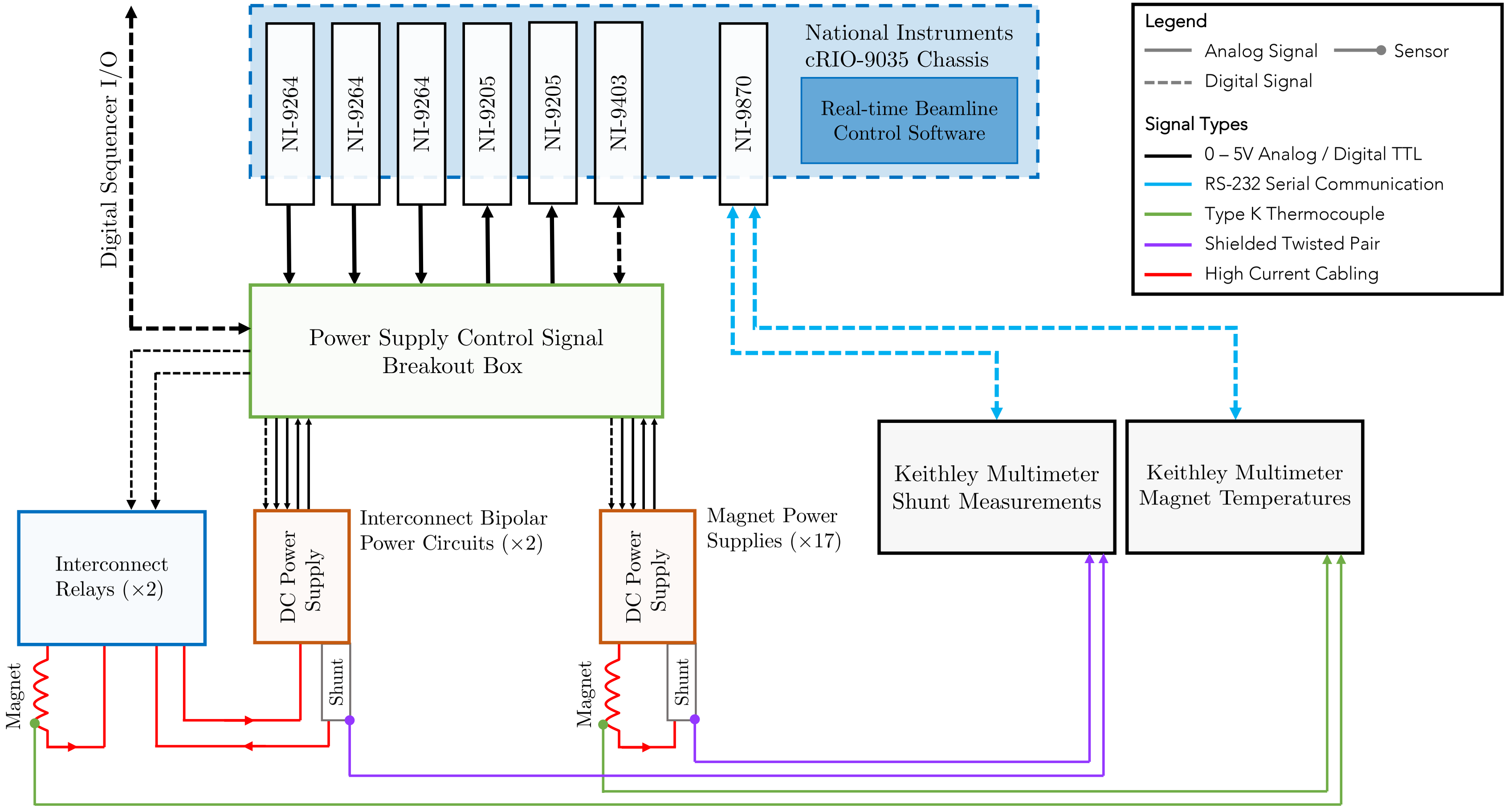

Figure 5.1: Schematic showing the basic structure of the ALPHA-g beamline control system. Repeated elements such as power supplies have not been shown in full for the purpose of clarity. Large bundles of similar signals are shown as a single wide line.

As discussed later in this chapter, this device runs control software that can manage the beamline independently during normal operation of the experiment, eliminating the need for user input under most circumstances.

Analog programming signals for the magnet power supplies are output by a trio of NI-9264 modules [134], which can produce voltages between ±10 V across 48 independently isolated channels. These signals are generated using an array of 16 bit Digital-to-Analog Converters (DAC), resulting in an absolute voltage resolution of 0.3 mV for each channel. At this resolution, the output current of each power supply can theoretically be programmed to an accuracy of ±3.7 mA or better. In reality, this resolution will be degraded by electrical noise that is coupled into the control system from external sources, and therefore represents the performance of an control ideal system in an isolated environment. Similarly, the monitoring outputs of the power supplies are read out using a pair of NI-9205 modules [135], which provide a total of 64 analog voltage input channels with an absolute resolution of ± 0.3 mV.

Finally, the input and output of digital signals from the control system is handled by a single NI-9403 module [136]. This module provides a total of 32 channels that can be configured either as inputs or outputs from the control system. The majority of these channels are configured as outputs, and are used to individually program the remote shutdown states of the magnet power supplies. However, a number of channels that are not allocated to the magnet power supplies are used for communication with the overall control system of the ALPHA experiment.

While communication with the power supplies needs to be programmed at a high frequency, monitoring of the beamline environment can take place more slowly, recording one measurement every few seconds. The magnet temperatures and shunt currents are therefore read out using a pair of Keithley 2701 multimeters [138].

These devices are multiplexed [139] to take measurements from a large number of similar inputs. Both multimeters host 40 independent channels, which can be configured as either voltage measurements or thermocouple inputs. These devices communicate with the control system through a pair of RS232 serial communication ports on an NI-9870 interface module [137].

5.2.3 Software

Software for the beamline control system was implemented in the LabVIEW programming environment and divided into two separate components. The real time component of the control software runs onboard the processor of the cRIO, and communicates directly with the interface modules to handle high-frequency operations such as the programming of magnet ramps. A secondary component of the software reports information about the magnets through a graphical user interface, and allows some level of manual control and configuration of the system as a whole.

Primarily, the real time component of the software is responsible for managing the states of the magnets at small time intervals, issuing new settings to the power supplies at a rate of around 100 Hz. The outputs of the interface modules are updated more frequently at a rate of 1 kHz. At this time resolution, the currents supplied to the magnets can be incremented gradually during a ramp, producing a magnetic field that increases smoothly as a function of time. Magnet ramps are defined by setting a target current and fixed ramp rate for each magnet that is configured within the control system.

In addition to managing ramp operations, the real time control software also collects measurements of the magnet temperatures once every five seconds. Based on these measurements, software interlocks are automatically enforced to protect magnets that have exceeded a pre-defined temperature.

Initially, the control system was configured conservatively so that the beamline magnets could not be operated above a temperature of 60 °C. Once an interlock has been triggered, the affected magnets are turned off immediately and cannot be powered until their state is reset manually through the graphical user interface. Measurements of the magnet temperatures, currents and voltages are logged periodically to an online database [140].

The overall control system of the ALPHA experiment is built around a number of high-frequency digital sequencers, which commmunicate with external devices through an array of digital lines and analog output channels. Experimental procedures are defined by sequence files, which program the states of these channels at a time resolution of 12.5 ns. The beamline control software was written to accept commands from a dedicated beamline sequencer, so that the operation of the beamline can be synchronised with other parts of the experiment such as particle traps and diagnostic devices.

The beamline sequencer can issue commands to the beamline by programming five digital inputs to the control system. Four of these bits are used to select from a list of sixteen pre-defined ramp states for the beamline magnets, while the final bit is used as a trigger to initiate the selected ramp. When a rising edge is detected on the trigger bit, the beamline magnets will immediately ramp to whichever state was previously selected using the other four configuration bits. Once the ramp has been completed, the control system will indicate to the sequencer that it is ready to receive particles using a single digital output from the control system. At this point, the sequencer can issue further commands to initiate a $\bar{\mathrm{p}}$ or e^+ transfer, before requesting that the beamline magnets are ramped down after the transfer has been completed.

Parameter	**Value**	**Units**
Power Supplies		
Number of power supplies	19	
Output current ripple	3	mA
Output voltage ripple	10	mV
Output rise time	11	ms
Control System		
Time Resolution	1.0	ms
Analog programming range	0 - 5	V
Analog voltage resolution	0.3	mV
Programming noise level	< 5	mV
Output current resolution	3.7	mA
Output current noise level	60	mA
Output voltage resolution	20	mV
Output vontrol noise level	330	mV

Table 5.4: Summary of key parameters for the control system that was implemented to manage the ALPHA-g beamline magnets. Power supply specifications are taken from manufacturer's data sheets [132].

Table 5.4 summarises a number of parameters defining the expected performance of the beamline control system. These values conservatively assume that the control system is contaminated by electrical noise with an amplitude of around 5 mV.

At this level, the currents supplied to the beamline magnets should be stable to within ± 60 mA. While the performance of the control system may be significantly better than these values suggest, it was not possible to resolve noise within the control system below the level of 5 mV during commissioning. Nonetheless, this level of performance is sufficient to ensure shot-to-shot stability in the positions of $\bar{\text{p}}$ and e^+ bunches delivered to the ALPHA-g atom trap. By referring to the simulated steering scans in Chapter 4 of this thesis, it can be shown that antiprotons should consistently arrive within ~ 0.15 mm of the ALPHA-g trap axis after passing through the interconnect.

5.3 Summary

The following section gives a brief summary of the results presented in this chapter. In particular, this section focuses on parameters that have a direct influence on the performance of the beamlines.

Table 5.2 lists the final electromechanical specifications for the ALPHA-g beamline magnets. At their nominal operating points, each of the magnets requires a current of $\sim$ 15.5 A or less to produce its specified magnetic field. The majority of the magnets have resistances of less than 6.5 Ω. However, the two large transfer coils (AGBL08) that are installed directly below the ALPHA-g experiment each have a resistance of 14.5 Ω. As a result, these magnets will dissipate 1.3 kW of power through the resistive heating of their windings at their nominal operating point of 10 A. To some extent, the operating points of the magnets are limited by the dissipative heating of their windings.

Appendix B lists the properties of the DC power supplies that are used to power the beamline magnets. Nominal operating points for the magnets were identified using the specifications listed in Chapter 3. In practice, the maximum current that can be supplied to any magnet is limited by the current and voltage range of its corresponding power supply, as well as its own electrical resistance. Power supplies must therefore be chosen to accomodate the nominal operation of the beamline, while also leaving some modest safety margin.

Suitable power supplies were chosen so that most of the magnets could operate at up to 150% of their nominal magnetic fields. Within the interconnect (beamline section D) this range was increased to 200% to accomodate corrections to the steering of $\bar{\mathrm{p}}$ and e^+ bunches. The maximum current that can be supplied to any of the beamline magnets is approximately $\sim$ 30 A.

Each of the magnet power supplies is remotely programmed through an external control system. Programming signals for the power supplies are generated using a number of analog interface cards, which are mounted on a National Instruments Compact RIO [133] device.

The stability of the beamline is limited by electrical noise that is coupled into the control system from external sources. By measuring the amplitude of this noise, we conservatively estimate that the current supplied to each magnet is stable to within $\lesssim 60$ mA. At this resolution, the $\bar{\mathrm{p}}$ beam position directly above the interconnect should be stable to within ~ 0.15 mm. This is sufficient to ensure that the number of antiprotons captured from each $\bar{\mathrm{p}}$ bunch does not vary due to shot-to-shot variation in the beam position. Table 5.4 gives a full summary of the characteristics of the control system.

6 | Experimental Results and Analysis

The following chapter describes a range of experimental data that was taken during the commissioning of the ALPHA-g beamlines. Section 6.1 reviews the performance of the temporary beamline that was initially used to transfer positrons into the ALPHA-II experiment. Section 6.2 describes the commissioning of the interconnect magnet, with an emphasis on the steering and transverse dynamics of charged particle beams. Finally, Section 6.3 explores how the longitudinal dynamics of $\bar{\text{p}}$ and e^+ bunches were optimised in order to capture them in the ALPHA-g atom trap. Throughout this chapter, the performance of the beamline is evaluated by comparing experimental data to the numerical simulations described in Chapter 4 of this thesis.

After their installation, the ALPHA-g beamlines were commissioned quickly, and often in parallel with other parts of the experiment. Table 6.1 lists a number of significant milestones that were reached towards the commissioning of the beamlines throughout 2018. The original, temporary installation of the beamline was commissioned during the final week of June 2018. The majority of commissioning activities for the full beamline took place between September and October 2018 after the installation of the interconnect magnet. By the end of the year, the beamlines were fully functional and were routinely being used to transfer positrons and antiprotons into the ALPHA-g atom trap.

6.1 The Horizontal Beamline

As described in Chapter 5 of this thesis, the ALPHA-g beamlines were originally installed without the interconnect to facilitate a short period of $\bar{\mathrm{H}}$ physics using the ALPHA-II experiment. In this configuration, e^+ bunches were transported along a horizontal beamline between the positron accumulator and the ALPHA-II atom trap. In addition, $\bar{p}$ bunches were extracted to the BDS in order to commission the antiproton beamline up to this point. Section 6.1.1 describes how the horizontal beamline was used to transfer e^+ bunches into the ALPHA-II atom trap, while Section 6.1.2 reviews the initial commissioning of the antiproton beamline.

6.1.1 Positrons for ALPHA-II

The performance of the horizontal positron beamline is mainly dictated by the alignment of e^+ bunches to the axis of the ALPHA-II experiment. As a result, the initial commissioning of the beamline was directed towards aligning the beamline magnets so that positrons would arrive close to the axis of the ALPHA-II atom trap. The magnetic alignment of the beamline was equally important to the later commissioning of the ALPHA-g atom trap using antiprotons transferred from the catching trap.

As shown in Chapter 2, light particles should robustly follow the direction of the magnetic field after being ejected from a Penning-Malmberg trap. The trajectories of positron bunches can therefore be modified by making small changes to the positions of magnets along their intended path. The magnetic alignment of the ALPHA-g positron beamline was mainly corrected by adjusting the orientations of the beamline module end coils. After each change, the transverse position of either an electron or positron beam was measured at one of several diagnostics stations (see Section 1.3.3) spaced along the beamline. The beamline was considered to be well aligned when the position of an electron beam emitted from the atom trap would overlap with that of a counter-propagating e^+ beam imaged at the same location.

Date	**Description**
May 22nd	First beamline components arrive at CERN
June 24th	First positron bunches captured in ALPHA-II
June 28th	First trapped antihydrogen atoms of 2018
July 16th	End of ALPHA-II physics run
September 15th	First electrons transferred through the interconnect
September 26th	First positrons transferred through the interconnect
October 30th	First antiprotons transferred through the interconnect
November 1st	First antiprotons captured inside ALPHA-g
November 10th	First positrons captured inside ALPHA-g
November 12th	End of ALPHA-g physics run

Table 6.1: Table of significant dates during the installation and commissioning of the ALPHA-g beamlines over the course of 2018.

Figure 6.1 shows the transverse profile of a positron plasma delivered to the ALPHA-II atom trap. This image was produced using an MCP mounted at the AT stick, approximately ~ 2.0 m from the magnetic centre of the ALPHA-II experiment (see Figure 1.5). Assuming that the MCP is aligned to the centre of the atom trap, the e^+ bunch in Figure 6.1 is located within $\pm$ 0.8 mm of the trap axis. As expected, the beam envelope was found to be circular, with positrons normally distributed around the centre of the beam. Due to the weak magnetic field of $\sim$ 220 Gauss around the location of the MCP, e^+ bunches will expand to a transverse size of $\sim$ 7.8 mm. Assuming that positrons move adiabatically throughout the beamline, this corresponds to a beam radius of $\sigma_\perp \sim 1.2$ mm in the 1.0 T magnetic field of the atom trap, and approximately 3.0 mm in the positron accumulator.

The number of positrons transmitted through the ALPHA-II experiment was measured using a Faraday cup mounted at the CT stick. Depending on the initial conditions within the positron accumulator, up to $(10.1 \pm 0.7) \times 10^6$ e^+ could be delivered to the atom trap in a single pulse.

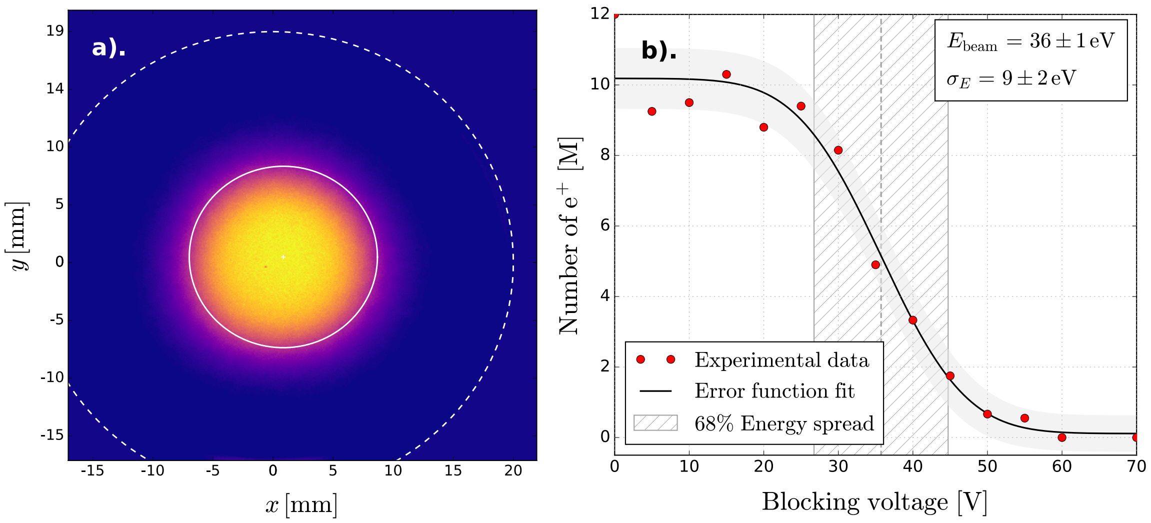

Figure 6.1: Plots showing a). the transverse distribution of positrons on an MCP mounted at the AT stick, and b). measurement of the positron energy distribution within the ALPHA-II experiment. The orientation of the axes in panel a). are indicated in Figure 1.5. A dashed white line is shown to indicate the circumference of the MCP. Equation 6.1 has been fitted to the data in panel b). and is shown as a solid black line.

Annihilation losses during particle transfers were monitored using an array of CsI detectors that were deployed between each section of the beamline. In general, significant annihilation losses were not observed unless the beamline was deliberately obstructed using an MCP or other diagnostic device. It can therefore be inferred that large numbers of positrons were not lost due to collisions with structures in the UHV space of the beamline. As such, the number of positrons captured within the atom trap was likely limited by the longitudinal structure of each bunch rather than its transverse size or position.

In general, e^+ bunches are emitted from the positron accumulator with a large energy spread, which causes them to expand longitudinally from an initial length of $\sim$ 300 mm while propagating along the beamline. The energy distributions of positron bunches were measured in the beamline by applying blocking voltages within the ALPHA-II atom trap, and counting the number of particles that were transmitted to the Faraday cup.

The second panel of Figure 6.1 shows a measurement of the positron energy distribution before any optimisation of the beam formation process had taken place. Assuming a Gaussian distribution of particle energies, the number of transmitted particles can be expressed as a function of the on-axis blocking potential ϕ

$$f(\phi) = \frac{N}{2}\left[1 - \operatorname{erf}\left(\frac{q\phi - E_{\mathrm{beam}}}{\sigma_E\sqrt{2}}\right)\right], \tag{6.1}$$

where $\operatorname{erf}(x)$ denotes the error function, N is the number of particles in each bunch, E_{beam} is the centroid beam energy and σ_E is the characteristic spread of particle energies. The energy distribution of a particle source can therefore be inferred by fittting Equation 6.1 to the number of particles transmitted through a range of different blocking potentials.

Initially, e^+ bunches were ejected from the positron accumulator at a mean energy of $E_{\mathrm{beam}} = (36 \pm 1)$ eV, with a large energy spread of $\sigma_E = (9 \pm 2)$ eV. Assuming that positrons move along the beamline with a constant kinetic energy, this distribution will produce a bunch length of around 5100 mm by the end of the beamline. In comparison, the potential well used to capture e^+ bunches in the ALPHA-II atom trap has a length of only ~ 200 mm. Even after optimising this potential to maximize the number of captured positrons, only 30% of particles were retained from each bunch delivered with this energy distribution.

By optimising the potentials used to extract plasmas from the accumulator, the energy spread of each pulse was reduced to (2.9 ± 0.6) eV around a mean energy of (48.1 ± 0.4) eV. This resulted in a significant compression of the physical bunch length to an expected value of ~ 1070 mm. In this regime, up to $(71 \pm 5)\%$ of positrons could be caught from each e^+ bunch that was delivered to the ALPHA-II atom trap. This efficiency represents a small improvement relative to earlier configurations of the experiment that were used before the addition of the new beamlines.

As a result, antihydrogen atoms were easily produced and almost immediately trapped at an average rate of 21 $\bar{\mathrm{H}}$ per attempt. This rate is consistent with the performance of the ALPHA-II experiment during 2017 [2] prior to the installation of ALPHA-g.

6.1.2 Commissioning with Antiprotons

As well as sending e^+ plasmas to the ALPHA-II atom trap, the temporary horizontal beamline was used to commission new parts of the apparatus using antiprotons. Prior to the installation of the interconnect, $\bar{p}$ bunches extracted from the catching trap could be made to propagate as far as the beamline diagnostics station (BDS). The horizontal portion of the antiproton beamline was initially commissioned by imaging $\bar{p}$ bunches using an MCP located at the BDS. As discussed later in Section 6.3.2, the $\bar{p}$ bunch length can also be characterised whenever antiprotons are measured destructively at a known point along the beamline. Demonstrating that antiprotons could be sent along the beamline to the BDS would therefore provide a wealth of information about their transverse and longitudinal dynamics.

Figure 6.2 shows the transverse profile of an antiproton bunch that was imaged at the BDS. At this stage of the commissioning process, the beamline was optimised so that e^+ bunches would arrive close to the horizontal axis of the ALPHA-II atom trap. Since no attempt had been made to steer antiprotons through the beamline, the $\bar{p}$ bunch is displaced by approximately ~ 4 mm along the x axis. Following the installation of the interconnect, the orientations of the beamline magnets were adjusted so that both $\bar{p}$ and e^+ were well-aligned throughout the apparatus.

During the initial commissioning of the beamline, $\bar{p}$ bunches were extracted from the catching trap with a mean energy of approximately 24 eV. As shown in Figure 6.2, the $\bar{p}$ beam profile at the BDS is essentially circular, with a maximum transverse size of $\sigma_\perp = 3.8$ mm.

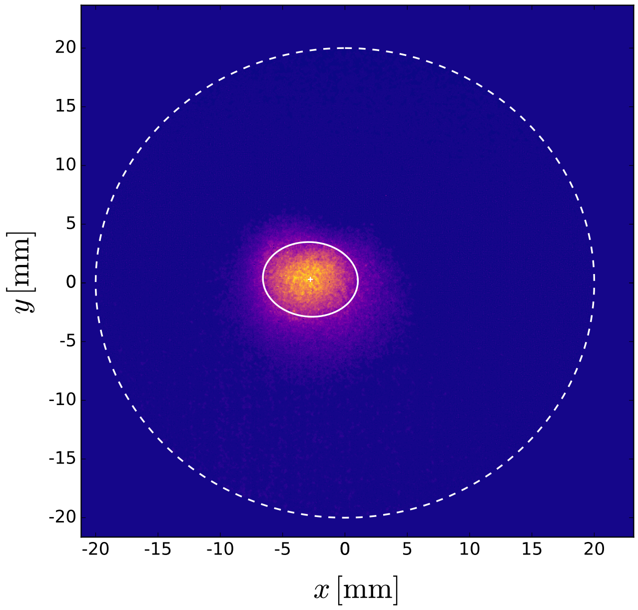

Figure 6.2: MCP image showing the $\bar{\mathrm{p}}$ beam profile at the beamline diagnostics station (BDS). The orientation of the x and y axes are shown in Figure 1.5. The dashed white line indicates the circumference of the MCP, while the solid white line shows the beam envelope $\sigma_\perp$.

This beam envelope is consistent with numerical solutions to Equation 2.33 for beam energies of $\sim$ 24 eV, which predict a transverse beam envelope of $\sim$ 4.0 mm.

6.2 The Interconnect

After successfully operating the ALPHA-II experiment for 18 days, the ALPHA-g beamlines were shut down so that the interconnect magnet could be installed. The following sections of this thesis describe experimental data that was taken during the commissioning of the interconnect. Section 6.2.1 reviews how the basic functionality of the magnet was established by steering electrons, positrons and antiprotons into the ALPHA-g experiment. Finally, Section 6.2.2 explores how the trajectories of charged particles respond to changes in the magnetic field of the interconnect.

6.2.1 Initial Commissioning

The basic operation of the interconnect was demonstrated by imaging different species of particles using an MCP at the lower diagnostics station (LDS).

Initially, we chose to steer each type of particle through the interconnect while the ALPHA-g external solenoid was not energised. In each case, suitable currents for the interconnect magnets were identified using the particle tracing simulations described in Chapter 4 of this thesis.

Typically, some adjustment to these currents was required to align the beam relative to the centre of the MCP. After observing a signal from particles striking the MCP, the currents in the two crossed coils (AGBL07) and the curvature drift correction coils (AGBL06) were tuned until the beam appeared to be well aligned. Table 6.2 gives a summary of the currents that were used to steer electrons, positrons and antiprotons into the ALPHA-g experiment while the external solenoid was operated at a magnetic field of 1.0 T.

As shown in Table 6.2, the currents that were used to transfer particles through the interconnect are generally very similar to those predicted by simulations of the beamline. This implies that the complex magnetic field of the interconnect is accurately described by the numerical models that are used throughout this thesis.

Notably, the operating currents of the two curvature drift correction coils (AGBL06) deviate significantly from the currents that were predicted by numerical simulations of the beamline. These magnets could not be installed at their nominal separation of 420 mm around the centre of the interconnect, and were instead installed at a larger separation of approximately 500 mm. Even after accounting for this difference, simulations of the antiproton beamline still predict a current that is ~ 3 A lower than in reality. The appearance of a similar error in both the $\bar{\mathrm{p}}$ and e^+ setpoints suggests that the MCP itself may be misaligned by 3–4 mm along the x axis of the beamline. Since the MCP is mechanically inserted into the beamline along this axis, the existence of a small misalignment is entirely plausible.

Identifier	**Simulation (Ideal Beamline)**		**Simulation (With Errors)**		**Experiment**
	Current Density [A/cm^2]	Current [A]	Current Density [A/cm^2]	Current [A]	Current [A]
Antiproton Setpoint					
AGBL04	400	15.1	400	15.1	15.0
AGBL05	420	15.8	420	15.8	16.0
AGBL06	260	9.8	350	13.2	16.0
AGBL07	495	18.7	440	16.6	16.0
AGBL08	250	9.5	250	9.5	9.5
Electron / Positron Setpoint					
AGBL04	280	10.6	280	10.6	10.5
AGBL05	260	9.8	260	9.8	10.0
AGBL06	0	0.0	0	0.0	2.0
AGBL07	265	15.0	265	15.0	15.0
AGBL08	250	9.5	250	9.5	9.5

Table 6.2: Interconnect magnet currents used to steer $\bar{\mathrm{p}}$ and e^+ into the ALPHA-g atom trap, with the external solenoid at a field of 1.0 T. For each setpoint, we compare the currents predicted by numerical particle tracing simulations to those used during the actual operation of the beamline. Simulations were carried out for an ideal beamline, and also for a beamline that includes known mechanical errors in the apparatus. Currents that diverge from the simulations by more than 1 A are highlighted in red.

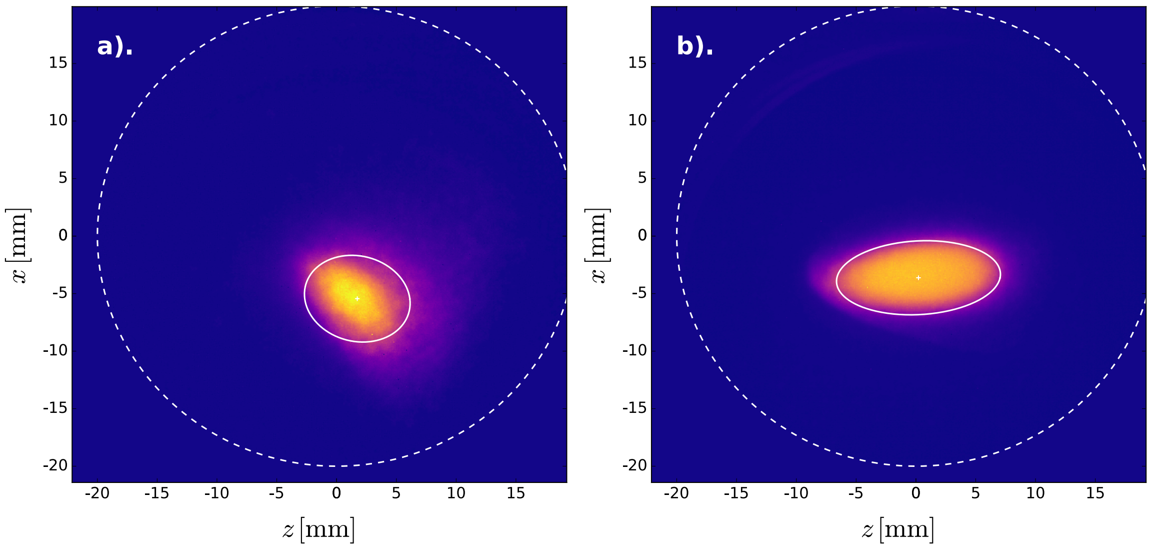

Figure 6.3: MCP images showing the transverse beam profiles of a). antiprotons and b). positrons imaged at the LDS. The orientation of the x and z axes are shown in Figure 3.13. The dashed white line indicates the circumference of the MCP, while the solid white line indicates the beam envelope $\sigma_\perp$.

While the steering of electrons and positrons through the interconnect does not depend on the beam energy to first order, $\bar{\text{p}}$ bunches are affected by large curvature drifts that depend on their longitudinal energies. As discussed later in Section 6.3, antiprotons were generally transported through the ALPHA-g beamlines at an energy of $\sim$ 50 eV. At different energies, the trajectories of $\bar{\text{p}}$ bunches were corrected by adjusting the currents in the two correction coils (AGBL06) installed on either side of the interconnect.

Figure 6.3 shows the transverse beam profiles of antiprotons and positrons imaged at the LDS. In each image, the beam position has been adjusted to maximise the number of $\bar{\text{p}}$ and e^+ passing through the ALPHA-g atom trap, rather than centering the beam relative to the MCP. The envelope of the positron bunch has clearly become elongated along the horizontal direction of the beamline, resulting in an elliptical beam profile. The antiproton beam profile is similarly elongated, but is noticeably more diffuse, with particles distributed irregularly around the edges of the $\bar{\text{p}}$ bunch.

The development of an elliptical beam profile was identified in Chapter 4 as an effect of the interconnect magnet. However, it is not immediately clear why the antiproton beam appears to have been rotated with respect to the axes of the beamline.

The antiproton bunch shown in the left-hand panel of Figure 6.3 has an overall radius of approximately 3.9 mm. Since these images were produced at a magnetic field of ~ 270 Gauss, $\bar{\mathrm{p}}$ bunches should contract to a transverse size of $\sigma_\perp = 0.64$ mm inside the ALPHA-g atom trap. These measurements are generally consistent with numerical simulations of the antiproton beamline, which predict a beam envelope of 4.0 mm at the LDS. Similarly, the e^+ bunch shown in panel b). of Figure 6.3 has a typical size of 6.0 mm along the z axis, and a radius of 2.8 mm perpendicular to the beamline.

The number of particles in each e^+ bunch can be varied by accumulating plasmas over different timescales inside the positron accumulator. The number of positrons delivered to the PDS and LDS was measured for a range of accumulation times using a Faraday cup mounted at each location. Figure 6.4 shows how the number of positrons delivered to the ALPHA-g experiment varies as a function of the number measured at the PDS. By fitting a linear function to this data, it can be shown that $(92 \pm 3)\%$ of positrons are trasmitted along the beamline and through the interconnect. This efficiency is independent of the number of accumulated positrons, meaning that at least 3.5×10^7 e^+ can be delivered in a single pulse. This number of positrons is more than sufficient for antihydrogen production at a rate consistent with the pre-existing ALPHA-II experiment.

Measuring the efficiency of antiproton transport is significantly more difficult for a number of reasons. Since a maximum of $\sim 10^5$ $\bar{\mathrm{p}}$ are captured during each AD cycle, the amount of charge in an antiproton bunch is too small to be measured using a Faraday cup with the readout electronics that are currently deployed at ALPHA.

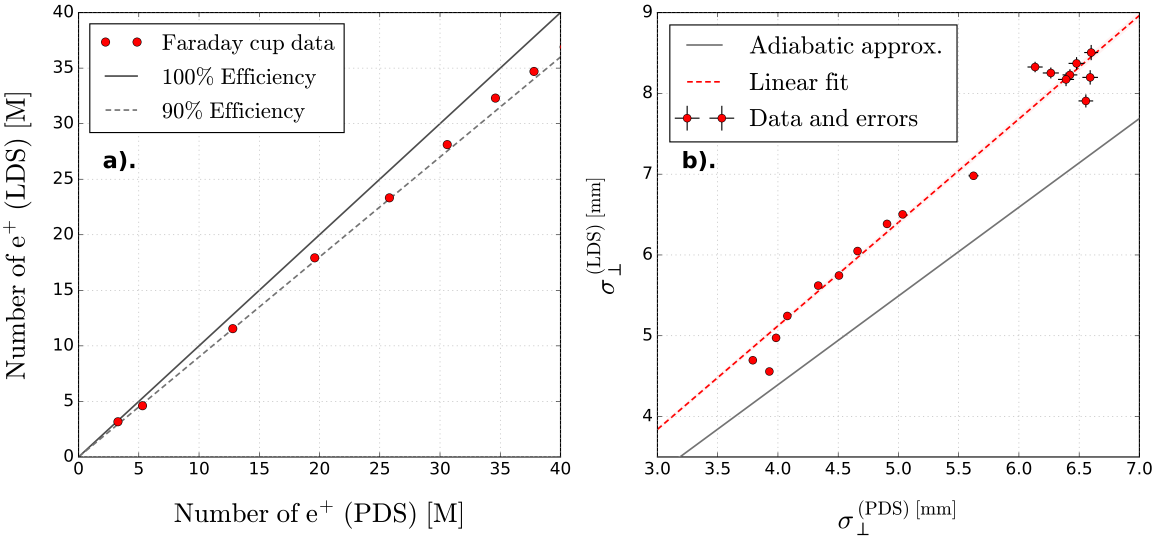

Figure 6.4: Comparison of positron bunches delivered to the positron diagnostics station (PDS) and lower diagnostics station (LDS). Panel a). shows the number of positrons measured at the LDS as a function of the number at the PDS. The error bars are too small to be visible. Panel b). shows the transverse size $\sigma_\perp$ of e$^+$ bunches at the LDS as a function of their initial size at the PDS. A linear fit to the data is shown for comparison.

While individual $\bar{\text{p}}$ annihilations can be counted using a range of detectors such as the ALPHA-g TPC, the counting efficiencies of these detectors were not calibrated at the time of writing this thesis. As a result, it was not possible to measure the absolute number of antiprotons that are delivered to the ALPHA-g atom trap during each transfer. In Section 6.3 of this chapter, we derive an upper limit for the number of captured antiprotons by considering their longitudinal dynamics.

Figure 6.4 shows how the transverse size of e$^+$ bunches measured at the LDS varies as a function of their original size at the PDS. Each data point represents a pair of MCP images that were taken for a fixed accumulation time between 20 and 500 seconds. At longer accumulation times, trapped positron plasmas will gradually expand due to imperfections in the trap geometry and collisions with residual background gases [141]. As a result, varying the accumulation time will produce a range of beam envelopes without controlling other factors such as the density or space charge of the resulting positron beam.

After being released from the positron accumulator, positrons are expected to move adiabatically through the ALPHA-g beamlines. The beam envelope of each e^+ bunch should therefore scale as a path-independent function of the magnetic field according to Equation 2.32. The expected scaling of the beam envelope between the PDS and LDS is shown as a dashed grey line in Figure 6.4, with a dimensionless gradient of ~ 1.10.

As shown in Figure 6.4, the transverse size of the beam at the LDS is consistently larger than the value predicted by Equation 2.32. However, the beam envelope at the LDS clearly scales as a linear function of the original beam radius at the PDS. A linear fit to the data shows that e^+ bunches expand to (1.28 ± 0.01) times their original size between these two points along the beamline. This difference is most likely to be caused by the cylindrical symmetry of the beamline being lost as e^+ bunches pass through the interconnect. Despite their increased transverse size, the e^+ bunches in Figure 6.4 are already smaller than the minimum aperture of the ALPHA-g experiment. As a result, large numbers of positrons should not be lost due to ballistic collisions within the atom trap itself.

6.2.2 Steering Scans

As discussed in Section 3.1.3 of this thesis, $\bar{p}$ and e^+ bunches must be delivered close to the axis of the ALPHA-g experiment if they are to be captured and held over long timescales. It is therefore important to understand how the beam position in the atom trap will vary as a function of the current in each of the interconnect magnets. The following section describes measurements that were undertaken to characterise the effect of the interconnect magnets on the beam position at the LDS.

As discussed in Section 5.2.3, some amount of shot-to-shot variation in the beam position is expected due to the finite resolution of the beamline control system.

The stability of the antiproton beamline was measured by repeatedly imaging $\bar{\mathrm{p}}$ bunches on an MCP at the LDS. In each case, the currents provided to the beamline magnets were kept constant to within the stability of the control system. The antiproton beam position was found to be stable to within ± 0.06 mm, which is considerably better than the conservative estimate of ± 0.15 mm that was derived in Section 5.2.3 of this thesis.

As discussed in Chapter 4 of this thesis, the positions of $\bar{\mathrm{p}}$ and e^+ bunches at the LDS can be adjusted using only two pairs of interconnect magnets. These magnets should move the beam position along a pair of axes that are almost orthogonal to one another. For example, the two crossed solenoids (AGBL07) are expected to move the beam primarily along the z axis indicated in Figure 3.13. Similarly, the two curvature drift correction coils (AGBL06) should translate the beam along the x axis perpendicular to the direction of the beamline.

Figure 6.5 shows how the $\bar{\mathrm{p}}$ beam position at the LDS varies as a function of the current supplied to each of the interconnect magnets. The experimental data in Figure 6.5 was collected during a period when the external solenoid was not energised. As a result, the currents supplied to the interconnect magnets were modified relative to the values listed in Table 6.2. The two crossed solenoids (AGBL07) were operated around a nominal current of 8.5 A, while the curvature drift correction coils were initially supplied with a current of 15.0 A. The current in each magnet was scanned within a range of ± 25% around its nominal value, or until the beam was no longer visible on the MCP.

Figure 6.5 also shows simulated current scans that were designed to replicate the experimental measurements described above. These simulations account for known mechanical errors in the construction of the interconnect to provide an accurate comparison to the experimental data.

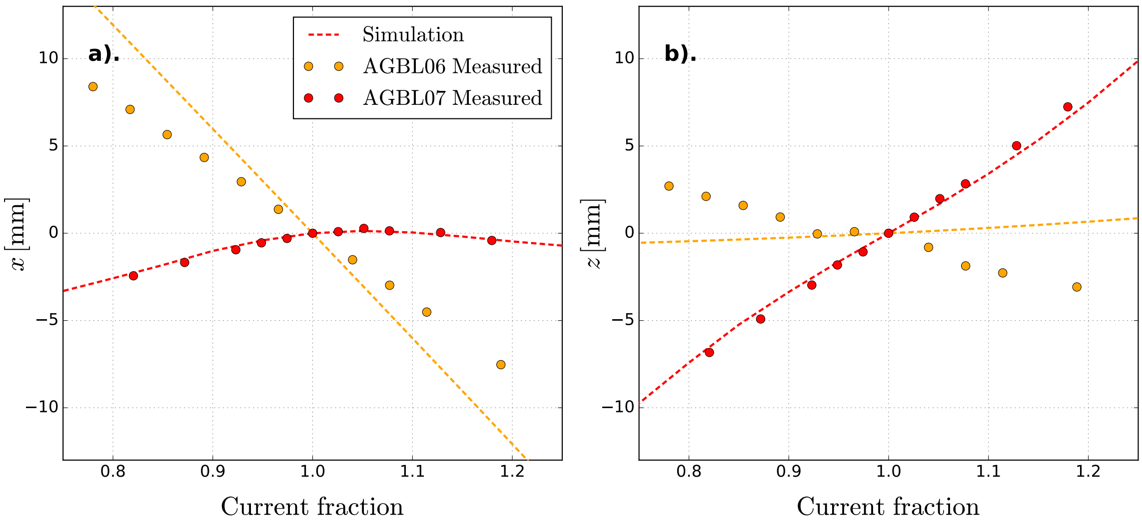

Figure 6.5: Antiproton beam position at the lower diagnostics station (LDS) as a function of the currents supplied to the interconnect magnets (with no external solenoid). Panels a). and b). show the components of the beam position along the x and z axes indicated in Figure 3.13, repsectively. Equivalent steering curves from numerical particle tracing simulations are shown for comparison.

For example, the interconnect was rotated about the horizontal x axis in each simulation, so that it leans towards the positron accumulator by $\sim$ 35 mrad as in the final installation. As described in Section 6.2.1, the two AGBL06 magnets were also separated by an additional $\sim$ 80 mm relative to the original beamline design.

Even after accounting for all known mechanical errors in the installation of the beamline, there are significant differences between the measurements and simulations shown in Figure 6.5. The simulations accurately predict the effect of the two crossed solenoids (AGBL07) on the $\bar{\text{p}}$ beam position when the ALPHA-g external solenoid is not energised. However, the AGBL06 magnets are less effective at translating the beam along the x axis than may be expected from the simulations. In addition, these magnets also displace the beam along the z axis is a way that was not predicted by the beamline simulations.

It is possible that these diagreements are the result of one or more mechanical errors in the beamline that are yet to be identified or characterised.

Due to the complex geometry of the interconnect, a number of small mechanical errors can add constructively to have a large effect on the trajectories of $\bar{\mathrm{p}}$ and e^+ bunches. For this reason, it is difficult to anticipate the effect of every possible mechanical error that may exist within the interconnect.

Equally, diagreement with the simulations may be caused by $\bar{\mathrm{p}}$ bunches being displaced from the horizontal axis of the beamline at the entrance to the interconnect. Antiprotons that arrive significantly off-axis will sample different magnetic fields as they pass through the central chamber of the interconnect. As a result, these particles will respond differently to changes in the magnet currents.

As described in Section 3.2.4, the ALPHA-g external solenoid generates a stray magnetic field that will affect the trajectories of $\bar{\mathrm{p}}$ and e^+ bunches. The steering scans shown in Figure 6.5 can be used to correct against the effect of the external solenoid when it is operated at its nominal magnetic field of 1T. After initially steering antiprotons through the interconnect while the external solenoid was ramped down, the magnet was slowly energised over a period of approximately one hour. During this period, $\bar{\mathrm{p}}$ bunches were extracted into the beamline and imaged at the LDS at regular intervals. After imaging each $\bar{\mathrm{p}}$ bunch, the currents supplied to the interconnect magnets were adjusted so that the beam would remain aligned to the centre of the MCP.

In a separate experiment, the ALPHA-g external solenoid was slowly ramped to its full magnetic field while $\bar{\mathrm{p}}$ bunches were repeatedly imaged at the LDS. The interconnect magnet currents were kept constant at all times to independently measure the effect of the external solenoid on the $\bar{\mathrm{p}}$ beam position. Figure 6.6 shows how position of $\bar{\mathrm{p}}$ bunches measured at the LDS varies as function of the magnetic field inside the ALPHA-g external solenoid.

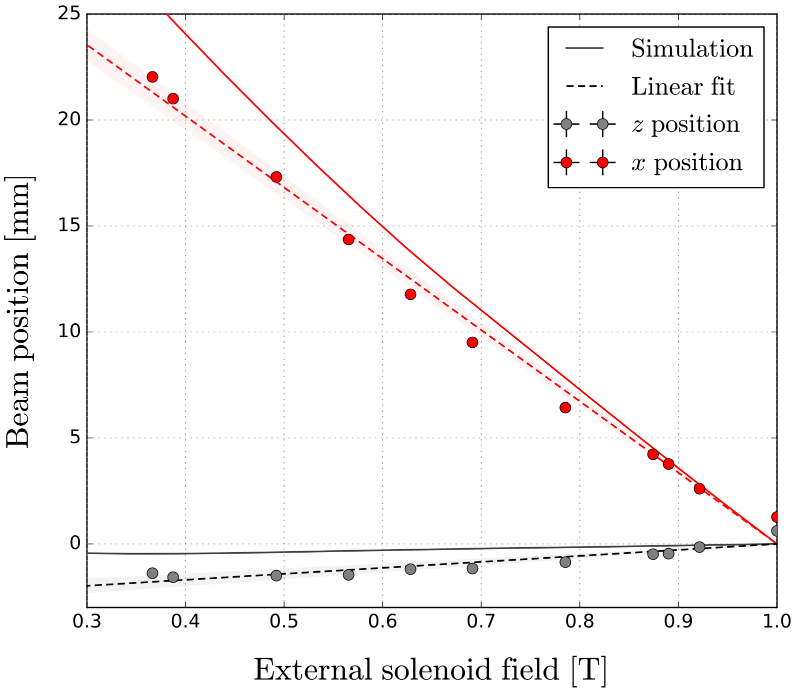

Figure 6.6: Transverse position of $\bar{\mathrm{p}}$ bunches at the LDS as a function of the magnetic field inside the ALPHA-g external solenoid. The beam position has been decomposed along the x and z axes shown in Figure 3.13. The results of particle tracing simulations are shown as a pair of solid lines, and a linear fit to each data set is shown as a dashed line. The error bars are too small to be visible.

At its full current, the external solenoid will displace antiproton bunches by approximately ~ 27 mm relative to their position when the magnet is completely ramped down.

Figure 6.6 also shows the results of numerical particle tracing simulations that were designed to replicate the experimental protocol described above. These simulations are successful in reproducing qualitative trends in the experimental data, with the external solenoid having a large effect on the beam position along the z axis. However, there are once again clear discrepancies between the experimental data and simulations. Magnetometry surveys of the ALPHA-g external solenoid have already shown that it does not suffer from large magnetic field errors. Simulations of the ALPHA-g beamlines have also shown that the solenoid can be displaced by up to $\pm$ 30 mm in any direction, with no appreciable effect on the final beam position.

These differences between the data and simulations therefore provide further support to the idea that there are uncharacterised mechanical errors in the interconnect.

6.3 Longitudinal Dynamics

As discussed in Section 3.1.3, long $\bar{\mathrm{p}}$ and e^+ bunches with $\sigma_\tau \gtrsim 1$ μs cannot be captured efficiently inside the ALPHA-g experiment. The following sections of this thesis describe how the longitudinal dynamics of both species were optimised to produce shorter bunch lengths within the ALPHA-g atom trap. Sections 6.3.1 and 6.3.2 describes how the bunch lengths and energy distributions of $\bar{\mathrm{p}}$ and e^+ were measured throughout the ALPHA-g beamlines. Finally, Section 6.3.3 reviews how antiprotons were captured within the ALPHA-g experiment and cooled into an electron plasma.

6.3.1 Energy Measurements

As shown in Section 6.1.1 of this thesis, the energy distributions of $\bar{\mathrm{p}}$ and e^+ bunches can be reconstructed by measuring the number of particles that are transmitted through a range of blocking potentials. Since antiprotons are only captured from the AD every $\sim$ 100 seconds, measuring of the $\bar{\mathrm{p}}$ energy distribution using this method is extremely time consuming. As a result, only the energy distribution of $\bar{\mathrm{p}}$ bunches launched at a nominal energy of $\sim$ 50 eV was characterised in detail using this method.

Figure 2.3 shows the on-axis potentials that are used to extract antiproton bunches from the catching trap at an energy of $\sim$ 50 eV. Short bunches of antiprotons are formed by rapidly decreasing the depth of an asymmetric electrostatic potential well that is imposed along the axis of the catching trap. The mean energy of each $\bar{\mathrm{p}}$ bunch is determined by the potential at the centre of the trap immediately before particles begin to escape confinement.

Similarly, the distribution of particle energies is shaped by fast changes in the electric potential that take place during beam formation. As a result, the longitudinal dynamics of p̄ bunches are determined immediately after their extraction from the catching trap.

The energy distributions of p̄ bunches were measured by applying fixed potentials within the ALPHA-II Penning trap and measuring the number of particles that arrived at the BDS. Since small numbers of antiprotons cannot be counted using a Faraday cup, the number of antiprotons was inferred from the intensity of an MCP image taken at each blocking potential. To correct for shot-to-shot variations in the number of p̄ delivered by the AD, a fixed fraction of antiprotons were deliberately released from the catching trap by manipulating the potentials along the trap axis. The number of p̄ annihilations during this window was counted using a scintillator panel, and used to to normalize the intensity of the beam for each blocking potential.

Figure 6.7 shows the energy distribution of p̄ bunches ejected from the catching trap at an energy of approximately $\sim$ 50 eV, along with a fit of Equation 6.1. Assuming a Gaussian distribution of particle energies, the mean energy of the beam was found to be (50.7 ± 0.1) eV with a typical spread of (1.9 ± 0.1) eV. If p̄ bunches are initially extracted from the catching trap with no axial length, this energy distribution will produce a bunch length of $\sigma_\tau = 8.85$ μs inside the ALPHA-g experiment. By comparing this bunch length to the simulations in Figure 4.10, it can be shown that less than 30% of antiprotons would be captured from this distribution.

6.3.2 Bunch Length Measurements

As discussed in Section 1.3.3 of this thesis, the ALPHA apparatus includes a number of plastic scintillator panels backed with photomultiplier tubes that can be deployed around the experiment.

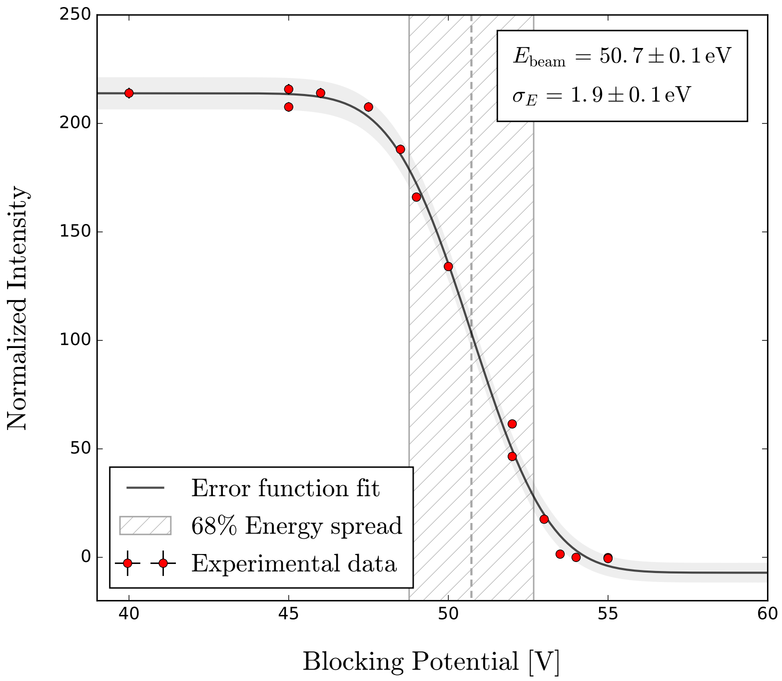

Figure 6.7: Measurement of the energy distribution of antiprotons launched from a potential of 50 V inside the catching trap. Equation 6.1 has been fitted to the data and is shown as a solid line. The standard deviation of the fit is shown as a shaded region around the central line. The error bars are too small to be visible.

Since the time resolution of these detectors ($\sim$ 2 ns) is much faster than the typical length of a $\bar{\mathrm{p}}$ or e^+ bunch, they can be used to directly measure the time structure of a single pulse of charged particles. Bunch length measurements were made by detecting the annihilations that are produced when a $\bar{\mathrm{p}}$ or e^+ bunch is launched into a solid target such as an MCP. The output of a detector was connected to a digital oscilloscope with a high input impedance. The resulting voltage waveforms were recorded at a sample rate of at least 10 MHz, and analysed to extract the length of each $\bar{\mathrm{p}}$ or e^+ bunch.

The antiproton bunch length was primarily measured by launching $\bar{\mathrm{p}}$ bunches into an MCP at the BDS. Figure 6.8 shows the time structure of antiproton bunches arriving at the BDS at an energy of 50 eV. This measurement incorporates data from fourteen identical trials that have been averaged together. The error bars shown in Figure 6.8 indicate the standard error of the distribution of measurements.

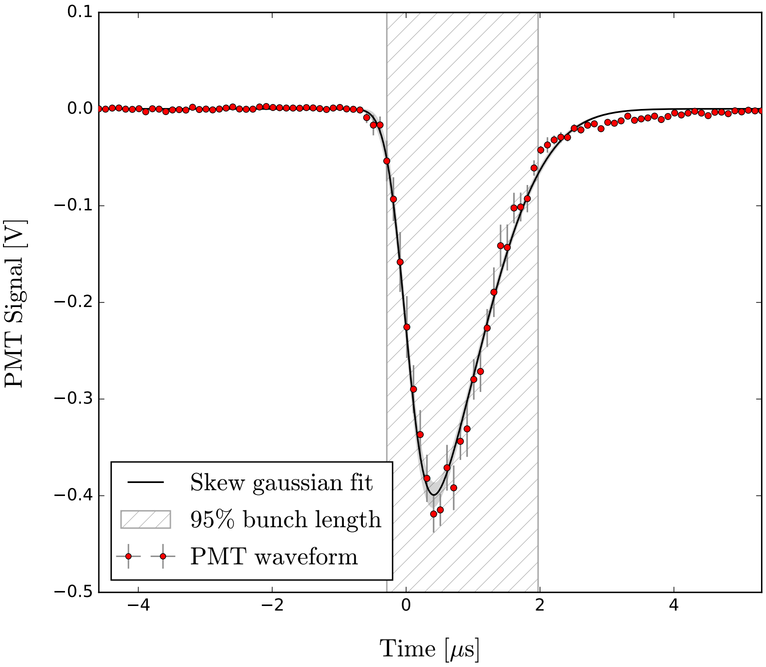

Figure 6.8: Measurement of the bunch length σ_τ for 50 eV antiprotons annihilating at the beamline diagnostics station (BDS). Equation 6.2 has been fitted to the data, and is shown as a solid black line.

The experimental data in Figure 6.8 is well modelled by a skew Gaussian function

$$f(t) \sim \left[1 + \mathrm{erf}\left(\alpha \frac{t - t_0}{\sqrt{2}\,\sigma_{\mathrm{skew}}}\right)\right] \exp\left[-\frac{(t - t_0)^2}{2\sigma_{\mathrm{skew}}^2}\right], \tag{6.2}$$

where $\mathrm{erf}(x)$ is the error function, α is the skewness parameter and t_0 is the centre of the peak in the time domain. The parameter σ_{skew} indicates the width of the peak, but is not equal to the 95% bunch length σ_τ. For $\alpha = 0$, Equation 6.2 reduces to a standard Gaussian function with a maximum at $(t = t_0)$.

The fit to the data in Figure 6.8 has a skewness parameter of $\alpha = (4.40 \pm 0.04)$. This measurement is therefore inconsistent with the standard Gaussian distribution that was assumed throughout Section 4.3 of this thesis, with an excess of particles towards the head of each $\bar{\mathrm{p}}$ bunch. The fitted distribution has a 95% bunch length of $\sigma_\tau = (2.31 \pm 0.04)$ μs, corresponding to a physical bunch length of (226 ± 4) mm at the BDS.

Beam Energy [eV]	Bunch length [μs]	Physical length [mm]
Beamline Diagnostics Station		
24	6.7 ± 0.1	450 ± 30
50	2.31 ± 0.04	226 ± 4
70	2.4 ± 0.2	280 ± 20
Lower Diagnostics Station		
24	6.18 ± 0.06	419 ± 4
50	1.66 ± 0.02	162 ± 2

Table 6.3: Measured lengths of antiproton bunches delivered to beamline diagnostics station (BDS) and lower diagnostics station (LDS) with beam energies up to 70 eV.

Clearly, this bunch length is already comparable to the length of the potential that is used to capture $\bar{\mathrm{p}}$ bunches inside the ALPHA-g atom trap (Figure 3.2). Comparing this bunch length to the simulation data shown in Figure 4.9, approximately $\sim 75\%$ of $\bar{\mathrm{p}}$ would be captured from each bunch if this distribution was delivered to the ALPHA-g atom trap.

A number of parameters such as the beam energy were varied in an attempt to reduce the bunch length measured at the BDS. While increasing the beam energy will naturally produce shorter bunches in the time domain, the physical length of each bunch is a function of both its energy and time structure. Equation 3.2 shows that the maximum bunch length that can be captured within a given potential will decrease as the beam energy increases. As a result, increasing the beam energy alone will not necessarily increase the fraction of $\bar{\mathrm{p}}$ that are caught from each bunch within the ALPHA-g experiment. However, reducing the fractional energy spread $\sigma_E/E_{\mathrm{beam}}$ of $\bar{\mathrm{p}}$ bunches extracted from the catching trap will result in shorter bunches irrespective of the beam energy.

Table 6.3 details measurements of the $\bar{\mathrm{p}}$ bunch length that were taken at the BDS for a range of beam energies between 24 and 70 eV.

Clearly, antiprotons that are launched with an energy of $\sim$ 24 eV adopt much longer bunch lengths than those that are launched at higher energies. However, $\bar{\text{p}}$ bunches extracted at an energy of either 50 eV or 70 eV have comparable bunch lengths at the BDS. As a result, the beam energy was primarily selected based on measurements of the transverse dynamics at each energy. Since $\bar{\text{p}}$ bunches launched with an energy of 70 eV were found to adopt a diffuse beam profile in MCP images taken at the BDS, a nominal energy of $\sim$ 50 eV was used throughout the commissioning of the ALPHA-g atom trap.

Finally, a small number of bunch length measurements were taken around the lower diagnostics station (LDS) directly beneath the ALPHA-g atom trap. Table 6.3 details the results of these measurements for beam energies of 24 eV and 50 eV. For both energies, the bunch length measured at the LDS is significantly shorter than the corresponding measurement taken at the BDS.

These measurements contradict the idea that the $\bar{\text{p}}$ bunch length should increase monotonically as antiprotons move along the beamline. Futher evidence for this disagreement can be found by comparing the $\bar{\text{p}}$ energy distribution to direct measurements of the bunch length at different points along the beamline. For example, the measurement in Figure 6.7 indicates that 50 eV antiprotons should have a bunch length of $\sigma_\tau = 7.5$ μs ($\sim$ 740 mm) at the LDS. This is much longer than any of the measurements in Table 6.3. This disagreement suggests that the $\bar{\text{p}}$ bunch length is influenced by additional factors, and not only the initial distribution of particle energies. Detailed simulations of the processes involved in $\bar{\text{p}}$ beam formation are required to fully understand the longitudinal dynamics of antiproton bunches.

Figure 6.9 shows the time structure of a e^+ bunch delivered to the LDS. The experimental data in Figure 6.9 is well modelled by Equation 6.2 with a skewness parameter $\alpha = (8.0 \pm 0.8)$.

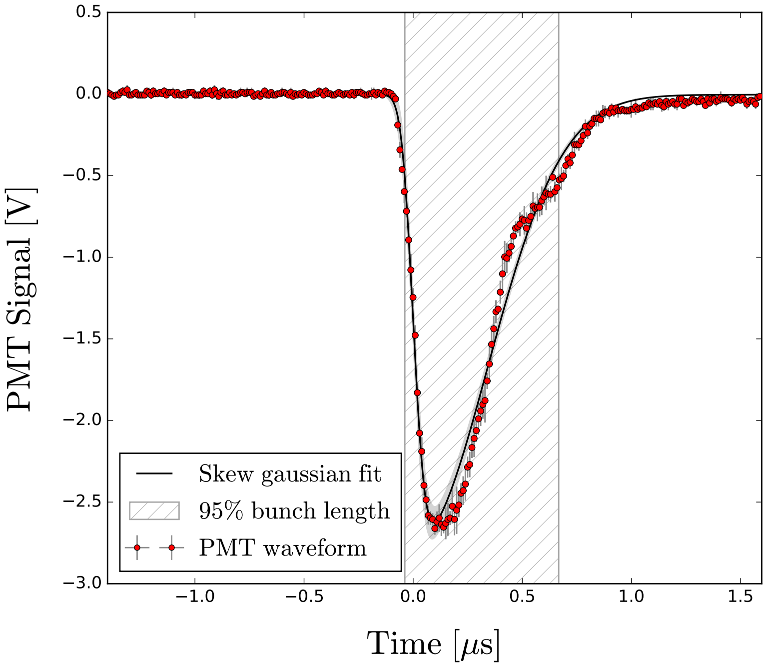

Figure 6.9: Measurement of the e^+ bunch length at the lower diagnostics station (LDS). Equation 6.2 has been fitted to the data, and is shown as a solid black line. The standard deviation of the fit is shown as a shaded region around this line.

When extracted at an energy of 48.1 eV, e^+ bunches have a bunch length of $\sigma_\tau = (0.71 \pm 0.01)$ μs at the LDS. This corresponds to a physical bunch length of (2920 ± 40) mm at the same location. This bunch length is much longer than the electrostatic potential well used to capture $\bar{p}$ bunches inside the ALPHA-g experiment. However, by optimising the shape of this potential well (see Section 7.1.2), more than 10^7 e^+ were eventually captured from each bunch. At the time of writing, there are ongoing efforts to compress e^+ bunches using an electrostatic buncher within the UHV space of the ALPHA-g beamlines.

6.3.3 Antiprotons for ALPHA-g

After successfully steering $\bar{p}$ and e^+ bunches through the beamlines, both species were captured within the Penning trap of the ALPHA-g experiment. Unfortunately, the ALPHA-g atom trap could not be maintained at temperatures below ~ 30 K during the 2018 physics run.

As a result, the experiment initially suffered from poor vacuum, and the superconducting trap magnets could not be operated.

Under these conditions, it was not possible to commission the ALPHA-g experiment using trapped antihydrogen during 2018. However, by catching and holding clouds of antiprotons inside the Penning trap, other critical subsystems such as the Penning trap and TPC detector could be commissioned individually. The following section of this thesis describes how $\bar{\mathrm{p}}$ bunches were captured from the beamlines and used to commission other parts of the ALPHA-g apparatus. As discussed in Section 3.1.3 of this thesis, charged particles are captured in the ALPHA-g atom trap by closing a potential well around an incoming $\bar{\mathrm{p}}$ or e^+ bunch.

In order for any particles to be captured using this method, the time when the potential well is closed (known as the gate time) must be tuned to within $\lesssim 1$ μs. The antiproton gate time was estimated by applying blocking potentials in the ALPHA-g atom trap at different times after $\bar{\mathrm{p}}$ bunches were extracted from the catching trap. In each case, the number of $\bar{\mathrm{p}}$ transmitted through the atom trap was counted using a scintillator panel installed on top of the experiment. For $\bar{\mathrm{p}}$ bunches at an energy of ~ 50 eV, no annihilations were detected when a blocking potential was applied less than ~ 130 μs after the antiprotons were ejected from the catching trap. This is broadly consistent with simulations of the ALPHA-g beamlines, which predict that 50 eV $\bar{\mathrm{p}}$ bunches should arrive within the atom trap after ~ 118 μs.

Once an approximate gate time had been found using this method, a finer scan was conducted for a range of gate times between 128 μs and 135 μs. In each case, the potentials shown in Figure 3.2 were used to catch antiprotons without loading electrons into the ALPHA-g atom trap. Under these conditions, any antiprotons that are captured will quickly escape from confinement or annihilate with background gases within the trap volume.

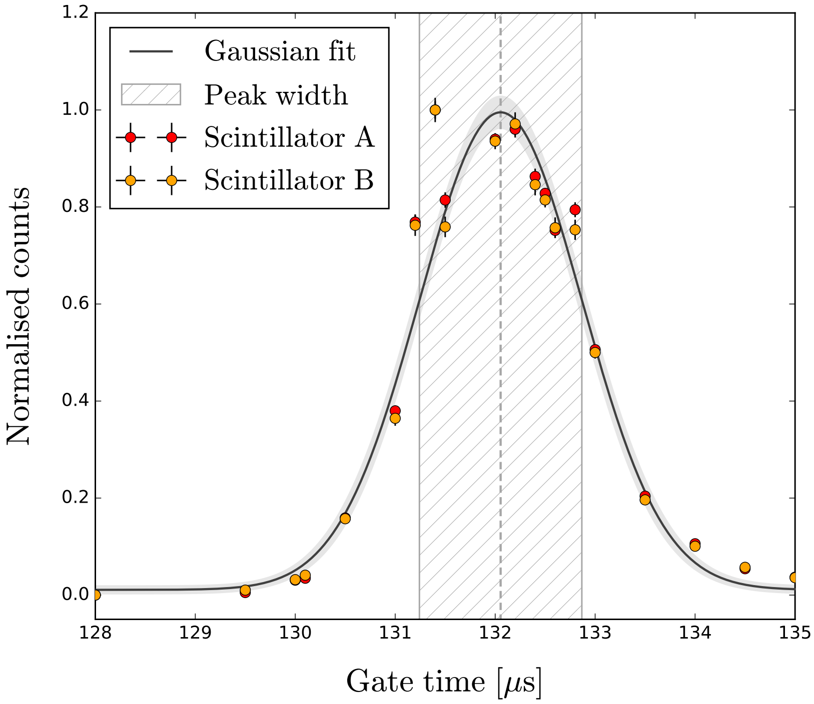

Figure 6.10: Number of annihilations detected within a five second window after $\bar{\mathrm{p}}$ are caught from the ALPHA-g beamlines for a range of gate times between 128 μs and 135 μs. Data is shown for two scintillator panels that were arranged on either side of the ALPHA-g atom trap.

Without electron cooling, the number of annihilations recorded by the TPC was consistent with background within ~ 0.8 seconds after each $\bar{\mathrm{p}}$ bunch was captured.

The gate time can therefore be optimised by counting the number of annihilations within a five second window after $\bar{\mathrm{p}}$ bunches are caught from the ALPHA-g beamlines. The resulting annihilations were counted either using a pair of scintillator panels arranged on either side of the ALPHA-g atom trap, or by counting the number of triggers recorded by the TPC during each window.

Figure 6.10 shows the number of counts recorded by the scintillator panels in each five second window as a function of the $\bar{\mathrm{p}}$ gate time. Each data point represents at least one attempt to catch an incoming $\bar{\mathrm{p}}$ bunch using a fixed gate time. The number of counts for each trial has been normalised to the total number of antiprotons that were originally captured from the AD.

The error bars reflect counting uncertainties estimated based on Poisson statistics.

Originally, the gate time was optimised based on the number of triggers recorded by the TPC within each five second window. However, a retrospective analysis of the detector data showed that the readout rate of the TPC had been saturated, resulting in a flattened curve that does not resemble the data shown in Figure 6.10. The number of TPC triggers for each gate time has not been plotted for clarity.

A number of interesting parameters can be extracted by fitting a Gaussian function to the experimental data in Figure 6.10. Based on the fit shown in Figure 6.10, the optimum gate time was found to be (132.05 ± 0.04) μs. By comparing the width of the fitted peak to the simulations presented in Section 4.3 of this thesis, the final bunch length delivered to the ALPHA-g atom trap can also be estimated. After combining data from both scintillator panels, the fitted width of the peak was found to be (0.81 ± 0.04) μs. This corresponds to a bunch length of approximately (2.4 ± 0.2) μs inside the ALPHA-g atom trap, which is broadly consistent with other measurements that were described earlier in this chapter. For this bunch length, simulations suggest that at least $(78 \pm 3)\%$ of particles are captured from each $\bar{\mathrm{p}}$ bunch. This figure does not account for additional losses that may occur due to magnetic mirroring, or collisions with structures in the UHV space of the beamline.

While a significant fraction of antiprotons could now be captured from each $\bar{\mathrm{p}}$ bunch, the antiproton lifetime within the trap was severely limited without any electron cooling. Electron plasmas were therefore loaded from an electron gun mounted at the LDS, and used to demonstrate the sympathetic cooling of antiprotons within the ALPHA-g atom trap. Typically, around $\sim 2.5 \times 10^7$ electrons were pre-loaded into the atom trap before the arrival of each $\bar{\mathrm{p}}$ bunch.

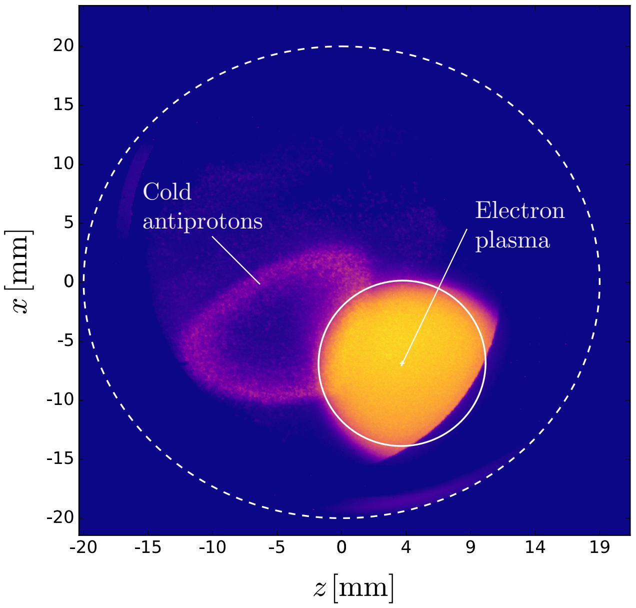

Figure 6.11: MCP image showing cold antiprotons that have radially separated from an electron plasma while held inside the ALPHA-g atom trap for 50 seconds. The centre of the $\bar{\mathrm{p}}$ cloud is displaced from that of the electron plasma when extracted towards the lower diagnostics station (LDS).

The resulting e^- plasma was expanded to a radius of ~ 1.15 mm using the rotating wall technique [90] to maximise the amount of overlap with incoming $\bar{\mathrm{p}}$ bunches. After establishing electron cooling, antiprotons could be held within the ALPHA-g Penning trap for more than 300 seconds with no appreciable drop in the rate of annihilations detected by the TPC.

When cooled into an electron plasma over long timescales, antiprotons will separate centrifugally [142] and move towards the outer radius of the overlapping e^- cloud. In this regime, antiprotons appear as a hollow ring when extracted from the atom trap and imaged onto an MCP. Figure 6.11 shows the distribution of antiprotons that have been cooled in an electron plasma for approximately 50 seconds. Typically, a series of pulsed electric fields would be applied to clear any remaining electrons from the trap volume prior to $\bar{\mathrm{H}}$ synthesis. However, the electron plasma in Figure 6.11 has not yet been cleared from the trap volume, and so both species are visible in the same image.

In Figure 6.11, the electrons and antiprotons are both displaced from the centre of the MCP. This is primarily due to the imperfect alignment of the MCP itself relative to the vertical axis of the ALPHA-g atom trap. However, the antiproton cloud is also displaced from the electron plasma due to misalignments in the magnetic field along the extraction path, and the different imaging characteristics of each species on the MCP [96].

The confinement of antiprotons within the ALPHA-g trap volume allowed for extensive commissioning of the TPC annihilation detector (see Section 1.3.5). Initially, $\bar{\mathrm{p}}$ bunches were captured and held without electron cooling to generate large numbers of annihilations within one region of the TPC. However, cold antiprotons can be held over much longer timescales, and can therefore be moved along the trap axis to generate annihilations at a range of different positions. Moving antiprotons around the trap in this manner allowed the performance of the detector to be characterised as a function of axial position.

Figure 6.12 shows the axial positions of annihilation vertices reconstructed using the TPC detector. During this experiment, a single $\bar{\mathrm{p}}$ cloud was held for 100 seconds in three potential wells centered at different locations along the trap axis. A separate histogram is shown for each 100 second window. Clearly, the axial distribution of the annihilation vertices moves along the trap axis as the $\bar{\mathrm{p}}$ cloud is moved to different locations.

During the final hours of the 2018 physics run, three attempts were made to mix trapped $\bar{\mathrm{p}}$ and e^+ plasmas and produce antihydrogen within the ALPHA-g experiment. However, no evidence was found to suggest that antihydrogen had been produced during any of these attempts. The properties of the $\bar{\mathrm{p}}$ and e^+ plasmas used in these experiments were not optimised due to the limited time that was available for commissioning the ALPHA-g Penning trap.

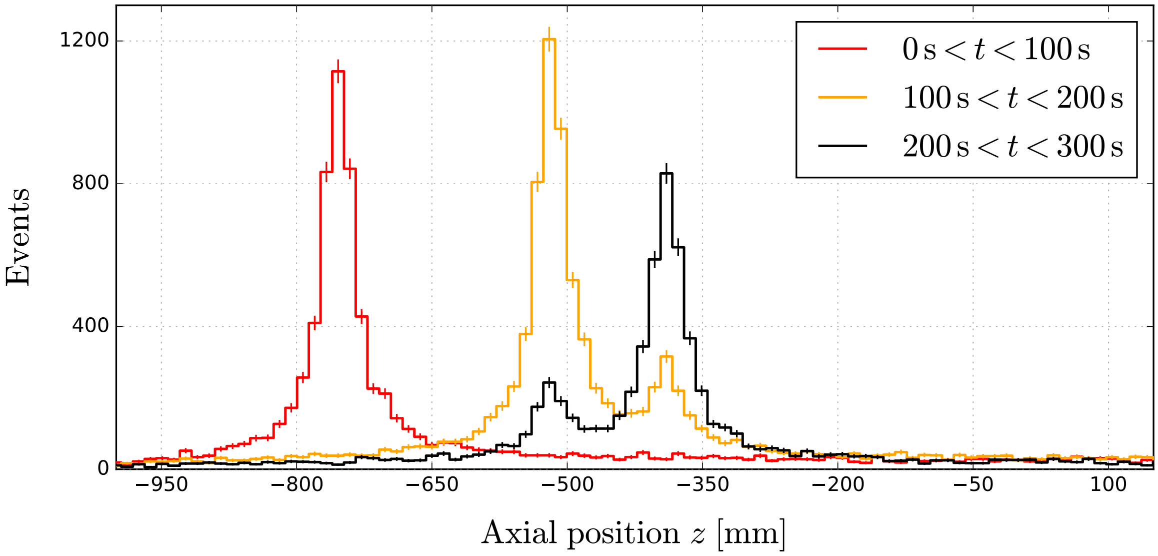

Figure 6.12: Histogram showing the axial positions of annihilation vertices reconstructed using the ALPHA-g TPC while antiprotons where confined within the atom trap. The $\bar{\mathrm{p}}$ cloud was held for 100 seconds at three discrete locations along the trap axis. A separate histogram is shown for each 100 second window.

As a result, neither species of particle was cooled to the cryogenic temperatures that are routinely achieved using the ALPHA-II apparatus. Under these conditions, the cross section for $\bar{\mathrm{H}}$ recombination is extremely small [101].

Ultimately, it was not possible to commission the ALPHA-g experiment using trapped antihydrogen during 2018. However, the results in this chapter show that signficant progress has already been made towards commissioning the beamlines that are the focus of this thesis. We have demonstrated that $\bar{\mathrm{p}}$ and e^+ bunches can efficiently be moved between different areas of the ALPHA apparatus. Furthermore, the properties of both species have been measured at multiple locations throughout the apparatus, indicating good agreement with the simulations in Chapter 4 of this thesis. Charged particles delivered by the beamlines have been used to commission major subsytems of the ALPHA-g experiment, including the Penning traps and TPC detector.

Furthermore, we have shown that charged particles can be held within the atom trap for long timescales, and extracted to nearby diagnostics stations in a controlled manner. In summary, the ALPHA-g beamlines have already met many of their design goals, and will be ready to provide charged particles to the ALPHA-II and ALPHA-g experiments after the CERN accelerator complex resumes operations in 2021.

7 | Future Work and Conclusions

The following chapter presents the conclusions of this thesis, and outlines how the work described within it could be built upon in the future. Section 7.1 explores studies that could be undertaken to improve or expand upon the results of this thesis. Section 7.2 summarises the work presented in this thesis, and gives a short discussion of its wider relevance.

7.1 Future Work

As shown in Chapter 6, significant progress has already been made towards fully commissioning the ALPHA-g beamlines. However, this thesis has highlighted several areas where the operation of the beamlines could still be improved. Section 7.1.1 describes work towards the commissioning of the ALPHA-g beamlines that could not be completed during 2018. In Section 7.1.2, we discuss how the extraction and capture of $\bar{\mathrm{p}}$ and e^+ bunches could be optimised to improve the performance of the ALPHA-g beamlines. Section 7.1.3 describes how the longitundinal dynamics of positrons and antiprotons could be corrected using an electrostatic buncher.

The final parts of this section explore work that goes beyond the original scope of this project. Section 7.1.4 reviews how charged particles could be extracted into a region with no magnetic field, to facilitate new ways of operating the ALPHA experiment. Section 7.1.5 outlines how the improved capabilites of the ELENA decelerator could be exploited by transferring much larger numbers of antiprotons through the ALPHA-g beamlines.

7.1.1 Further Commissioning

In the ALPHA-II experiment, $\bar{p}$ bunches are usually captured within a magnetic field of 3.0 T. This increased magnetic field is achieved by powering a pair of superconducting solenoids, which enclose either end of the ALPHA-II Penning trap. Capturing antiprotons in a stronger magnetic field allows for more efficient electron cooling after each $\bar{p}$ bunch has been captured [56]. During 2018, antiprotons were captured in the ALPHA-g experiment using a magnetic field of 1.0 T, since the atom trap could not be maintained at $\sim$ 4 K for long enough to operate the superconducting trap magnets.

As shown in Chapter 4, antiprotons move non-adiabatically through the ALPHA-g beamlines, and are therefore vulnerable to magnetic mirroring as they move into stronger magnetic fields. Further optimisation of the beamline may therefore be required to capture antiprotons in an increased magnetic field of 3.0 T. However, no antiprotons will be available for commissioning activities until 2021, when the CERN accelerator complex is restarted after a two-year long shutdown.

Over the coming years, a number of alternative tools could be used to optimise the transfer of antiprotons in stronger magnetic fields. For example, the simulation tools described in Chapter 4 can already be used to model small changes in the beamline, such as different magnetic fields within the ALPHA-g experiment itself. In addition, experimental studies using negative hydrogen (H^-) ions could also be used to test different configurations of the ALPHA-g beamlines. Since hydrogen ions have almost exactly the same charge-to-mass ratio as antiprotons, they should have identical dynamics as they propagate through the ALPHA-g beamlines. At the time of writing, there are ongoing efforts to produce dense clouds of H^- ions within the antiproton catching trap for a variety of uses.

7.1.2 Beam Formation and Capture

As shown in Section 6.3, the efficiency of the ALPHA-g beamlines is primarily limited by the longitudinal dynamics of $\bar{\mathrm{p}}$ and e^+ bunches. Based on experimental measurements taken during 2018, at least 20% of antiprotons are lost from each $\bar{\mathrm{p}}$ bunch due to its finite bunch length. The most obvious way to improve the performance of the ALPHA-g beamlines is therefore by optimising the longitudinal dynamics of $\bar{\mathrm{p}}$ and e^+ bunches.

As discussed in Section 3.1.3, the longitudinal dynamics of $\bar{\mathrm{p}}$ bunches are determined immediately after their extraction from the catching trap. Experimental optimisation of the beam formation process is extremely time consuming, since antiprotons are only delivered from the AD every ~ 100 seconds. Ideally, antiproton beam time should be used for antihydrogen physics, rather than improving the performance of the apparatus itself. Instead, numerical simulations can be used to optimise the $\bar{\mathrm{p}}$ beam formation dynamics before making further experimental measurements.

As shown in Section 4.3, particle tracing simulations can be used to model the capture of $\bar{\mathrm{p}}$ bunches using an electrostatic potential. Similar simulations can be used to optimise the extraction of antiprotons from the catching trap. In these calculations, the initial states of the antiprotons must be chosen to represent a real $\bar{\mathrm{p}}$ cloud held inside the catching trap.

In the ALPHA experiment, $\bar{\mathrm{p}}$ clouds are cooled sympathetically by allowing them to equilibrate with a much denser electron plasma. These plasmas have considerable self fields that dictate the spatial distribution of both electrons and antiprotons. The distribution of charge within a non-neutral plasma is related to the electric potential by the Poisson-Boltzmann equation (Equations 2.28 and 2.29). Generally, solving this equation for charged particles in an arbitrary potential well is non-trivial.

However, numerical tools have already been developed by members of the ALPHA collaboration for this purpose. For example, a waterbag plasma solver [143] is used to iteratively calculate the self potential of low temperature plasmas by treating them as a smooth distribution of charge.

Before antiprotons are extracted from the catching trap, electrons are cleared from the trap volume using a series of pulsed electric fields. This process is known to heat the remaining antiprotons, and may leave them with a non-equilibrium distribution of positions and velocities. Fast processes cannot be modelled using the Poisson-Boltzmann equation, which is only valid for equilibrium non-neutral plasmas. Instead, Particle in Cell (PIC) simulations [124] could be used to model how these electric fields modify the distribution of antiprotons in a self-consistent manner.

After estimating the initial state of the $\bar{\mathrm{p}}$ cloud, electrostatic simulations can be used to model its extraction from the catching trap. In the absence of electrons, the space charge of the $\bar{\mathrm{p}}$ cloud can be neglected for the reasons outlined in Section 4.1.2 of this thesis. This approximation reduces the computational requirements of each simulation, so that many iterations of the extraction potentials can be tested in succession. New techniques for extracting $\bar{\mathrm{p}}$ bunches can be evaluated by comparing how particles are distributed within the longitudinal (δt, $\delta E_{\parallel}$) phase space.

Simulations can also be used to optimise how $\bar{\mathrm{p}}$ and e^+ bunches are captured within the ALPHA-g Penning trap. In Section 3.1.3, a simple model was used to estimate the maximum bunch length that can be captured using an electrostatic potential well. This estimate assumes that $\bar{\mathrm{p}}$ and e^+ bunches move along the length of the catching potential at a fixed velocity. In reality, the potentials used to capture charged particles can be modified to accept much longer bunch lengths. For example, Figure 7.1 shows the electrostatic potential used to capture e^+ bunches within the ALPHA-II experiment during 2018.

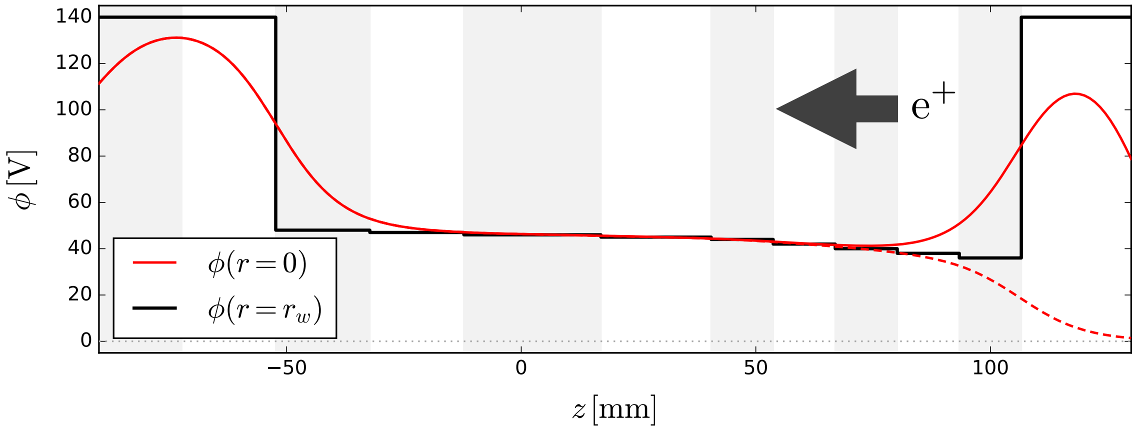

Figure 7.1: Electric potential used to capture e^+ bunches in the ALPHA-II experiment during 2018. The dashed (smooth) red line shows the potential immediately before (after) positrons have been captured. The final potential well is shifted by $\sim$ 45 V in order to minimise the velocities of incoming positrons.

The entire potential has been shifted by an offset of $\sim$ 45 V, with a slight gradient in $\phi(z)$ along the length of the trap. Within this potential, the kinetic energy of each positron is reduced to a few electron volts as it moves along the beamline. Incoming e^+ bunches therefore spend much longer within the Penning trap, allowing more positrons to be collected from each bunch. In effect, this decreases the beam energy $E_\parallel$ in Equation 3.2, so that longer e^+ bunches can be captured more efficiently. Similar strategies can be used to maximise the number of antiprotons caught within the ALPHA-g experiment.

7.1.3 Positron and Antiproton Bunching

Even after optimising their longitudinal dynamics, $\bar{p}$ and e^+ bunches delivered to the ALPHA-g experiment may still be too long to be captured efficiently. In this regime, it is important to develop techniques that allow charged particles to be bunched as they propagate along the beamline.

In general, the particles in a $\bar{p}$ or e^+ bunch will separate longitudinally according to their kinetic energy along the direction of the beamline.

Bunching can be achieved by manipulating the longitudinal phase space, so that particles towards the head of each bunch are slowed down, while those in the tail are accelerated along the beamline. After applying this manipulation, the bunch length σ_τ will decrease until it reaches a minimum (focal point) further along the beamline. Among other factors, this focal length will depend on the initial energy spread, bunch length, and space charge of each e^+ bunch.

One way to achieve bunching at low energies is to apply a time-dependent sinusoidal electric potential to one or more electrodes along the beam path [122]. The frequency and phase of the potential are set so that particles around the centre of each bunch will experience no net change of energy as they pass through the electrodes. However, particles that are displaced from the centre will either gain or lose kinetic energy depending on their initial longitudinal position. The frequency of the bunching potential is determined by the time taken for the reference particle to pass through the electrodes. For the typical parameters of e^+ bunches in the ALPHA experiment, the bunching potentials is in the very low radiofrequency band.

In the ALPHA-g beamlines, an electrode stack has already been installed to compress e^+ bunches extracted from the positron accumulator. This buncher incorporates 26 cylindrical electrodes, each with a length of $\sim$19.4 mm and an inner diameter of 41 mm. Although there is currently no dedicated buncher installed for antiprotons, the techniques described above are equally applicable to $\bar{\text{p}}$ bunches.

At the time of writing, there are ongoing efforts to compress e^+ bunches extracted from the positron accumulator. In each attempt, positrons are extracted from the accumulator with a fixed energy distribution, and a time-dependent electric potential is applied to the buncher electrodes. Based on simple scaling laws, we expect to observe bunching if the applied potential has a frequency of $\sim$ 8.3 MHz and an amplitude of $\sim$ 6 V.

For each choice of parameters, the resulting bunch length can be measured using the techniques described in Section 6.3.2 of this thesis.

7.1.4 Field Extraction and Reversal

The final two parts of this section outline work that expands beyond the original scope of this project, and envisages the future development of the ALPHA experiment. Here, we discuss the extraction of $\bar{\mathrm{p}}$ and e^+ bunches into a region with no residual magnetic field.

As shown in Chapter 2, charged particles will follow the direction of a slowly-varying magnetic field as they undergo cyclotron motion in the transverse plane. The ALPHA-g beamlines exploit this behaviour by transporting charged particles along the magnetic field lines between two separate particle traps. In regions where the strength of the magnetic field decreases to zero, the envelope of a passing beam will become divergent according to Equation 2.32. For this reason, the direction of the magnetic field cannot be reversed at any point along the ALPHA-g beamlines.

During 2018, the magnetic fields of the catching trap and ALPHA-II experiment were inverted, so that both $\bar{\mathrm{p}}$ and e^+ could be transported into the ALPHA-g experiment. In this configuration, the magnetic field of the ALPHA-II atom trap has the opposite polarity to that of the positron accumulator. It is therefore not possible to transfer positrons into the ALPHA-II atom trap during operation of the ALPHA-g experiment. In order to conduct antihydrogen physics with both experiments simultaneously, e^+ bunches must pass through a region with zero magnetic field before entering the ALPHA-II atom trap.

A number of authors have already demonstrated the extraction of magnetically-guided positron beams into regions with no axial magnetic field [113–115].

In general, the extraction of e^+ bunches into zero magnetic field is achieved by creating a small region where γ is extremely large. In this region, individual positrons will no longer follow the direction of the magnetic field, and can be extracted non-adiabatically without the beam envelope becoming divergent. Similar techniques could be used to transport $\bar{p}$ and e^+ bunches through an area of the beamline where the direction of the magnetic field is suddenly reversed.

The ALPHA-g beamlines already include several regions where a sudden reversal of the magnetic field could be possible. For example, the beamline diagnostics station (BDS) incorporates two magnets (AGBL03) that could be operated as anti-Helmholtz coils. In this configuration, the direction of the magnetic field would be reversed in less than $\sim$ 26 cm, producing a considerable field gradient across the extraction region. Furthermore, voltages of up to $\sim$ 5 kV can be applied to an electrode mounted at the BDS in order to use it as an Einzel lens. This electrode would provide electrostatic focusing for e^+ bunches as they pass through the minimum in the magnetic field [117].

Due to the complex electromagnetic fields experienced by charged particles in this scheme, numerical simulations are required to assess its viablity. In preliminary simulations using a similar geometry, it was shown that 50 eV $\bar{p}$ bunches could be transmitted through the zero-field region without colliding with structures in the UHV space of the beamline. Further simulations are required to assess whether this scheme is viable for positrons, and to fully understand the complex beam dynamics that are likely to be involved.

In the longer term, there are compelling motivations to extract $\bar{p}$ and e^+ bunches into a region with no residual magnetic field. As discussed in Section 1.2.3, many transitions in the spectrum of atomic hydrogen are dramatically shifted by strong magnetic fields.

Recent measurements of the ground state hyperfine splitting in trapped $\bar{\mathrm{H}}$ have been limited by uncertainties in the magnetic field of the neutral atom trap [4]. In addition, even small magnetic field errors within the ALPHA-g experiment will result in large systematic uncertainties for gravitational measurements using trapped antihydrogen. The most obvious way to eliminate these uncertainties is to study antihydrogen atoms in an environment with no residual magnetic field.

By extracting charged particles into a zero-field region, it may be possible to produce and trap $\bar{\mathrm{H}}$ using a geometry that does not employ strong magnetic fields. For example, $\bar{\mathrm{p}}$ and e^+ plasmas could be captured and mixed using devices such as Paul traps [144], which do not require a magnetic field for charged particle confinement.

7.1.5 ELENA Integration

From 2021, $\bar{\mathrm{p}}$ bunches will be delivered to the AD experiments at a lower energy of 100 keV after circulating within the ELENA decelerator [44]. After hardware upgrades to the antiproton catching trap, it may be possible to capture up to $\sim 10^7$ from each pulse of antiprotons delivered by the AD. However, the ALPHA experiment has not yet been optimised to produce antihydrogen using such large numbers of antiprotons. We therefore anticipate that the ALPHA experiment will not be positioned to fully exploit the capabilites of the ELENA decelerator right away. Over the coming years, each part of the ALPHA apparatus should be optimised to handle much denser antiproton plasmas.

The transport of up to 10^7 $\bar{\mathrm{p}}$ in a single pulse is likely to pose significant challenges for the ALPHA-g beamlines. With such large numbers of antiprotons, space charge effects will have a much stronger influence on the dynamics of each $\bar{\mathrm{p}}$ bunch. As a result, existing models of the beamlines will need to be adapted to account for space charge effects.

As discussed in Section 3.3, p̄ bunches already have complex beam dynamics within the ALPHA-g beamlines. These dynamics will only become more complicated as the space charge of each antiproton bunch is increased. For instance, it is unclear how the self fields of dense p̄ bunches will modify the curvature drifts that they experience within the interconnect.

A variety of approaches can be used to optimise the ALPHA-g beamlines for much larger numbers of antiprotons. Initially, more advanced simulations of the beamlines could be used to investigate how the increased self fields of p̄ bunches will modify their beam dynamics. These simulations will require accurate modelling of space charge effects, and are likely to be much more computationally intensive. In addition, the development of a H^- ion source for the ALPHA experiment would allow the dynamics of intense p̄ beams to be investigated experimentally. As mentioned previously, hydrogen ions launched from the catching trap would serve as a useful analogue for real p̄ bunches.

7.2 Conclusions

The aims of this thesis were as follows:

- To develop and characterise a beamline design for the ALPHA experiment
- To translate this design into a full set of electromechanical specifications for the implementation of the beamline
- To assemble a suitable control system for the beamlines
- To install and commission the ALPHA-g beamlines at CERN during 2018.

The work presented in this thesis has been successful in meeting each of these goals. As shown in Chapter 6, the beamlines that were installed at CERN have already met all of their design requirements.

The following section reviews the work presented in this thesis. Section 7.2.1 summarises the conclusions of each chapter, while Section 7.2.2 discusses the wider context and relevance of this work.

7.2.1 Summary of Presented Work

Chapter 1 of this thesis outlined the main motivations for studying antimatter. Since its prediction and discovery almost a century ago, the absence of antimatter in our universe has raised challenging questions for fundamental physics. In recent years, experimental studies of antimatter have focused on searching for new sources of CP violation in high-energy phenomena. However, precision measurements of trapped antimatter can also provide unique, stringent tests of fundamental symmetries. The ALPHA collaboration has recently succeeded in making the first spectroscopic measurements of trapped antihydrogen atoms, and now aims to measure the gravitational acceleration of antihydrogen using the ALPHA-g experiment. The second half of Chapter 1 reviewed the experimental methods that are used to produce trapped $\bar{\mathrm{H}}$ using the ALPHA experiment, and discussed the role of charged particle beamlines in recent upgrades to the apparatus.

A range of analytical and numerical methods have been developed to study the motions of $\bar{\mathrm{p}}$ and e^+ bunches through the ALPHA-g beamlines. In Chapter 2, we reviewed approximations that can be used to estimate the paths of charged particles in simple electromagnetic fields. Throughout this thesis, the guiding centre approximations were used extensively to model the motions of positrons and antiprotons in the ALPHA experiment. In addition, figures of merit were derived to identify regions where these approximations are likely to break down. We have reviewed the dynamics of non-neutral plasmas in Penning-Malmberg traps, to determine the properties of pulsed $\bar{\mathrm{p}}$ and e^+ beams extracted from these devices. In the final section of Chapter 2, we considered numerical methods that can be used to solve the equations of motion for charged particles in complex electromagnetic fields.

Chapter 3 reviewed the design of the ALPHA-g beamlines. The ALPHA experiment provides a challenging enviroment for the operation of charged particle beamlines. For example, $\bar{\mathrm{p}}$ and e^+ bunches can only be extracted from Penning-Malmberg traps with beam energies of $\lesssim 100$ eV. As a result, both species are strongly affected by the residual magnetic fields that permeate the ALPHA experiment. In the first half of Chapter 3, we reviewed the design requirements for the ALPHA-g beamlines, and showed that common beam transport schemes are unsuitable to meet many of these requirements.

The latter half of Chapter 3 described the different beamline elements that are used to guide $\bar{\mathrm{p}}$ and e^+ bunches through the ALPHA apparatus. Throughout this chapter, the approximations derived in Chapter 2 were used to evaluate and optimise the performance of each element. Particular attention was given to the interconnect magnet, which is used to steer $\bar{\mathrm{p}}$ and e^+ bunches through a complex superposition of magnetic fields.

Throughout this thesis, numerical simulations were used extensively to model the paths of charged particles through the ALPHA-g beamlines. In Chapter 4, particle tracing simulations were developed to calculate the motions of $\bar{\mathrm{p}}$ and e^+ bunches through an arbitrary magnetic field. These tools were used to validate simple analytical models of the ALPHA-g beamlines, and to accurately trace charged particles through complex beamline elements such as the interconnect. In this chapter, it was shown that the motions of antiprotons through the beamline are highly non-adiabatic, potentially resulting in particle losses due to magnetic mirroring. The final part of Chapter 4 described simulations of how $\bar{\mathrm{p}}$ bunches can be captured within the ALPHA-g Penning trap. These calculations show how different parameters can be tuned to increase the number of antiprotons captured from each $\bar{\mathrm{p}}$ bunch.

Chapter 5 described the implementation of the final beamline design at CERN during 2018. The electromechanical properties of each beamline magnet were measured, and shown to be consistent with their original design specifications. In the second half of Chapter 5, we reviewed the control system that was used to manage the ALPHA-g beamlines. We showed that this control system achieves a high level of stability, ensuring that $\bar{\mathrm{p}}$ and e^+ bunches can be transported through the beamline in an accurate and reproducible manner.

After their installation, the ALPHA-g beamlines were commissioned quickly and used to operate both of the ALPHA antihydrogen mixing traps. In Chapter 6, we presented an analysis of experimental data that was collected during the commissioning of the new beamline. We described how a temporary installation of the beamline was initially used to transport e^+ bunches into the ALPHA-II experiment, facilitating a short period of $\bar{\mathrm{H}}$ physics. A range of diagnostic tools were developed, and used to characterise the transverse and longitudinal dynamics of $\bar{\mathrm{p}}$ and e^+ bunches. During the final weeks of the 2018 AD physics run, the full beamline was successfully used to transfer $\bar{\mathrm{p}}$ and e^+ bunches into the ALPHA-g experiment. In the final part of Chapter 6, we showed that the ALPHA-g beamlines were instrumental to the initial commissioning of the new experiment. Antiprotons delivered by the beamlines were used to commission a range of critical systems, such as charged particle traps and annihilation detectors.

Finally, in Chapter 7, we identified a number of areas where the performance of the ALPHA-g beamlines could already be improved. Future work is likely to focus on optimising the longitudinal dynamics of $\bar{\mathrm{p}}$ and e^+ bunches. We have described how simulations could be used to improve the extraction and capture of charged particle beams, and reviewed experimental techniques for the bunching of positrons and antiprotons.

In addition, we have briefly discussed how charged particles could be extracted from a strong magnetic field into a region with no magnetic field at all. The development of these techniques will be critical to the future operation of the ALPHA experiment, and further precision measurements using trapped $\bar{\mathrm{H}}$.

7.2.2 Final Remarks

As stated previously, the work presented in this thesis was instrumental to the operation of the ALPHA experiment during 2018. As shown in Table 6.1, the beamlines were commissioned extremely quickly, maximising the amount of time that was available to work with other parts of the apparatus. This rapid commissioning can be attributed in large part to detailed simulations of the beamline that were carried out over the course of this PhD project.

Throughout this thesis, we have used simple analytical models as well as extensive numerical simulations to develop a comprehensive design for the ALPHA-g beamlines. This approach allows a great deal of physical insight into the beamline design, as well as facilitating detailed optimisation of its performance. By comparing experimental measurements to both models of the beamlines, we have highlighted the merits and limitations of both approaches. The methods that were used to develop the ALPHA-g beamlines could serve as a guide to future efforts of a similar nature.

As well as commissioning the ALPHA-g experiment, the new beamlines were used to facilitate a short period of $\bar{\mathrm{H}}$ physics with the ALPHA-II experiment. Despite lasting for less than three weeks, this period was highly productive, and has yielded a number of exciting physics measurements. Many of these results are expected to be published over the coming months.

Many experiments at the AD have already developed efficient beamlines to transport low energy $\bar{\mathrm{p}}$ and positron bunches around their apparatus [32, 145].

However, the beamlines described in this thesis use a relatively simple design, which likely contributed to their rapid commissioning and straightforward operation during 2018. Unusually, the ALPHA-g beamlines are able to transport both positrons and antiprotons in multiple directions without any significant changes to the setup of the apparatus. As a result, the design of the ALPHA-g beamlines may be relevant to future experiments based at the AD or other similar facilities.

The work presented in this thesis may have further applications for experiments using trapped ions [146–148] or positron plasmas [94]. In many of these experiments, charged particles must be transported between separate traps with strong magnetic fields. Particularly in smaller experiments, stray magnetic fields can cause significant disruption to particle transport between different areas of the apparatus. However, many of the beamline elements developed in this thesis could easily be adapted for use on other experiments. For example, the interconnect magnet can be used to guide low energy ($\lesssim 100$ eV) beams of ions or electrons around a small radius of curvature, even in the presence of considerable stray magnetic fields.

In summary, the work presented in this thesis was successful in designing and commissioning new beamlines for the ALPHA-g experiment. Over the coming years, it is hoped that these beamlines will play a significant role in making the first direct measurements of antihydrogen's gravitational acceleration. In parallel, future upgrades to the ALPHA apparatus should allow for ever more precise measurements of the $\bar{\mathrm{H}}$ spectrum. At the time of writing, the question of why antimatter is so scarce in our universe remains largely unanswered. However, a wide range of experiments are now probing the properties of different antimatter species in unprecedented detail. I hope that the work presented in this thesis can play even a small part in the future of this exciting field.

A | Particle Sources

Parameter	**Antiprotons** ($\bar{\mathrm{p}}$)	**Positrons** (e^+)	**Units**
Source Trap	Catching trap	Accumulator	
Magnetic Field B_z	3.0	0.15	T
Plasma radius $\sigma_\perp$	0.4	1.0	mm
Plasma length σ_z	4.0	150	mm
Cyclotron frequency ω_c	2.9×10^8	2.6×10^{10}	s^{-1}
Temperature T	350	1000	K
Larmor Radius r_L	8.37	6.61	μm
Beam Energy $E_\parallel$	50	50	eV
Magnetization Γ	235	3140	mm · mrad
Emittance $\varepsilon_\perp$	12.0	50.8	mm · mrad

Table A.1: Initial properties of typical $\bar{\mathrm{p}}$ and e^+ bunches extracted from the antiproton catching trap and positron accumulator, respectively. The variables listed in the left-hand column are defined throughout Chapter 2 of this thesis.

B | Beamline Power Supplies

Identifier	**Resistance [Ω]**	**Power Supply**		
		Model	Current [A]	Voltage [V]
Beamline Modules				
AGBL01-1	11.8	SM 330-AR-22	22	330
AGBL01-2	6.46	SM 120-13	13	120
AGL02	6.63	SM 330-AR-22	22	330
Diagnostics Stations				
AGBL03	2.32	SM 70-22	22	70
Interconnect				
AGBL04	2.25	SM 70-22	22	70
AGBL05	2.97	SM 70-22	22	70
AGBL06	2.45	SM 70-22	22	70
AGBL07-1	1.84	SM 52-AR-60	60	52
AGBL07-2	2.22	SM 52-AR-60	60	52
Transfer Coils				
AGBL08	14.5	SM 330-20	20	330

Table B.1: Maximum current and voltage specifications for the Delta Elektronika power supplies that were used to power the ALPHA-g beamline magnets [132]. The resistance of each magnet is given for comparison. Detailed descriptions of the beamline magnets can be found in Chapters 3 and 5 of this thesis. Some power supplies are limited by an autoranging (AR) function and cannot operate at their full current and voltage simultaneously.

Bibliography

[1] Ahmadi, M. *et al.* Observation of the 1S–2P Lyman-alpha Transition in Antihydrogen. *Nature* **561**, 211–215 (2018).

[2] Ahmadi, M. *et al.* Characterization of the 1S–2S Transition in Antihydrogen. *Nature* **557**, 71–75 (2018).

[3] Ahmadi, M. *et al.* Observation of the 1S-2S Transition in Trapped Antihydrogen. *Nature* **541**, 506–510 (2016).

[4] Ahmadi, M. *et al.* Observation of the Hyperfine Spectrum of Antihydrogen. *Nature* **548**, 66–69 (2017).

[5] Ahmadi, M. *et al.* Antihydrogen Accumulation for Fundamental Symmetry Tests. *Nature Commun.* **8**, 681 (2017).

[6] Ahmadi, M. *et al.* Enhanced Control and Reproducibility of Non-Neutral Plasmas. *Phys. Rev. Lett.* **120**, 025001 (2018).

[7] Dirac, P. A. M. The Quantum Theory of the Electron. *Proceedings of the Royal Society of London Series A* **117**, 610–624 (1928).

[8] Dirac, P. A. M. A Theory of Electrons and Protons. *Proc. Roy. Soc. Lond.* **A126**, 360–365 (1930).

[9] Weyl, H. Gravitation and the Electron. *Proceedings of the National Academy of Science* **15**, 323–334 (1929).

[10] Dirac, P. A. M. Quantised Singularities in the Electromagnetic Field. *Proc. Roy. Soc. Lond.* **A133**, 60–72 (1931).

[11] Anderson, C. D. The Apparent Existence of Easily Deflectable Positives. *Science* **76**, 238–239 (1932).

[12] Anderson, C. D. The Positive Electron. *Phys. Rev.* **43**, 491–494 (1933).

[13] Chamberlain, O., Segre, E., Wiegand, C. & Ypsilantis, T. Observation of Antiprotons. *Phys. Rev.* **100**, 947–950 (1955).

[14] Cork, B., Lambertson, G. R., Piccioni, O. & Wenzel, W. A. Anti-neutrons Produced from Anti-protons in Charge Exchange Collisions. *Phys. Rev.* **104**, 1193–1197 (1957).

[15] Canetti, L., Drewes, M. & Shaposhnikov, M. Matter and Antimatter in the Universe. *New J. Phys.* **14**, 095012 (2012).

[16] Friedmann, A. Über die Krümmung des Raumes. *Zeitschrift fur Physik* **10**, 377–386 (1922).

[17] Friedmann, A. Über die Möglichkeit Einer Welt mit Konstanter Negativer Krümmung des Raumes. *Zeitschrift fur Physik* **21**, 326–332 (1924).

[18] Lemaître, G. Un Univers Homogène de Masse Constante et de Rayon Croissant Rendant Compte de la Vitesse Radiale des Nébuleuses Extra-galactiques. *Annales de la Société Scientifique de Bruxelles* **47**, 49–59 (1927).

[19] Hubble, E. A Relation between Distance and Radial Velocity among Extra-Galactic Nebulae. *Proceedings of the National Academy of Science* **15**, 168–173 (1929).

[20] Aghanim, N. *et al.* Planck 2015 Results. XI. CMB Power Spectra, Likelihoods, and Robustness of Parameters. *Astron. Astrophys.* **594**, A11 (2016).

[21] Fields, B. D., Molaro, P. & Sarkar, S. Big-Bang Nucleosynthesis. *Chin. Phys.* **C38**, 339–344 (2014).

[22] Cyburt, R. H., Fields, B. D., Olive, K. A. & Yeh, T. H. Big Bang Nucleosynthesis: Present Status. *Reviews of Modern Physics* **88**, 015004 (2016).

[23] Sakharov, A. D. Violation of CP Invariance, C Asymmetry, and Baryon Asymmetry of the Universe. *Pisma Zh. Eksp. Teor. Fiz.* **5**, 32–35 (1967).

[24] Wu, C. S., Ambler, E., Hayward, R. W., Hoppes, D. D. & Hudson, R. P. Experimental Test of Parity Conservation in Beta Decay. *Phys. Rev.* **105**, 1413–1414 (1957).

[25] Christenson, J. H., Cronin, J. W., Fitch, V. L. & Turlay, R. Evidence for the 2π Decay of the K_2^0 Meson. *Phys. Rev. Lett.* **13**, 138–140 (1964).

[26] Tanabashi, M. *et al.* Review of Particle Physics. *Phys. Rev.* **D98**, 030001 (2018).

[27] Greenberg, O. W. Why is CPT Fundamental? *Found. Phys.* **36**, 1535–1553 (2006).

[28] Aaij, R. *et al.* Precision Measurement of CP Violation in $B_S^0 \to J/\Psi K^+K^-$ Decays. *Phys. Rev. Lett.* **114**, 041801 (2015).

[29] Aaij, R. *et al.* Measurement of CP Observables in $B^\pm \to D^{(*)}K^\pm$ and $B^\pm \to D^{(*)}\pi^\pm$ Decays. *Phys. Lett.* **B777**, 16–30 (2018).

[30] Aaij, R. *et al.* Measurement of CP Asymmetry in $B_s^0 \to D_s^\mp K^\pm$ Decays. *JHEP* **03**, 059 (2018).

[31] Abe, K. *et al.* Search for CP Violation in Neutrino and Antineutrino Oscillations by the T2K Experiment with 2.2×10^{21} Protons on Target. *Phys. Rev. Lett.* **121**, 171802 (2018).

[32] Hori, M. & Walz, J. Physics at CERN's Antiproton Decelerator. *Prog. Part. Nucl. Phys.* **72**, 206–253 (2013).

[33] Hajdukovic, D. S. Do We Live in the Universe Successively Dominated by Matter and Antimatter? *Astrophysics and Space Science* **334**, 219–223 (2011).

[34] Benoit-Lévy, A. & Chardin, G. Introducing the Dirac-Milne Universe. *Astronomy and Astrophysics* **537**, A78 (2012).

[35] Liddle, A. *An Introduction to Modern Cosmology (2nd Edition)* (Wiley, Chichester, UK, 2003).

[36] Riess, A. G. *et al.* Observational Evidence from Supernovae for an Accelerating Universe and a Cosmological Constant. *Astron. J.* **116**, 1009–1038 (1998).

[37] Frieman, J., Turner, M. & Huterer, D. Dark Energy and the Accelerating Universe. *Ann. Rev. Astron. Astrophys.* **46**, 385–432 (2008).

[38] Adelberger, E. G., Heckel, B. R., Stubbs, C. W. & Su, Y. Does Antimatter Fall with the Same Acceleration as Ordinary Matter? *Physical Review Letters* **66**, 850–853 (1991).

[39] Amole, C. *et al.* Description and First Application of a New Technique to Measure the Gravitational Mass of Antihydrogen. *Nature Commun.* **4**, 1785 (2013).

[40] Zhmoginov, A. I., Charman, A. E., Fajans, J. & Wurtele, J. S. Nonlinear Dynamics of Antihydrogen in Magnetostatic Traps: Implications for Gravitational Measurements. *Class. Quant. Grav.* **30**, 205014 (2013).

[41] Gabrielse, G. *et al.* First Capture of Antiprotons in a Penning Trap: A Kiloelectronvolt Source. *Phys. Rev. Lett.* **57**, 2504–2507 (1986).

[42] Gabrielse, G. *et al.* Cooling and Slowing of Trapped Antiprotons Below 100 meV. *Phys. Rev. Lett.* **63**, 1360–1363 (1989).

[43] Bylinsky, Y., Lombardi, A. M. & Pirkl, W. RFQD: A 'Decelerating' Radio Frequency Quadrupole for the CERN Antiproton Facility. *eConf* **C000821**, TUD05 (2000).

[44] Chohan, V. *et al. Extra Low ENergy Antiproton (ELENA) Ring and its Transfer Lines: Design Report* (2014).

[45] Colladay, D. & Kostelecky, V. A. Lorentz Violating Extension of the Standard Model. *Phys. Rev.* **D58**, 116002 (1998).

[46] Parthey, C. G. *et al.* Improved Measurement of the Hydrogen 1S - 2S Transition Frequency. *Phys. Rev. Lett.* **107**, 203001 (2011).

[47] Matveev, A. *et al.* Precision Measurement of the Hydrogen 1S - 2S Frequency via a 920-km Fiber Link. *Phys. Rev. Lett.* **110**, 230801 (2013).

[48] Perez, P. *et al.* The GBAR Antimatter Gravity Experiment. *Hyperfine Interact.* **233**, 21–27 (2015).

[49] Scampoli, P. & Storey, J. The AEgIS Experiment at CERN for the Measurement of Antihydrogen Gravity Acceleration. *Mod. Phys. Lett.* **A29**, 1430017 (2014).

[50] Baur, G. *et al.* Production of Antihydrogen. *Physics Letters B* **368**, 251–258 (1996).

[51] Blanford, G. *et al.* Observation of Atomic Antihydrogen. *Phys. Rev. Lett.* **80**, 3037–3040 (1998).

[52] Amoretti, M. *et al.* Production and Detection of Cold Antihydrogen Atoms. *Nature* **419**, 456–459 (2002).

[53] Amoretti, M. *et al.* The ATHENA Antihydrogen Apparatus. *Nucl. Instrum. Meth.* **A518**, 679–711 (2004).

[54] Gabrielse, G. *et al.* Background-Free Observation of Cold Antihydrogen with Field-Ionization Analysis of Its States. *Phys. Rev. Lett.* **89**, 213401 (2002).

[55] van der Werf, D. P. *et al.* The ATHENA Positron Accumulator. *Appl. Surf. Sci.* **194**, 312–316 (2002).

[56] Amole, C. *et al.* The ALPHA Antihydrogen Trapping Apparatus. *Nucl. Instrum. Meth.* **A735**, 319–340 (2014).

[57] Andresen, G. B. *et al.* Search For Trapped Antihydrogen. *Phys. Lett.* **B695**, 95–104 (2011).

[58] Gabrielse, G. *et al.* Trapped Antihydrogen in Its Ground State. *Phys. Rev. Lett.* **108**, 113002 (2012).

[59] Andresen, G. B. *et al.* Confinement of Antihydrogen for 1000 Seconds. *Nature Phys.* **7**, 558–564 (2011).

[60] Topçu, T. & Robicheaux, F. Radiative Cascade of Highly Excited Hydrogen Atoms in Strong Magnetic Fields. *Phys. Rev. A* **73**, 043405 (2006).

[61] Amole, C. *et al.* An Experimental Limit on the Charge of Antihydrogen. *Nature Commun.* **5**, 3955 (2014).

[62] Ahmadi, M. *et al.* An Improved Limit on the Charge of Antihydrogen from Stochastic Acceleration. *Nature* **529**, 373–376 (2016).

[63] Gabrielse, G. *et al.* Antihydrogen Production within a Penning-Ioffe Trap. *Phys. Rev. Lett.* **100**, 113001 (2008).

[64] Juhász, B. & Widmann, E. Planned Measurement of the Ground-state Hyperfine Splitting of Antihydrogen. *Hyperfine Interact.* **193**, 305–311 (2009).

[65] Diermaier, M. *et al.* In-beam Measurement of the Hydrogen Hyperfine Splitting and Prospects for Antihydrogen Spectroscopy. *Nature Commun.* **8**, 5749 (2017).

[66] Enomoto, Y. *et al.* Synthesis of Cold Antihydrogen in a Cusp Trap. *Phys. Rev. Lett.* **105**, 243401 (2010).

[67] Kuroda, N. *et al.* A Source of Antihydrogen for In-flight Hyperfine Spectroscopy. *Nature Commun.* **5**, 3089–3092 (2014).

[68] Aghion, S. *et al.* A moiré Deflectometer for Antimatter. *Nature Commun.* **5**, 4538 (2014).

[69] Aghion, S. *et al.* Prospects for Measuring the Gravitational Free-fall of Antihydrogen with Emulsion Detectors. *JINST* **8**, P08013 (2013).

[70] Walz, J. & Hansch, T. W. A Proposal to Measure Antimatter Gravity Using Ultracold Antihydrogen Atoms. *Gen. Rel. Grav.* **36**, 561–570 (2004).

[71] Hilico, L. *et al.* Preparing Single Ultra-cold Antihydrogen Atoms for Free-fall in GBAR. *Int. J. Mod. Phys. Conf. Ser.* **30**, 1460269 (2014).

[72] Amole, C. *et al.* Resonant Quantum Transitions in Trapped Antihydrogen Atoms. *Nature* **483**, 439–443 (2012).

[73] Setija, I. D. *et al.* Optical Cooling of Atomic Hydrogen in a Magnetic Trap. *Phys. Rev. Lett.* **70**, 2257–2260 (1993).

[74] Donnan, P. H., Fujiwara, M. C. & Robicheaux, F. A Proposal for Laser Cooling Antihydrogen Atoms. *J. Phys.* **B46**, 025302 (2013).

[75] Michan, J. M., Fujiwara, M. C. & Momose, T. Development of a Lyman-α Laser System for Spectroscopy and Laser Cooling of Antihydrogen. *Hyperfine Interact.* **228**, 77–80 (2014).

[76] Smorra, C. *et al.* BASE – The Baryon Antibaryon Symmetry Experiment. *Eur. Phys. J. ST* **224**, 3055–3108 (2015).

[77] Ulmer, S. *et al.* High-precision Comparison of the Antiproton-to-proton Charge-to-mass Ratio. *Nature* **524**, 196–199 (2015).

[78] DiSciacca, J. *et al.* One-Particle Measurement of the Antiproton Magnetic Moment. *Phys. Rev. Lett.* **110**, 130801 (2013).

[79] Nagahama, H. *et al.* Sixfold Improved Single Particle Measurement of the Magnetic Moment of the Antiproton. *Nature Commun.* **8**, 14084 (2017).

[80] Smorra, C. *et al.* A Parts-per-billion Measurement of the Antiproton Magnetic Moment. *Nature* **550**, 371–374 (2017).

[81] Hori, M. *et al.* Two-photon Laser Spectroscopy of Antiprotonic Helium and the Antiproton-to-electron Mass Ratio. *Nature* **475**, 484–488 (2011).

[82] Hori, M. *et al.* Buffer Gas Cooling of Antiprotonic Helium to 1.5 to 1.7 K, and Antiproton-to-electron Mass Ratio. *Science* **354**, 610–614 (2016).

[83] Corradini, M. *et al.* Measurement of the Antiproton-nucleus Annihilation Cross-section at Very Low Energies. *Hyperfine Interact.* **194**, 305–311 (2009).

[84] Bianconi, A. *et al.* Measurement of the Antiproton–Nucleus Annihilation Cross Section at 5.3 MeV. *Phys. Lett.* **B704**, 461–466 (2011).

[85] Aghai-Kozani, H. *et al.* Experimental Apparatus for Antiproton-Nucleus Annihilation Cross Section Measurements at Low Energy. *JPS Conf. Proc.* **18**, 011037 (2017).

[86] Malmberg, J. H. & deGrassie, J. S. Properties of Nonneutral Plasma. *Phys. Rev. Lett.* **35**, 577–580 (1975).

[87] Malmberg, J. H. & Driscoll, C. F. Long-Time Containment of a Pure Electron Plasma. *Phys. Rev. Lett.* **44**, 654–657 (1980).

[88] G. Greaves, R. & M. Surko, C. Antimatter Plasmas and Antihydrogen. *Physics of Plasmas - PHYS PLASMAS* **4** (1997).

[89] Sellner, S. *et al.* Improved Limit on the Directly Measured Antiproton Lifetime. *New J. Phys.* **19**, 083023 (2017).

[90] Huang, X. P., Anderegg, F., Hollmann, E. M., Driscoll, C. F. & O'Neil, T. M. Steady-State Confinement of Non-neutral Plasmas by Rotating Electric Fields. *Phys. Rev. Lett.* **78**, 875–878 (1997).

[91] Mills, A. P., Jr. & Gullikson, E. M. Solid Neon Moderator for Producing Slow Positrons. *Applied Physics Letters* **49**, 1121–1123 (1986).

[92] Surko, C. M., Leventhal, M. & Passner, A. Positron Plasma in the Laboratory. *Phys. Rev. Lett.* **62**, 901–904 (1989).

[93] Murphy, T. J. & Surko, C. M. Positron Trapping in an Electrostatic Well by Inelastic Collisions with Nitrogen Molecules. *Phys. Rev. A* **46**, 5696–5705 (1992).

[94] Danielson, J. R., Dubin, D. H. E., Greaves, R. G. & Surko, C. M. Plasma and Trap-based Techniques for Science with Positrons. *Rev. Mod. Phys.* **87**, 247–306 (2015).

[95] Knoll, G. F. *Radiation Detection and Measurement (4th Edition),* (Wiley, New York, NY, 2010).

[96] Andresen, G. B. *et al.* Antiproton, Positron, and Electron Imaging with a Microchannel Plate/Phosphor Detector. *Rev. Sci. Instrum.* **80**, 123701 (2009).

[97] Amole, C. *et al.* In-situ Electromagnetic Field Diagnostics with an Electron Plasma in a Penning-Malmberg Trap. *New J. Phys.* **16**, 013037 (2014).

[98] Eggleston, D. L., Driscoll, C. F., Beck, B. R., Hyatt, A. W. & Malmberg, J. H. Parallel Energy Analyzer for Pure Electron Plasma Devices. *Physics of Fluids B* **4**, 3432–3439 (1992).

[99] Mikhailik, V. B., Kapustyanyk, V., Tsybulskyi, V., Rudyk, V. & Kraus, H. Luminescence and Scintillation Properties of CsI - a Potential Cryogenic Scintillator. *Phys. Status Solidi* **B252**, 804 (2015).

[100] Andresen, G. B. *et al.* Evaporative Cooling of Antiprotons to Cryogenic Temperatures. *Phys. Rev. Lett.* **105**, 013003 (2010).

[101] Radics, B., Murtagh, D. J., Yamazaki, Y. & Robicheaux, F. Scaling Behavior of the Ground-state Antihydrogen Yield as a Function of Positron Density and Temperature from Classical-trajectory Monte Carlo Simulations. *Phys. Rev. A* **90**, 032704 (2014).

[102] Andresen, G. B. *et al.* Antihydrogen Annihilation Reconstruction with the ALPHA Silicon Detector. *Nucl. Instrum. Meth.* **A684**, 73–81 (2012).

[103] Hoecker, A. *et al.* TMVA - Toolkit for Multivariate Data Analysis. *arXiv e-prints* physics/0703039 (2007).

[104] Breiman, L. Random Forests. *Machine Learning* **45**, 5–32 (2001).

[105] Kim, Y. B., Hempstead, C. F. & Strnad, A. R. Critical Persistent Currents in Hard Superconductors. *Phys. Rev. Lett.* **9**, 306–309 (1962).

[106] Hilke, H. J. Time Projection Chambers. *Rept. Prog. Phys.* **73**, 116201 (2010).

[107] Capra, A. *et al.* Design of a Radial TPC for Antihydrogen Gravity Measurement with ALPHA-g. *JPS Conf. Proc.* **18**, 011015 (2017).

[108] Dellacasa, G. *et al.* ALICE: Technical Design Report of the Time Projection Chamber (2000).

[109] Ereditato, A. & Rubbia, A. The Liquid Argon TPC: A Powerful Detector for Future Neutrino Experiments and Proton Decay Searches. *Nucl. Phys. Proc. Suppl.* **154**, 163–178 (2006).

[110] Bruning, O. S. *et al. LHC Design Report.* CERN Yellow Reports: Monographs (CERN, Geneva, 2004).

[111] Courant, E. D. & Snyder, H. S. Theory of the Alternating Gradient Synchrotron. *Annals Phys.* **3**, 1–48 (1958).

[112] Russenschuck, S. *Field Computation for Accelerator Magnets: Analytical and Numerical Methods for Electromagnetic Design and Optimization* (Wiley-VCH, Weinheim, 2010).

[113] Weber, T. R., Danielson, J. R. & Surko, C. M. Electrostatic Beams from Tailored Plasmas in a Penning-Malmberg Trap. *Physics of Plasmas* **17**, 123507 (2010).

[114] R. Weber, T., R. Danielson, J. & M. Surko, C. Note: Electrostatic Beams from a 5 T Penning-Malmberg Trap. *Review of Scientific Instruments* **82**, 016104 – 016104 (2011).

[115] Hurst, N. C., Danielson, J. R. & Surko, C. M. Magnetic Field Extraction of Trap-based Electron Beams Using a High-permeability Grid. *Physics of Plasmas* **22**, 073503 (2015).

[116] Chen, F.F. *Introduction to Plasma Physics and Controlled Fusion* (Springer US).

[117] Reiser, M. *Theory and Design of Charged Particle Beams* (Wiley, New York, USA, 1995).

[118] Bellan, P. M. *Fundamentals of Plasma Physics* (Cambridge University Press, Cambridge, 2006).

[119] Gurnett, D. & Bhattacharjee, A. *Introduction to Plasma Physics: With Space, Laboratory and Astrophysical Applications* (Cambridge University Press, 2017).

[120] Knoop, M., Madsen, N. & Thompson, R. C. *Physics with Trapped Charged Particles: Lectures from the Les Houches Winter School* (2014).

[121] Piot, P. & Sun, Y. E. Generation and Dynamics of Magnetized Electron Beams for High-Energy Electron Cooling (2014).

[122] Aghion, S. *et al.* Positron Bunching and Electrostatic Transport System for the Production and Emission of Dense Positronium Clouds into Vacuum. *Nucl. Instrum. Meth.* **B362**, 86–92 (2015).

[123] Qin, H. *et al.* Why is Boris algorithm So Good? *Physics of Plasmas* **20** (2013).

[124] Birdsall, C. K. & Langdon, A. B. *Plasma Physics via Computer Simulation* (McGraw-Hill, Inc., New York, NY, USA, 1985).

[125] Vector Fields Limited, Kidlington, Oxford, OX5 1LH, UK. *OPERA-3D Reference Manual* (2017).

[126] Pulsar Physics, Burghstraat 47, 5614 BC Eindhoven, The Netherlands. *General Particle Tracer (GPT) Software Package* (2018). `http://www.pulsar.nl/gpt` [Accessed 18-April-2019].

[127] Pöplau, G., van Rienen, U., van der Geer, B. & De Loos, M. Multigrid Algorithms for the Fast Calculation of Space-Charge Effects in Accelerator Design. *Magnetics, IEEE Transactions on* **40**, 714 – 717 (2004).

[128] van der Geer, B., Luiten, J., De Loos, M., Pöplau, G. & van Rienen, U. 3D Space-charge Model for GPT Simulations of High-brightness Electron Bunches. *Institute of Physics Conference Series* **175**, 101–110 (2003).

[129] Fornberg, B. Generation of Finite Difference Formulas on Arbitrarily Spaced Grids. *Mathematics of Computation - Math. Comput.* **51**, 699–699 (1988).

[130] Matsumoto, M. & Nishimura, T. Mersenne Twister: a 623-dimensionally Equidistributed Uniform Pseudo-random Number Generator. *ACM Transactions on Modeling and Computer Simulation* **8**, 3–30 (1998).

[131] Thain, D., Tannenbaum, T. & Livny, M. Distributed Computing in Practice: the Condor Experience. *Concurrency - Practice and Experience* **17**, 323–356 (2005).

[132] Delta Elektronika B.V., Vissersdijk 4, 4301 ND Zierikzee, Netherlands. *SM1500 Series Data Sheet* (2019). `https://www.delta-elektronika.nl/en/` [Accessed 17-March-2019].

[133] National Instruments Corporation (U.K.) Ltd., Measurement House, Newbury, Berkshire RG14 2PZ. *NI cRIO-9035 User Manual* (2016). `http://www.ni.com/en-gb/support/model.crio-9035.html` [Accessed 03-April-2019].

[134] National Instruments Corporation (U.K.) Ltd., Measurement House, Newbury, Berkshire RG14 2PZ. *NI-9264 Data Sheet* (2017). `http://www.ni.com/pdf/manuals/378025a_02.pdf` [Accessed 03-April-2019].

[135] National Instruments Corporation (U.K.) Ltd., Measurement House, Newbury, Berkshire RG14 2PZ. *NI-9205 Data Sheet* (2017). `http://www.ni.com/pdf/manuals/378020a_02.pdf` [Accessed 03-April-2019].

[136] National Instruments Corporation (U.K.) Ltd., Measurement House, Newbury, Berkshire RG14 2PZ. *NI-9403 Data Sheet* (2015). http://www.ni.com/pdf/manuals/374069a_02.pdf [Accessed 03-April-2019].

[137] National Instruments Corporation (U.K.) Ltd., Measurement House, Newbury, Berkshire RG14 2PZ. *NI-9870 Data Sheet* (2014). http://www.ni.com/datasheet/pdf/en/ds-276 [Accessed 03-April-2019].

[138] Tektronix UK Ltd., Wokingham Road, Berkshire, RG42 1NG, United Kingdom. *Model 2700 Multimeter / Switch System User's Manual* (2016). https://download.tek.com/manual/2700-900-01K_Feb_2016.pdf [Accessed 03-April-2019].

[139] Tektronix UK Ltd., Wokingham Road, Berkshire, RG42 1NG, United Kingdom. *Model 7700, 7702 and 7703 Multiplexer Modules* (2015). https://download.tek.com/manual/PA-695(D-Oct2006)(7700).pdf [Accessed 03-April-2019].

[140] TRIUMF, Vancouver, British Columbia, Canada. *Maximum Integrated Data Acquisition System (MIDAS) Wiki* (2019). https://midas.triumf.ca/ [Accessed 03-April-2019].

[141] Surko, C. *Accumulation, Storage and Manipulation of Large Numbers of Positrons in Traps I - The Basics*, chap. 4, 83–128 (2014).

[142] Andresen, G. B. *et al.* Centrifugal Separation and Equilibration Dynamics in an Electron-Antiproton Plasma. *Physical review letters* **106**, 145001 (2011).

[143] So, C. *Antiproton and Positron Dynamics in Antihydrogen Production*. Ph.D. thesis, University of California, Berkeley (2014).

[144] Leefer, N. *et al.* Investigation of Two-frequency Paul traps for Antihydrogen Production. *Hyperfine Interact.* **238**, 12 (2017).

[145] Kuroda, N. *et al.* Development of a Monoenergetic Ultraslow Antiproton Beam Source for High-precision Investigation. *Phys. Rev. ST Accel. Beams* **15**, 024702 (2012).

[146] Blaum, K. High-Accuracy Mass Spectrometry with Stored Ions. *Physics Reports10.Dr* **42520** (2006).

[147] Repp, J. *et al.* PENTATRAP: a Novel Cryogenic Multi-Penning-trap Experiment for High-precision Mass Measurements on Highly Charged Ions. *Applied Physics B: Lasers and Optics* **107**, 983–996 (2012).

[148] Kreim, S. *et al.* Recent Exploits of the ISOLTRAP Mass Spectrometer. *Nucl. Instrum. Meth.* **B317**, 492–500 (2013).